NECMETTİN ERBAKAN ÜNİVERSİTESİ

FEN VE MÜHENDİSLİK BİLİMLERİ DERGİSİ

NECMETTIN ERBAKAN UNIVERSITY JOURNAL OF SCIENCE AND ENGINEERING

Yıl/Year:2025 Cilt/Volume:7 Sayı/Issue:1 E-ISSN: 2667-7989

NEU PRESS

NECMETTİN ERBAKAN ÜNİVERSİTESİ FEN VE MÜHENDİSLİK BİLİMLERİ DERGİSİ
NECMETTIN ERBAKAN UNIVERSITY JOURNAL OF SCIENCE AND ENGINEERING
E-ISSN: 2667-7989
Cilt/*Volume*: 7, Sayı/*Issue*: 1, (Nisan/*April*, 2025)
Uluslararası Hakemli Dergi/*International Referred Journal*

İmtiyaz Sahibi/*Holder of Concession*
Necmettin Erbakan Üniversitesi Rektörü
Rector of Necmettin Erbakan University
Prof. Dr. Cem ZORLU

Yazışma Adresi/*Correspondence Address*
Necmettin Erbakan Üniversitesi Rektörlüğü, 42090, Meram, Konya, Türkiye
Telefon/*Phone*: +90 (332) 221 05 00 **web:** www.dergipark.gov.tr/neufmbd **e-posta/*e-mail*:** neufmbd@erbakan.edu.tr

Necmettin Erbakan Üniversitesi Fen ve Mühendislik Bilimleri Dergisi, yılda üç kez yayınlanan uluslararası hakemli bir dergidir.
Necmettin Erbakan University Journal of Science and Engineering is an international referred journal published three issues per year.

İÇİNDEKİLER/*CONTENTS*

FEN ve MÜHENDİSLİK BİLİMLERİ DERGİSİ

Cilt/Vol: 7 Sayı/No: 1 Yıl/Year: 2025 Araştırma Makalesi/Research Article e-ISSN: 2667-7989

https://doi.org/10.47112/neufmbd.2025.70

Timokinon ve Timol'ün Histamin Reseptörleri Üzerinde Moleküler Kenetleme Analizi

Emre Fatih EDİZ [1*] Meltem DEMİREL KARS [2]

[1] Necmettin Erbakan University, Research and Application Center of Science and Technology (BITAM), Konya, Türkiye

[2] Necmettin Erbakan University, Faculty of Engineering, Department of Biomedical Engineering, Konya, Türkiye

Makale Bilgisi

Geliş Tarihi: 31.01.2024
Kabul Tarihi: 30.06.2024
Yayın Tarihi: 30.04.2025

Anahtar Kelimeler:
Timokinon,
Timol,
Histamin reseptörleri,
Moleküler kenetlenme,
Nigella sativa L.

ÖZET

Çörek otu veya *N. sativa* L., dünya çapında geniş bir alana yayılmış olan değerli bitkiler arasında popüler bir şifalı ottur. Geleneksel tıpta, solunum, sindirim ve kardiyovasküler sistemlerle ilgili hastalıkları tedavi etmek için kullanılmıştır. Timokinon, özellikle *Nigella sativa* L. bitkisinde bulunan bitki kökenli bir bileşik olan timolün türevidir ve antioksidan, anti-enflamatuar ve antitümör özelliklere sahip doğal bir fenolik bileşiktir. Timol ise bir monoterpendir ve çeşitli bitkilerde doğal olarak bulunan bir uçucu yağ bileşenidir. Antioksidan, antiseptik, antimikrobiyal ve anti-enflamatuar özelliklere sahiptir. Timokinon ve timol, anti-alerjik etkilere sahiptir ve alerjik reaksiyonları hafifletmek veya önlemek için kullanılan bileşenler olarak bilinir. Bu çalışmada insan vücudunda bulunan alerji reseptörü olan H1R, H2R, H3R, and H4R histamine reseptörleri tercih edilmiştir. Yapılan moleküler yerleştirme çalışmaları sonucunda timokinon ve timolün H1R, H2R, H3R, and H4R histamine reseptörleri için önemli afiniteye sahip bir molekül olduğu gösterilmiştir.

Molecular Docking Analysis of Thymoquinone and Thymol on Histamine Receptors

Article Info

Received: 31.01.2024
Accepted: 30.06.2024
Published: 30.04.2025

Keywords:
Thymoquinone,
Thymol,
Histamine receptors,
Molecular docking,
Nigella sativa L.

ABSTRACT

Black cumin or *N. sativa* L. is a popular medicinal herb among the valuable plants, native to a wide range of areas around the world. In traditional medicine, it was used to treat diseases related to the respiratory, digestive, and cardiovascular systems. Thymoquinone is a derivative of thymol, a plant-derived compound primarily found in *Nigella sativa* L., and it is a natural phenolic compound with antioxidant, anti-inflammatory, and antitumor properties. Thymol, on the other hand, is a monoterpene and a volatile oil component naturally occurring in various plants. It possesses antioxidant, antiseptic, antimicrobial, and anti-inflammatory properties. Both thymoquinone and thymol exhibit anti-allergic effects and are known as components used to alleviate or prevent allergic reactions. In this study, the allergy receptors present in the human body, namely H1R, H2R, H3R, and H4R histamine receptors, were specifically targeted. Molecular docking studies revealed that thymoquinone and thymol exhibited significant affinity towards H1R, H2R, H3R, and H4R histamine receptors, indicating their potential as molecules of importance in the context of allergic reactions.

Bu makaleye atıfta bulunmak için:

Ediz, E.F. & Demirel Kars, M. (2025). Molecular docking analysis of thymoquinone and thymol on histamine receptors. *Necmettin Erbakan University Journal of Science and Engineering*, *7*(1), 1-11. https://doi.org/10.47112/neufmbd.2025.70

***Sorumlu Yazar:** Emre Fatih Ediz, *emrefatihediz@gmail.com*

INTRODUCTION

The use of plants as medicine dates back to the beginning of human history. Among the promising medicinal plants, *Nigella Sativa L*. is considered a sacred seed in Islamic countries, believed to possess the cure for every ailment except death. Both Ibn Sina and Hippocrates accorded special importance to black cumin in their prescriptions [1]. Black cumin or *N. sativa L*. is a popular medicinal herb among the valuable plants, native to a wide range of areas around the world [2]. In traditional medicine, it was used to treat diseases related to the respiratory, digestive, and cardiovascular systems. Moreover, many publications have exhibited a wide range of potential beneficial effects for *N. sativa*, such as antiviral, anti-inflammatory, hypotensive, hypoglycemic, and antitumor properties. Furthermore, the beneficial effects of it have been reported by various studies for some allergic disorders such as allergic asthma, allergic diarrhea, allergic rhinitis, and allergic conjunctivitis [3]. These beneficial properties are related to certain phytochemicals found in *N. sativa*, such as thymoquinone, terpenes, saponins, flavonoids, and essential oils [4]. Thymoquinone is present in *N. sativa* oil seeds as the highest amount of volatile oil. The most beneficial features of *N. sativa* are essentially related to thymoquinone. According to research, thymoquinone exhibits several important health-friendly properties, including antioxidant activity, anti-inflammatory properties, immunomodulatory effects, antihistaminic effects, antimicrobial effects and antitumor effects. Moreover, it has been reported that thymoquinone demonstrates gastroprotective, hepatoprotective, nephroprotective, and neuroprotective effects [5]. Thymol is another important bioactive compound in *N. sativa*. It has antimicrobial, anti-inflammatory, antitumor and fungicidal effects [6,7]. Histamine was formally defined by Windaus and Vogt in 1907, with its biological roles later elucidated by Sir Henry Dale and Laidlaw in 1910 [8]. Until 1932, the role of histamine in allergic reactions was not clearly defined. However, from that point onward, researchers identified histamine as a key regulator of allergic reactions [9]. On the other hand, histamine can be considered as one of the principal mediators of the inflammatory response [10]. The H1 receptor is implicated in early-type hypersensitivity reactions, encompassing symptoms such as itching, redness, swelling, rhinitis, bronchospasm, anaphylaxis, conjunctivitis, and urticaria. Additionally, it exerts central nervous system effects, impacting sleep, attention, convulsions, and food consumption. The H2 receptor contributes to immune system activities, including mast cell degranulation, antibody synthesis, and Th1 cytokine production. The H3 receptor plays a role in the regulation of the sleep-wake cycle, cognition and learning, inflammation, and energy level maintenance. As for H4R, it is involved in functions such as immune cell chemotaxis, cytokine production, autoimmune diseases, and the modulation of colon and breast cancer, as well as nociception [11]. The advent of computer-based approaches has transformed research in life sciences, alleviating the financial burden associated with laboratory expenses and animal experimentation for medical institutions. In silico methods prove valuable for classifying proteins according to their structure and function, offering assistance in the examination of molecular interactions. Molecular docking becomes a valuable tool for assessing potential ligands and receptor complexes in natural therapeutics, contributing significantly to future studies in genetic engineering, biotechnology, and drug development [12]. Thymoquinone and thymol are known compounds that may possess anti-allergic potential. Therefore, performing molecular docking with histamine receptors aims to understand their effects on histamine receptors and elucidate potential anti-allergic mechanisms. This is the first study on the application of molecular docking of thymoquinone and thymol against Histamine 1, Histamine 2, Histamine 3, and Histamine 4 receptors. In this study, the aim is to understand and delineate how the molecular docking of histamine receptors with thymoquinone and thymol affects the allergenic reactions of cells.

MATERIALS AND METHODS

Preparation of Receptors and Ligands

The crystal structures of H1R, H2R, H3R, and H4R histamine receptors were obtained from the Protein Data Bank (PDB) [13] with the following accession numbers: 3RZE, 7UL3, 7F61, and 3P0G, respectively. The resolutions of these receptors were 3.10 Å, 3.00 Å, 2.60 Å, and 3.50 Å, respectively.

To prepare the receptors for molecular docking, the water molecules were removed, and hydrogen atoms and Kollman charges were added to the protein structures using AutoDockTools-1.5.7 software. The structures were then optimized, and output files were obtained in PDBQT format.

The ligands used in the molecular docking, thymoquinone and thymol, were obtained from the PubChem databases (Thymoquinone: 10281 and Thymol: 6989). The molecular structures of thymoquinone and thymol were optimized using PerkinElmer Chemdraw V.22.0.0.22 at the Hartree-Fock theory level prior to the molecular docking. In summary, the crystal structures of histamine receptors H1R, H2R, H3R, and H4R were obtained from PDB. The receptors were then prepared for molecular docking by removing water molecules, adding hydrogen atoms and Kollman charges, and optimizing the protein structures. The ligands, thymoquinone and thymol, were obtained from PubChem, and their molecular structures were optimized prior to the molecular docking.

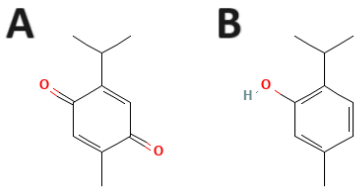

Figure 1

Molecular structures of A) thymoquinone [14] and B) thymol [15]

Molecular Docking

Molecular docking was performed using AutoDock Vina v1.1.2. The values for the dimensions of the grid box and the coordinates of its center are presented in Table 1. The dimensions of the grid box were selected to fully encompass the entire proteins for blind docking. The positions of receptor-ligand binding were visualized using Pymol Edu v.2.5.4, and the resulting binding structures were identified in 2D visual form using the BIOVIA Discovery Studio 2021 software [16,17].

Table 1

Grid box dimensions and center coordinate values for thymoquinone and thymol

RECEPTOR NAME	CODE	Center Coordinate Values (X, Y, Z)	Grid Box Values (X, Y, Z)
H1R	3RZE	27, 30, 46	70, 70, 97
H2R	7UL3	165, 165, 185	47, 40, 59
H3R	7F61	-19, 46, 0	41, 94, 42
H4R	3P0G	42, 15, 11	101, 48, 62

Determination of Pharmacokinetic/ADMET Profile

The ADMET (absorption, distribution, metabolism, excretion, and toxicity) profiles of thymoquinone and thymol were determined using the SwissADME online software from the Swiss Institute of Bioinformatics [18] to assess their pharmacokinetic properties. The SMILES strings of thymoquinone and thymol were calculated using the PubChem OEChem V2.3.0 software and shown in Table 2. The canonical SMILES strings of thymoquinone and thymol were input into the online software to calculate various parameters, including blood-brain barrier permeability, Log Kp value, binding to P-

glycoprotein, inhibition of cytochrome P450 (CYP450), clearance and volume distribution, Lipinski's rule, and bioavailability. Additionally, the *in silico* toxicity of thymoquinone and thymol was evaluated based on the OECD guidelines for oral LD50 in mice using the GUSAR-Online web-based server [19].

Table 2
SMILES strings of thymoquinone and thymol

LIGAND	SMILES STRINGS
thymoquinone	[H]C1=C(C(=O)C([H])=C(C1=O)C([H])(C([H])([H])[H])C([H])([H])[H])C([H])([H])[H]
thymol	[H]OC1=C(C([H])=C([H])C(=C1[H])C([H])([H])[H])C([H])(C([H])([H])[H])C([H])([H])[H]

RESULTS

Thymoquinone and thymol molecules were molecularly docked to four different histamine receptors (H1R, H2R, H3R, and H4R) at the molecular level, and the binding energies were calculated. The highest affinity values for each receptor were shown in Table 3 for thymoquinone and in Table 4 for thymol.

Table 3
Molecular docking results of thymoquinone to target receptors

RECEPTOR CODE	RECEPTOR NAME	BINDING ENERGY (KCAL/MOL)	RMSD Å	INTERACTIONS	INTERACTION TYPE
3RZE	H1R	-5.3	1.859	LEU A:201, LEU A:205, PHE A:119, ILE A:120, PHE A:116, ALA A:151, LEU A:154, PRO A:202	Van Der Waals, Pi-Sigma
7UL3	H2R	-5.5	1.197	LEU A:124, PRO A:123, PRO A:127, ALA A:119, TYR A:126, LEU A:229, ARG A:116, ILE A:232	Van Der Waals, Pi-Pi, Pi-Alkyl, Conventional Hydrogen Bond, Pi-Sigma
7F61	H3R	-6.4	2.333	ALA A:372, PHE A:207, PHE A:211, TRP A:371, GLY A:368, PRO A:210, PHE A:367, VAL A:214, VAL A:364, ILE A:125, THR A:215	Van Der Waals, Pi-Pi
3P0G	H4R	-6.2	1.245	LEU A:340, LEU A:53, VAL A:54, GLY A:50, PRO A:323, LEU A:324, CYS A:327, PHE A:336, ARG A:333	Van Der Waals, Pi-Pi, Conventional Hydrogen Bond

Table 4
Molecular docking results of thymol to target receptors

RECEPTOR CODE	RECEPTOR NAME	BINDING ENERGY (KCAL/MOL)	RMSD Å	INTERACTIONS	INTERACTION TYPE
3RZE	H1R	-5.8	3.427	ILE A:160, PRO A:161, PHE A:190, VAL A:187, HIS A:167, PHE A:184, TRP A:189	Van der Waals, Pi-Pi, Alkyl, Pi-Alkyl
7UL3	H2R	-5.9	2.019	FO A:9401, CYS A:102, VAL A:99, TYR A:250, ASP A:186, GLY A:187, PHE A:254, THR A:190, PHE A:251, THR A:103, TRP A:247, ASP A:98, VAL A:176	Van der Waals, Unfavorable Bump, Pi-Pi, Pi-Alkyl, Pi-Sulfur, Pi-Sigma
7F61	H3R	-6.3	1.829	SER A:365, VAL A:364, GLY A:368, VAL A:214, TRP A:371, PRO A:210, PHE A:211, PHE A:367, THR A:215, ILE A:125	Van Der Waals, Pi-Sigma, Alkyl, Pi-Alkyl
3P0G	H4R	-6.4	0.997	ARG A:333, PHE A:336, CYS A:327, ARG A:328, LEU A:324, PRO A:323, GLY A:50, LEU A:53, VAL A:54	Van der Waals, Conventional Hydrogen Bond, Pi-Pi, Alkyl

The highest affinity binding position of thymoquinone to the H1R receptor is shown and the binding interactions are illustrated in Figure 2. Thymoquinone binds to the H1R receptor with an affinity of -5.3 kcal/mol.

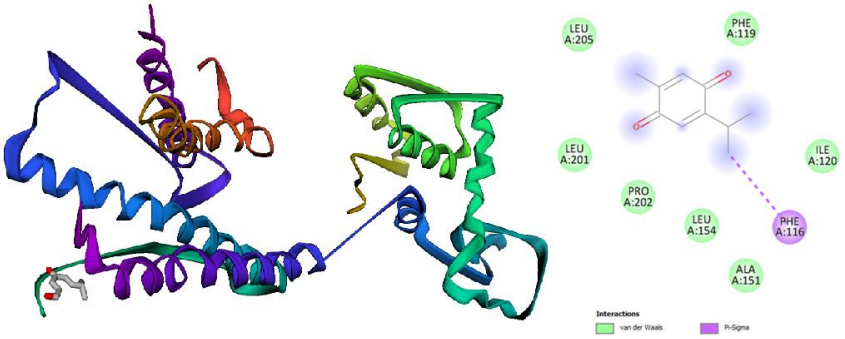

Figure 2

Interaction of the thymoquinone analog with the H1R receptor with the highest energy and two-dimensional depiction of thymoquinone binding interactions with H1R receptor

Thymoquinone's highest affinity binding position to the H2R receptor is shown and the binding interactions are illustrated in Figure 3. Thymoquinone binds to the H2R receptor with a binding energy of -5.5 kcal/mol.

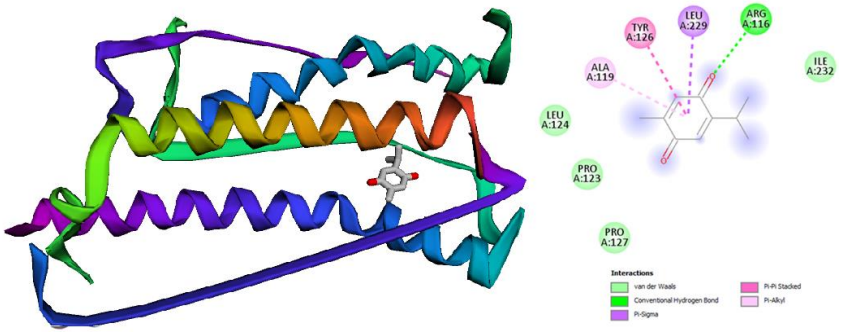

Figure 3

Interaction of the thymoquinone analog with the H2R receptor showing the highest energy conformation and two-dimensional representation of the binding interactions of thymoquinone with the H2R receptor

The highest affinity binding position of thymoquinone to the H3R receptor is depicted and the binding interactions are illustrated in Figure 4. Thymoquinone binds to the H3R receptor with a binding energy of -6.4 kcal/mol.

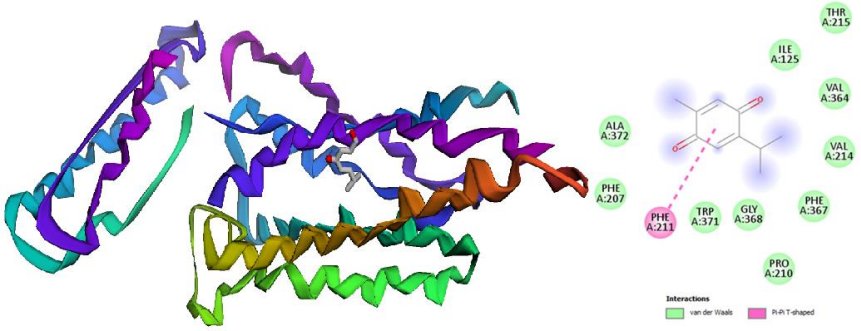

Figure 4

Interaction of the highest energy thymoquinone analog with the H3R receptor and two-dimensional representation of the interaction of thymoquinone with the H3R receptor

The binding position of thymoquinone with the highest affinity to the H4R receptor is shown and along with the binding interactions displayed in Figure 5. Thymoquinone has a binding affinity of -6.2

kcal/mol to the H4R receptor.

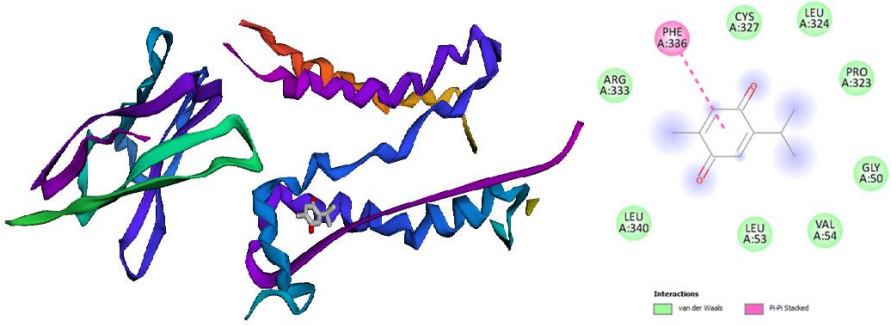

Figure 5

Interaction of the highest energy thymoquinone analogue with the H4R receptor and two-dimensional depiction of the binding interactions of thymoquinone with the H4R receptor

The binding position of thymol with the highest affinity to the H1R receptor is shown and along with the binding interactions displayed in Figure 6. Thymol has a binding affinity of -5.8 kcal/mol for the H1R receptor.

Figure 6

Interaction of the highest energy thymol analogue with the H1R receptor and two-dimensional depiction of the binding interactions of thymol with the H1R receptor.

The binding position of thymol with the highest affinity to the H2R receptor is shown and along with the binding interactions displayed in Figure 7. Thymol has a binding affinity of -5.9 kcal/mol for the H2R receptor.

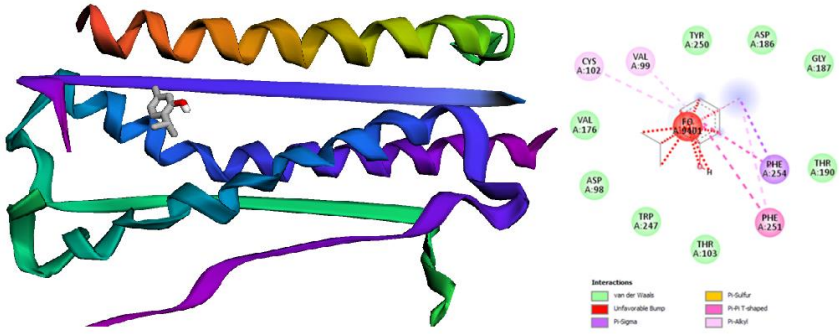

Figure 7

Interaction of the highest energy thymol analogue with the H2R receptor and two-dimensional depiction of the binding interactions of thymol with the H2R receptor.

The binding position of thymol with the highest affinity to the H3R receptor is shown and along with the binding interactions displayed in Figure 8. Thymol has a binding affinity of -6.3 kcal/mol for the H3R receptor.

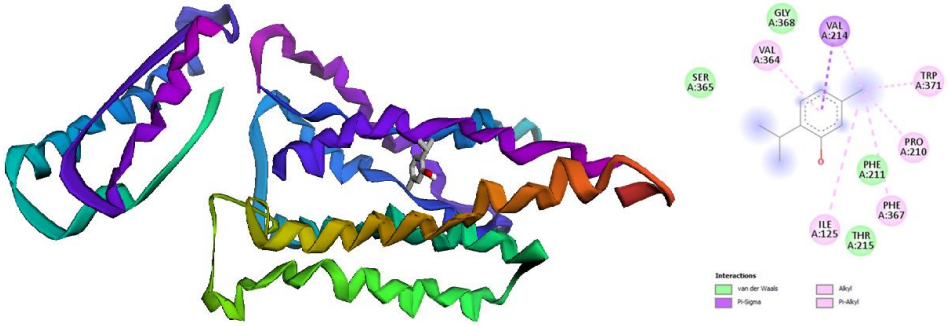

Figure 8

Interaction of the highest energy thymol analogue with the H3R receptor and two-dimensional depiction of the binding interactions of thymol with the H3R receptor.

The binding position of thymol with the highest affinity to the H4R receptor is shown and along with the binding interactions displayed in Figure 9. Thymol has a binding affinity of -6.4 kcal/mol for the H4R receptor.

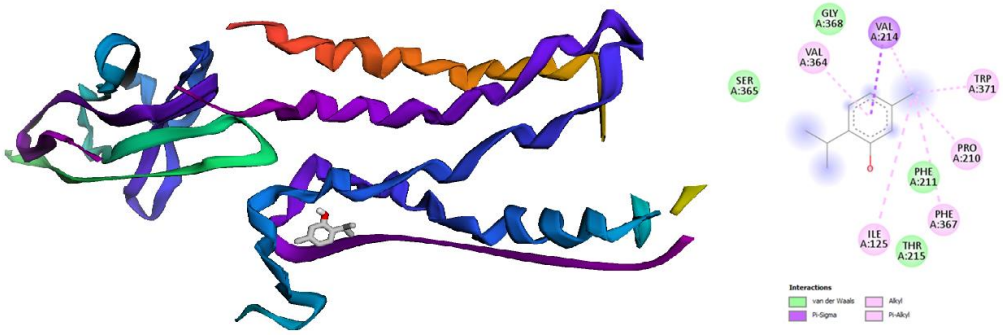

Figure 8

Interaction of the highest energy thymol analogue with the H4R receptor and two-dimensional depiction of the binding interactions of thymol with the H4R receptor.

Thymoquinone and thymol's pharmacokinetic/ADMET profile results, which were conducted to determine whether they can be considered as potential drug-like compounds, are listed in Table 5.

Table 5

ADMET parameters and acute oral toxicity of Thymoquinone and Thymol predicted by SwissADME and GUSAR online estimations

PARAMETER	THYMOQUINONE	THYMOL
Blood-brain barrier (BBB) permeability	BBB+	BBB+
Gastrointestinal drug absorption (GI-DA)	High	High
P-glycoprotein (P-gp) substrate	Non-substrate	Non-substrate
CYP1A2 inhibitor	No	Yes
CYP2C19 inhibitor	No	No
CYP2C9 inhibitor	No	No
CYP2D6 inhibitor	No	No
CYP3A4 inhibitor	No	No
Daily Kp (skin permeability)	−5.74 cm/sn	-4.87 cm/sn
Lipinski's Rule	Acceptable	Acceptable
(MW ≤ 500, logP ≤5, HBD ≤5, HBA ≤10)	MLOGP>4.15	MLOGP>4.15
Bioavailability score	0.55	0.55
Rat LD_{50} lethal dose (mg/kg) / OECD Class	1979 / (IV)	1303 / (IV)

DISCUSSION AND CONCLUSIONS

In this study, the specific allergy receptors present in the human body, namely H1R, H2R, H3R, and H4R histamine receptors, were targeted. Molecular docking studies revealed that thymoquinone and thymol exhibited significant affinity towards H1R, H2R, H3R, and H4R histamine receptors, indicating their potential importance as molecules in the context of allergic reactions.

Within the scope of this study, thymol and thymoquinone molecules were modelled in a computer environment, and their binding to histamine receptors and possible interactions are discussed in the conclusion section. Table 3 demonstrates that thymoquinone has the lowest binding energy among the target receptors and Table 4 illustrates the lowest binding energies among the target receptors for thymol. As a result of docking, the H3 receptor exhibits the highest affinity. When the RMSD is high, as shown in Figure 2, thymoquinone exhibits a strong affinity for binding to the active site. However, due to the presence of methyl groups in its structure on the receptors ALA A:372, PHE A:207, PHE A:211, TRP A:371, GLY A:368, PRO A:210, PHE A:367, VAL A:214, VAL A:364, ILE A:125, and THR A:215, there is a steric hindrance that results in a high value of 2,333 A in the same plane as the amino acid groups. This is the structure of thymoquinone, with an RMSD value of 1.245 and a bond energy of -6.2 kcal/mol to its active site, LEU A:340, LEU A:53, VAL A:54, GLY A:50, PRO A:323, and LEU in its active region. Van der Waals, Pi-Pi, and conventional hydrogen bonds involving structures A:324, CYS A:327, PHE A:336, and ARG A:333 suggest a preference for the H4R receptor, indicating selective blocking. In Table 4, ARG A:333, PHE A:336, CYS A:327, ARG A:328, LEU A:324, and PRO are located in the active site with a binding energy of -6.4 kcal/mol to H4R and 0.997 RMSD of the thymol target receptor. A:323, GLY A:50, LEU A:53, VAL A:54, and Van der Waals, Conventional Hydrogen Bond, Pi-Pi, and Alkyl interactions with amino acids in the region closer to the active center, compared to the thymoquinone structure, showed no steric effect as much as thymoquinone. In Figure 7, FO9401 exhibits an interaction classified as an Unfavorable Bump. Such interactions typically involve physical clashes or steric hindrances between molecules. This scenario can prevent the molecules from aligning or binding properly, thereby negatively impacting the overall binding affinity. The binding position of FO9401 may involve one or more of these unfavorable interactions. Consequently, the interaction between FO9401 and the H2R receptor is characterized as unfavorable. It is shown in Figure 9 that it adapts more to the active center conformation. Both thymoquinone and thymol exhibit similar properties in terms of ADMET parameters and oral toxicity trials (Table 5). Both thymokinon and thymol possess the ability to cross the blood-brain barrier (BBB+), indicating their potential effects on the central nervous system [20]. Both compounds are highly absorbed from the gastrointestinal system, suggesting that they could possess high bioavailability when administered orally [21]. Thymoquinone and thymol are not substrates of P-glycoprotein, meaning they are not actively pumped out of cells, which may suggest that their effects could be more prolonged. Specifically, thymoquinone has been shown not to inhibit any CYP isozymes, indicating a low potential for interactions with other drugs [22]. However, thymol has slower skin permeability compared to thymoquinone. Herein, we suggest that inhibiting CYP1A2, one of the most crucial enzymes in the microsomal P450 system, may extend the bioavailability of thymol-based drugs. In particular, we suggest that the thymol-based formulations may serve as an alternative to chemically synthesized drugs, for the symptomatic treatment of allergic asthma, pruritus, and dermatitis symptoms, as Histamine H4R receptor antagonists. In the existing literature, Badary et al. (1998) reported in their study that the LD50 value of thymoquinone was determined to 2400 mg/kg (1520-3770 mg/kg) following oral administration [15]. This value surpasses the prediction obtained through the GUSAR online tool. In a study conducted by Tisserand and Young in 2013, an acute toxicity investigation associated with oral administration of thymol revealed an LD50 dose of 1220 mg/kg [16]. The GUSAR online prediction estimated LD50 values lower than the in vivo experimental results, with a dose value of 1979 mg/kg for thymoquinone and 1303 mg/kg for thymol.

The results obtained from GUSAR online prediction align with the findings of in vitro studies. Considering the results, predictions emerged from in silico analyses are noteworthy as such they ease to estimate the interactions of thymol and thymoquinone based drugs to a considerable extent and reduce the number of animal experiments during drug development.

Acknowledgements
We gratefully acknowledge Necmettin Erbakan University R.A.C. of Science and Technology (BITAM) for their support.

Ethical Statement
The present study is an original research article designed and produced by the authors.

Author Contributions
Research Design (CRediT 1) E.E. (%50) - M.D.K. (%50)
Data Collection (CRediT 2) E.E. (%50) - M.D.K. (%50)
Research - Data Analysis - Validation (CRediT 3-4-6-11) E.E. (%50) - M.D.K. (%50)
Writing the Article (CRediT 12-13) Author 1 E.E. (%50) - M.D.K. (%50)
Revision and Improvement of the Text (CRediT 14) E.E. (%50) - M.D.K. (%50)

Financing
This research was not supported by any public, commercial, or non-profit organization.

Conflict of interest
The authors declare no conflict of interest for the present study.

Sustainable Development Goals (SDG)
Sustainable Development Goals: Not supported.

REFERENCES

[1] S. Çakmakçı, Y. Çakır, Çörekotu (Nigella sativa L.): Bileşimi, gıda sanayinde kullanımı ve sağlık üzerine etkileri, *Akademik Gıda / Academic Food Journal*. 9 (2011), 61-69.

[2] K. Hayashi, N. Kato, M. Kato, K. Ishikawa, Impacts of channel direction on bone tissue engineering in 3D-printed carbonate apatite scaffolds, *Materials and Design*. 204 (2021). doi:10.1016/j.matdes.2021.109686

[3] S. Saadat, M.R. Aslani, V. Ghorani, R. Keyhanmanesh, M.H. Boskabady, The effects of Nigella sativa on respiratory, allergic and immunologic disorders, evidence from experimental and clinical studies, a comprehensive and updated review, *Phytotherapy Research*. 35 (2021), 2968-2996. doi:10.1002/ptr.7003

[4] Z. Li, Y. Wang, Q. Xu, J. Ma, X. Li, J. Yan, Y. Tian, Y. Wen, T. Chen, Nigella sativa and health outcomes: An overview of systematic reviews and meta-analyses, *Frontiers in Nutrition*. 10 (2023). doi:10.3389/fnut.2023.1107750

[5] S. Darakhshan, A. Bidmeshki Pour, A. Hosseinzadeh Colagar, S. Sisakhtnezhad, Thymoquinone and its therapeutic potentials, *Pharmacological Research*. 95-96 (2015), 138-158. doi:10.1016/j.phrs.2015.03.011

[6] G. Avci, A. Bülbül, Çörek Otu Tohumu Esansiyel Yağının Antioksidan Etkinliğinin in vitro Yöntemlerle Araştırılması, *Avrasya Sağlık Bilimleri Dergisi*. 4 (2021) 154-161. doi:10.53493/avrasyasbd.862336

[7] Ş. Yildiz, S. Turan, Timokinon, Timol ve Karvakrolün Antioksidan Aktiviteleri ve Lipit Oksidasyonunu Önleme Kapasiteleri, *Atatürk Üniversitesi Ziraat Fakültesi Dergisi*. 52(1) (2021), 108-118. doi:10.17097/ataunizfd.773499

[8] G. Barger, H. Dale, Chemical structure and sympathomimetic action of amines, *The Journal of Physiology*. 41 (1910), 19-59. doi:10.1113/jphysiol.1910.sp001392

[9] P. Lieberman, The basics of histamine biology, *Annals of Allergy, Asthma and Immunology*. 106 (2011). doi:10.1016/j.anai.2010.08.005

[10] T. Moriguchi, J. Takai, Histamine and histidine decarboxylase: Immunomodulatory functions and regulatory mechanisms, *Genes to Cells*. 25 (2020), 443-449. doi:10.1111/gtc.12774

[11] A.F. Kalpaklıoğlu, İ. Koca Kalkan, A. Baççıoğlu Kavut, Histamin ve antihistaminler, *Turkiye Klinikleri Immunology Allergy-Special Topics*. 5 (2012), 12-24.

[12] M. Moradi, R. Golmohammadi, A. Najafi, M. Moosazadeh Moghaddam, M. Fasihi-Ramandi, R. Mirnejad, A contemporary review on the important role of in silico approaches for managing different aspects of COVID-19 crisis, *Informatics in Medicine Unlocked*. 28 (2022). doi:10.1016/j.imu.2022.100862

[13] H.M. Berman, J. Westbrook, Z. Feng, G. Gilliland, T.N. Bhat, H. Weissig, I.N. Shindyalov, P.E. Bourne, The protein data bank, *Nucleic Acids Research*. 28 (2000), 235-242. doi:10.1093/nar/28.1.235

[14] S. Pagola, A. Benavente, A. Raschi, E. Romano, M.A.A. Molina, P.W. Stephens, Crystal structure determination of thymoquinone by high-resolution x-ray powder diffraction, *AAPS PharmSciTech*. 5 (2004). doi:10.1208/pt050228

[15] E. Zhou, Y. Fu, Z. Wei, Y. Yu, X. Zhang, Z. Yang, Thymol attenuates allergic airway inflammation in ovalbumin (OVA)-induced mouse asthma, *Fitoterapia*. 96 (2014), 131-137. doi:10.1016/j.fitote.2014.04.016

[16] E.F. Ediz, M. Demirel Kars, Moleküler yerleştirme yöntemi ile kanabidiolün reseptör-ligant etkileşiminin incelenmesi, *Karadeniz Fen Bilimleri Dergisi*. 13 (2023), 398-414. doi:10.31466/kfbd.1214649

[17] W. Suttithumsatid, M.A. Shah, S. Bibi, P. Panichayupakaranant, α-Glucosidase inhibitory activity of cannabidiol, tetrahydrocannabinol and standardized cannabinoid extracts from Cannabis sativa, *Current Research in Food Science*. 5 (2022), 1091-1097. doi:10.1016/j.crfs.2022.07.002

[18] A. Daina, O. Michielin, V. Zoete, SwissADME: A free web tool to evaluate pharmacokinetics, drug-likeness and medicinal chemistry friendliness of small molecules, *Scientific Reports*. 7 (2017). doi:10.1038/srep42717

[19] A. Lagunin, A. Zakharov, D. Filimonov, V. Poroikov, QSAR modelling of rat acute toxicity on the basis of PASS prediction, içinde: *Molecular Informatics*, *Wiley-VCH Verlag*, 2011: ss. 241-250. doi:10.1002/minf.201000151

[20] W.M. Pardridge, Drug transport across the blood-brain barrier, *Journal of Cerebral Blood Flow and Metabolism*. 32 (2012), 1959-1972. doi:10.1038/jcbfm.2012.126

[21] W. Löscher, H. Potschka, Blood-brain barrier active efflux transporters: ATP-binding cassette gene family, *NeuroRx*. 2 (2005), 86-98. doi:10.1602/neurorx.2.1.86

[22] S.-F. Zhou, Drugs behave as substrates, inhibitors and inducers of human cytochrome P450 3A4, *Current Drug Metabolism*. 9 (2008), 310-322. doi:10.2174/138920008784220664

FEN ve MÜHENDİSLİK BİLİMLERİ DERGİSİ

Cilt/Vol: 7 Sayı/No: 1 Yıl/Year: 2025 Araştırma Makalesi/Research Article e-ISSN: 2667-7989

https://doi.org/10.47112/neufmbd.2025.71

FPGA Donanımı için Tek Taramalı Bağlantılı Bileşen Etiketlemenin Uygulanması

İsmail YABANOVA[1*] Tarık ÜNLER [2]

[1] Manisa Celal Bayar Üniversitesi, Hasan Ferdi Turgutlu Teknoloji Fakültesi, Elektrik Mühendisliği Bölümü, Manisa, Türkiye

[2] Necmettin Erbakan Üniversitesi, Havacılık ve Uzay Bilimleri Fakültesi, Havacılık Elektrik ve Elektroniği Bölümü, Konya, Türkiye

Makale Bilgisi

Geliş Tarihi: 13.05.2024
Kabul Tarihi: 15.07.2024
Yayın Tarihi: 30.04.2025

Anahtar Kelimeler:
Bağlantılı Bileşen Etiketleme,
Blob Analizi,
FPGA.

ÖZET

Görüntü işleme dijital görüntüyü işleyip analiz ederek belirli bilgileri çıkarmayı ve nesnelerin tanımlanmasını hedefleyen bilgisayar bilimidir. Görüntüleme sistemleri günümüzde tıp, savunma sanayi, güvenlik, otomotiv ve otomasyon alanları başta olmak üzere hayatımızın her alanında yer almaktadır. Bundan dolayı görüntünün belirlenen amaçlar doğrultusunda işlenmesi gerekmektedir. Blob tespiti görüntü işlemede nesne tanıma, algılama için kullanılan bir kavramdır ve görüntüdeki bir nesnenin sınırlarını belirleyen bir grup pikseli ifade eder. Blob analizi için farklı algoritmalar geliştirilmiştir. Bu algoritmalardan birisi görüntü işlemede yaygın olarak kullanılan ve amacı bir nesneye ait tüm piksellere aynı etiketi atamak olan bağlantılı bileşen etiketleme algoritmasıdır. Bu çalışmada görüntüdeki nesnelerin tespiti için bağlantılı bileşen etiketleme algoritması FPGA yapısı üzerinde uygulanmak üzere hazırlanmış ve simülasyon ortamında test edilmiştir. Bir görüntü karesinin tamamının aynı anda işlenmesi bellek kaynakları açısından verimsiz olduğundan dolayı görüntü satır satır okunup işlenmiştir. Görüntü karesinden tek geçişte her piksel etiketlenmiş ve bağlantılı pikseller birleştirilerek her blobun alanı, sınırları ve ağırlık merkezi hesaplanmıştır. Bu şekilde PL-PS yapılarının bir arada kullanılmasına imkân sağlayacak CCL algoritmasının uygulanması için altyapı sağlanmıştır. İlerde yapılacak çalışmalarda blob tespiti işlemi ZYNQ yapısının PS ve PL kısımlarına uygulanarak verimli bir sistem geliştirilmesi hedeflenmektedir.

Implementation of Single-Scan Connected Component Labeling for FPGA Hardware

Article Info

Received: 13.05.2024
Accepted: 15.07.2024
Published: 31.12.2024

Keywords:
Blob analysis,
Connected Component Labeling,
FPGA.

ABSTRACT

Image processing is a branch of computer science that tries to extract information and identify objects from digital photographs through processing and analysis. Today, imaging systems are used in almost every aspect of our lives, particularly in medicine, the defense industry, security, automobile, and automation. As a result, the image must be processed in accordance with the intended purposes. Blob detection is a concept used in image processing to recognize and detect objects. It refers to a group of pixels that define the borders of an object in the image. Blob analysis algorithms vary. One of these techniques is the linked component labeling algorithm, which is commonly used in image processing and assigns the same label to all pixels of an object. In this study, the connected component labeling algorithm for detecting objects in the image was prepared to be implemented on the FPGA structure and tested in a simulation environment. Since processing a full image frame at once is inefficient in terms of memory resources, the image was read and processed line by line. Each pixel was labeled in a single pass through the image frame, and the area, boundaries, and centroid of each blob were determined by combining the corresponding pixels. This provides the foundation for the application of the CCL algorithm, allowing the use of PL-PS structures together. Future research will focus on constructing an efficient system that applies the blob identification procedure to the PS and PL components of the ZYNQ structure.

To cite this article:
Yabanova, İ. &Ünler, T. (2025). Implementation of single-scan connected component labeling for FPGA hardware, *Necmettin Erbakan University Journal of Science and Engineering*, *7*(1), 12-21. https://doi.org/10.47112/neufmbd.2025.71

***Corresponding Author:** İsmail Yabanova, *iyabanova@gmail.com*

INTRODUCTION

Camera systems have grown commonplace in many aspects of our life as technology has advanced. The images must be processed in order to get the desired information. As a result, image processing algorithms are continually improving. The majority of this improvement is due to the development of new data processing methods, but the development of image sensors has resulted in higher refresh rates and image resolutions over time. The development of image sensors has improved not only image quality but also the efficiency of vision algorithms. However, increasing the resolution increases the amount of data to be processed [1].

Image processing has been useful in practically any field. When combined with optimization methods, they produce particularly successful results. For example, it has been reported that multi-level image thresholding, a popular image processing technique for segmenting images into highly meaningful features, can be combined with metaheuristic optimization algorithms to achieve successful results in terms of calculation time [2]. Another example of using image processing tools in a different field is to generate 3D body measurements from 2D images [3]. It will be a useful application for users, particularly if electronic purchasing becomes more widespread. Artificial intelligence is another topic that is fast evolving today. The most important factor in this progress is the development of high-performance computing equipment. Today, artificial intelligence is widely employed in a variety of industries, including health, the defense industry, image processing, security, voice and text processing, autonomous cars, and weather forecasting [4].

The connected component labeling (CCL) algorithm, which assigns a unique label to all pixels of each object (connected components) in a binary image, is critical for distinguishing different objects in the image and is required for image analysis and object recognition. As a result, CCL is a critical process in image analysis, understanding, perception, pattern recognition, segmentation, and computer vision [5-9].

Raster approaches are often preferred for the CCL algorithm, as they involve sequential processes based on label assignment and merging of equivalent labels [10]. Because the physical design and connectivity of connected components might be complicated, the CCL algorithm can be time-consuming, and the microprocessor in an embedded system frequently fails to analyze input binary images efficiently. As a result, hardware architectures tailored to the CCL algorithm have received significant attention [11]. There are three kinds of labeling algorithms for computer architectures and pixel representation images: 1) Raster scanning and label equivalence resolution methods; 2) search and label propagation algorithms; and 3) contour tracing and label propagation algorithms. Raster scanning and label equivalence resolution techniques scan an image in a raster direction (line by line, beginning in the upper-left corner and moving downward) and give a temporary label to each new pixel that is not linked to the previously scanned pixels. Temporary labels assigned to the same linked component are referred to as equivalent labels. There are three approaches for resolving label equivalence [12]. These methods can be classified into three groups based on the number of scans of the image frame in CCL algorithms [13]. Single-scan algorithms execute labeling and label merging on all picture pixels at the same time. Studies [14-18] are instances of this strategy. The two-scan approach stores the label equivalences discovered during the first scan in a 1-D or 2-D table array. Following the initial scanning, label equivalences are resolved using a search technique. The parsed results are typically kept in a 1D table. Then, during the second scan, the temporary labels are replaced with the smallest equivalent label from the table [12]. Studies [12], [19-21] provide instances of two scan approaches. Multiscan approach scans the image in both forward and reverse directions, propagating label equivalents until no labels change. The geometric complexity of the connecting components determines how many scans are

performed [12].

Some selected studies on the use of the CCL algorithm are summarized below. Selçuk et al. studied how different enzymes and additives affected bread production quality. They used the CCL algorithm to find pores in the bread [22]. Grana, et al. in their study, they compared the two most advanced CCL algorithms and evaluated their performance on an FPGA-based SoC architecture [23]. Pandey et al. proposed an FPGA platform-based strategy to implementing an efficient and improved two-scan equivalence-based linked component labeling algorithm [24]. Zhao et al. They suggested a single-scan, resource-efficient parallel CCL algorithm [25].

In this study, the CCL algorithm was used in the FPGA structure to recognize objects in the image. CCL typically utilizes an 8-element neighborhood; however, a 4-element neighborhood can also be employed. Labeling in the application was done using a single scan of an 8-element neighborhood. The CCL algorithm was originally tested using the Vivado program simulation environment. For this aim, an image file was read and given to the CCL algorithm line by line, the blob values discovered were read and painted on the image file, and the CCL algorithm's performance was evaluated. Since the constructed system was intended to be used for blob identification in video pictures in future investigations, video control signals were added to the read image frame and sent to the CCL algorithm. Then it was tested on the ZYNQ SoC.

MATERIALS AND METHODS

Zynq System on Chip

The FPGA development environment consisted of a Zedboard development board with the Zynq-7000 architecture. Figure 1 depicts the appearance of the Zedboard development board. The Z-7020 family chip is used on the Zedboard development board [26]. The Zynq architecture is known as System on Chip (SoC). A SoC structure is one that integrates various hardware components required for an application onto a single chip. These structures may include programmable logic structures, processors, microcontrollers, and digital signal processing units, as needed. These structures allow a complicated set of system functions to be executed on a single chip.

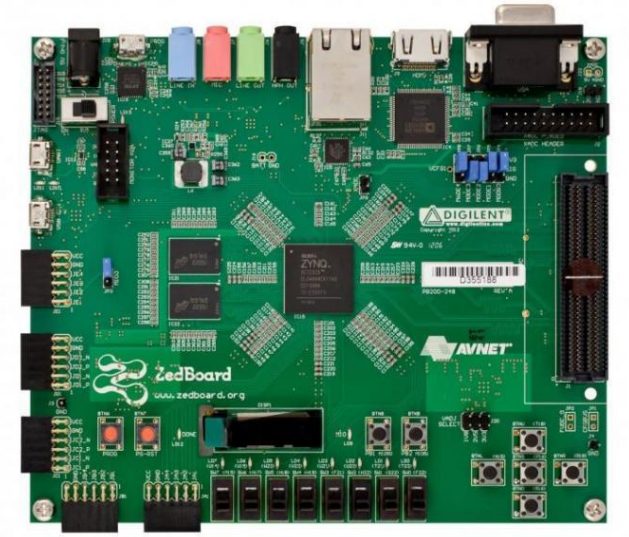

Figure 1
Zedboard development board

It has a fully programmable structure that includes an FPGA and a dual-core ARM Cortex-

A9 architecture CPU on the Zynq-7020 chip. AXI (Advanced eXtensible Interface) buses are used to transmit data between the FPGA and the ARM processor. AXI is a bus and control interface specifically intended for high-performance systems. AXI4 has several versions, including AXI4-Lite and AXI4-Stream, each designed to meet a specific requirement. The AXI interface offers a large bandwidth for high data transmission, allowing for high performance and rapid data connection between the FPGA and the processor. This ensures that these two parts collaborate in order to ensure that a complicated system runs smoothly. The programmable logic unit of the Zynq-7020 chip is referred to as PL (Programmable Logic), whereas the processor unit is known as PS (Processing System) [27]. Figure 2 shows a simplified representation of the ZYNQ 7000 architecture.

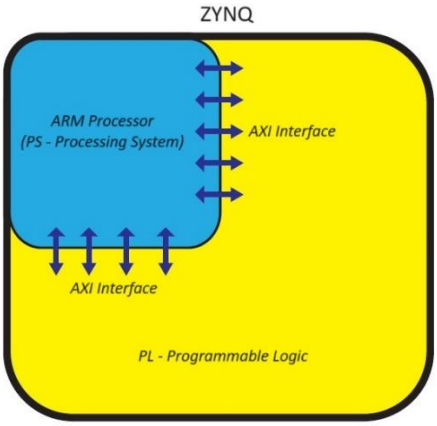

Figure 2
Zynq-7000 simplified architecture

Connected component labeling

The CCL method attempts to recognize objects in images by assigning the same label to adjacent pixels in black-and-white images. The algorithm's primary goal is to identify various items or sections of the image and assign them unique labels. The CCL algorithm can employ either four or eight neighborhoods. CCL algorithms are often designed as single-scan, double-scan, or multi-scan. These scan types specify how pixels in a picture are processed and related components are identified. The single-scan CCL algorithm analyzes the image in a single scan and discovers connected components after passing through it once. Single-scan algorithms are generally simple and fast, but they might be difficult to label precisely when coupled components are too close together. Two-scan algorithms label images using two independent scans. The first scan detects related components, and the second scan performs additional analysis and accurately labels connected components. Although it produces more accurate findings, it may incur a greater computational load. Multi-scan CCL techniques are used to scan more than two image frames. Multi-scan algorithms are employed in situations that need handling of exceptional instances or the reduction of greater detail. This approach may achieve great accuracy in complicated image frames, however each scan may result in increased computational load and delay. Which scan type to utilize in the CCL algorithm is governed by the application's requirements and the hardware resources to be used in the calculation.

The CCL algorithm labels pixels with a value of 1 on binary pictures. A pixel can get a label value of top-left, top-right, top-right, or one of the label values of the pixel to its left. If none of these pixels have a label, the label counter is increased and a new label is applied to the current pixel. Figure 3 illustrates the labeling process for the current pixel.

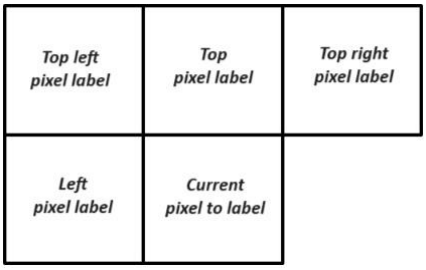

Figure 3
Labeling process of the current pixel

While labeling, you may come across more than one pixel with a different label than the adjacent pixels. Although the connected components labeled 1 and 2 appear to be two different components, when it comes to the current pixel to be labeled, the upper left neighbor pixel has label 1, and the upper right neighbor pixel has label 2. While the current pixel is being labeled, the algorithm determines that labels 1 and 2 need to be merged and marks them for correction. Components with labels 1 and 2 are actually part of the same blob, and after correction, all pixels with label 2 have label value 1. This ensures that all connected components are properly labeled in a single scan.

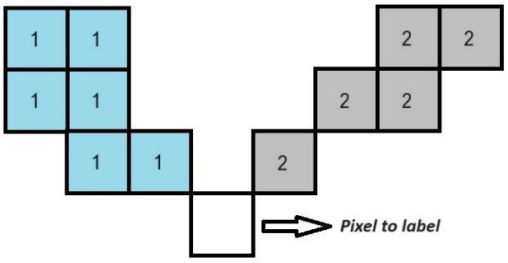

Figure 4
The process of combining labels

Simulation and Testing

The CCL algorithm was tested using a testbench file created using the Vivado program. The appropriate signals were generated by reading the image file that would be tested with this file. Because image processing is typically performed on a pixel, line, or neighboring pixels rather than a whole image frame, and to make better use of resources, the lines of the image file received by another module were taken one at a time and supplied to the CCL algorithm with video control signals. Figure 5 depicts the simulation screen.

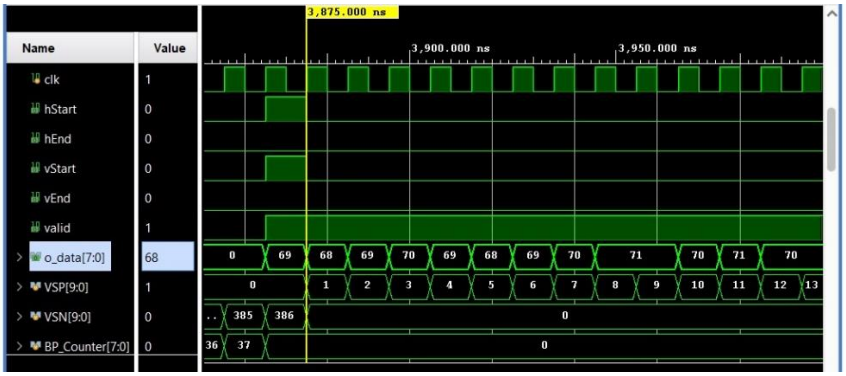

Figure 5
Realized simulation image

Video images are made up of two signals: data and control signals. Pixel values are supplied serially via data signals, while the position of these pixels in the image is defined by control signals. The video frame is sent from left to right and top to bottom. Gap signals are used to modify the timing of visual frames. The horizontal space range generated between the end of one image line and the beginning of the next line is known as the back porch and the front porch. The vertical gap signal [28] refers to the space between the image square's final active line and the beginning of the next active line. Figure 6 depicts the framework utilized to transport video images.

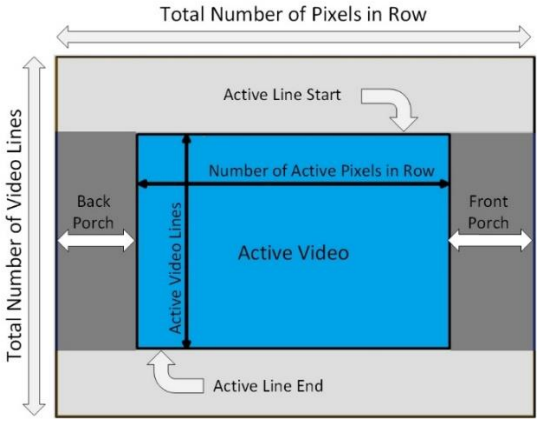

Figure 6
Transmission structure of the video frame

Figure 7 depicts an example of sending a 2x3-pixel image frame with video control signals. The zero-value pixels surrounding the image frame generate horizontal and vertical gaps. In the example, one line space precedes the first active line and one line space follows the last active line. Similarly, there is one pixel of backspace and two pixels of front space. Video control signals are made up of five signals: hStart, hEnd, vStart, vEnd, and valid. With these control signals, the position of each pixel within the image frame is determined.

0	0	0	0	0	0
0	45	60	75	0	0
0	100	120	140	0	0
0	0	0	0	0	0

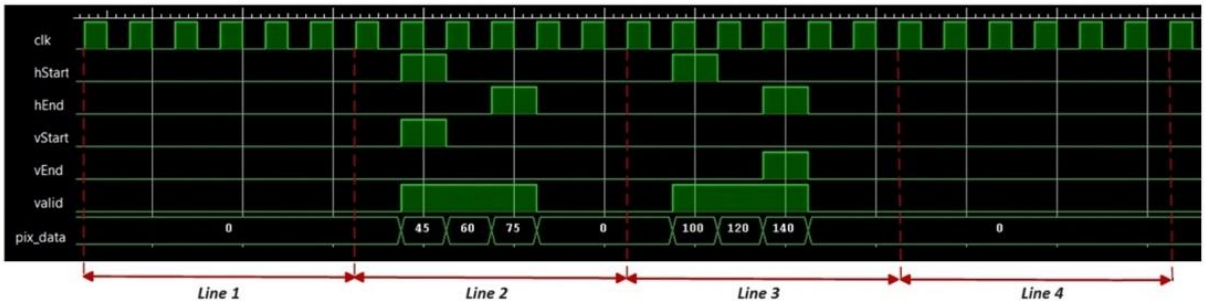

Figure 7
Transmission signals of an example video frame

RESULTS

The CCL algorithm was tested by creating several image files. With the written testbench, image files were read and passed to the CCL algorithm, which read the frame and center of gravity data that constituted the borders of the connected components and drawn on the corresponding image file. Figure 8 depicts an example image frame with the boundaries of the related components discovered as a consequence of the simulation marked in green and the center of gravity noted in red. As seen in the image, the CCL algorithm successfully identified all of the items in the image frame.

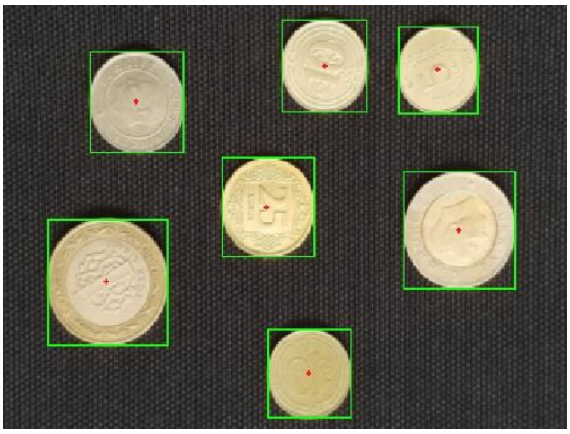

Figure 8
Finding connected components in a sample image frame

To ensure that the CCL algorithm successfully classifies items in a single scan, an image frame identical to Figure 4 was used. The simulation was used to conduct the test, which involved merging the three coins in the bottom left corner of Figure 9. There is no pixel connecting the coins in the upper left and upper right before reaching the image pixels of the coin in the lower middle, hence these two coins are labeled differently. However, as the pixels on the bottom coin began to be labeled, the labels were updated, and the same label was assigned to all three coins as the pixels on the top coins were merged. Drawing the boundaries of the components in Figure 9 showed that the related components were accurately identified. Figure 10 depicts a binary (black-white) image demonstrating that the labeling was correct.

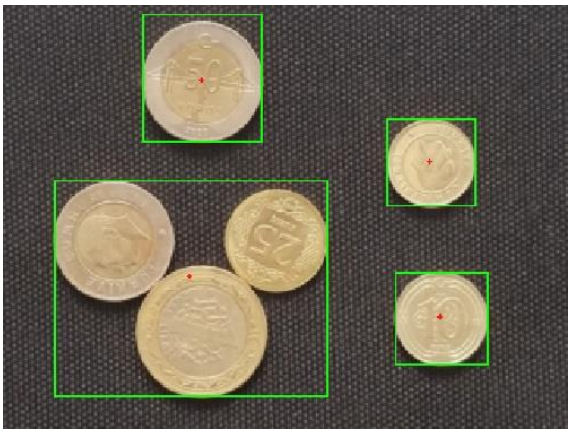

Figure 9
Example of correct labeling of connected components

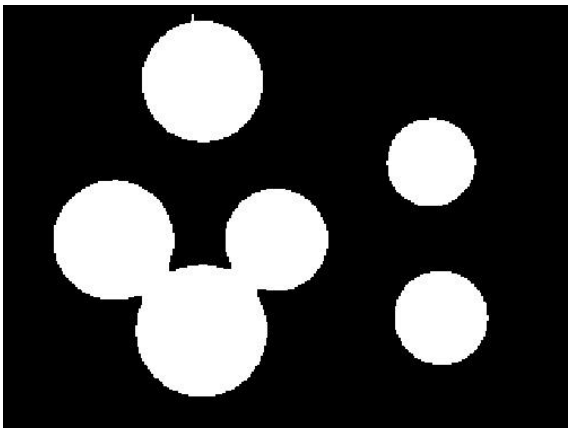

Figure 10
Binary (black-white) image of found connected components

DISCUSSION AND CONCLUSIONS

In this study, the single-scan CCL algorithm was developed, implemented to the FPGA structure, and tested in a simulation environment. The prepared images were read and delivered as lines to the CCL algorithm, which then read and drew the values of the related components. Data for connected components includes a frame and a center of gravity, which indicate the component's limits. Its performance was tested by running the CCL algorithm on various image files. The simulation results showed that the BBE algorithm correctly identified and labeled all components in the images. At a clock frequency of 100 MHz, all connected components in a 240x320 pixel image are detected in around 980 microseconds. Future research will focus on testing the CCL algorithm on real-time video images utilizing the Zynq SoC.

Ethical Statement

This article is the authors' own original work, which has not been previously published elsewhere. The article reflects the authors' own research and analysis in a truthful and complete manner. The results are appropriately placed in the context of prior and existing research.

Author Contributions

Research Design (CRediT 1) İ.Y. (%60) - T.Ü. (%40)
Data Collection (CRediT 2) İ.Y. (%70) - T.Ü. (%30)
Research - Data Analysis - Validation (CRediT 3-4-6-11) İ.Y. (%60) - T.Ü. (%40)
Writing the Article (CRediT 12-13) İ.Y. (%60) - T.Ü. (%40)
Revision and Improvement of the Text (CRediT 14) İ.Y. (%50) - T.Ü. (%50)

Financing

This research was not supported by any public, commercial, or non-profit organization.

Conflict of Interest

The authors have no conflict of interest to disclose for this study.

REFERENCES

[1] M. Kowalczyk, T. Kryjak, A Connected Component Labelling algorithm for a multi-pixel per clock cycle video stream, içinde: *24th Euromicro Conference on Digital System Design (DSD)*, Palermo, Italy, 2021, 43-50.

[2] A. Ünlü, İ. İlhan, A novel hybrid gray wolf optimization algorithm with harmony search to solve multi-level image thresholding problem, *Necmettin Erbakan University Journal of Science and Engineering.* 5(2) (2023), 230- 245. doi:10.47112/neufmbd.2023.21

[3] N.G. Şengöz, F. Zeybek, Sharp Silhouettes for Obtaining 3D Body Measurements from 2D Images, *Necmettin Erbakan University Journal of Science and Engineering.* 4(2) (2022), 8-25.

[4] F. Özen, R. Ortaç Kabaoğlu, T.V. Mumcu, Deep learning based temperature and humidity prediction, *Necmettin Erbakan University Journal of Science and Engineering*, 5(2) (2023), 219-229. doi:10.47112/neufmbd.2023.20

[5] L. He, X. Ren, Q. Gao, X. Zhao, B. Yao, Y. Chao, The connected-component labeling problem: A review of state-of-the-art algorithms, *Pattern Recognition.* 70 (2017), 25-43. doi:10.1016/j.patcog.2017.04.018

[6] B. Aissou, A. Aissa, An adapted connected component labeling for clustering non-planar objects from airborne lidar point cloud, *Volume XLIII-B2-2020: The International Archives of the Photogrammetry, Remote Sensing and Spatial Information Sciences (ISPRS)*, 2020, pp:191–195.

[7] D. Jaiswal, P. Kumar, Real-time implementation of moving object detection in UAV videos using GPUs, *Journal of Real-Time Image Process.* 17 (2019), 1301–1317, doi:10.1007/s11554-019-00888-5

[8] A. A. Kalinin, V. I. Iglovikov, A. Rakhlin, A. A. Shvets, Medical Image Segmentation Using Deep Neural Networks with Pre-trained Encoders. In: M. Wani, M. Kantardzic, M. Sayed-Mouchaweh, (eds) *Deep Learning Applications. Advances in Intelligent Systems and Computing*, *Springer Singapore*, 2020: pp. 39–52 doi: 10.1007/978-981-15-1816-4_3

[9] V. S. N. Virothi, M. S. Janapareddy, Signature Extraction Using Connected Component Labeling. In: S.C. Satapathy, V. Bhateja, M. Ramakrishna Murty, N. Gia Nhu, Jayasri Kotti (eds) *Communication Software and Networks. Lecture Notes in Networks and Systems, Springer, Singapore*, 2021: pp. 619-629 doi: 10.1007/978-981-15-5397-4_62.

[10] C. Zhao, G. Duan, N. Zheng, A Hardware-Efficient method for extracting statistic ınformation of connected component, *Journal of Signal Processing Systems*. 88 (2016), 55–65. doi:10.1007/s11265-016-1126-5

[11] C. Zhao, W. Gao, F. Nie, A memory-efficient hardware architecture for connected component labeling in embedded system, *IEEE Transactions on Circuits and Systems for Video Technology*. 30 (2019), 3238–3252. doi:10.1109/tcsvt.2019.2937189

[12] L. He, Y. Chao, K. Suzuki, A run-based two-scan labeling algorithm, *IEEE Transactions on Image Processing.* 17(5) (2008), 749-756. doi: 10.1109/TIP.2008.919369

[13] H. Zhou, R. Dou, L. Cheng, J. Liu, N. Wu, A provisional labels-reduced, real-time connected component labeling algorithm for edge hardware, *IEEE Transactions on Circuits and Systems II: Express Briefs.* 69(6) (2022), 2997-3001. doi: 10.1109/TCSII.2022.3152783

[14] A. AbuBaker, R. Qahwaji, S. Ipson and M. Saleh, One Scan Connected Component Labeling Technique, *IEEE International Conference on Signal Processing and Communications*, Dubai, United Arab Emirates, 2007, 1283-1286

[15] J.-W. Jeong, G.-B. Lee, M.-J. Lee, J.-G. Kim, A single-pass connected component labeler without label merging period, *Journal of Signal Processing Systems*. 84 (2015), 211–223. doi:10.1007/s11265-015-1048-7

[16] C. T. Johnston, D. G. Bailey, FPGA implementation of a Single Pass Connected Components Algorithm, *4th IEEE International Symposium on Electronic Design, Test and Applications,* Hong Kong, China, 2008, 228-231

[17] N. Ma, D. G. Bailey and C. T. Johnston, Optimised single pass connected components analysis, *International Conference on Field-Programmable Technology*, Taipei, Taiwan, 2008, 185-192.

[18] J. Trein, A. Th. Schwarzbacher, and B. Hoppe, FPGA implementation of a single pass real-time blob analysis using run length encoding, *MPC-Workshop,* Ravensburg-Weingarten, Germany, (2008).

[19] K. Wu, E. Otoo, K. Suzuki, Optimizing two-pass connected-component labeling algorithms, *Pattern Analysis and Applications*. 12 (2008) 117–135. doi:10.1007/s10044-008-0109-y.

[20] L. He, Y. Chao, K. Suzuki, K. Wu, Fast connected-component labeling, *Pattern Recognition.* 42(9) (2009), 1977-1987. doi:10.1016/j.patcog.2008.10.013

[21] L. He, X. Zhao, Y. Chao, K. Suzuki, Configuration-transition-based connected-component labeling, *IEEE Transactions on Image Processing*. 23(2) (2014), 943-951. doi:10.1109/TIP.2013.2289968

[22] A. Alkan, T. Selcuk, A. S. Çolakoğlu, Görüntü işleme teknikleri kullanılarak ekmek doku analizi ve arayüz programının oluşturulması, *Journal of the Faculty of Engineering and Architecture of Gazi University*. 33(1) (2018), 31-41. doi: 10.17341/gazimmfd.406777

[23] C. Grana, D. Borghesani, P. Santinelli, R. Cucchiara, High Performance Connected Components Labeling on FPGA, *Workshops on Database and Expert Systems Applications,* Bilbao, Spain, 2010, 221-225.

[24] J. G. Pandey, A. Karmakar, A. K. Mishra, C. Shekhar and S. Gurunarayanan, Implementation of an İmproved Connected Component Labeling Algorithm Using FPGA-based Platform, *International Conference on Signal Processing and Communications (SPCOM),* Bangalore, India, 2014, 1-6.

[25] C. Zhao, W. Gao and F. Nie, A resource-efficient parallel connected component labeling algorithm and its hardware implementation, *IEEE Transactions on Multimedia*. 23 (2021), 4184-4197. doi: 10.1109/TMM.2020.3037511.

[26] Avnet Inc., Zedboard Hardware User's Guide, (2014), https://www.avnet.com/wps/wcm/connect/onesite/922900e3-3d57-4cc7-883f-a8b9fbea0cd0/ZedBoard_HW_UG_v2_2.pdf?MOD=AJPERES&CACHEID=ROOTWORKSPACE.Z18_NA5A1I41L0ICD0ABNDMDDG0000-922900e3-3d57-4cc7-883f-a8b9fbea0cd0-nxyWMFS (Access 10 March 2024).

[27] Xilinx Inc., Zynq-7000 All Programmable SoC Data Sheet: Overview (DS190), (2018), https://docs.amd.com/v/u/en-US/ds190-Zynq-7000-Overview (Access 15 March 2024).

[28] MathWorks, Inc., Streaming Pixel Interface, https://www.mathworks.com/help/visionhdl/ug/streaming-pixel-interface.html (Access 18 March 2024)

FEN ve MÜHENDİSLİK BİLİMLERİ DERGİSİ

Cilt/Vol: 7 Sayı/No: 1 Yıl/Year: 2025 Araştırma Makalesi/Research Article e-ISSN: 2667-7989

https://doi.org/10.47112/neufmbd.2025.72

Titanyum Alaşımlaması ile AlCrMnV Tabanlı Hafif Yüksek Entropili Alaşımın Mikroyapı ve Sertlik Gelişimi

Tuğba Selcen ATALAY KALSEN [1*] Gökhan POLAT [2]

[1] Necmettin Erbakan University, Faculty of Engineering, Department of Metallurgical and Materials Engineering, Konya, Türkiye

[2] İzmir Katip Çelebi University, Faculty of Engineering and Architecture, Department of Metallurgy and Materials Engineering, İzmir, Türkiye

Makale Bilgisi

Geliş Tarihi: 23.01.2024
Kabul Tarihi: 24.07.2024
Yayın Tarihi: 30.04.2025

Anahtar Kelimeler:
Hafif Alaşımlar,
Mikroyapı,
Sertlik,
Yüksek Entropili Alaşımlar.

ÖZET

Yüksek entropili alaşımlar (YEA'lar), mukavemet-süneklik dengesi gibi benzersiz mekanik özellikler sergiler. Son zamanlarda hafif YEA düşük yoğunlukları ve karakteristik özellikleri nedeniyle dikkat çekmektedir. Bu çalışmada, hafif $(AlCrMnV)_{100-x}Ti_x$ (x=0, 5, 25, 50 at. %) YEA'sı içerisine Ti eklenmiş ve ark ergitme metodu ile üretilerek, Ti ilavesinin yapısal ve mekanik özelliklere etkisi incelenmiştir. Döküm numunelerin faz analizi, mikro yapıları, bileşimsel heterojenliği sırasıyla X-ışını difraktometresi (XRD), taramalı elektron mikroskobu (SEM) ve enerji dağılımlı spektrometre (EDS) ile belirlenmiştir. Döküm numunelerinin sertliği ise Vickers sertlik testiyle tespit edilmiştir. Elde edilen sonuçlara göre AlCrMnV YEAsında V-Cr ve Al-Mn açısından zengin bölgeler görülürken $(AlCrMnV)_{95}Ti_5$ YEAsında herhangi bir segregasyon gözlemlenmemiştir. Artan titanyum içeriği ile yapıya ait kafes parametresi büyüyerek, difraksiyon pikleri sola kaymasına sebep olmuştur. Titanyum içeriği at. % 0'dan at. % 25'e çıkarıldığında ise döküm numunelerinin sertliği 471 HV'den 494 HV değerine artmıştır. %5 ve %50 Ti içeren numunelerde kalıp kenarlarına yakın bölgelerde kolonsal, orta bölgelerde ise dendritik yapılar içeren ingot döküm yapıları gözlemlenmiştir. Titanyum ilavesinin $(AlCrMnV)_{100-x}Ti_x$'in mikroyapısal ve mekanik özellikleri üzerinde önemli etkisi vardır.

Microstructure and Hardness Evolution of AlCrMnV-based Lightweight High Entropy Alloy through Titanium Alloying

Article Info

Received: 23.01.2024
Accepted: 24.07.2024
Published: 30.04.2025

Keywords:
Lightweight alloys,
Microstructure,
Hardness,
High Entropy Alloy.

ABSTRACT

High-entropy alloys (HEAs) exhibit unique mechanical properties such as strength-ductility balance. Recently, light HEAs have attracted attention due to their low density and characteristic properties. In this study, Ti was gradually added to lightweight $(AlCrMnV)_{100-x}Ti_x$(x=0, 5, 25, 50 at. %) HEAs and produced by the arc melting method, and the effect of Ti addition on structural and mechanical properties was examined. Phase analysis, microstructures and compositional heterogeneity of the cast samples were determined by X-ray diffractometer (XRD), scanning electron microscope (SEM) and energy dispersive spectrometry (EDS), respectively. The hardness of the casting samples was determined by the Vickers hardness test. The results showed that V-Cr and Al-Mn rich regions were observed in the AlCrMnV sample, while no segregation was observed in the $(AlCrMnV)_{95}Ti_5$ sample. As the titanium content increased, the lattice parameter of the structure increased, causing the diffraction peaks to shift to the left. Accordingly, when the Ti content was increased from 0 at. % to 25 at. %, the hardness of the casting samples increased from 471 HV to 494 HV, respectively. Ingot cast structures, columnar at the edges, and dendritic structures, at the center zones were obtained in samples with 5 at% and 50 at.% Ti. The addition of titanium has a substantial impact on the structural and mechanical properties of $(AlCrMnV)_{100-x}Ti_x$.

To cite this article:
Atalay Kalsen, T.S. & Polat, G. (2025). Microstructure and hardness evolution of AlCrMnV-based lightweight high entropy alloy through titanium alloying. *Necmettin Erbakan University Journal of Science and Engineering, 7*(1), 22-30. https://doi.org/10.47112/neufmbd.2025.72

***Sorumlu Yazar:** Tuğba Selcen Atalay Kalsen, *tsatalay@erbakan.edu.tr*

INTRODUCTION

The concepts of high entropy alloys (HEAs) or multi-principal elements alloys (MPEAs) were first introduced and defined in 2004 by Cantor et al.[1] and Yeh et al. [2] as alloys consisting of at least five principle elements causing large configurational entropy values. These alloys can also be broadly defined as solid solution alloys, including equiatomic or near equiatomic concentration [2,3]. Although this first definition of HEAs includes the exact number and amount of the elements in the composition [4], the subsequent studies showed that this definition is restrictive and not adequate for the formation of single solid solutions [2,5]. That is, the non-equiatomic ratios and minor alloying strategy can also result in the formation of solid solution phases [6,7].

The four core effects, including high configurational entropy, lattice distortion, sluggish diffusion, and cocktail effects, are defined to reveal the influence of the different elements on the structural and mechanical properties of HEAs [6]. The application of HEAs could be expanded by tuning these basic four effects [8]. For instance, the increased number of elements can cause stable single-solid solution phases, even at elevated temperatures, due to the increased configurational entropy (ΔS_{mix}). In addition, the microstructure and mechanical properties of HEAs can be enhanced with the lower diffusion rates of the atoms, resulting from high ΔS_{mix} [9]. HEAs show high strength, hardness, high wear and corrosion resistance, high-temperature strength, and also the combination of these properties compared to conventional alloys and other materials such as composites [9–12]. Thus, HEAs have a critical role in engineering applications such as aerospace, civil transportation, catalytic, energy, biomedical, and automotive industry [6,13].

Recently, lightweight high entropy alloys (LWHEAs) having solid solution phases and enhanced properties for aerospace, transportation, and energy applications have received much attention [14,15]. Although LWHEAs consist of relatively low-density elements such as Al, Ti, Si, and Mg, the combination of Al and Ti elements with high concentrations is used to produce lightweight alloys [16–18]. Huang et al. [17] stated that Ti content significantly affects the mechanical properties of AlCrTiV alloy [17]. They also stated that increasing Ti content leads to an increase in ductility because of the reduced degree of ordering. For $Al_{10}Cr_{10}Ti_{70}V_{10}$ HEA, 877 MPa yield strength and 889 MPa ultimate tensile strength were obtained from the tensile test, according to Huang et al. [17]. Liao et al. [14] studied the effect of different amounts of V on the mechanical properties and microstructure of AlTiCrMn alloy. Accordingly, $Al_{50}(TiCrMn)_{45}V_5$ alloy showed the highest compression strength of 1995 MPa and a ductility of 30% [14].

In this study, $(AlCrMnV)_{100-x}Ti_x$ (x=0, 5, 25, 50 at. %) HEAs were prepared by vacuum arc melting, and the structural and microstructural analyses were conducted using X-ray Diffractometer (XRD) and Scanning Electron Microscope (SEM) techniques, respectively. In addition, the influence of Ti on the mechanical properties was investigated by micro Vickers tests.

MATERIALS AND METHODS

High-purity Al shots (99.9%), Ti granules (99.99%), Cr pieces (99.2%), Mn pieces (99.95%), and V pieces (99.7%) supplied from Alfa Aesar were used to produce the $(AlCrMnV)_{100-x}Ti_x$ (x=0, 5, 25, 50 at. %). The nominal compositions of the HEAs are provided in Table 1. A total metal mixture of 3 gr was prepared precisely for each set of the alloy mixture. From now on, the 0, 5, 25, and 50 at. % added HEAs were denoted as Ti0, Ti5, Ti25 and Ti50, respectively.

HEAs were produced via vacuum arc melter (Optosense, Turkey) using the current values of 130-180 A under an argon atmosphere. The ingots were remelted at least three times to ensure chemical homogeneity in the alloys. Then, the ingots were suction cast into a water-cooled cylindrical copper mold with 5 mm diameter. The cylindrical samples were mounted vertically in polyester resin to

Table 1
Nomenclatures of Samples and Concentration of Elements

HEAs	Al (at. %)	Cr (at. %)	Mn (at. %)	V (at. %)	Ti (at. %)
Ti0	25.00	25.00	25.00	25.00	-
Ti5	23.75	23.75	23.75	23.75	5.00
Ti25	18.75	18.75	18.75	18.75	25.00
Ti50	12.50	12.50	12.50	12.50	50.00

investigate the vertical cross-sections of the HEAs. Then, conventional metallographic techniques (grinding and polishing) were performed to prepare the as-cast samples. The densities of samples were measured using the Archimedes technique setup combined with a balance (RADWAG, AS 220.R2 Plus).

Phase analysis of as-cast HEAs was performed via PANalytical EMPYREAN X-ray diffractometer with Cu-Kα radiation with 0.01 step size between 10 and 100 degrees at a scanning rate of 1°/min. Hardness values of polished HEAs were obtained using the Vickers microhardness test (Emcotest, Durascan G5) under 0.5 kgf and ten seconds of indentation duration. The hardness values representing the mechanical properties [19] of the HEAs taken from five different points were used as the average hardness for each sample. The microstructure of samples was examined before and after the etching process to detect reactive phases. Etching was carried out with a solution of 5 mL HF, 4 mL HNO_3, and 65 mL H_2O for 1 min etching duration. Imaging and compositional analysis were performed via scanning electron microscope (SEM) with a tungsten filament (HITACHI, SU1510) and energy dispersive spectrometer (EDS) (Oxford Instruments, X-Act).

RESULTS AND DISCUSSION

X-ray diffraction patterns of as-cast HEAs are given in Figure 1. Phases and indexed planes were labeled on the top of the peaks. Ti0 and Ti5 samples have similar patterns compared with Ti25 and Ti50 samples, as shown in Figure 1. According to Qui et al. [20], since the BCC and B2 phases have similar lattice parameters, the XRD method cannot be sufficient to distinguish the corresponding reflections. That is, the exact amount of the B2 and BCC phases in Ti0 and Ti5 HEAs cannot be determined due to the overlapping diffraction lines in the XRD technique. In the XRD pattern, only the BCC phase peaks are visible. However, studies indicate that the B2 structure is also present in the alloys of similar composition to the samples in this study [20–22]. However, since the amount of the phase formed in this study is below 3%, it may not be visible in XRD [23]. However, the peaks could be distinguishable at higher diffraction angles, as can be seen in the XRD pattern of Ti0 and Ti5 samples, which have multiple peaks around 77-80°. A zoom-in view of the peak pattern for the Ti0 sample is given in Figure 1. These findings agree well with the previous studies by Knipling et al. [24]. However, peak positions of the BCC structures were shifted towards lower angles with increasing Ti content. As can be seen in Figure 1, 2θ degrees of the diffraction peaks belonging to $(111)_{BCC}$ plane appeared at 43.11°, 42.75°, 42.10°, and 41.07° with increasing Ti content from 0 to 50 (at. %). Accordingly, the lattice parameters of BCC structures were calculated to be 2.969 Å, 2.988 Å, 3.033 Å, and 3.111 Å for the Ti contents of 0, 5, 25, 50 (at. %), respectively. This suggests that the increasing Ti content causes a systematic increase in the lattice parameters of the HEAs due to solid solution. It can be indicated that severe lattice distortion occurred with the increasing Ti content having a relatively large atomic radius.

The formation of the BCC phase was also confirmed by thermo-physical calculations [23] provided in Table 2. As can be seen in the table, the atomic size differences (δ %) of the HEAs are well below the critical value of 6.67 % to form the solid solution in HEAs. In addition, the valance electron concentration (VEC) values of the HEAs are between 4.62 and 5.25, indicating the BCC solid solution. However, the VEC value decreases up to 4.62 in the Ti50 HEA, which further stabilizes the BCC phase,

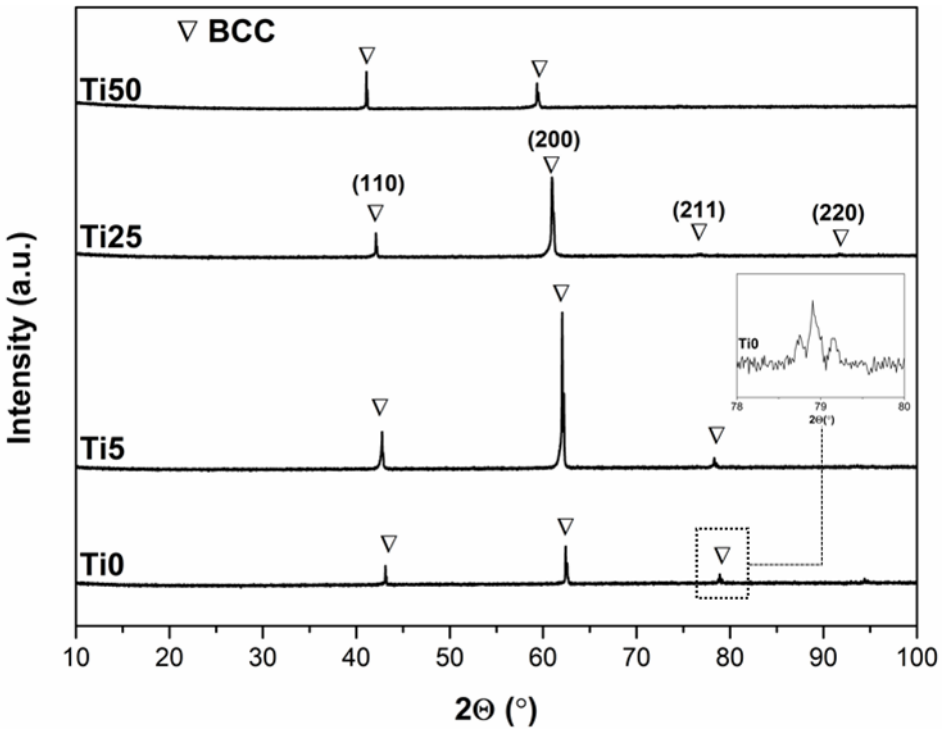

Figure 1
X-ray diffraction patterns of as-cast HEAs

and the ΔH_{mix} values of the HEAs are below the critical value of -22 kJ/mol to form solid solution phases in HEAs [25]. In addition, the thermo-physical calculation showed a decrease in the density values of the HEAs from 4.54 gr/cm^3 to 3.64 gr/cm^3 with increasing Ti. Nevertheless, the results showed the formation of solid solution phases and a decrease in the density of the HEAs with the increasing Ti content. The density values of the samples measured experimentally by Archimedes method were found to be 5.43±0.05, 5.36±0.05, 5.29±0.05, 4.94±0.03 g/cm^3 for Ti0, Ti5, Ti25, and Ti50 samples, respectively. The experimental densities of the samples show very slight deviations from the theoretical values provided in Table 2, indicating negligible porosity defects in the as-cast samples [26].

Table 2
Calculated thermo-physical properties of the HEAs

HEA	*Density (g/cm^3)*	*δ (%)*	*ΔH_{mix} (kJ/mol)*	*VEC*	*ΔS_{mix} (kJ/mol.K)*	*T_m (K)*	*VEC Predicted Phase(s)*
Ti0	5.6	4.54	-11.50	5.25	11.53	1686	BCC
Ti5	5.5	4.49	-12.61	5.19	12.60	1698	BCC
Ti25	5.3	4.20	-15.28	4.94	13.32	1748	BCC
Ti50	5.0	3.64	-14.62	4.62	11.53	1810	BCC

EDS mapping was conducted on the Ti0 and Ti5 HEAs to reveal the elemental distribution in the microstructure of Ti-free and Ti-added unetched samples. Figure 2 shows Ti0 HEA has two main regions, including Al-Mn rich and Cr-V rich phases. The segregation could be explained by mixing enthalpy (ΔH_{mix}) values of binary systems using Miedema's model [27,28]. According to Table 3, the mixing enthalpy of the Cr-V pair is -2 kJ/mol, indicating the formation of Cr-V solid solution phases in the matrix. However, the mixing enthalpy of the Al-Mn pair is -19 kJ/mol, which triggers the formation of Al-Mn intermetallic compounds (ICs).

Similarly, Son et al. [21] determined that Cr-V segregation occurred due to the mixing enthalpy in $Al_{50}VCr$ alloy. However, the distributions of the elements are more homogenous in Ti5 HEA, as seen

in Figure 2. Huang et al. [29] stated that Ti -V and Cr-V are miscible couples and Ti- Cr can dissolve in each other to form a solid solution. In addition, Al has a wide range of solubility in Ti, Cr, and V elements [29]. Therefore, the Ti5 sample has a relatively more homogeneous structure regarding elemental dispersion than Ti-free samples. These results are in line with the EDS mapping provided in Figure 2.

The HEAs were etched for detailed microstructural analyses and investigated using secondary electrons (SE) under SEM from the surface of the samples close to the mold and up to its center. Figure 3 showed SEM images taken from the overall (up to center from the surface), edge, and center regions of etched Ti5 and Ti50 samples. Cooling gradient during solidification caused ingot cast structure across both materials, as seen in Figures 3b and 3e. Columnar structures were seen at the edge of the Ti5 and Ti50 samples, while dendritic structures were formed at the center regions of the samples.

Similar microstructural features were observed by Cao et al. [30] with the addition of the V into $CoCrFeNiV_x$ (x = 0, 0.25, 0.5, 0.7, 0.8, 0.9, and 1.0). They showed the transformation of dendritic structure to distinct equiaxed grains with 0.9-1.0 V addition, which is in line with the current study.

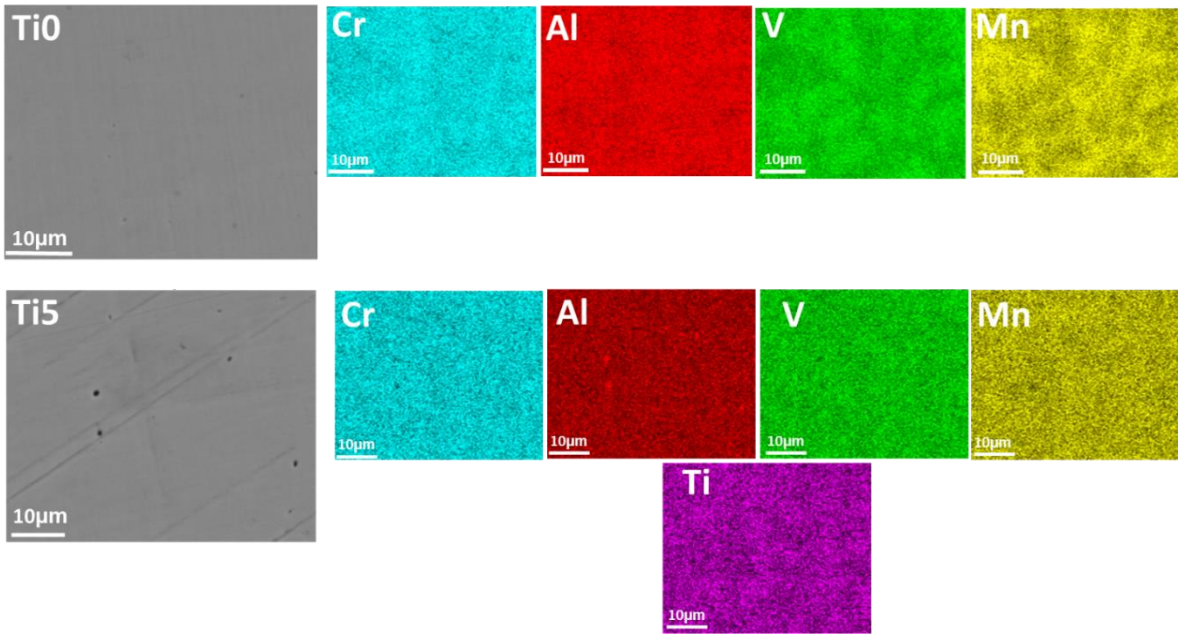

Figure 2
X-ray diffraction patterns of as-cast HEAs

Table 3
ΔH_{mix} values for atomic pairs calculated with Miedema's Model [28]

	Al	Cr	Mn	V	Ti
Al	0	-10	-19	-16	-30
Cr		0	2	-2	-7
Mn			0	-1	-8
V				0	-2
Ti					0

The chemical composition of the as-cast HEAs obtained by the EDS method is given in Table 4. It can be seen that the Al, Cr, and V contents have almost the same atomic ratios as indicated in Table 1. However, although similar amounts of Mn with Al, Cr, and V were expected in the composition, it is well below these critical ratios. This indicates the depletion of Mn in the microstructure, which can be due to the oxidation of the Mn with the trace amount of oxygen in the melting system.

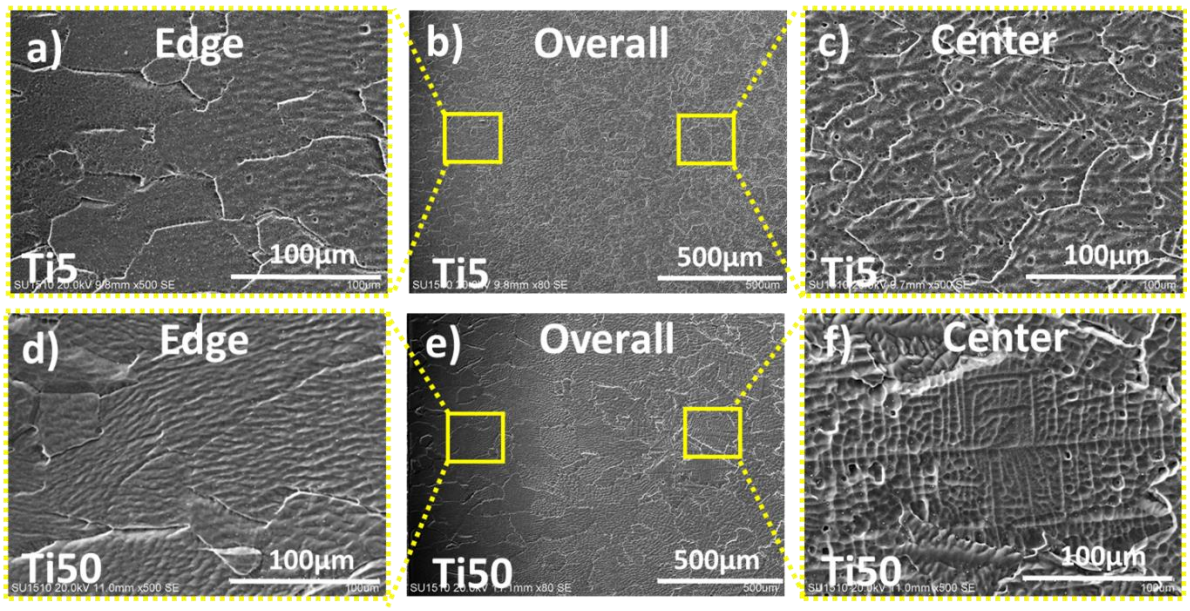

Figure 3

SEM images of etched a) Edge of Ti5 (500x), b) Overall structure of Ti5 (80x), c) Center of Ti5 (500x), d) Edge of Ti50 (500x), e) Overall structure of Ti50 (80x), f) Center of Ti50 (500x).

Table 4

Chemical composition of HEAs obtained by EDS (without etching)

	at. %			
Element	**Ti0**	**Ti5**	**Ti25**	**Ti50**
Al	27.18	24.79	18.98	12.84
Cr	27.27	24.53	18.31	12.27
Mn	17.51	19.60	17.98	12.11
V	28.04	25.07	18.41	11.74
Ti	-	6.01	26.32	51.04

The Vickers hardnesses of as-cast HEAs are given in Figure 4. Hardness values were found to be 471±7 HV, 494±5 HV, 652±4 HV, and 532±11 HV for Ti0, Ti5, Ti25 and Ti50 HEAs, respectively. That is, a systematic increase was observed in the hardness of the HEAs up to 25 at. % Ti addition. The increase in the hardness could be attributed to the increased lattice distortion of the HEAs with increasing Ti into the base (Ti0) HEA. The increasing lattice distortion could be correlated with the XRD patterns provided in Figure 1. As can be seen, the systematic addition of Ti causes a shift in the main peaks of the BCC lattice towards lower angles, indicating the expansion of the lattice

On the other hand, further increase in Ti content of 50 at. % resulted in a decrease in the hardness from 652±4 HV to 532±11 HV. The reason for the decrease in the hardness of the Ti50 HEA can be seen in Figure 1, the Ti content increased by 50%, disappearing B2 phase and causing almost a single BCC phase in the microstructure. That is, the brittle B2 phases transform into a relatively soft BCC phase, softening the hardness. Moreover, Huang et al. [17] stated that Ti has a vital role in increasing the hardness of AlCrTiV HEA. However, an excess amount of titanium in AlCrTiV alloy decreases hardness due to a reduced degree of ordering and decreasing lattice distortion. That is, as shown in Table 2, the atomic size difference of the HEAs decreases by 3.64 % in Ti50 HEA, thus triggering solid solution strengthening [17]. Nevertheless, a decrease in the hardness of the HEAs was observed in the Ti50 HEA due to formation of a relatively soft single BCC phase, and decreasing lattice distortion.

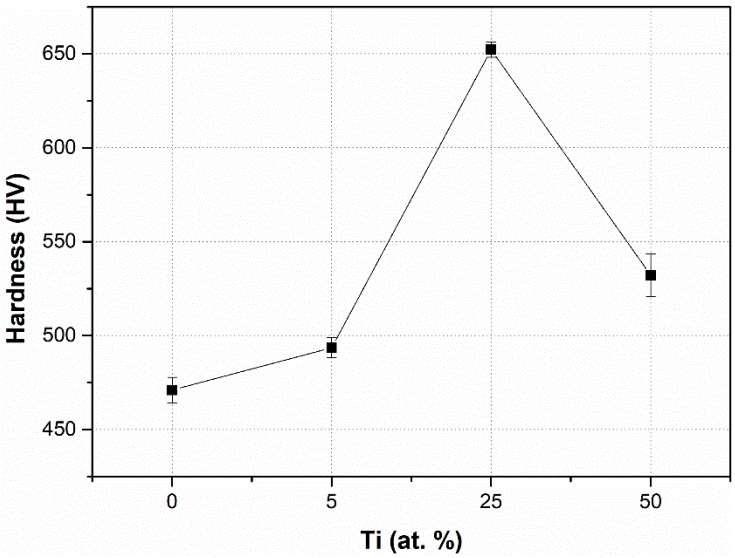

Figure 4
Ti effect on hardness of as-cast HEAs

CONCLUSIONS

In this study, 5 mm cylindrical $(AlCrMnV)_{100-x}Ti_x$ (x=0, 5, 25, 50 at. %) low-density HEAs were produced by vacuum arc melting, and the influence of Ti on the microstructural and mechanical properties was investigated. The XRD results showed the formation of the BCC phase in HEAs. The XRD analysis also indicates that the diffraction peaks of the BCC phase shifted toward the lower angles due to the increasing lattice parameter. The increasing Ti content caused a lattice distortion and increased the hardness of the HEAs. However, hardness decreased from 652 HV to 532 HV. The microstructures of HEAs were examined using SEM to investigate the cooling gradient effect. Columnar structures were found near the outer edges close to the mold, while dendritic structures were present in the central zones of the samples. The results also showed that Ti addition provided almost a homogeneous distribution of the elements in the matrix of the HEAs. In conclusion, Ti addition has a significant effect on the properties of $(AlCrMnV)_{100-x}Ti_x$ in terms of the formation of solid solution phases and tuning the corresponding mechanical properties.

Ethical Statement
This study is an original research article designed and developed by the authors.

Acknowledgements
The authors would like to thank the Necmettin Erbakan University Science and Technology Research and Application Center (BITAM) for their support in the production and characterization of alloys.

Author Contributions
Research Design (CRediT 1) T.S.A.K. (%50) - G.P. (%50)
Data Collection (CRediT 2) T.S.A.K. (%60) - G.P. (%40)
Research - Data Analysis – Validation (CRediT 3-4-6-11) T.S.A.K. (%50) - G.P. (%50)
Writing the Article (CRediT 12-13) T.S.A.K. (%60) - G.P. (%40)
Revision and Improvement of the Text (CRediT 14) T.S.A.K. (%50) - G.P. (%50)

Financing
This research was not supported by any public, commercial, or non-profit organization.

Conflict of Interest
The authors declare no conflict of interest.

REFERENCES

[1] B. Cantor, I.T.H. Chang, P. Knight, A.J.B. Vincent, Microstructural development in equiatomic multicomponent alloys, *Materials Science and Engineering: A*. 375–377 (2004), 213–218. doi:10.1016/J.MSEA.2003.10.257

[2] J.-W. Yeh, S.-K. Chen, S.-J. Lin, J.-Y. Gan, T.-S. Chin, T.-T. Shun, C.-H. Tsau, S.-Y. Chang, Nanostructured high-entropy alloys with multiple principal elements: novel alloy design concepts and outcomes, *Advanced Engineering Materials*. 6 (2004), 299–303. doi: 10.1002/adem.200300567

[3] Y. Zhang, T.T. Zuo, Z. Tang, M.C. Gao, K.A. Dahmen, P.K. Liaw, Z.P. Lu, Microstructures and properties of high-entropy alloys, *Progress in Materials Science*. 61 (2014), 1–93. doi: 10.1016/j.pmatsci.2013.10.001

[4] D.B. Miracle, O.N. Senkov, A critical review of high entropy alloys and related concepts, *Acta Materialia*. 122 (2017), 448–511. doi:10.1016/j.actamat.2016.08.081

[5] F. Otto, Y. Yang, H. Bei, E.P. George, Relative effects of enthalpy and entropy on the phase stability of equiatomic high-entropy alloys, *Acta Materialia*. 61 (2013), 2628–2638. doi: 10.1016/j.actamat.2013.01.042

[6] J.W. Yeh, Recent progress in high-entropy alloys, *Annales de Chimie Science Des Materiaux (Paris)*. 31 (2006), 633–648

[7] D. Ma, M. Yao, K.G. Pradeep, C.C. Tasan, H. Springer, D. Raabe, Phase stability of non-equiatomic CoCrFeMnNi high entropy alloys, *Acta Materialia*. 98 (2015), 288–296. doi: 10.1016/j.actamat.2015.07.030

[8] B.S. Murty, J.W. Yeh, S. Ranganathan, Chapter 2 - High-Entropy Alloys: Basic Concepts, in: B.S. Murty, J.W. Yeh, S.B.T.-H.E.A. Ranganathan (Eds.), *Butterworth-Heinemann*, Boston, 2014: pp. 13–35. doi: 10.1016/B978-0-12-800251-3.00002-X

[9] N. Nayan, G. Singh, S.V.S.N. Murty, A.K. Jha, B. Pant, K.M. George, U. Ramamurty, Hot deformation behaviour and microstructure control in AlCrCuNiFeCo high entropy alloy, *Intermetallics*. 55 (2014), 145–153. doi: 10.1016/j.intermet.2014.07.019

[10] Y.J. Zhou, Y. Zhang, Y.L. Wang, G.L. Chen, Solid solution alloys of AlCoCrFeNiTix with excellent room-temperature mechanical properties, *Applied Physics Letters*. 90 (2007), 181904. doi:10.1063/1.2734517

[11] E. Madenci, Fonksiyonel derecelendirilmiş malzeme plakların statik analizinde mikro-mekanik modellerin katkısı, *Necmettin Erbakan Üniversitesi Fen ve Mühendislik Bilimleri Dergisi*. 5 (2023), 23–37. doi:10.47112/neufmbd.2023.7

[12] L. Gemi, M. Azeem, Ş. Yazman, M. Kayrıcı, O. Gök, Investigation of mechanical properties and damage development of filament wound GFRP composite pipes by ring tensile test, *Necmettin Erbakan Üniversitesi Fen ve Mühendislik Bilimleri Dergisi*. 6 (2024), 93–104. doi:10.47112/neufmbd.2024.34

[13] E.P. George, W.A. Curtin, C.C. Tasan, High entropy alloys: A focused review of mechanical properties and deformation mechanisms, *Acta Materialia*. 188 (2020), 435–474. doi: 10.1016/j.actamat.2019.12.015

[14] Y.-C. Liao, P.-S. Chen, C.-H. Li, P.-H. Tsai, J.S.C. Jang, K.-C. Hsieh, C.-Y. Chen, P.-H. Lin, J.C. Huang, H.-J. Wu, Y.-C. Lo, C.-W. Huang, I.-Y. Tsao, Development of novel lightweight dual-phase Al-Ti-Cr-Mn-V medium-entropy alloys with high strength and ductility, *Entropy*. 22 (2020). doi:10.3390/e22010074

[15] O. Maulik, D. Kumar, S. Kumar, S.K. Dewangan, V. Kumar, Structure and properties of lightweight high entropy alloys: a brief review, *Materials Research Express*. 5 (2018), 52001. doi:10.1088/2053-1591/aabbca

[16] M.J. Chae, A. Sharma, M.C. Oh, B. Ahn, Lightweight AlCuFeMnMgTi high entropy alloy with high strength-to-density ratio processed by powder metallurgy, *Metals and Materials International*. 27 (2021), 629–638. doi:10.1007/s12540-020-00823-5

[17] X. Huang, J. Miao, A.A. Luo, Order-disorder transition and its mechanical effects in lightweight AlCrTiV high entropy alloys, *Scripta Materialia*. 210 (2022), 114462. doi: 10.1016/j.scriptamat.2021.114462

[18] K.M. Youssef, A.J. Zaddach, C. Niu, D.L. Irving, C.C. Koch, A Novel Low-Density, High-Hardness, High-entropy Alloy with Close-packed Single-phase Nanocrystalline Structures, *Materials Research Letters*. 3 (2015), 95–99. doi:10.1080/21663831.2014.985855

[19] İ. Oral, Prediction of hardness values of some wooden materials using computer-aided tap testing, *Necmettin Erbakan Üniversitesi Fen ve Mühendislik Bilimleri Dergisi*. 5 (2023), 257–266. doi:10.47112/neufmbd.2023.23

[20] [Y. Qiu, Y.J. Hu, A. Taylor, M.J. Styles, R.K.W. Marceau, A. V. Ceguerra, M.A. Gibson, Z.K. Liu, H.L. Fraser, N. Birbilis, A lightweight single-phase AlTiVCr compositionally complex alloy, *Acta Materialia*. 123 (2017), 115–124. doi:10.1016/J.ACTAMAT.2016.10.037

[21] S. Son, P. Asghari-Rad, J. Choi, A. Kim, J.-H. Jeong, S. Cho, H.S. Kim, Design and mechanical properties of body-centered cubic AlVCr medium-entropy aluminum alloys, *Journal of Materials Research and Technology*. 24 (2023), 7302–7312. doi: 10.1016/j.jmrt.2023.05.021

[22] K. Knipling, P. Narayana, L. Nguyen, D. Beaudry, Microstructures and properties of as-cast AlCrFeMnV, AlCrFeTiV, and AlCrMnTiV multi-principal element alloys, *Journal of Applied Physics*. 133 (2023), 104901. doi:10.1063/5.0135276

[23] G. Polat, Z.A. Erdal, Y.E. Kalay, Design of Novel Non-equiatomic Cu-Ni-Al-Ti Composite Medium-Entropy Alloys, *Journal of Materials Engineering and Performance*. 29 (2020), 2898–2908. doi:10.1007/s11665-020-04830-w

[24] K.E. Knipling, P.U. Narayana, L.T. Nguyen, Microstructures and properties of As-Cast AlCrFeMnV, AlCrFeTiV, and AlCrMnTiV high entropy alloys, *Microscopy and Microanalysis*. 23 (2017), 702–703. doi:10.1017/S1431927617004172

[25] S. Guo, C.T. Liu, Phase stability in high entropy alloys : Formation of solid-solution phase or amorphous phase, *Progress in Natural Science: Materials International*. 21 (2011), 433–446. doi:10.1016/S1002-0071(12)60080-X

[26] G. Polat, T.S. Atalay Kalsen, Al içeriğinin (CoCrFe)60AlxNi(40-x) Yüksek entropili alaşımının yapısal ve mekanik özellikleri üzerindeki etkisi, *Kahramanmaraş Sütçü İmam Üniversitesi Mühendislik Bilimleri Dergisi*. 26 (2023), 812–822. doi:10.17780/ksujes.1279081

[27] C. Li, Y. Yuan, F. Li, Q. Wei, Y. Huang, Modification and verification of Miedema model for predicating thermodynamic properties of binary precipitates in multi-element alloys, *Physica B: Condensed Matter*. 627 (2022), 413540. doi:10.1016/j.physb.2021.413540

[28] A. Takeuchi, A. Inoue, Classification of bulk metallic glasses by atomic size difference, heat of mixing and period of constituent elements and ıts application to characterization of the main alloying element, *Materials Transactions*. 46 (2005), 2817–2829. doi:10.2320/matertrans.46.2817

[29] X. Huang, J. Miao, A.A. Luo, Lightweight AlCrTiV high-entropy alloys with dual-phase microstructure via microalloying, *Journal of Materials Science*. 54 (2019) 2271–2277. doi:10.1007/s10853-018-2970-4

[30] L. Cao, L. Zhu, H. Shi, Z. Wang, Y. Yang, Y. Meng, L. Zhang, Y. Cui, microstructural evolution from dendrites to core-shell equiaxed grain morphology for $CoCrFeNiV_x$ high-entropy alloys in metallic casting mold, *Metals*, 9 (2019), 1172. doi:10.3390/MET9111172

NEU PRESS

FEN ve MÜHENDİSLİK BİLİMLERİ DERGİSİ

Vol: 7 No: 1 Year: 2025 | Araştırma Makalesi/Research Article | e-ISSN: 2667-7989

https://doi.org/10.47112/neufmbd. 2025.73

Konutlarda Reel Enerji Tüketimi Kestiriminde Güncel Yapay Zeka Algoritmalarının Uygulanması

Fatih ATALAR[1*] Ertuğrul ADIGÜZEL[1] Aysel ERSOY[1]

[1] Istanbul University-Cerrahpaşa, Faculty of Engineering, Department of Electrical and Electronics Engineering, İstanbul, Türkiye

Makale Bilgisi

Geliş Tarihi: 09.03.2024
Kabul Tarihi: 02.09.2024
Yayın Tarihi: 30.04.2025

Anahtar Kelimeler:
Akıllı sistemler,
Derin öğrenme,
Makine öğrenmesi.

ÖZET

Sanayileşmenin hızlanmasıyla birlikte artan enerji arz talebi artık konutlarda da kullanılan yeni nesil elektronik ekipmanlar nedeniyle her geçen gün artmaktadır. Enerjinin klasik yöntemlerle (doğalgaz, sosil yakıtlar vb.) üretilmesine alternatif olarak geliştirilen be yeşil enerji adı verilen yenilenebilir enerjinin kullanımının yaygınlaşmasıyla beraber bazı sorunlar ortaya çıkmaktadır. Elde edilen elektriğin sisteme entegre bir şekilde verilip takip edilebilmesi için veri izlemesi büyük önem arz etmektedir. Bu amaçla kurulan mikro ve makro ölçekteki akıllı şebekelerin dinamik röle haberleşmesi sayesinde büyük ölçeklerde enerji verileri elde edilmektedir. Nesnelerin interneti (IoT) çağında elde edilen bu verilerin işlenmesi ve analiz edilmesi için derin öğrenmek algoritmaları ve makine öğrenmesi yöntemleri kullanılmaktadır. Bu yöntemlerin sağlamış olduğu doğru analizler sayesinde akıllı şebekeler daha az kayıpla (yüksek verimle) çalışmaktadır. En küçük ölçekli bir kullanıcının enerji tüketim hesabı kestirimi optimize bir enerji yönetimi sağlamaktadır. Elektriğin doğru miktarda (güçte) akışı sağlandıktan sonra ortaya çıkabilecek israfın da önüne geçilebilmektedir. Makine ve derin öğrenme algoritmalarının hızlı ve gelişmiş tepkileri sayesinde hem kullanıcılar hem de üreticiler daha planlı ve sürdürülebilir bir enerji yönetimine sahip olmaktadırlar. Bu çalışmada konutlara ait 4 yıllık elektrik enerji verileri Convolutional Neural Network, Long Short-Term Memory, Random Forest ve K-Nearest Neighbors Regression gibi yöntemlerle analiz edilmiştir. Bu analizler neticesinde tüketilecek enerjinin tahmini yapılmıştır. Çalışmadaki öğrenme algoritmalarının etkinliğini değişen eğitim ve test veri oranlarına göre değerlendirmek için veri seti üç farklı bölme yöntemi kullanılarak bölümlendi: %90 eğitim - %10 test, %80 eğitim - %20 test ve %67 eğitim - %33 test bölümü. Ek olarak, daha ileri değerlendirme için 10 katlı çapraz doğrulama yaklaşımı kullanıldı. Karşılaştırmalı analiz, LSTM modelinin günlük tahminler için en düşük MSE değeri olan 0,0054 ile en iyi performans gösteren model olarak ortaya çıktığını ortaya çıkardı.

Application of Contemporary Artificial Intelligence Algorithms in Real Energy Consumption Estimation in Residences

Article Info

Received: 09.03.2024
Accepted: 02.09.2024
Published: 30.04.2025

Keywords:
Smart systems,
Deep learning,
Machine learning.

ABSTRACT

The acceleration of industrialisation has resulted in a corresponding increase in the demand for energy supplies, driven by the growing use of new generation electronic equipment in residential settings. The advent of renewable energy, or green energy, has prompted a shift away from traditional methods of energy production, such as the use of natural gas and fossil fuels. However, this transition has given rise to a number of challenges. It is of great importance to monitor data in order to integrate the obtained electricity into the system and to monitor it. The acquisition of energy data on a large scale is made possible by the implementation of dynamic relay communication within micro and macro scale smart grids, which have been specifically designed for this purpose. Deep learning algorithms and machine learning methods are employed for the processing and analysis of data obtained in the context of the Internet of Things (IoT). The implementation of these methods enables smart grids to operate with reduced loss and enhanced efficiency. The estimation of energy consumption at the smallest scale facilitates the implementation of optimised energy management strategies. By ensuring the flow of electricity in the optimal amount (power), the potential for waste can be mitigated. The rapid and sophisticated responses of machine and deep learning algorithms facilitate more structured and sustainable energy management for both users and producers. In this study, four years' worth of electrical energy data from residential sources was analysed using techniques such as Convolutional Neural Network, Long Short-Term Memory, Random Forest and K-Nearest Neighbours Regression. The resulting analyses enabled the estimation of energy consumption. To assess the efficacy of learning algorithms in the study across varying training and test data ratios, the dataset was partitioned using three distinct division methods: hold-out (90% training - 10% testing), hold-out (80% training - 20% testing), and a 67% training - 33% testing split. Additionally, a 10-fold cross-validation approach was employed for further evaluation. Comparative analysis revealed that the LSTM model emerged as the top-performing model, boasting the lowest MSE value of 0.0054 for daily forecasts.

To cite this article:
Atalar, F., Adıgüzel, E. & Ersoy, A. (2025). Application of contemporary artificial intelligence algorithms in real energy consumption estimation in residences. *Necmettin Erbakan University Journal of Science and Engineering, 7*(1), 31-47. https://doi.org/10.47112/neufmbd. 2025.73

***Sorumlu Yazar:** Fatih Atalar, *fatih.atalar@iuc.edu.tr*

INTRODUCTION

In the current landscape, residential and commercial buildings account for approximately 30% to 40% of total energy demand [1,2], with projections indicating a further rise in this proportion. This escalation in energy demand underscores the growing significance of renewable energy production. The effective integration of renewable energy into the grid requires the development of efficient energy transfer mechanisms, which has led to a significant increase in research activity focused on smart electricity grids and the ability to meet societal demands.

Smart grids, characterized by enhanced communication channels between producers and consumers [3,4], enable real-time monitoring, prediction, scheduling, and adaptive production based on local energy consumption patterns. These networks promise substantial environmental and economic benefits, including optimized electricity transmission with minimized energy losses due to shorter transmission lines, expedited outage resolution, heightened security against sabotage, seamless integration of renewable energy sources, and reduced costs associated with fault detection and repair [5].

The incorporation of artificial intelligence (AI) in electrical network management facilitates efficient planning and real-time control of dynamically evolving power supplies. Consequently, recent research efforts have increasingly delved into this domain [6], with a notable emphasis on leveraging deep learning and machine learning techniques for energy consumption estimation. Such endeavors hold the promise of enabling future electricity networks to forecast energy consumption accurately, allowing users to implement energy-saving measures at the building level. Traditionally, energy consumption forecasting encompasses three temporal categories: short-term forecasts (ranging from one day to one week), medium-term forecasts (spanning from one week to one year), and long-term forecasts (extending beyond one year).

Energy estimation of buildings is a difficult problem because it depends on many different factors (climatic conditions, devices used by the consumer, frequency of use, etc.) [7]. Therefore, taking everything into account when estimating energy will produce more efficient results. Estimating energy consumption; It will make it easier to calculate the amount of energy that needs to be produced and the amount of energy that needs to be stored. In addition, it will enable quick decisions in energy management as it will allow predicting where, when and how much cost will be required. In this way, time-saving methods will be implemented more easily. Future programming will be healthier and more reliable.

In the 2016 study led by Elena Mocanu and her colleagues, the focus was on estimating energy consumption in buildings using deep learning methodologies. Specifically, newly developed stochastic models, namely CRBM (Conditional Restricted Boltzmann Machine) and FCRBM (Fully Conditional Restricted Boltzmann Machine), were employed for this purpose. The researchers utilized the "Individual Household Electric Power Consumption Data Set" obtained by Hebrail and Berard, which is publicly available in the UCI Machine Learning Repository [8]. This dataset comprises individual residential customer data recorded at 1-minute intervals over a span of four years.

The study encompassed the application of predictions under seven distinct scenarios, each employing various machine learning techniques. Specifically, Artificial Neural Networks (ANN), Support Vector Machines (SVM), Recurrent Neural Networks (RNN), CRBM, and FCRBM methods were employed across these scenarios. The scenarios investigated are delineated as in Table 1:

Table 1
Different scenarios for deep learning (DL) application

Scenario	Energy Consumption	Solution Duration for DL
1	15 minutes	1 minute
2	1 hour	1 minute
3	1 day	1 minute
4	1 day	15 minutes
5	1 week	15 minutes
6	1 week	1 hour
7	1 year	1 week

In summary, the Fully Conditional Restricted Boltzmann Machine (FCRBM) demonstrated superior performance compared to state-of-the-art prediction methods such as Artificial Neural Networks (ANN), Support Vector Machines (SVM), Recurrent Neural Networks (RNN), and the Conditional Restricted Boltzmann Machine (CRBM). As the prediction horizon expands, both FCRBM and CRBM exhibit heightened efficacy, with error rates approximately half that of the ANN method. These methodologies yield comparable results and demonstrate potential for real-time applications in home and building automation systems. Notably, rather than estimating total active power directly, a more efficient approach involves estimating and aggregating sub-measurements to arrive at total active power.

In a separate study by Tae-Young Kim et al., minute, hourly, daily, and weekly predictions were conducted using Linear Regression, Long Short-Term Memory (LSTM), and Convolutional Neural Network-Long Short-Term Memory (CNN-LSTM) algorithms [9]. The "Individual Household Electric Power Consumption Data Set" by Hebrail and Berard served as the dataset [10]. Results indicate that the CNN-LSTM algorithm outperformed other algorithms, achieving mean squared error (MSE) values of 0.3738 per minute, 0.3549 per hour, 0.1037 per day, and 0.0952 per week.

In the research conducted by Xiaoou Monica Zhang and colleagues, the Support Vector Regression (SVM) modeling approach served as the predictive algorithm. This methodology was applied to conduct hourly and daily predictions for 15 distinct households' electricity usage data spanning the years 2014 to 2016 [11]. Feature selection and data visualization techniques were employed through exploratory data analysis. The ensuing analyses revealed the feasibility and reliability of predicting residential energy consumption by leveraging weather conditions, calendar parameters, and time-of-use pricing. Notably, the SVM model exhibited satisfactory accuracy in both daily and hourly forecasts for specific residential applications.

Yasemin Kocadayi and her team endeavored to estimate the annual energy consumption of the TR81 region (comprising Zonguldak, Karabuk, and Bartin) utilizing artificial neural networks (ANNs). Input data for the ANN model included building surface areas, population figures, as well as import and export data [12]. The model's performance was evaluated based on metrics such as mean square error, mean absolute error, and correlation coefficient. Through the ANN model, energy consumption projections for the TR81 region spanning 2016 to 2020 were obtained. The findings underscored the ANN model's proficiency in accurately predicting electrical energy consumption within the region, demonstrating a high level of precision.

Derya Yılmaz and her team investigated project risks with a specific focus on heating and electricity demands in buildings. They introduced an innovative model for predicting performance gaps using machine learning classification techniques. The study gathered data on performance gaps and project risks through a web-based survey conducted across 77 buildings. Four machine learning algorithms—Naive Bayes, k-NN, SVM and RF—were evaluated to determine the most effective model.

The results revealed that Naive Bayes demonstrated superior accuracy in predicting the direction

of heating performance gaps (72.50%), negative heating performance gaps (71.81%), positive electricity performance gaps (77.08%), and negative electricity performance gaps (83.85%). Furthermore, both k-NN and SVM exhibited higher accuracy in predicting the direction of electricity performance gaps (79.00%) and positive heating performance gaps (76.04%) [13].

A study performed by Flavian Emmanuel_Sapnken et al. utilizes a dataset from 7,559 buildings and employs nine Machine Learning (ML) models to estimate their energy consumption. Results indicate that the deep neural network (DNN) emerges as the most effective ML model, achieving MAE, MSD, and RMSE of 0.93, 1.12, and 1.06, respectively, in less than 7 seconds, despite the large dataset size. Its R^2 value is also the highest at 0.96, indicating that the DNN approach can explain 96% of the energy consumption in buildings, with only 4% remaining unexplained, likely due to limitations in independent variables. Moreover, this outcome remains consistent across building clusters and various climate zones. Their model proposes a model that professionals can utilize during the design phase of construction projects. This model enables consideration of all critical aspects for designing energy-efficient buildings. It serves as a decision-making tool to control and optimize projects, allowing for anticipation of energy consumption even before construction begins [14].

P. Balakumar et. al. suggest implementing a Demand Side Management (DSM) program within a smart grid to decrease the utility grid's Peak to Average Ratio (PAR) and lower end-users' electricity tariffs. It advocates for the use of renewable energy combined with an Energy Storage System (ESS) in the DSM controller to improve both economic and environmental aspects for end-users. To develop the DSM program, the article proposes a framework based on Recurrent Neural Network (RNN), specifically Long Short-Term Memory (LSTM), for forecasting Science Block (SCB) energy consumption every minute and 5 minutes for Energy Production Control (EPC) and Renewable Energy Generation (REG). The performance of this deep learning model is evaluated using metrics such as Mean Squared Error (MSE), Mean Absolute Error (MAE), Root Mean Square Error (RMSE), and R-squared. The suggested LSTM framework demonstrates superior performance compared to other listed rival techniques in short-term Energy Production Control (EPC) for Science Block (SEIB) and Renewable Energy Generation (REG). For both short-term REG and EPC forecasting, the LSTM model achieves an accuracy with an R^2 value nearly close to one. With their proposed deep learning-based real-time DSM controller, the electricity tariff of SEIB is reduced by 4.4% on January 1st, 2022, and by 14.86% on January 2nd, 2022. Similarly, the utility grid's Peak to Average Ratio (PAR) is minimized to 5.10% and 11.79%, respectively [15].

This study examined the estimation of energy consumption in a house where smart systems are used, comparing it with DL and ML methods. The findings may vary depending on the type of house, for example if it is a smart building or in an urban area. Therefore, in this study, commercial enterprises were excluded, as their consumption could not be evaluated. Within the scope of this study it is not to estimate the demand factor or consumption, but rather to identify the most efficient method using existing consumption data.

MATERIALS AND METHODS

With the advent of technological advancements, researchers are fervently engaged in enhancing efficiency across various domains [16-18]. Among these endeavors, numerous studies are dedicated to advancing the energy sector. Notably, smart grids represent a pivotal facet of these efforts, offering streamlined energy distribution, management capabilities, and integration of renewable energy sources into production processes [19-21]. Across such endeavors, the efficacy of predictive methodologies has seen significant enhancement through the development of novel algorithms [22,23].

The principal objective of this study is twofold: firstly, to glean insights into future energy

consumption patterns through the estimation of energy usage employing deep learning and machine learning techniques; and secondly, to devise a model that not only aids in curbing energy consumption but also facilitates prudent household expenditure planning.

Data Set

The dataset utilized in this study originates from the Individual Household Electric Power Consumption dataset retrieved from the UCI Machine Learning Repository database. This dataset comprises records of electrical power consumption, measured in kilowatt-hours, recorded every minute within a household located in France, spanning from December 2006 to November 2010 (47 months). The dataset, a time series, encompasses a total of 2,075,259 measurements, capturing various time-dependent power-related variables. Notably, the dataset primarily focuses on the total active power measurement values, denoted as "Global_active_power," representing kilowatts consumed by households, amidst seven distinct variables [10].

To facilitate compatibility with machine learning and deep learning algorithms, the dataset necessitated preprocessing and conversion into a suitable format. Notably, the household electrical power consumption dataset exhibited some missing values within the measurements, such as observed on April 28, 2007. Addressing this issue, missing values were imputed by replacing them with the average power consumption values recorded during corresponding minutes across other years. Subsequently, the processed dataset was saved as a new entity, ready for analysis.

In the final stage of data preprocessing, the observations recorded every minute were transformed into daily electrical power consumption quantities measured in kilowatt-hours (kWh). This conversion was implemented to facilitate the estimation of daily energy consumption, thereby condensing minute-by-minute observations into daily totals. Consequently, the dataset encompasses a total of 1442 daily observation values. The actual daily electrical power consumptions following the data preprocessing phase are visually depicted in Figure 1, illustrating the variations in kWh consumption over time. Furthermore, the characteristics of the active power data subsequent to the conversion of the dataset into daily values are detailed in Table 2, providing insights into the statistical properties and distributional aspects of the transformed dataset.

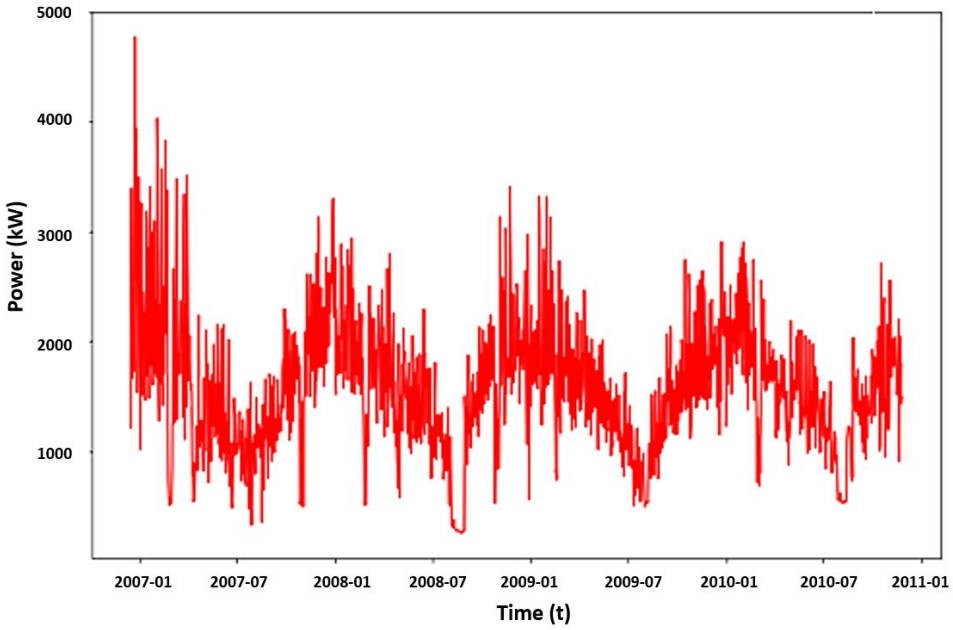

Figure 1
Actual daily electrical power consumption graph after data preview phase

Table 2
Properties of the data set

Data Set Length	1442
Average	1567.839069
Std	597.306856
Minimum	250.298000
25%	1176.195000
50%	1543.253000
75%	1894.467500
Maximum	4773.386000

When conducting time series analysis, the first step involves assessing whether the series exhibits stationarity. Stationarity is characterized by consistent mean and variance of observations over time, indicating that the series does not undergo significant changes across time periods. A stationary time series typically lacks discernible trends or seasonality, making it more amenable to modeling. Statistical modeling techniques often presuppose stationarity for effective application.

In contrast, non-stationary time series display temporal variations such as trends, seasonal effects, or other structural dependencies on the time index. In such cases, summary statistics like mean and variance may fluctuate over time, complicating the modeling process by introducing shifts in the underlying data dynamics. Traditional time series analysis and forecasting methodologies aim to stabilize non-stationary data by identifying and mitigating trends and seasonal effects.

Several approaches exist to assess stationarity in a time series dataset. These include:

Graphical Examination: Time series plots can be visually inspected for evident trends or seasonal patterns.

Summary Statistics: Statistical metrics computed over different seasons or random segments of the data can be compared to identify any pronounced differences, which may indicate non-stationarity.

Statistical tests serve as a valuable tool for assessing whether time series data meet the criteria for stationarity. While these tests rely on certain data assumptions, they offer a swift means of confirming stationarity or non-stationarity. In this study, the Augmented Dickey-Fuller (ADF) test was employed to scrutinize the stationarity of the time series [24]. The ADF test belongs to a class of statistical tests known as unit root tests and is among the most widely utilized methods in this domain. This test leverages an autoregressive model and employs an information criterion to optimize across various lag values.

The null hypothesis (H0) posited by the ADF test suggests that the time series contains a unit root and is thus non-stationary. Conversely, the alternative hypothesis (H1) refutes the null hypothesis, indicating that the time series lacks a unit root and is stationary. The outcome of the ADF test is typically interpreted through the computed p-value. A p-value below a specified threshold (e.g., 5% or 1%) signifies rejection of the null hypothesis, signaling stationarity. Conversely, a p-value surpassing the threshold indicates failure to reject the null hypothesis, implying non-stationarity.

In the context of the Augmented Dickey-Fuller (ADF) test:

- When the p-value is greater than 0.05, the null hypothesis (H0) is not rejected. This indicates that the data contains a unit root and is non-stationary.

- Conversely, when the p-value is less than or equal to 0.05, the null hypothesis (H0) is rejected.

This suggests that the data lacks a unit root and is stationary.

The results of the Augmented Dickey-Fuller (ADF) test are presented in Table 3. The computed ADF test statistics yielded a value of -3.697385. In the context of the ADF test, a more negative statistic increases the likelihood of rejecting the null hypothesis. Notably, the calculated ADF value fell below the critical value corresponding to a significance level of 1%. This discrepancy implies that the null hypothesis will indeed be rejected with a significance level of less than 1%. Moreover, the computed p-value was found to be less than or equal to 0.05. This observation leads to the rejection of the null hypothesis, indicating that the time series exhibits stationarity or lacks a time-dependent structure. In summary, both the ADF test statistic and the p-value converge to suggest the rejection of the null hypothesis, thus affirming the stationarity of the time series data.

Table 3
ADF test results

ADF Statistics	-3.697385
p-value	0.004150
Critical Values	
1%	-3.4357
5%	-2.8645
10%	-2.5686

Application of MLA

In machine and deep learning algorithms, it is worth noting that the percentages of training and testing data can vary for different applications [25,26]. In studies involving large data sets, it is often the case that set division is done at different percentages in order to get the most accurate results [27-29]. Therefore, in our study, we tested data division percentages at different rates in order to gain a better understanding of the impact of this on the results.

To assess the efficacy of learning algorithms in the study across varying training and test data ratios, the dataset was partitioned using three distinct division methods: hold-out (90% training - 10% testing), hold-out (80% training - 20% testing), and a 67% training - 33% testing split. Additionally, a 10-fold cross-validation approach was employed for further evaluation. The implementation of the proposed models was executed utilizing Keras version 2.2.4 with Tensorflow backend, leveraging the Python 3.6 programming language. The machine learning and deep learning algorithms employed in our investigation are extensively documented in scholarly literature. These methodologies find application across various disciplines and are notably prevalent in estimating household energy consumption, which constitutes the focal point of our research [30,31].The selected machine learning algorithms for time series prediction tasks included RF, KNN and LR. By employing a range of diverse partitioning strategies and meticulous algorithmic selections, the study sought to conduct a comprehensive evaluation of the efficacy and resilience of the learning models in accurately forecasting time series data.

Random Forest Algorithm

The Random Forest algorithm is comprised of multiple decision trees operating as an ensemble. In this approach, each individual tree generates a set of predictions, and the class with the highest number of votes among the trees is selected as the final prediction of the model [32].

$$\mathrm{RFfii} = \frac{\sum_{j \in all\ tress} * normfiij}{\mathrm{T}} \quad (1)$$

Rffii = Importance of feature calculated from all trees in RF algorithm

$normfiij$ = Normalized coefficient for i in tree j

T= Total number of decision trees

The "n_estimators" parameter, which indicates how many decision trees will be drawn in the RF algorithm, is taken as 10.

K-Nearest Neighbours Regression

The k-NNR algorithm is often employed in applications prioritizing interpretability of output, computational efficiency, and predictive accuracy. When utilizing the k-NNR algorithm, the Euclidean distance metric (as represented in equation 2) is frequently employed as the distance measure. This metric is applicable to real-valued vectors and quantifies the straight-line distance between the query point and another observed point, as depicted by the following formula [33].

$$\sqrt{\sum_{i=1}^{k}(x_i - y_i)^2} \tag{2}$$

The Manhattan distance, denoted by Equation 3, is an alternative distance measure commonly used in various applications. This metric calculates the absolute difference between two points (x_i ve y_i). Due to its visualization resembling movement along city blocks, it is also known as taxi distance or city block distance. This distance measure is often depicted using a grid, illustrating the path one must traverse via city streets to travel from one address to another.

$$\sum_{i=1}^{k}|x_i - y_i| \tag{3}$$

$$\left(\sum_{i=1}^{k}(x_i - y_i)^q\right)^{1/q} \tag{4}$$

The Minkowski distance, as expressed in Equation 4, serves as a versatile distance metric that encompasses both Euclidean and Manhattan distance measurements. The parameter *p* within the formula facilitates the creation of additional distance metrics. Specifically, when *p* equals two, the formula reduces to represent the Euclidean distance, while when *p* equals one, it represents the Manhattan distance. In the context of the k-Nearest Neighbors Regression (k-NNR) algorithm, the *n_neighbors* parameter, indicating the value of *k*, is set to 3.

Linear Regression

Linear Regression stands as one of the fundamental models in machine learning, employed to discern the relationship between one or more predictor variables and outcome variables. This technique is widely utilized for predictive analysis and modeling purposes, known by various names such as simple linear regression, multiple regression, multivariate regression, ordinary least squares regression, and simply regression.

The formulation of linear regression is represented by the equation:

$$y = ax + b$$

where: y denotes the dependent variable, x represents the independent variable(s), b signifies the slope of the line, and a denotes the intersection point of the line with the y-axis.

The objective of this model is to establish a linear relationship that optimally describes the association between the independent and dependent variables by fitting a straight line to the data points.

Application of Deep Learning Algorithms

Traditionally, linear methods have been favored in time series forecasting due to their well-established principles and effectiveness in handling simple forecasting tasks. However, deep learning methods offer a compelling alternative by enabling the automatic learning of complex mappings from inputs to outputs, accommodating multiple inputs and outputs simultaneously. CNNs are a specialized type of neural network architecture tailored for processing image data. They are highly effective for tasks like image recognition, classification, and object detection. Leveraging their capacity to autonomously extract intricate features from raw input data, CNNs can be effectively applied to time series forecasting problems. On the other hand, Recurrent Neural Networks (RNNs), such as the Long Short-Term Memory (LSTM) network, possess the capability to directly learn across multiple parallel sequences of input data. This characteristic makes them particularly well-suited for time series forecasting tasks. Given the effectiveness demonstrated by CNNs and LSTM methods in addressing time series forecasting challenges, these methodologies were selected for inclusion in the study.

Convolutional Neural Networks

The foundational principles of the Convolutional Neural Network (CNN) algorithm were initially introduced by Kunihiko Fukushima in 1980 [34]. Since its inception, continuous development has led to its current state, where the CNN algorithm has emerged as one of the most prevalent techniques within the realm of deep learning. Notably, CNNs are primarily utilized for the analysis of visual images and are also referred to as invariant space artificial neural networks [35]. Their applications span diverse domains including image and video recognition, recommendation systems, image classification, medical image analysis, natural language processing, and data prediction.

In the proposed CNN model, a series of layers were employed, each serving specific functions within the architecture. These layers include a 1D convolution layer, a dropout layer, a 1D maximum pooling layer, a flatten layer, a fully connected layer (hidden layer), and a final fully connected layer for output. Figure 2 illustrates the arrangement of these layers along with their respective parameter values.

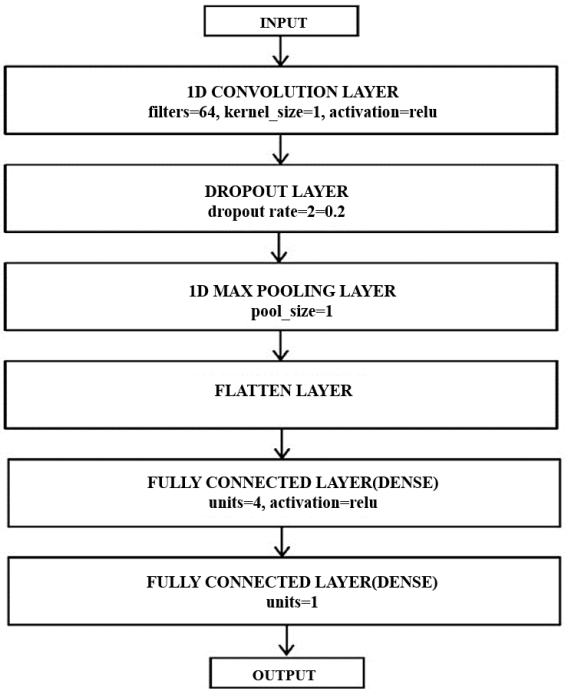

Figure 2
The layers of CNN model

Long-Short Term Memory

LSTM networks are a type of Recurrent Neural Network (RNN) architecture designed to effectively handle sequential data and address the vanishing gradient problem typically found in traditional RNNs. LSTMs are widely used in deep learning for tasks involving time-series data, natural language processing, and other sequence prediction problems [36]. The motivation behind the development of the LSTM algorithm stems from the inherent long-term memory recall challenges observed in traditional RNN algorithms. In contrast to the single layer in RNN models, LSTM models incorporate four distinct layers, each representing feedback connections. These layers encompass various gates, including the input gate, forget gate, and output gate [37].

LSTM algorithms are particularly well-suited for tasks involving classification, processing, and prediction based on time series data. In the proposed Bidirectional LSTM (BLSTM) model, an LSTM layer and a fully connected layer are employed for the output. Figure 3 provides a visual representation of the model's layers, along with their respective parameter values.

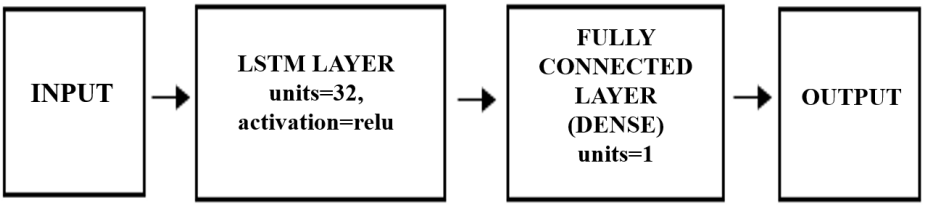

Figure 3
The layers of LSTM Model.

Evaluation Criterias

Root Mean Squared Error

RMSE serves as a metric to quantify the error rate between two datasets, specifically comparing predicted values to observed values. As depicted in Equation 5, RMSE calculates the square root of the average of the squared differences between predicted and observed values. A smaller RMSE value indicates a closer correspondence between the predicted and observed values, reflecting higher accuracy in the predictive model.

$$\sqrt{\frac{1}{n}\sum_{i=1}^{n}(f_i - o_i)^2} \tag{5}$$

f = expected values, o = observed values, n = number of samples

Mean Squared Error

MSE quantifies the proximity of a regression line to a set of data points. It serves as a risk function, representing the expected value of the square of the error loss. Calculated by averaging the squared errors from the data regarding a function, MSE is expressed as the mean of these squared errors. Unlike RMSE, which involves taking the square root of the average squared errors, the formula for MSE (equation 6) does not include the root operation, thereby providing a measure of the average squared discrepancy between predicted and observed values [38].

$$\frac{1}{n}\sum_{i=1}^{n}(f_i - o_i)^2 \tag{6}$$

The implemented code encompasses the following steps:

1. Perform the data reading operation: Read the dataset containing the relevant information for the

analysis.

2. Prepare for cross-validation: Define the parameters and setup necessary for conducting cross-validation.
3. Normalize the data: Scale the input features to ensure uniformity and facilitate the modeling process.
4. Separate the data into training and testing: Partition the dataset into training and testing subsets for model evaluation.
5. Model building: Construct the machine learning or deep learning model using the training data.
6. Make predictions: Utilize the trained model to predict outcomes for the testing data.
7. Obtain cross-validation results: Evaluate the model's performance using cross-validation techniques to assess its generalization ability.
8. Calculate MSE, RMSE, and Accuracy Rates: Compute performance metrics such as MSE, RMSE and Accuracy Rates to quantify the model's predictive accuracy and effectiveness.

These steps collectively form a structured approach to data analysis and model building, ensuring thoroughness and reliability in the analytical process.

RESULTS

In this article, various algorithms were applied with optimized parameter values using different data splitting methods (90% training - 10% test, 80% training - 20% test, and 67% training - 33% test) and cross-validation techniques. Performance analysis results were then presented. Specifically, evaluations of the algorithms applied to the dataset, where training and test data were different splitting rate test method, were conducted based on performance criteria, focusing on daily and weekly data. The findings of these evaluations are summarized in Table 4.

According to the results presented in Table 4, the LSTM model yielded the lowest MSE value of 0.0055. Comparatively, the CNN algorithm achieved an MSE of 0.0056, the RF algorithm attained 0.0066, the k-NNR algorithm resulted in 0.0073 MSE, and the LR algorithm produced an MSE of 0.0058.

Table 4

The comparison of algorithms based on different splitting data rate

Data Splitting	Algorithm	Daily			Weekly		
		MSE	RMSE	Accuracy rate	MSE	RMSE	Accuracy rate
90% training 10% testing	CNN	0.0056	0.0750	0.9944	0.01	0.10	0.9899
	LSTM	0.0054	0.0748	0.9946	0.01	0.1022	0.9896
	RF	0.0066	0.0816	0.9933	0.015	0.122	0.9849
	k-NNR	0.0073	0.0856	0.9927	0.0085	0.0919	0.9915
	LR	0.0058	0.0765	0.9941	0.0090	0.0949	0.9909
80% training 20% testing	CNN	0.0057	0.0760	0.9943	0.0068	0.0828	0.9931
	LSTM	0.0056	0.0753	0.9944	0.0075	0.0866	0.9925
	RF	0.0072	0.0851	0.9927	0.0098	0.0988	0.9902
	k-NNR	0.0084	0.0921	0.9915	0.0067	0.0825	0.9932
	LR	0.0055	0.0745	0.9945	0.0073	0.084	0.9927
67% training 33% testing	CNN	0.0061	0.0785	0.9939	0.0084	0.0919	0.9916
	LSTM	0.0059	0.0774	0.9941	0.0089	0.0944	0.9910
	RF	0.0075	0.0868	0.9924	0.010	0.10	0.9891
	k-NNR	0.0094	0.0973	0.9905	0.012	0.1122	0.9874
	LR	0.0062	0.0786	0.9938	0.0088	0.094	0.9911

According to the results in Table 4, it was seen that the Linear Regression model was the model that gave the smallest MSE value with a value of 0.0055. When MSE values of other methods are examined; The CNN algorithm showed performance with 0.0057, LSTM algorithm 0.0056, RF algorithm 0.0072 and k-NNR algorithm 0.0084 MSE values, respectively.

The LSTM model demonstrated the lowest MSE value, registering at 0.0059. In comparison, the CNN algorithm exhibited an MSE of 0.0060, the RF algorithm yielded 0.0075, the k-NNR algorithm resulted in 0.0094 MSE, and the LR algorithm achieved an MSE of 0.0062.

Additionally, Table 5 outlines the accuracy rates obtained from transactions conducted with Cross-Validation. These results provide further insights into the performance of the algorithms under evaluation.

Table 5
Comparison of Algorithms According to Transactions Performed with Cross-validation.

Algorithm	Daily			Weekly		
	MSE	RMSE	Accuracy rate	MSE	RMSE	Accuracy rate
RF	0.006011	0.07752	0.993998	0.013841	0.11764	0.986162
k-NNR	0.03121	0.17665	0.96884	0.11812	0.34374	0.88198

According to the comparisons made, the loss rate graph of the LSTM model, which is the best performing model applied to the data set for which training and test data were created with the 90% training-10% test splitting method, is shown in Figure 4.

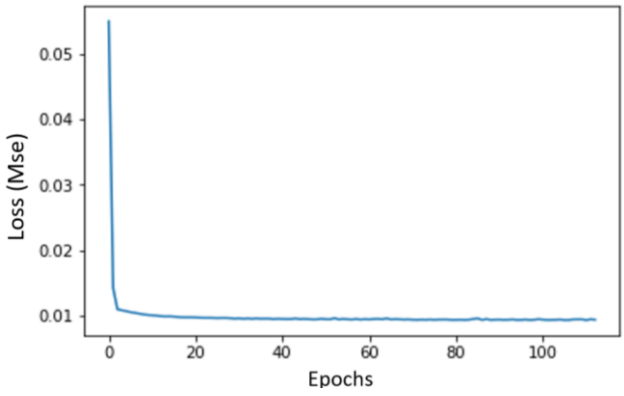

Figure 4
LSTM model loss rate graph (90% training-10% testing)

The figure depicting the comparison between predictions generated by the LSTM model and actual observations from the dataset, where training and test data were partitioned using the 90% training-10% test splitting approach, is presented in Figure 5.

Figure 6 illustrates the graph comparing the actual values and predicted values of the k-NNR algorithm, utilizing the highly effective 80% training-20% test splitting method for estimating weekly consumption values.

DISCUSSION AND CONCLUSIONS

Given the surge in smart grid technologies and the widespread adoption of electricity generation methods, the measurement of energy usage and the formulation of savings plans have gained paramount significance. The literature abounds with numerous studies aimed at estimating consumption through various methodologies. This is owing to the profound potential of modeling and forecasting future electricity consumption, which can lead to substantial energy conservation efforts.

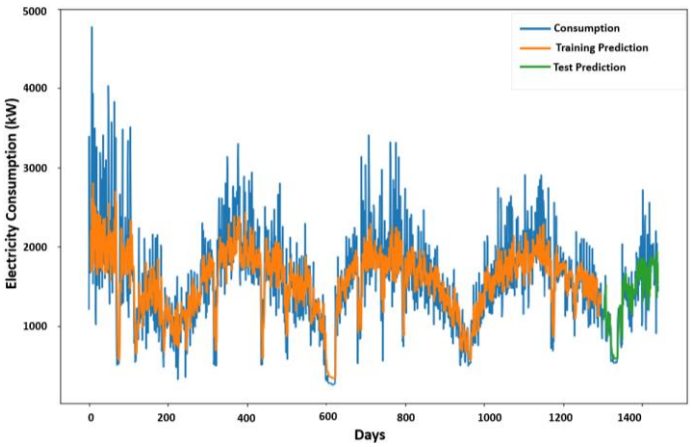

Figure 5
Comparison of real data and LSTM prediction (Daily) values

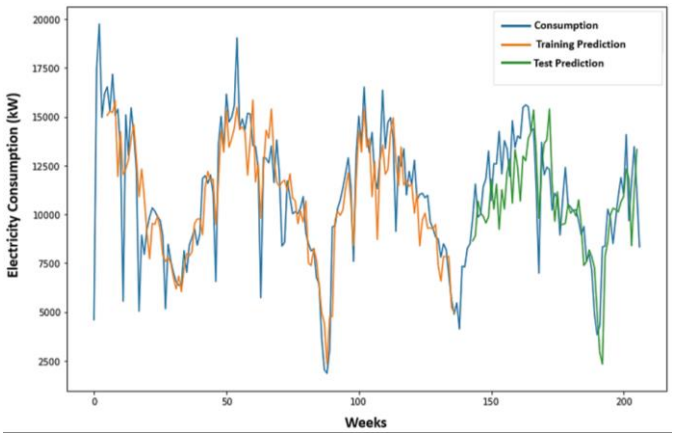

Figure 6
Comparison of real data and k-NNR predicted (weekly) values

The main goal of our work is to establish an infrastructure capable of forecasting future energy consumption by leveraging DL and ML techniques for estimating energy usage. Moreover, the envisaged model is poised to contribute significantly to curbing energy consumption and facilitating the planning of household expenditures. Furthermore, insights will be gleaned into the requisite production levels. The methodologies selected for our study are extensively employed in scholarly literature. Specifically, the LSTM method has demonstrated a noteworthy increase in accuracy percentage compared to existing literature in our research [39,40]. This achievement is readily apparent upon comparison with the literature, where other utilized methods have also exhibited substantial success [41]. The research yielded favorable outcomes in estimating electrical power consumption through the application of CNN, LSTM, RF, k-NNR, and Linear Regression methods. Comparative analysis revealed that the LSTM model emerged as the top-performing model, boasting the lowest MSE value of 0.0054 for daily forecasts. Conversely, for weekly predictions, the k-NNR algorithm exhibited superior performance with an MSE value of 0.0067. Notably, the study indicated a higher success rate in estimating daily energy consumption compared to weekly energy consumption.

Furthermore, when subjected to Cross-Validation, the Linear Regression algorithm demonstrated perfect accuracy with an accuracy rate of 1.0, signifying an exact match with the dataset. The developed model is poised to estimate electrical power consumption with remarkable precision, closely approximating actual observation values. Consequently, the LSTM model, which demonstrated superior performance in estimating electrical power consumption, was deemed the most suitable choice. Moreover, the developed LSTM model showcased enhanced efficacy in smart grid management or

evaluation compared to other applied methods. Through the predictions generated by this approach, savings plans can be formulated effortlessly and with heightened reliability.

When evaluating the performances of LSTM models across different division methods, notably, a superior success rate was attained with the LSTM model applied to the dataset partitioned with the 90% training-10% test splitting method, surpassing other splitting techniques. Similarly, for CNN models, enhanced performance was evident when employing the 90% training-10% test splitting method compared to alternative methods. In the case of RF models, optimal success rates were achieved when utilizing the 90% training-10% test splitting method. Likewise, for k-NNR models, superior performance was observed with the 90% training-10% test splitting method. Conversely, when analyzing the performances of Linear Regression models across division methods, intriguingly, a higher success rate was attained with the Linear Regression model applied to the dataset partitioned with the 80% training-20% test splitting method, diverging from the trends observed with other algorithms. It is noteworthy that Linear Regression did not exhibit a proportional increase in efficiency with the extension of the training series, distinguishing it from other algorithms.

Upon examining the impact of training and test data splitting methods on the performance of the proposed models, a discernible trend emerges: as the size of the training set increases across the utilized splitting methods, the prediction performance of the models demonstrates a consistent improvement. This observation underscores the pivotal role of a larger training set in enhancing model training and subsequently yielding more accurate and reliable predictions. This finding underscores the importance of expanding the dataset for future studies, as it facilitates the development of more robust models and ensures greater consistency in predictions. Moreover, future endeavors may explore the potential of enhancing predictions through the utilization of different deep learning models, leveraging increased dataset sizes to further refine and optimize model performance.

Acknowledgements
The authors extend their heartfelt gratitude to Erol YAVUZ for his invaluable technical support, which significantly contributed to the efficient and expeditious execution of simultaneous analyses in the software employed during the application of artificial intelligence methods. His expertise and assistance were instrumental in the successful completion of this research endeavor.

Ethical Statement
This article is derived from the master's thesis entitled "Comparison of deep learning and machine learning methods for estimating energy consumption in houses" that was completed under the supervision of Prof. Dr. Aysel ERSOY (Master's Thesis, Istanbul University-Cerrahpaşa, Istanbul, Türkiye, 2020). The data and insights presented herein are based on the findings of the aforementioned thesis, with permission from the author. This work aims to build upon and expand the research conducted in the original thesis, contributing to the ongoing discourse in the field.

Author Contributions
Research Design (CRediT 1) F.A. (%60) – E.A. (%20) A.E. (%20)
Data Collection (CRediT 2) F.A. (%60) – E.A. (%20) A.E. (%20)
Research - Data Analysis - Validation (CRediT 3-4-6-11) F.A. (%50) – E.A. (%30) A.E. (%20)
Writing the Article (CRediT 12-13) F.A. (%50) – E.A. (%30) A.E. (%20)
Revision and Improvement of the Text (CRediT 14) F.A. (%50) – E.A. (%30) A.E. (%20)

REFERENCES

[1] S. Fathi, R. Srinivasan, A. Fenner, S. Fathi, Machine learning applications in urban building energy performance forecasting: A systematic review, *Renewable and Sustainable Energy Reviews*. 133 (2020), 110287. doi:10.1016/J.RSER.2020.110287

[2] S. Yang, M.P. Wan, W. Chen, B.F. Ng, S. Dubey, Model predictive control with adaptive machine-learning-based model for building energy efficiency and comfort optimization, *Applied Energy*. 271 (2020), 115147. doi:10.1016/J.APENERGY.2020.115147

[3] N.T. Mbungu, R.M. Naidoo, R.C. Bansal, M.W. Siti, D.H. Tungadio, An overview of renewable energy resources and grid integration for commercial building applications, *Journal of Energy Storage*. 29 (2020), 101385. doi:10.1016/J.EST.2020.101385

[4] A. Rejeb, K. Rejeb, S. Simske, H. Treiblmaier, S. Zailani, The big picture on the internet of things and the smart city: a review of what we know and what we need to know, *Internet of Things (Netherlands)*. 19 (2022), 100565. doi:10.1016/J.IOT.2022.100565

[5] A.H. Al-Badi, R. Ahshan, N. Hosseinzadeh, R. Ghorbani, E. Hossain, Survey of smart grid concepts and technological demonstrations worldwide emphasizing on the Oman perspective, *Applied System Innovation*. 3 (2020) 1–27. doi:10.3390/ASI3010005

[6] M. Hacıbeyoglu, M. Çelik, Ö. Erdaş Çiçek, Energy Efficiency Estimation in Buildings with K Nearest Neighbor Algorithm, *Necmettin Erbakan University Journal of Science and Engineering*. 5(2) (2023), 65–74. doi:10.47112/neufmbd.2023.10

[7] Y. Liu, H. Chen, L. Zhang, X. Wu, X. jia Wang, Energy consumption prediction and diagnosis of public buildings based on support vector machine learning: A case study in China, *Journal of Cleaner Production*. 272 (2020), 122542. doi:10.1016/J.JCLEPRO.2020.122542

[8] E. Mocanu, P.H. Nguyen, M. Gibescu, W.L. Kling, Deep learning for estimating building energy consumption, *Sustainable Energy, Grids and Networks*. 6 (2016), 91–99. doi:10.1016/J.SEGAN.2016.02.005

[9] T.Y. Kim, S.B. Cho, Predicting residential energy consumption using CNN-LSTM neural networks, *Energy*. 182 (2019), 72–81. doi:10.1016/J.ENERGY.2019.05.230

[10] H. Georges and B. Alice. Individual household electric power consumption, *UCI Machine Learning Repository*. 2012. https://doi.org/10.24432/C58K54.

[11] X.M. Zhang, K. Grolinger, M.A.M. Capretz, L. Seewald, Forecasting Residential Energy Consumption: Single Household Perspective, içinde: *Proceedings - 17th IEEE International Conference on Machine Learning and Applications, ICMLA 2018*, 2018: ss. 110–117. doi:10.1109/ICMLA.2018.00024

[12] Y. Kocadayi, O. Erkaymaz, R. Uzun, Estimation of Tr81 area yearly electric energy consumption by artificial neural networks, *Bilge International Journal of Science and Technology Research*. 1 (2017), 59–64.

[13] D. Yılmaz, A.M. Tanyer, I.D. Toker, A data-driven energy performance gap prediction model using machine learning, *Renewable and Sustainable Energy Reviews*. 181 (2023), 113318. doi:10.1016/J.RSER.2023.113318

[14] F.E. Sapnken, M.M. Hamed, B. Soldo, J. Gaston Tamba, Modeling energy-efficient building loads using machine-learning algorithms for the design phase, *Energy and Buildings*. 283 (2023), 112807. doi:10.1016/J.ENBUILD.2023.112807

[15] P. Balakumar, T. Vinopraba, K. Chandrasekaran, Deep learning based real time Demand Side Management controller for smart building integrated with renewable energy and Energy Storage System, *Journal of Energy Storage*. 58 (2023), 106412. doi:10.1016/J.EST.2022.106412

[16] B. Peker, F. A. Çuha, ve H. A. Peker, Analytical solution of Newton's law of cooling equation via kashuri fundo transform, *Necmettin Erbakan University Journal of Science and Engineering*.

6(1) (2024), 10–20. doi:10.47112/neufmbd.2024.29

[17] B. Akgayev, S. Akbayrak, M. Yılmaz, M. S. Büker, ve V. Unsur, Assessing the feasibility of photovoltaic systems in Türkiye: Technical and economic analysis of on-grid, off-grid, and utility-scale PV installations, *Necmettin Erbakan University Journal of Science and Engineering*. 6(1) (2024), 69–92. doi: 10.47112/neufmbd.2024.33

[18] N. Kulaksız, M. Hançer, Flight tests for aircraft in simulink-flightgear environments and comparison of aerodynamic effects on stability/frame axes, *Asrel Aerospace Research Letters*. 1 (2022), 69–83. doi:10.56753/ASREL.2022.2.1

[19] J.C. Kim, S.M. Cho, H.S. Shin, Advanced power distribution system configuration for smart grid, *IEEE Transactions on Smart Grid*. 4 (2013), 353–358. doi:10.1109/TSG.2012.2233771

[20] O. Majeed Butt, M. Zulqarnain, T. Majeed Butt, Recent advancement in smart grid technology: Future prospects in the electrical power network, *Ain Shams Engineering Journal*. 12 (2021), 687–695. doi:10.1016/J.ASEJ.2020.05.004

[21] C. Crozier, T. Morstyn, M. McCulloch, The opportunity for smart charging to mitigate the impact of electric vehicles on transmission and distribution systems, *Applied Energy*. 268 (2020), 114973. doi:10.1016/J.APENERGY.2020.114973

[22] M. Karakoyun, A. Özkış, Development of binary moth-flame optimization algorithms using transfer functions and their performance comparison, *Necmettin Erbakan University Journal of Science and Engineering*. 3(2) (2021), 1-10.

[23] T. Ahmad, R. Madonski, D. Zhang, C. Huang, A. Mujeeb, Data-driven probabilistic machine learning in sustainable smart energy/smart energy systems: Key developments, challenges, and future research opportunities in the context of smart grid paradigm, *Renewable and Sustainable Energy Reviews*. 160 (2022), 112128. doi:10.1016/J.RSER.2022.112128

[24] R.I.D. Harris, Testing for unit roots using the augmented Dickey-Fuller test: Some issues relating to the size, power and the lag structure of the test, *Economics Letters*. 38 (1992), 381–386. doi:10.1016/0165-1765(92)90022-Q

[25] Y.H. Bhosale, K.S. Patnaik, Bio-medical imaging (X-ray, CT, ultrasound, ECG), genome sequences applications of deep neural network and machine learning in diagnosis, detection, classification, and segmentation of COVID-19: a Meta-analysis & systematic review, *Multimedia Tools and Applications.* 82 (2023), 39157–39210. doi:10.1007/S11042-023-15029-1

[26] M.M. Islam, F. Karray, R. Alhajj, J. Zeng, A Review on deep learning techniques for the diagnosis of novel coronavirus (COVID-19), *IEEE Access*. 9 (2021), 30551–30572. doi:10.1109/ACCESS.2021.3058537

[27] P. Manikandan, U. Durga, C. Ponnuraja, An integrative machine learning framework for classifying SEER breast cancer, *Scientific Reports.* 13 (2023), 1–12. doi:10.1038/s41598-023-32029-1

[28] R. Anand, S.V. Lakshmi, D. Pandey, B.K. Pandey, An enhanced ResNet-50 deep learning model for arrhythmia detection using electrocardiogram biomedical indicators, *Evolving Systems*. 15 (2024), 83–97. doi:10.1007/S12530-023-09559-0/TABLES/7

[29] A. Uddin, M. Islam, A. Talukder, A.A. Hossain, A. Akhter, S. Aryal, M. Muntaha, Machine learning based diabetes Detection Model for false negative reduction, *Biomedical Materials & Devices*. 2 (2023), 427–443. doi:10.1007/s44174-023-00104-w

[30] R. Olu-Ajayi, H. Alaka, I. Sulaimon, F. Sunmola, S. Ajayi, Building energy consumption prediction for residential buildings using deep learning and other machine learning techniques, *Journal of Building Engineering*. 45 (2022), 103406. doi:10.1016/J.JOBE.2021.103406

[31] H. Ma, L. Xu, Z. Javaheri, N. Moghadamnejad, M. Abedi, Reducing the consumption of household systems using hybrid deep learning techniques, *Sustainable Computing: Informatics and Systems*. 38 (2023), 100874. doi:10.1016/J.SUSCOM.2023.100874

[32] M. Schonlau, R.Y. Zou, The random forest algorithm for statistical learning, *Stata Journal*. 20 (2020), 3–29. doi:10.1177/1536867X20909688

[33] O. Kramer, K-Nearest Neighbors. In: Dimensionality Reduction with Unsupervised Nearest Neighbors. *Intelligent Systems Reference Library*, vol 51. (2013). Springer, Berlin, Heidelberg. https://doi.org/10.1007/978-3-642-38652-7_2

[34] K. Fukushima, Neocognitron: A self-organizing neural network model for a mechanism of pattern recognition unaffected by shift in position, *Biological Cybernetics*. 36 (1980), 193–202. doi:10.1007/BF00344251/METRICS

[35] X. Wang, Y. Zhao, F. Pourpanah, Recent advances in deep learning, *International Journal of Machine Learning and Cybernetics*. 11 (2020), 747–750. doi:10.1007/S13042-020-01096-5/METRICS

[36] A. Sherstinsky, Fundamentals of recurrent neural network (RNN) and long short-term memory (LSTM) network, *Physica D: Nonlinear Phenomena*. 404 (2020), 132306. doi:10.1016/J.PHYSD.2019.132306

[37] R.C. Staudemeyer, E.R. Morris, Understanding LSTM -- a tutorial into long short-term memory recurrent neural networks, *Neural and Evolutionary Computing*. (2019). https://arxiv.org/abs/1909.09586v1

[38] E. Yavuz, Comparison Of Deep Learning And Machine Learning Methods For Estimating Energy Consumption In Houses, M.Sc. Thesis, *Istanbul University-Cerrahpaşa Institute of Graduate Studies Department of Electrical and Electronic Engineering*, Istanbul, 2020.

[39] J.Q. Wang, Y. Du, J. Wang, LSTM based long-term energy consumption prediction with periodicity, *Energy*. 197 (2020), 117197. doi:10.1016/J.ENERGY.2020.117197

[40] S. Alaloul, B.A. Tayeh, M.A. Musarat, D. Durand, J. Aguilar, M.D. R-Moreno, An analysis of the energy consumption forecasting problem in smart buildings using LSTM, *Sustainability*. 14 (2022), 13358. doi:10.3390/SU142013358

[41] R. Olu-Ajayi, H. Alaka, I. Sulaimon, F. Sunmola, S. Ajayi, Building energy consumption prediction for residential buildings using deep learning and other machine learning techniques, *Journal of Building Engineering*. 45 (2022), 103406. doi:10.1016/J.JOBE.2021.103406

FEN ve MÜHENDİSLİK BİLİMLERİ DERGİSİ

Vol: 7 No: 1 Year: 2025 | Araştırma Makalesi/Research Article | e-ISSN: 2667-7989

https://doi.org/10.47112/neufmbd.2025.74

Metastatik Meme Kanseri Hücrelerinde EGF Uyarımına Bağlı Olarak PKA, AKT(PKB) ve PKC Hedefli AKT Substratlarının Fosforilasyon Düzeylerinin Değişimi

Merve ÖZCAN TÜRKMEN [1*] Şebnem PEHLİVANOĞLU [2] Suray PEHLİVANOĞLU [1]

[1] Necmettin Erbakan University, Faculty of Science, Department of Molecular Biology and Genetics, Konya, Türkiye

[2] Necmettin Erbakan University, Institute of Health Sciences, Department of Medical Biology, Konya, Türkiye

Makale Bilgisi

Geliş Tarihi: 31.08.2024
Kabul Tarihi: 20.11.2024
Yayın Tarihi: 30.04.2025

Anahtar Kelimeler:
PI3K/AKT Yolağı,
AKT Substratı,
PKA, PKB ve PKC
inhibisyonu.

ÖZET

Protein kinaz B (PKB/AKT), hücre metabolizması, büyüme, çoğalma ve tümör invazyonu dahil olmak üzere çok çeşitli fizyolojik ve patolojik süreçleri düzenleyen fosfatidilinositol-3-kinaz (PI3K)/AKT sinyal yolağının temel düzenleyicisidir. AKT enzimi, EGF gibi hücresel uyarıcı moleküller tarafından aktive edilebilen bir serin/treonin kinazdır. Aktive AKT enzimi, hedef substratlarını RxRxxS/T konsensus dizisine bağlanarak fosforile eder. Bazı AKT hedefleri, farklı serin/treonin kinazlar tarafından benzer rezidulardan fosforile edilebilmektedir. Bu substratlar üzerinde yapılan birçok çalışma, sinyal yolakları arası etkileşimi sağlayan ortak moleküllerin ve yeni terapötik hedeflerin belirlenmesi için değerli bilgiler sunmaktadır. Bu bağlamda söz konusu çalışmada, EGF uyarımına bağlı olarak MDA-MB-231 üçlü negatif metastatik meme kanseri hücrelerinde, AKT substrat fosforilasyonlarını mimik eden PKA, PKB(AKT) ve PKC hedefli yeni moleküllerin belirlenmesi amaçlanmıştır. AKT substratlarının fosforilasyon düzeyleri Western blot analizi ile değerlendirildi. Elde edilen sonuçlara göre, PKA, PKB ve PKC inhibitörlerinin varlığında ve EGF uyarımı ile birlikte 30 kDa ağırlığında bir fosfo-proteininin (pp30), AKT substrat fosforilasyon düzeyinin değiştiği saptandı. EGF uyarımına bağlı olarak, beklendiği üzere AKT substratlarının fosforilasyon düzeyleri artarken, inhibitörler bu fosforilasyonları baskılamaktadır. Dikkat çekici bir şekilde, PKC inhibitörü varlığında pp30'un fosforilasyon düzeyinin, EGF uyarımına rağmen kontrole kıyasla azaldığı belirlendi. Bu sonuç, pp30'un hücresel regülasyonunun PKC tarafından AKT ile aynı bölgeden gerçekleşebileceğini ortaya koymaktadır. Çalışmamızdaki metodoloji, AKT ile PKC sinyal yolakları arasındaki etkileşimde rolü olabilecek yeni potansiyel düzenleyicilerin tanımlanabilmesinin mümkün olduğunu göstermektedir. Ancak, bu etkileşimin ne yönde olduğunu açıklayabilmek için ileri çalışmalara ihtiyaç vardır.

Changes in Phosphorylation Levels of PKA, AKT(PKB) and PKC Targeted AKT Substrates Upon EGF Stimulation in Metastatic Breast Cancer Cells

Article Info

Received: 31.08.2024
Accepted: 20.11.2024
Published: 30.04.2025

Keywords:
PI3K/AKT pathway,
AKT substrate,
PKA, PKB and PKC
inhibition.

ABSTRACT

Protein kinase B (PKB/AKT) is a crucial regulator of the phosphatidylinositol 3-kinase (PI3K)/AKT signaling pathway, which regulates a wide range of physiological and pathological processes, including cell metabolism, growth, proliferation, and tumor invasion. The AKT enzyme is a serine/threonine kinase that can be activated by cellular stimuli such as EGF. Once activated, the AKT enzyme phosphorylates its target substrates by binding to the RxRxxS/T consensus sequence. Some AKT targets can be phosphorylated at similar residues by different serine/threonine kinases. Numerous studies on these substrates provide valuable insights into common molecules facilitating cross-talk between signaling pathways and the identification of new therapeutic targets. In this study, we aimed to identify novel molecules that target PKA, PKB (AKT), and PKC and mimic AKT substrate phosphorylation in EGF-stimulated MDA-MB-231 triple-negative metastatic breast cancer cells. Phosphorylation levels of AKT substrates were assessed using Western blot analysis. According to the results, the phosphorylation level of a 30 kDa phosphoprotein (pp30) varied in the presence of PKA, PKB, and PKC inhibitors, as well as upon EGF stimulation. As expected, phosphorylation levels of AKT substrates increased with EGF stimulation, while the inhibitors suppressed these phosphorylations. Interestingly, in the presence of the PKC inhibitor, the phosphorylation level of pp30 was found to be decreased compared to the control, despite EGF stimulation. This suggests that cellular regulation of pp30 by PKC might occur through the same region as AKT. Our methodology demonstrates the potential to identify new regulators that may play a role in the interaction between AKT and PKC signaling pathways. However, further studies are required to elucidate the specifics of this interaction.

To cite this article:
Özcan Türkmen, M., Pehlivanoğlu, Ş. & Pehlivanoğlu, S. (2025). Changes in phosphorylation levels of PKA, AKT(PKB) and PKC targeted AKT substrates upon EGF stimulation in metastatic breast cancer cells. *Necmettin Erbakan University Journal of Science and Engineering, 7*(1), 48-55. https://doi.org/10.47112/neufmbd.2025.74

***Sorumlu Yazar:** Merve Özcan Türkmen, *mozcanturkmen@erbakan.edu.tr*

INTRODUCTION

Cancer is the second leading cause of death globally after ischemic heart disease [1-2]. According to the Global Cancer Statistics 2022, there were nearly 20 million new cancer cases and 9.7 million deaths due to cancer in that year [3]. In women, breast cancer was the most common, while in men, lung cancer was the most frequent, both in terms of cases and deaths in 2022 [3]. Breast cancer is the most frequently diagnosed cancer and one of the main causes of cancer-related deaths in women worldwide [4-5]. This cancer is characterized by the abnormal growth and proliferation of cells originating in the breast tissue [6]. It is a metastatic cancer and often spreads to distant organs such as the liver, bone, lung, and brain, which primarily accounts for its incurability [7]. Numerous risk factors associated with breast cancer have been established, including older age, female gender, early menarche, late menopause, positive family history, long-term hormone replacement therapy, a history of radiation therapy to the chest, and *BRCA1/2* gene mutations [5, 8-9]. The prognosis of breast cancer and the patient's response to distinct types of therapies vary among subtypes of this heterogeneous disease [10]. These subtypes are typically classified into four categories depending on the immunohistochemical expression of specific biomarkers: estrogen receptor-positive (ER+), progesterone receptor-positive (PR+), human epidermal growth factor receptor 2-positive (HER2+), and triple-negative breast cancer (TNBC), which is characterized by the absence of expression of any of these receptors [11]. HER2-positive and endocrine-sensitive diseases can be treated with targeted therapies, whereas chemotherapy remains the primary treatment for TNBC [12]. The effectiveness of targeted treatments is limited by primary or secondary resistance [12]. Increasing evidence indicates that the active phosphatidylinositol 3-kinase (PI3K)/protein kinase B (AKT)/mammalian target of rapamycin (mTOR) signaling pathway plays a key role in treatment resistance and disease progression [12].

The persistence of proliferation stimulation is among the distinguishing features of cancer and many genes and proteins, especially kinases and kinase receptors, play an active role in this process. [13]. One member of the protein kinase family is protein kinase B (PKB) which is also known as AKT [14]. PKB/AKT is a serine-threonine kinase which is a member of the AGC (protein kinase A, PKC, PKG) kinase superfamily [14-15]. It has three isoforms (AKT1, AKT2 and AKT3) in mammals and their kinase domains have extensive homology to these AGC kinases [16]. AKT is activated by growth factors, cytokines and other cellular stimulatory molecules and activated AKT phosphorylates a large number of substrates which play roles in many cellular signaling pathways [16]. These pathways are involved in several important cellular processes including cell survival, proliferation, cell size in response to nutrient availability, growth, metabolism, angiogenesis, and tumor invasion [14]. Furthermore, the activation of AKT involves the phosphorylation of two regulatory phosphorylation sites, threonine-308 (Thr308) and serine-473 (Ser473) [17]. Co-phosphorylation of these two amino acids is essential for full activation of AKT [18]. Activated AKT specifically phosphorylates many downstream substrates harboring the recognition motif R-X-R-X-X-S/T-B (where X is any amino acid and B represents a bulky hydrophobic amino acid) in the cytosol and nucleus [16, 19-20] (Figure 1).

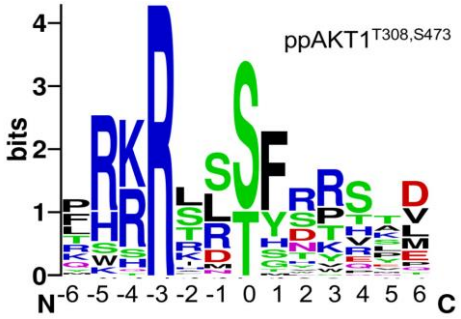

Figure 1
Target sequences of substrate recognition motif for Activated AKT (phosphorylated on S473 and T308) [20]

Various factors such as proteins, ligands, receptors and effector molecules play a role in AKT activation [21]. In this context, AKT serves as a central node within a signaling pathway that includes numerous components, and various cellular signaling pathways intersect at the AKT molecule. [14]. Therefore, AKT has a significant number and variety of downstream substrates or targets [22] (Table 1). Studies investigating these substrates are crucial because they provide an effective approach to discovering new therapeutic targets. In this study, we aimed to determine the potential AKT substrates in the presence of different protein kinase inhibitors in MDA-MB-231 breast adenocarcinoma cells which belong to the TNBC category. For this purpose, PKA, PI3K/PKB and PKCs, were targeted and an inhibitor of one of these proteins was used each time. Phospho-forms of AKT substrates were determined by Western blot analysis from cell lysates after stimulation with epidermal growth factor (EGF), which is one of the important factors that enable AKT activation.

Table 1
List of some of the known AKT substrates and their phosphorylation sites

GENE SYMBOL	GENE NAME	P-SITE	FUNCTION
FOXO1A	*Forkhead box O1A*	T24	FoxO Signaling
FOXO1A	*Forkhead box O1A*	S256	FoxO Signaling
FOXO1A	*Forkhead box O1A*	S319	FoxO Signaling
FOXO3	*Forkhead box O3*	S253	FoxO Signaling
FOXO3	*Forkhead box O3*	T32	FoxO Signaling
FOXO4	*Forkhead box O4*	S197	FoxO Signaling
FOXO4	*Forkhead box O4*	T32	FoxO Signaling
FOXO4	*Forkhead box O4*	S262	FoxO Signaling
NOS3	*Nitric oxide synthase 3*	S1177	NO Signaling
BRF1	*B - related factor 1*	S92	RNA Metabolism
PFKFB2	*6-phosphofructo-2-kinase/fructose-2,6-biphosphatase 2*	S466	Insulin and carbohydrate metabolism
PFKFB2	*6-phosphofructo-2-kinase/fructose-2,6-biphosphatase 2*	S483	Insulin and carbohydrate metabolism
CLK2	*CDC-like kinase 2*	S34	Insulin and carbohydrate metabolism
CLK2	*CDC-like kinase 2*	T127	Insulin and carbohydrate metabolism
BRCA1	*Breast cancer gene 1*	T509	DNA repair, modification, and chromatin regulation
BRCA1	*Breast cancer gene 1*	S694	DNA repair, modification, and chromatin regulation
ESR1	*Estrogen receptor 1*	S167	Hormone receptors
ESR1	*Estrogen receptor 1*	S305	Hormone receptors
AR	*Androgen receptor*	S791	Hormone receptors
AR	*Androgen receptor*	S213	Hormone receptors
AKT1	*RAC-alpha serine/threonine-protein kinase*	S246	Cell growth and survival
AKT1	*RAC-alpha serine/threonine-protein kinase*	T72	Cell growth and survival
BRAF	*B-Raf proto-oncogene, serine/threonine kinase*	S365	Cell growth and survival
BRAF	*B-Raf proto-oncogene, serine/threonine kinase*	S429	Cell growth and survival
TSC2	*Tuberous sclerosis complex 2*	S939	Cell growth and survival
TSC2	*Tuberous sclerosis complex 2*	S981	Cell growth and survival
MDM2	*Mouse double minute 2 homolog*	S186	Apoptosis
MDM2	*Mouse double minute 2 homolog*	S188	Apoptosis
MDM2	*Mouse double minute 2 homolog*	S166	Apoptosis
PDCD4	*Programmed cell death 4*	S67	Apoptosis
PDCD4	*Programmed cell death 4*	S457	Apoptosis

MATERIALS AND METHODS

Cell Culture

The MDA-MB-231 (ATCC, HTB-26) breast adenocarcinoma cells were obtained from American Type Culture Collection. The cells were incubated in an incubator (ESCO-CCL-170B-8) 5% CO_2 atmosphere, 90% humidified air at 37°C. The culture medium was DMEM high glucose medium (D5796, Sigma-Aldrich, St. Louis, Missouri, USA) supplemented with 10% heat-inactivated fetal bovine serum (FBS) (F9665, Merck, Darmstadt, Germany) and 1% penicillin-streptomycin (15140122, Gibco, ThermoFisher Sci., Waltham, Massachusetts, USA) in 25 cm^2 culture flask (CLS430639, Corning, New York, USA). Cell morphologies and confluency were visualized using an inverted microscope (Primovert, Zeiss, Jena, Germany).

EGF Stimulation and Treatment of Cells with PKA, PI3K/PKB and PKC Inhibitors

The MDA-MB-231 cells were seeded into a 6-well culture plate at 1×10^5 cells/well concentration. The day before treatment, the cells were incubated in serum-free media overnight and then treated with protein kinase inhibitors: H-89 Dihydrochloride (MedChemExpress, HY-15979) as a PKA inhibitor, LY294002 (Thermo Fisher Scientific, Inc., PHZ1144) as a PI3K/PKB inhibitor, and RO318220 (Abcam, ab120374) as a PKC inhibitor. After washing the cells with 1×PBS, they were treated for 2 hours with two different inhibitor concentrations: 2 and 5 μM for H-89 Dihydrochloride (PKA inhibitor) [23], 1 and 5 μM for LY294002 (PI3K/PKB inhibitor) [24], and 1 and 5 μM for RO318220 (PKC inhibitor) [25]. Following treatment, the cells were stimulated with EGF (10 ng/mL) in medium containing 1% FBS and incubated for 72 hours [26]. Cells that were not treated with EGF or inhibitors were used as controls.

Western blot

Following treatment with inhibitors and EGF described above at the indicated times, the cells were harvested and the cell lysates were prepared from the untreated and treated MDA-MB-231 cells. Cell lysates were obtained by 1X cell lysis buffer (cat.9806, Cell Signaling Tech., USA) and incubated on ice for 30 min. The cell lysate samples were clarified by centrifugation at 10.000 rpm for 1 min, and the total protein concentration was determined by the Bradford method. A hundred micrograms of total protein were size-fractioned on a 10 % SDS page and transferred to the PVDF membrane (cat. 88518, ThermoFisher Sci., USA). For immunoblotting, the membranes were incubated overnight with primary antibody (1:1000) (rabbit Phospho-Akt Substrate (cat. 9614, Cell Signaling Tech., USA) and then with horseradish peroxidase-conjugated anti-rabbit secondary antibody (cat. sc-2357, Santa Cruz Biotechnology, Inc., USA) (1:5000) for 2 h. The protein immunoreactivity was visualized using X-ray imaging.

Statistical Analysis

Analyses of experimental data were performed using GraphPad Prism 9.0 software. *p* values of the results were calculated using One-way ANOVA (Dunnet t-test). A *p* value of <0.05 was considered statistically significant. The results were normalized and presented by determining ± standard error values.

RESULTS

To determine the potential AKT substrates in the presence of different protein kinase inhibitors, the MDA-MB-231 cells were treated or untreated with H-89 (PKA inhibitor), LY294002 (PKB inhibitor) or RO318220 (PKC inhibitor) and then subsequently exposed to EGF or not. Whole-cell lysates were blotted with phospho-AKT substrate antibody. In this study, we demonstrated that the phosphorylation level of an approximately 30 kDa AKT substrate (pp30), which has not been previously

described in the literature, varies depending on the presence of EGF and the specific inhibitors. We found that the phosphorylation level of pp30 increased by 1.11 to 1.44-fold with EGF stimulation compared to the control. In the presence of inhibitors, the phosphorylation level of pp30 decreased in a dose-dependent manner in both control and treated cells. Despite PKA and PKB inhibition, phosphorylation still increased with EGF, although PKC treatment suppressed this increase by %52 at 5 μM concentration. These results indicate that AKT targets are regulated not only by the PI3K/AKT axis but also by the PKC pathway under EGF stimulation. In this context, it can be inferred that AKT, which is known to have an inverse relationship with PKC signaling in cancer cells, could interacts with some of AKT substrates (Figure 2).

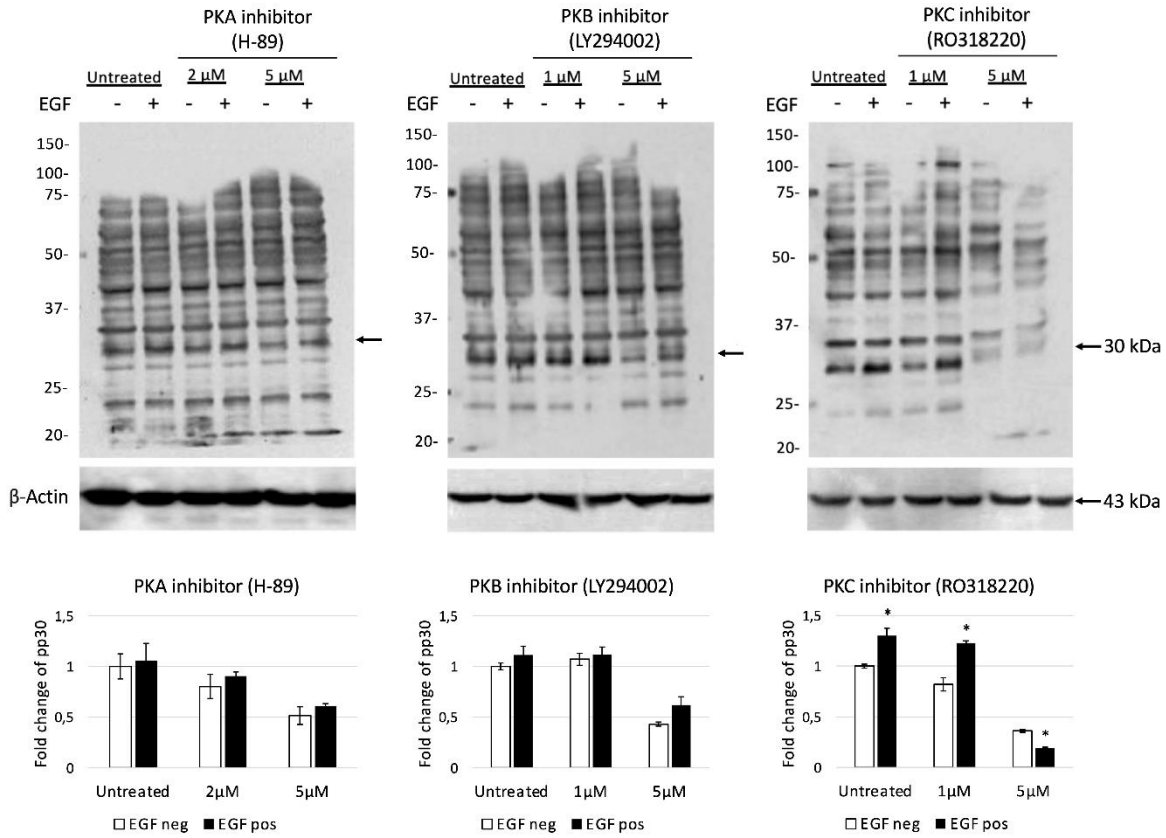

Figure 2

Western blot analysis of various phosphorylated AKT substrates in MDA-MB-231 cells, treated or untreated with PKA, PI3K/PKB, and PKC ınhibitors upon EGF stimulation, revealed a 30 kDa Phospho-protein (pp30) (black arrows) (, p<0.05).*

DISCUSSION

AKT (PKB) was discovered about 32 years ago and has since been the subject of tens of thousands of studies in various fields of medicine and biology [27]. The broad range of AKT's functions arises from its numerous downstream substrates, with over 200 AKT substrates identified to date [27-28]. The molecular interactions of the AKT signaling network are better understood by determining and identifying these diverse AKT substrates [27]. This study presents a method for identifying novel AKT substrates using specific inhibitors and phosphomotif-specific antibodies. The method involves activating the kinase through stimulation and comparing phosphoproteins based on the presence or absence of pathway blockade [29]. Using this approach, this study determined a novel candidate AKT substrate (pp30) regulated also by PKC (Figure 2). Similarly, Kane et al. [29] applied this method and isolated a novel 160-kDa substrate for AKT from adipocytes. Then, the characterization studies of the

protein revealed that the 160 kDa protein was a GTPase activating protein for Rab. AKT-mediated phosphorylation of this protein plays an important role in insulin-stimulated transport of the glucose transporter GLUT4 to the plasma membrane [30]. Another giving evidence, four novel phospho-proteins (47, 75, 105, and 250 kDa) were identified using an AKT phosphomotif-specific antibody through insulin stimulation [31]. In addition to this, the lack of change in the phosphorylation level of the described 75 kDa protein upon treatment with PI3K inhibitors suggests that this protein may not be an AKT substrate [31]. According to these findings, it can be said that the combination of different inhibition strategies is needed to confirm the data obtained.

The relationship between PKC inhibitor RO318220 and PI3K/AKT signal pathway was examined by Zhu et al [32]. They showed that adding the PKC inhibitor RO318220 increased AKT phosphorylation and neuronal survival suggesting that RO318220 protects rat cerebellar granule cell neurons by activating AKT [32]. Similarly, Wen et. al [33] showed that PKC inhibitors RO318220, bisindolylmaleimide VIII, and PKCβ inhibitor LY379196 increased phosphorylation and stimulation of AKT in human airway epithelial A549 cells and human embryonic kidney HEK293 cells. In another study, the regulation and role of mitogen-activated protein kinase (MAPK) and PI3K/AKT signaling in uveal melanoma responses to PKC inhibition were investigated [34]. They indicated that in UM patients treated with the PKC inhibitor IDE196, the PI3K/AKT pathway was active and not inhibited by PKC inhibition, whereas the (MAPK) signaling pathway was inhibited [34].

The results of the present study are preliminary and demonstrate how new AKT targets can be identified through the cooperation of different pathways. Whether pp30 is indeed phosphorylated by AKT can be confirmed through immunoprecipitation and *in vitro* kinase assays. Additionally, proteomic approaches using Matrix-Assisted Laser Desorption/Ionization Time-of-Flight/Time-of-Flight Mass Spectrometry (MALDI-TOF/TOF-MS) are needed for molecular characterization. In the next stage, it will be important to determine the phosphorylation site and cellular function of pp30.

In conclusion, studies investigating novel AKT targets are crucial for identifying new therapeutic options. Moreover, the methodology used in this study demonstrated that cellular pathways can crosstalk to achieve common goals. Different enzymes, such as PKC, can activate distinct signaling pathways and targets, including AKT substrates.

Ethical Statement

This study is an original research article designed and developed by the authors.

Ethics Committee Approval

This study does not require any ethics committee approval.

Author Contributions

Research Design (CRediT 1) M.O.T. (%30) - Ş.P. (%30) – S.P. (%40)
Data Collection (CRediT 2) M.O.T. (%25) - Ş.P. (%25) – S.P. (%50)
Research - Data Analysis – Validation (CRediT 3-4-6-11) M.O.T. (%30) - Ş.P. (%30) – S.P. (%40)
Writing the Article (CRediT 12-13) M.O.T. (%40) - Ş.P. (%30) – S.P. (%30)
Revision and Improvement of the Text (CRediT 14) M.O.T. (%40) - Ş.P. (%20) – S.P. (%40)

Financing

This research was not supported by any public, commercial, or non-profit organization.

Conflict of Interest

The authors declare no conflict of interest.

Sustainable Development Goals (SDG)

Sustainable Development Goals: 3 Healthy and quality life

REFERENCES

[1] C. Mattiuzzi, G. Lippi, Current cancer epidemiology, *Journal of Epidemiology and Global Health*. 9(4) (2019), 217–222. doi:10.2991/jegh.k.191008.001

[2] Z. Bıkmaz, S. Ünsar, Quality of life and social support levels in Leukemia patients, *Necmettin Erbakan Üniversitesi Genel Sağlık Bilimleri Dergisi*. 3(3) (2021), 200–214. doi: 10.51123/jgehes.2021.30

[3] F. Bray, M. Laversanne, H. Sung, J. Ferlay, R.L. Siegel, I. Soerjomataram, A. Jemal, Global cancer statistics 2022: GLOBOCAN estimates of incidence and mortality worldwide for 36 cancers in 185 countries, *CA a Cancer Journal for Clinicians*. 74 (2024), 229–263. doi:10.3322/caac.21834

[4] M. Davoodabadi-Farahani, Y. Mansoori, S. Ilbeigi, M. Barahman, M. Mazloomrezaei, P. Khani, S.M. Tabei, S. A. Dastgheib, H. Neamatzadeh, Expression levels of LINC01296 and LINC00152 in breast cancer tissue: Association with the use of oral contraceptives, *Eurasian Journal of Medicine and Oncology*. 6(1) (2022), 83–88. doi:10.14744/ejmo.2022.33174.

[5] A. Uslu, F. Hisar, Metastatik meme kanseri olan hastanın gordon'un fonksiyonel sağlık örüntüleri modeli'ne göre hemşirelik bakımı: Olgu sunumu, *Necmettin Erbakan Üniversitesi Genel Sağlık Bilimleri Dergisi*. 2(1) (2020), 59–69.

[6] G. N. Sharma, R. Dave, J. Sanadya, P. Sharma, K. K. Sharma, Various types and management of breast cancer: an overview, *Journal of Advanced Pharmaceutical Technology & Research*. 1 (2) (2010), 109–126.

[7] Y.S. Sun, Z. Zhao, Z. N. Yang, F. Xu, H. J. Lu, Z.Y. Zhu, W. Shi, J. Jiang, P.P. Yao, H. P. Zhu, Risk factors and preventions of breast cancer, *International Journal of Biological Sciences*. 13(11) (2017), 1387–1397. doi:10.7150/ijbs.21635

[8] K.P. Trayes, S.E.H. Cokenakes, Breast cancer treatment, *American Family Physician*. 104(2) (2021), 171–178.

[9] Z. Momenimovahed, H. Salehiniya, Epidemiological characteristics of and risk factors for breast cancer in the world, *Breast Cancer: Targets and Therapy*. 11 (2019), 151–164. doi:10.2147/BCTT.S176070

[10] T.T. Kunstič, N. Debeljak, K.F. Tacer, Heterogeneity in hormone-dependent breast cancer and therapy: Steroid hormones, HER2, melanoma antigens, and cannabinoid receptors, *Advances in Cancer Biology – Metastasis*. 7 (2023). doi:10.1016/j.adcanc.2022.100086

[11] E. Orrantia-Borunda, P. Anchondo-Nuñez, L.E. Acuña-Aguilar, F.O. Gómez-Valles, C.A. Ramírez-Valdespino, Subtypes of Breast Cancer, In: H. N. Mayrovitz (Ed.), Breast Cancer, Exon Publications, 2022: pp. 31-42. doi:10.36255/exon-publications-breast-cancer-subtypes

[12] F. Huemer, R. Bartsch, M. Gnant, The PI3K/AKT/MTOR signaling pathway: The role of pı3k and akt ınhibitors in breast cancer, *Current Breast Cancer Reports*. 6 (2014), 59–70. doi:10.1007/s12609-014-0139-y

[13] E. Bozgeyik, Kanserin ayırt edici özelliklerinde kodlanmayan RNA'ların rolü: Güncel bir bakış, *Selcuk Medical Journal*. 36(4) (2020), 381–396. doi:10.30733/std.2020.01268

[14] D.A. Altomare, J.R. Testa, Perturbations of the AKT signaling pathway in human cancer, *Oncogene*. 24(50) (2005), 7455–7464. doi:10.1038/sj.onc.1209085

[15] V. Marrocco, J. Bogomolovas, E. Ehler, C.G. dos Remedios, J. Yu, C. Gao, S. Lange, PKC and PKN in heart disease, *Journal of Molecular and Cellular Cardiology*. 128 (2019), 212–226. doi:10.1016/j.yjmcc.2019.01.029

[16] B.D. Manning, L.C. Cantley, AKT/PKB signaling: Navigating downstream, *Cell*. 129(7) (2007), 1261–1274. doi:10.1016/j.cell.2007.06.009

[17] G. Song, G. Ouyang, S. Bao, The activation of Akt/PKB signaling pathway and cell survival,

Journal of Cellular and Molecular Medicine. 9(1) (2005), 59–71. doi:10.1111/j.1582-4934.2005.tb00337.x

[18] J. Cicenas, The potential role of Akt phosphorylation in human cancers, *The International Journal of Biological Markers*. 23(1) (2008), 1–9. doi:10.1177/172460080802300101

[19] S.V. Madhunapantula, P.J. Mosca, G.P. Robertson, The Akt signaling pathway, *Cancer Biology & Therapy*. 12(12) (2011), 1032–1049. doi:10.4161/cbt.12.12.18442

[20] M. McKenna, N. Balasuriya, S. Zhong, S. S-C. Li, P. O'Donoghue, Phospho-Form specific substrates of protein kinase B (AKT1), *Frontiers in Bioengineering and Biotechnology*. 8 (2021). doi:10.3389/fbioe.2020.619252

[21] Y. He, M.M. Sun, G.G. Zhang, J. Yang, K.S. Chen, W.W. Xu, B. Li, Targeting PI3K/Akt signal transduction for cancer therapy, *Signal Transduction and Targeted Therapy*. 6 (2021). doi:10.1038/s41392-021-00828-5

[22] G. Risso, M. Blaustein, B. Pozzi, P. Mammi, A. Srebrow, Akt/PKB: one kinase, many modifications, *Biochemical Journal*. 468(2) (2015), 203–214. doi:10.1042/BJ20150041

[23] M. Yu, T. Liu, Y. Chen, Y. Li, W. Li, Combination therapy with protein kinase inhibitor H89 and Tetrandrine elicits enhanced synergistic antitumor efficacy, *Journal of Experimental & Clinical Cancer Research*. 37 (2018). doi:10.1186/s13046-018-0779-2

[24] K. Andreidesz, B. Koszegi, D. Kovacs, V.B. Vantus, F. Gallyas, K. Kovacs, Effect of oxaliplatin, olaparib and LY294002 in combination on Triple-Negative breast cancer cells, *International Journal of Molecular Sciences*. 22 (2021), 2056. doi:10.3390/ijms22042056

[25] S. Pehlivanoğlu, Ç. Aydın Acar, PAK4 promotes invasive potential of MCF-7 cells in PKC-dependent manner through downregulation of E-Cadherin, *Türk Hijyen ve Deneysel Biyoloji Dergisi*. 77(1) (2020), 107–116. doi:10.5505/TurkHijyen.2020.33340

[26] M.L. Ackland, D.F. Newgreen, M. Fridman, M.C. Waltham, A. Arvanitis, J. Minichiello, J.T. Price, E.W. Thompson, Epidermal growth Factor-Induced Epithelio-Mesenchymal transition in human breast carcinoma cells, *Laboratory Investigation*. 83 (2003), 435–448. doi:10.1097/01.lab.0000059927.97515.fd

[27] B.D. Manning, A. Toker, AKT/PKB signaling: Navigating the network, *Cell*. 169 (2017), 381–405. doi:10.1016/j.cell.2017.04.001

[28] P.-J. Tsai, Y.-H. Lai, R.K. Manne, Y.-S. Tsai, D. Sarbassov, H.-K. Lin, Akt: a key transducer in cancer, *Journal of Biomedical Science*. 29 (2022). doi:10.1186/s12929-022-00860-9

[29] S. Kane, H. Sano, S.C.H. Liu, J.M. Asara, W.S. Lane, C.C. Garner, G.E. Lienhard, A method to identify serine kinase substrates, *Journal of Biological Chemistry*. 277 (2002), 22115–22118.

[30] H. Sano, S. Kane, E. Sano, C.P. MîInea, J.M. Asara, W.S. Lane, C.W. Garner, G.E. Lienhard, Insulin-stimulated phosphorylation of a RAB GTPASe-activating protein regulates GLUT4 translocation, *Journal of Biological Chemistry*. 278 (2003), 14599–14602.

[31] S. Gridley, W.S. Lane, C.W. Garner, G.E. Lienhard, Novel insulin-elicited phosphoproteins in adipocytes, *Cellular Signalling*. 17 (2004), 59–66. doi:10.1016/j.cellsig.2004.05.013

[32] D. Zhu, X. Jiang, X. Wu, F. Tian, K. Mearow, R.H. Lipsky, A.M. Marini, Inhibition of protein kinase C promotes neuronal survival in low potassium through an Akt-dependent pathway, *Neurotoxicity Research*. 6 (2004), 281–289. doi:10.1007/bf03033438

[33] H.C. Wen, W.C. Huang, A. Ali, J.R. Woodgett, W.W. Lin, Negative regulation of phosphatidylinositol 3-kinase and Akt signalling pathway by PKC, *Cellular Signalling*. 15 (2003), 37–45. doi:10.1016/s0898-6568(02)00047-5

[34] J.J. Park, S.A. Hamad, A. Stewart, M.S. Carlino, S.Y. Lim, H. Rizos, PKC-independent PI3K signalling diminishes PKC inhibitor sensitivity in uveal melanoma, *Oncogenesis*. 13 (2024). doi:10.1038/s41389-024-00511-8

FEN ve MÜHENDİSLİK BİLİMLERİ DERGİSİ

Vol: 7 No: 1 Year: 2025 | Araştırma Makalesi/Research Article | e-ISSN: 2667-7989

https://doi.org/10.47112/neufmbd.2025.75

Gümüş Nanoparçacıklarına Çinko Katkılanmasının Toksik Organik Boyaların Bozunmasının Artırılmasına Etkilerinin İncelenmesi

Merve AKBAYRAK[1,3] Ümran ATA[2,3] Tuğba Nur ASLAN[2,3*]

[1] Necmettin Erbakan University, Faculty of Science, Department of Biotechnology, Konya, Türkiye
[2] Necmettin Erbakan University, Faculty of Science, Department of Molecular Biology and Genetics, Konya, Türkiye
[3] Necmettin Erbakan University, Science and Technology Research and Application Center (BITAM), Konya, Türkiye

Makale Bilgisi

Geliş Tarihi: 08.05.2024
Kabul Tarihi: 02.10.2024
Yayın Tarihi: 30.04.2025

Anahtar Kelimeler:
Çinko,
Gümüş,
Metil Turuncusu,
Metilen Mavisi,
Nanoparçacık.

ÖZET

Bu çalışmada, gümüş nanoparçacıkların katalitik verimliliğini artırmak amacıyla, Çinko katkılı Gümüş Nanoparçacıklar (Zn katkılı Ag NP'ler) sentezlenmiştir. Polygonum cognatum özütü ile çinko katkılama oranı sistematik olarak değiştirilerek (çıplak Ag NP, %1,6 Zn katkılı Ag NP ve %9,0 Zn katkılı Ag NP) kontrollü bir yeşil sentez yapılmıştır. Endüktif Eşleşmiş Plazma Optik Emisyon Spektroskopisi (ICP-OES), Taramalı Geçirimli Elektron Mikroskopisi (STEM), Enerji Dağılımlı X-Işını Spektroskopisi (EDS), X-ışını Floresansı (XRF), X-ışını Kırınımı (XRD) ve Fourier Dönüşümlü Kızılötesi Spektroskopisi (FTIR) analizleri, NP'lerin oluşumunu, elemental içeriğini, kristal yapısını ve Zn'nin Ag NP matrisine etkili bir şekilde dahil edildiğini doğrulamıştır. Yeşil sentezlenmiş Zn katkılı Ag NP'lerin, indirgeyici ajan olarak sodyum borohidrür (NaBH4) çözeltisi kullanılarak metil turuncusunun (MO) ve metilen mavisinin (MB) bozunmasındaki katalitik aktiviteleri araştırılmıştır. Sonuçlara göre, Zn katkılı Ag NP'ler çıplak Ag NP'lere kıyasla üstün katalitik performans sergilemiştir. Sonuçlar, %9,0 Zn katkılı Ag NP'nin MO'yu 15 dakika içinde 0,2199 dk^{-1} hız sabiti (kapp) ve 1,65 x 10-3 $mol.g^{-1}$ dk^{-1} devir frekansı (TOF) ile %96,56 oranında parçaladığını göstermektedir. MB degradasyonunda parçalama yüzdesi, 0,4445 dk^{-1} kapp ve 2,54 x 10^{-3} mol.g-1dk^{-1} TOF ile 10 dakikada %98,38'e, ulaşmıştır. Her iki boya için de Zn katkılama miktarının %1,6'dan %9,0'a çıkarılması reaksiyon sürelerini büyük ölçüde kısaltmış ve bozunma verimliliğini artırmıştır. 9.0 % Zn katkılı Ag NP'lerin toksik organik boyaların hızlı ve verimli bir şekilde bozunması için oldukça etkili katalizörler olduğu bulunmuştur. Bu çalışmanın bulguları, çevresel arıtma ve diğer uygulamalar için daha etkili ve özelleştirilebilir katalitik malzemelerin geliştirilmesini sağlayacak olan çinko katkılama yoluyla gümüş nanopartiküllerin etkinliğinin ayarlanabilirliği hakkında değerli bilgiler sağlamaktadır.

Influence of Zinc Doping Ratio on Silver Nanoparticles Synthesized via Green Method for Enhanced Catalytic Degradation of Toxic Organic Dyes

Article Info

Received: 08.05.2024
Accepted: 02.10.2024
Published: 30.04.2025

Keywords:
Metyl Orange,
Metylene Blue,
Nanoparticles,
Silver,
Zinc.

ABSTRACT

Zinc doped Silver Nanoparticles (Zn doped Ag NPs) were synthesized in this study to improve catalytic efficiency of Ag NPs. A controlled green synthesis was achieved with Polygonum cognatum extract by systematically varying zinc doping ratio (bare Ag NP, 1.6% Zn-doped Ag NP, and 9.0% Zn-doped Ag NP). Inductively Coupled Plasma Optical Emission Spectroscopy (ICP-OES), Scanning Transmission Electron Microscopy (STEM), Energy Dispersive X-ray Spectroscopy (EDS), X-ray Fluorescence (XRF), X-ray Diffraction (XRD), and Fourier Transform Infrared Spectroscopy (FTIR) analyses verified the NP formation, its elemental content, crystal structure and successful incorporation of Zn into the Ag NP matrix. The catalytic activity of green synthesized Zn doped Ag NPs was investigated in the degradation of methyl orange (MO) and methylene blue (MB) using sodium borohydride (NaBH4) as a reducing agent. According to results, Zn doped Ag NPs exhibited superior catalytic performance compared to bare Ag NPs. The results indicate that the 9.0% Zn-doped Ag NP degraded MO 96.56% in 15 minutes at a rate constant (kapp) of 0.2199 min^{-1} and turnover frequency (TOF) of 1.65 x 10^{-3} $mol.g^{-1}$ min^{-1}. In MB degradation, it reached 98.38% in 10 minutes with a kapp of 0.4445 min−1 and a TOF of 2.54 x 10-3 mol.g-1 min-1. For both dyes, increasing the doping amount of Zn from 1.6% to 9.0% greatly shortened reaction times and improved degradation efficiency. 9.0% Zn doped Ag NPs were found highly effective catalysts for the rapid and efficient degradation of toxic organic dyes. The findings of this study provide valuable insights into the tunability of silver nanoparticles' activity through zinc doping, which will enable the development of more effective and customizable catalytic materials for environmental treatment and other applications.

To cite this article:
Akbayrak, M., Ünüvar, Ü. & Aslan, T.N. (2025). Influence of zinc doping ratio on silver nanoparticles synthesized via green method for enhanced catalytic degradation of toxic organic dyes. *Necmettin Erbakan University Journal of Science and Engineering, 7*(1), 56-76. https://doi.org/10.47112/neufmbd.2025.75

***Corresponding Author:** Tuğba Nur Aslan, *taslan@erbakan.edu.tr*

INTRODUCTION

Environmental sustainability and resource management are among the most significant issues in today's world. Environmental treatment plays a vital role in protecting and improving natural resources as a comprehensive process. Environmentally friendly treatment efforts against some environmental pollutions may contribute to the sustainability of water and other resources such as air and soil [1]. Organic compounds such as methylene blue (MB) and methyl orange (MO) dyes are widely used indicators in industrial applications, however their environmental impact is also significant [2]. MO is used primarily in the colorant and dye industry and can cause environmental pollution by entering water systems through wastewater. MB is another indicator compound used in the textile, paper, and pharmaceutical industries and has an environmental impact by contaminating water systems [3]. Both compounds can cause toxic effects in aquatic ecosystems and can be harmful to various living organisms, especially in case of prolonged exposure to these substances [4]. Therefore, it is important to develop environmental management strategies for these organic indicator compounds considering their impact on the environment [5]. Conventional water treatment methods often fall short in effectively removing a wide range of pollutants, leading to a growing interest in advanced catalytic processes. Catalytic degradation of pollutants with the use of nanoparticles as catalysts can be considered as a sustainable and promising approach due to their high surface area and unique chemical properties for the removal of harmful substances [6-8].

Silver nanoparticles (Ag NPs) with unique properties, may have excellent catalytic performances, thus they have attracted attention for studies on improving catalytic processes [9]. The most important characteristics of Ag NPs are their high reactivity towards organic molecules thanks to their large surface area/volume ratio and their optical properties arising from metal surface plasmon resonances (SPR) [10]. Ag NPs efficiently absorb light and release their free electrons stimulatingly due to their SPR [11]. Therefore, the catalytic utility of Ag NPs holds great potential in environmental treatment and energy conversion [12]. However, it was revealed that the catalytic activities of NPs can be improved by metal doping due to a synergetic effect of two metals' intrinsic catalytic properties [13]. For better catalytic properties, doping Ag NPs with other metals, such as zinc (Zn), has been proposed [14]. Zn doping can modify the electronic properties and surface chemistry, thereby altering SPR properties of Ag NPs [15]. SPR causes concentrated electromagnetic fields on the surface, which increase the catalytic activity by creating a suitable environment for catalytic reactions [16]. The SPR of Zn doped Ag NPs influences the performance of Ag NPs in different reactions [17]. Moreover, Zn doping causes chemical alterations on the surface of nanoparticles [18]. The formation of the catalytic active sites on the surface of nanoparticles could be promoted by the introduction of Zn atom which can interfere with the reaction mechanisms and increase the rate of the reaction and optimize selectivity [19]. This synergistic effect between silver and zinc leads to improved performance in the catalytic degradation of pollutants, making Ag-Zn nanoparticles a superior choice for water treatment applications. Catalytic activity can be increased with optimal Zn doping ratios, while excessive doping can cause a decrease in the activity [20]. Activity loss with the excessive doping can be explained by three main factors. The first reason is that excessive Zn doping can distort SPR [21]. The second reason is that excessive amounts of Zn can cause the inappropriate location of the formation of critical chemical sites involved in catalytic reactions or cause agglomeration which decreases the chemically active sites [22, 23]. Finally, controlling electron and hole recombination may become challenging because of excessive Zn doping [24,25]. Consequently, to enhance the Ag NPs' catalytic performance, the doping ratio must be carefully adjusted [26].

Catalytic degradation using plants offers an ecological solution to environmental challenges. Green synthesis of nanoparticles using plant extracts has gained popularity as an environmentally friendly and sustainable method compared to conventional chemical and physical synthesis techniques

[27]. While chemical reduction methods are effective, they often contain dangerous chemicals and can produce toxic byproducts, which pose significant environmental and health risks [28]. Physical methods such as high-energy ball milling and laser ablation, on the other hand, are energy-intensive and require sophisticated equipment [29]. In contrast, green synthesis methods using biological materials are advantageous due to their simplicity, cost effectiveness and low environmental impact [30]. This biogenic approach not only reduces toxicity, but also utilizes the natural abundance and diversity of plant resources to produce nanoparticles with unique properties [31]. The effectiveness of plant extracts in NP synthesizes arise from extract's contents such as polyphenols, ascorbic acids, carboxylic acids, terpenoids, amides, flavones which are responsible for reducing metal ions to form nanoparticles and stabilizing the nanoparticle cores and preventing agglomeration [32, 33]. *Polygonum cognatum* extract is preferred in this study for its richness in phytochemicals, particularly polyphenols and flavonoids providing a controlled synthesis of nanoparticles [34].

Polygonum cognatum is a medicinal and aromatic perennial plant, known as 'Madımak' in Turkey [35]. All anatomical parts of the plant have been used for treatments of several diseases as antioxidant, antimicrobial and antidiabetic medicine thanks to its high phenolic compounds, vitamin, mineral and flavonoid contents [34-37]. *Polygonum cognatum* has gained attention in scientific research for its potential medicinal and culinary uses in green synthesis processes. The findings of the antimicrobial activity of the plant extract have displayed a higher effectivity against a broad spectrum of bacteria and fungi [36, 38]. Moreover, the antiproliferative properties of *Polygonum cognatum* against some cancer types were also reported in literature [35, 37, 39].

Green synthesized nanoparticles have improved biocompatibility and reduced toxicity, making them suitable for various environmental and biomedical applications [40]. Some kinds of green synthesized nanoparticles by using different kinds of extracts are extensively used for the degradation of lethal and pestilential dyes [41, 42]. Among them, silver, zinc oxide, gold, iron oxide, palladium NPs are concluded to be most promising and efficient decolorization catalysist against a wide range of dyes including MO, MB reported in literature [41- 46]. However, nanoparticles synthesized using *Polygonum cognatum* extract has not been used in MO and MB catalytic degradation reaction studies before.

In this study, we present the green synthesis of non-doped and Zn-doped Ag NPs using *Polygonum cognatum* extract and investigate their catalytic performance in the degradation of water pollutants, MO and MB. The methodology and synthesis method adopted for different types of NPs using *Polygonum cognatum* extract has been limitedly studied in the literature [47-53]. To the best of our knowledge, Zn doped Ag NPs were synthesized and stabilized using *Polygonum cognatum* extract for the first time. The originality of this study lies both in the novel combination of silver and zinc in a green synthesis method with *Polygonum cognatum* extract and the fact that it has not been previously experienced in environmental treatment field presenting the research a unique perspective. The successfully synthesized nanoparticles were characterized using advanced analytical techniques, including STEM, EDS, XRF, XRD, FTIR, and ICP-MS. The catalytic activities of the obtained NPs as catalysts were evaluated using MO and MB degradation reactions. The reaction progressions were monitored using UV-Vis spectroscopy to determine turnover frequency (TOF) values and apparent rate constants (kapp). The results revealed that 9.0% Zn-doped Ag NPs exhibited significantly higher activity compared to bare Ag and 1.6% Zn-doped Ag NPs. 9.0% Zn-doped Ag NPs degraded 96.56% of MO in 15 minutes with a k_{app} of 0.2199 min^{-1} and a TOF of 1.65 x 10^{-3} $mol.g^{-1}$ min^{-1} . Additionally, 9.0% Zn-doped Ag NPs degrade 98.38% of MB in 10 minutes with a k_{app} of 0.4445 min^{-1} and a TOF of 2.54 x 10^{-3} $mol.g^{-1}$ min^{-1}. According to the results, Zn doped Ag NPs offer enhanced catalytic effects for the degradation of pollutants, emerging as promising agents for this purpose.

MATERIALS AND METHODS

Materials

The chemicals and materials used in this study were of high purity and commercially obtained. Zinc acetate dihydrate ($Zn(Ac)_2$), Silver Nitrate ($AgNO_3$), Methyl Orange (MO), Methylene Blue (MB) and sodium borohydride ($NaBH_4$) were purchased from Sigma-Aldrich. These chemicals and solvents were used directly without any further purification.

Preparation of *Polygonum cognatum* Extract

Polygonum cognatum plant was collected from Sivas, Turkey and dried at ambient conditions. The dried plant was grounded into fine pieces and weighed as 10 mg. The powdered plant was dispersed in 100 mL distilled water and heated at 80 ^oC for 1 hour. The resulting extract was filtered using Whatman no: 1 filter paper to separate it from the pulp. Then, it was centrifuged at 9000 rpm and the supernatant-containing extract was kept at +4 ^oC to be used in nanoparticle synthesis and characterization processes.

Synthesizes of Ag and Zn doped Ag Nanoparticles

In this study, $AgNO_3$ and $Zn(Ac)_2$ were used as metal precursors in the synthesis of silver (Ag) and zinc-doped silver (Zn doped Ag) nanoparticles. Silver nanoparticles were first synthesized by using *Polygonum cognatum* extract according to the traditional green synthesis method in literature with some modifications such as pH, metal concentration and metal:extract volume ratio [54, 55]. These parameters were optimized by observing the agglomeration and stability of the NP suspension [56]. In a typical synthesis of Ag nanoparticles, 1 mL of extract was added to 9 mL of 6 mM $AgNO_3$ aqueous solution. The pH of the mixture was adjusted to 9 and color change was observed indicating the formation of Ag nanoparticles. The reaction mixture was left to stir for 2 hours for the complete formation of nanoparticles.

In the Zn doping method, core Ag nanoparticles were first synthesized, and these Ag nanoparticles acted as seeds for the nucleation of zinc nanoparticles on their surface [57]. It is generally proposed that Zn ions are reduced by components of extract, therefore zinc atoms are supposed to initially obtained in their metallic form on the surface of the Ag nanoparticles [58]. However, it would readily oxidize to ZnO under the reaction conditions. This is due to the dissolved oxygen in the reaction environment and the basic pH adjustments, which promote oxidation [59-61]. Likewise, for the synthesis of Ag nanoparticles to be acted as seeds for Zn; 1 mL of extract was added to 9 mL of 20 mM $AgNO_3$ aqueous solution [57]. The pH of the mixture was adjusted to 9 and left to stir for 2 hours. Then, 0.5 mL of 10 mM $Zn(Ac)_2$ aqueous solution was added to the Ag NP suspension. It is well known for the zinc nanoparticle formation that the average size decreases with increased pH [62, 63]. Therefore, pH of the mixture was brought to 10 and the mixture was left to stir for another hour. At the end of the reaction, the pH of the solutions was fixed at 7. The second synthesis for Zn doping was carried out again under the same conditions by increasing the Zn amount to 3 mL. All the nanoparticle suspensions were centrifuged at 9000 rpm to separate the agglomerated parts, and the dispersed nanoparticles remaining in the supernatant were stored at 4 °C for characterization and evaluation of their catalytic activities.

Characterization Studies

Nanoparticle size and morphology were displayed through Scanning Transmission Electron Microscopy (STEM, ZEISS Gemini SEM 500) using 5 µL of NP suspension by dropping and drying it on carbon-coated Cu grids. Elemental content of NP suspensions was identified by Energy Dispersive X-ray Spectroscopy (EDS) analysis (SEM, ZEISS Gemini SEM 500) by coating 10 µL of sample with a 4.30 nm thick layer of iridium on a carbon band. The elemental analysis was also achieved through

energy dispersive X-ray fluorescence (EDXRF, Rigaku NEX CG) spectrometry. The measurement conditions were 50 kV, 2.00 mA, helium atmosphere, and 300 s of measurement time with a 50 kV-50W end-window palladium-anode X-ray tube. The crystalline structure of NPs was investigated using X-ray Diffraction measurement (XRD, PANalytical EMPYREAN) with Cu Ka radiation for 2θ values between 10°-90°. The structural analysis of the extract and NPs synthesized with the same extract were carried out using Fourier Transform Infrared Spectroscopy (FTIR, Thermo Scientific-Nicolet IS20) to observe the functional groups of the samples. The quantitative analysis of Ag and Zn elements existing in NP suspension was achieved using inductively coupled plasma mass spectrometry (ICPMS, Agilent Technologies 7900) by dissolving samples in conc. HCI prior to the analysis.

Catalytic Studies

The catalytic activity of the biosynthesized Zn doped Ag NP was assessed against MO and MB using $NaBH_4$ as reducing agent. The catalytic tests were carried out by mixing aqueous solution of $NaBH_4$ (100 µL, 0.1 M) and MO (2 mL, 5 mg/mL) or MB (2 mL, 5 mg/mL) with varying amounts of NP suspensions (400, 600, 800, 900 µL) in 3 mL cuvette against constant Ag concentration (1400 ppm) for all type of NPs (bare Ag NP, 1.6% Zn doped Ag NP, 9.0% Zn doped Ag NP). The reaction progressions were followed with UV-Vis spectroscopy. The absorption spectra were recorded at RT.

The rate constants of the reduction reactions were determined by measuring the decrease in the absorbance of the MO and MB over time. In the degradation studies of MO and MB, $NaBH_4$ was employed at significantly high concentrations to achieve pseudo-first-order reaction conditions. Under these circumstances, the concentration of $NaBH_4$ remains substantially constant throughout the reaction, allowing the reaction kinetics to be simplified and treated as first-order with respect to the dye (MO or MB) alone. The apparent rate constant (kapp) was determined by plotting $\ln(C/C_0)$ versus time, where C is the concentration of the dye at a given time and C_0 is the initial concentration. The slope of this linear plot corresponds to the apparent rate constant, kapp, under the specified experimental conditions [64].

The turnover frequency (TOF) is another important parameter for determining the activities of catalysts and defined as moles of degraded dye per gram of catalyst per minute as given in equation (1), was further used for the catalyst activity evaluation [65, 66].

$$TOF = \frac{mole\ of\ dye}{g\ catalyst} x \frac{1}{min} \quad (1)$$

RESULTS AND DISCUSSION

Nanoparticle Characterization

Polygonum cognatum extract was used as a reductant and stabilizer for the green synthesis of non-doped Ag NPs and Zn-doped Ag NPs. After the optimized synthesis of NPs, the reaction mixture immediately turned into a dark brown color, indicating the formation of NPs. The NPs were then characterized using the following microscopic and spectroscopic techniques.

The Ag concentration in NP suspensions were determined from ICP-MS measurements. The catalyst and Zn amounts were estimated from Ag concentrations in NP suspensions and the results are given in Table 1 and 2. The catalytic reduction of MO and MB was monitored spectrophotometrically using a UV-Vis Spectrophotometer (Agilent Technologies Cary 60) at intervals of 1 or 5 minutes at room temperature.

STEM images and EDS analysis of non-doped and Zn-doped Ag NPs were investigated. Figure 1a shows the STEM image of non-doped Ag NPs and in Figure 1b, the EDS spectrum of the same sample is presented, and the presence of Ag elements is clearly detected. Figure 1c shows the STEM

image of NPs with 1.6 % Zn doping and in Figure 1d, the EDS spectrum of the same sample is presented, and the presence of Ag and Zn elements is clearly detected.

Table 1

Ag and Zn amounts (ppm) estimated from ICP-MS measurement in NP suspensions.

	Ag, ppm	Zn, ppm
Ag NP	1875.1	-
1.6 % (w/w) Zn doped Ag NP	1832.3	30.0
9.0 % (w/w) Zn doped Ag NP	1478.9	146.3

Table 2

Zn and catalyst amounts (mg) in 0.8 mL NP suspension with constant Ag concentration (1400 ppm Ag)

	Ag, ppm	Zn, ppm	Catalyst, mg
Ag NP	1.12	-	1.12
1.6 % (w/w) Zn doped Ag NP	1.12	0.017	1.137
9.0 % (w/w) Zn doped Ag NP	1.12	0.11	1.23

Similarly, the STEM image (Figure 1e) and EDS spectrum (Figure 1f) of Ag NPs with 9.0% Zn doping were also analyzed. The EDS spectra clearly reveal the presence of Ag and Zn and obvious increase in the Zn amount. According to the STEM images, both NPs synthesized through the green method are of spherical shapes. It was observed that with increasing Zn doping, the NPs had homogeneous size distribution with a ~15 nm particle size, low agglomeration, and enhanced stability in aqueous medium for 9.0% Zn doping.

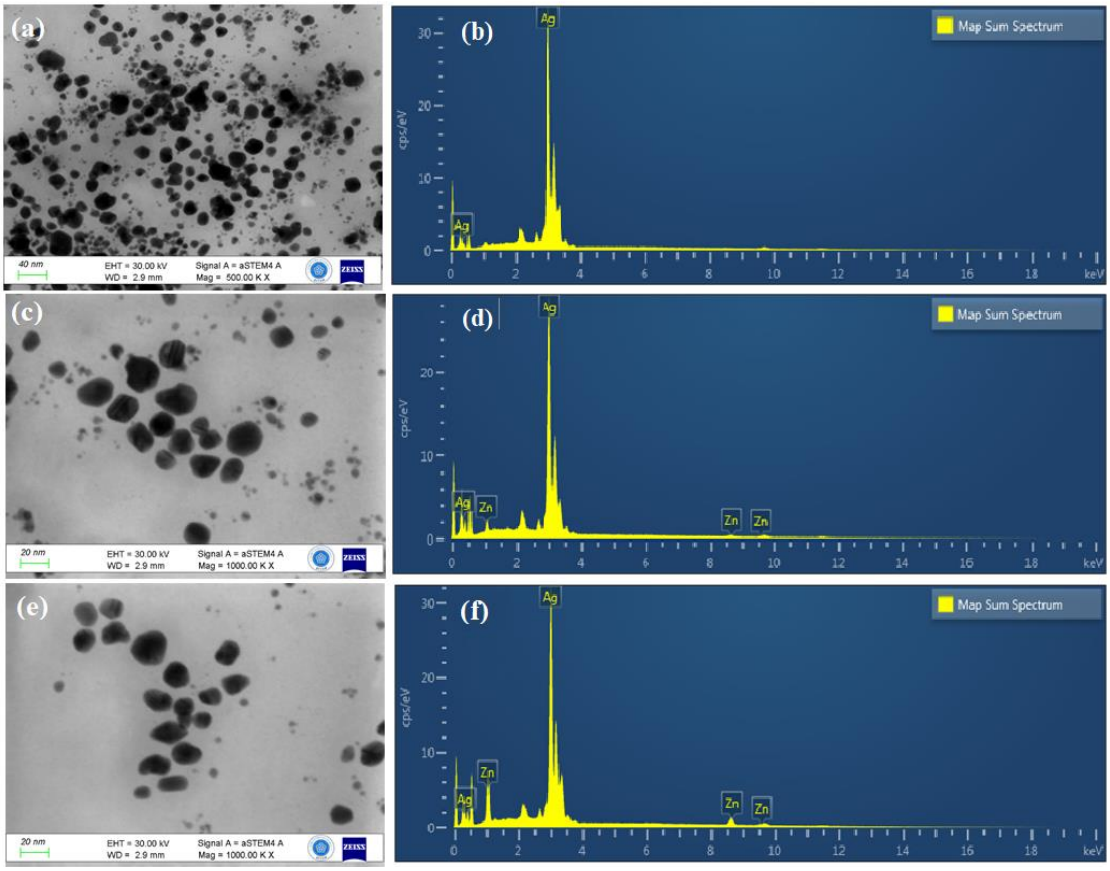

Figure 1

STEM image and its corresponding EDS spectra of Ag NPs (a-b), 1.6 % Zn Doped Ag NPs (c-d), 9.0 % Zn Doped Ag NPs (e-f)

In X-ray fluorescence (XRF) analysis, characteristic prominent peaks for each NP spectrum were observed at energy levels consistent with the elemental composition of the NPs, as seen in Figure 2. Additional peaks corresponding to Zn emerged in the spectrum, indicating the successful incorporation of Zn into the NP structure. Moreover, a proportional increase in the Zn-Kα peak intensity was observed with the increased Zn doping ratio from 1.6% to 9.0% since Zn incorporation into the lattice sites of Ag NPs alters the crystal structure and electronic configuration of the NPs, leading to a more pronounced emission of characteristic X-rays.

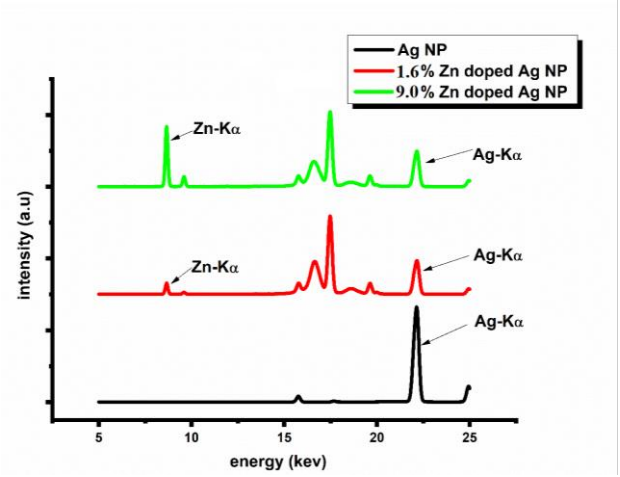

Figure 2
XRF spectra of Ag NPs, 1.6 % Zn doped Ag NPs and 9.0 % Zn doped Ag NPs

The X-ray diffraction (XRD) spectra presented in the Figure 3 depict the crystalline structure of Ag NPs, as well as Ag NPs doped with 9.0% Zn. For the Ag nanoparticles, the peaks are observed at approximately 38°, 44°, 64°, 77°, and 81°, corresponding to the (111), (200), (220), (311) and (222) crystallographic planes, respectively [52, 67-69]. The pure Ag NPs exhibit a crystal structure consistent with face-centered cubic (fcc) silver (JCPDS 87-0720) [69]. The Zn doped Ag NP spectrum presents both Zn and Ag peaks, despite small deviations for Ag peaks indicating that Zn doping occurred only at surface level and did not affect the crystalline structure of both species [70]. The peaks belonging ZnO are located at around 32°, 34°, 48°, 55°, 62°, 72° correspond to the (100), (002), (102), (110), (112) and (201) planes, respectively [71-73]. Sample reveals that the Zn-doped Ag NPs contain a phase corresponding to wurtzite ZnO (JCPDS 36–1451), indicating the successful doping of Ag NPs with Zn [74]. Unidentified peaks below 2θ values of 30° are likely attributed to the extract [75].

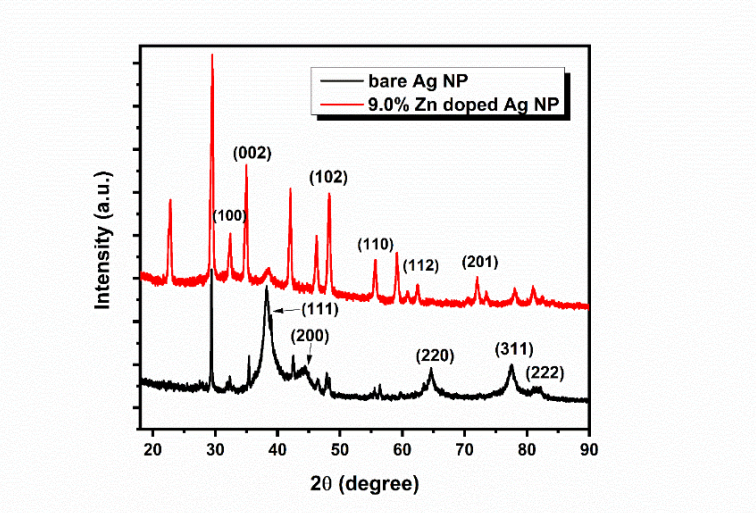

Figure 3
XRD spectra of Ag nanoparticles and 9.0% Zn doped Ag nanoparticles

FTIR analysis reveals similar spectral characteristics for the synthesized non-doped and Zn doped Ag NPs compared to the plant extract (Figure 4). In the FTIR spectrums, there are four peaks at similar positions with slight shifts in peak frequencies since the present functional groups of the extract are responsible for the reduction and capping of NPs proving the synthesis of NPs from the extract. The prominent peaks of extract are observed at 3253 cm^{-1}, 2921.08 cm^{-1}, 1598.53 cm^{-1}, 1293.99 cm^{-1}, indicating O-H stretching of phenolic groups [76], aliphatic C-H stretching vibrations [77], C=C stretching from aromatic rings [50], C-N vibrations [78], respectively. Ago generally absorbs very poorly in the infrared region and Ag-Ag metallic bond vibrations establish below 400 cm^{-1} [79]. Therefore, a distinct absorption band for Ag could not be seen in regions between (4000-400 cm^{-1}). Moreover, the amount of Zn in NP composition is as maximum %9 and the presence of the absorption bands of functional groups of the plant extract may mask some of the weak and unclear bands of metal nanoparticles in the FTIR spectrum [70]. Likewise, a distinct absorption band for Zn could not observed in the spectrum, too. However, an additional peak at 2363.40 cm^{-1} and 2335.88 cm^{-1} as distinct from that of the extract is expected from vibration of the C=O bond of the CO_2 molecule that is chemisorbed during drying of NP surfaces [80, 81]. Additionally, the peak at 808.10 cm^{-1} observed in both NPs' spectrum distinct from that of the extract arises from the adsorption of residual NO_3^- groups to the extract components [82, 83].

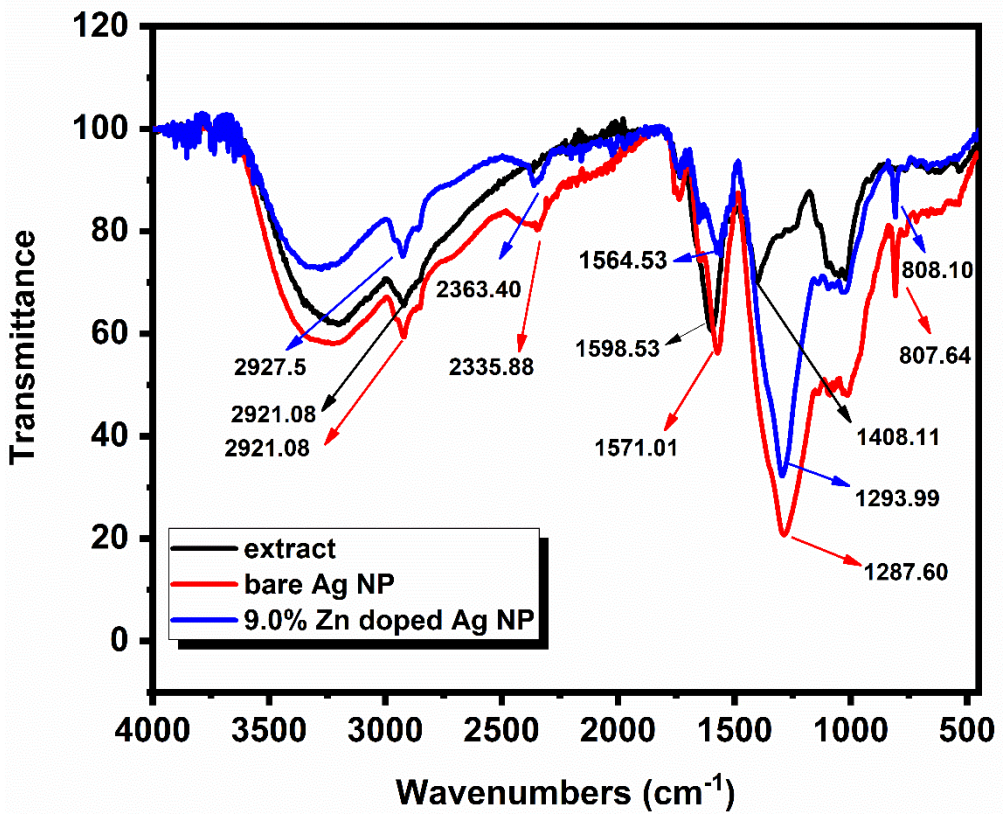

Figure 4
FTIR spectra of extract, Ag NPs, and 9.0% Zn doped Ag nanoparticles

Results of the Catalytic Studies

The degradation of MO and MB using Zn-doped Ag nanoparticles was carefully monitored by UV-Vis spectroscopy in the range 380-600 nm for 30 minutes. This method is a powerful tool to understand the evolution of the catalytic degradation process over time and to evaluate the efficiency of the nanomaterial. For monitoring the catalytic degradation of Methyl Orange by UV-Vis spectroscopy, the most prominent characteristic absorption peak which is around 464 nm is usually followed. When using UV-Vis spectroscopy to monitor the catalytic degradation of Methylene Blue, characteristic

absorption peaks at 664 nm are usually observed with time.

As can be seen from the UV-Vis absorption spectra in Figure 5a and Figure 6a, in the presence of bare Ag NPs, the reaction did not significantly progress, indicating that Ag NPs have a limited propensity to catalyze the degradation of MO and MB. In contrast, when Ag NPs were doped with Zn, the increase in activities was observed (Figure 5b, 5c and Figure 6b, 6c). Moreover, as the amount of Zn doping increased, the degradation of MO and MB increased while the degradation times decreased (Figure 5d and Figure 6d), indicating an acceleration of the reaction rate (Table 3).

The catalytic activity of bare Ag NPs can be considered very low because the percent degradation of MO and MB are 24.01 and 37.63, respectively at the end of the 30 min when the bare Ag NPs are used as the catalyst. On the other hand, when the 1.6 % Zn doped Ag NP was used as the catalyst, percent conversion was increased to 46.87 for MO degradation and the required time for the conversion decrease to 25 min (Figure 5b and Table 3). While the Zn doping amount was increased from 1.6 to 9.0 % methyl orange degradation also increased to 96.56% and the required time decreased to 15 min (Figure 5c).

As shown in Fig. 5c, nearly the complete degradation of MO could be observed in 15 min. Based on the linear relationship between ln(C/C0) and reaction time (Figure 7a), the apparent rate constant (kapp) was calculated as 0.2199 min-1 for the 9.0% Zn doped Ag NP catalyzed MO degradation. The rate of the reaction was increased nearly 10-fold with the increase of Zn doping. (Figure 7a and Table 3). The TOF value of the 9.0% Zn doped Ag NP was determined as 1.65 x 10-3 mol.g-1 min-1.

Similarly, the toxic MB dye can be degraded quickly in the presence of Zn doped Ag NPs as evidenced by the rapid disappearance of characteristic absorption peak of MB at 664 nm in 10 min (Fig. 6c), suggesting its high catalytic activity. When the spectra obtained for MB degradation were analyzed, it was found that the degradation of methylene blue increased from 78.36 % to 98.38 % when the doping amount was increased from 1.6% to 9.0% (Figure 6b and c). Further calculation based on the linear relationship between ln(C/C0) and reaction time yielded an apparent rate constant of 0.4445 min-1 for the reduction reaction of MB catalyzed by the 9.0 % Zn doped Ag NP (Figure 7b). The TOF value of the 9.0% Zn doped Ag NP was determined as 2.54x10-3 mol.g-1 min-1 and increased nearly 3 fold according to 1.6% Zn doped Ag NP (0.9x10-3 mol.g-1 min-1) suggesting the activity toward degradation of MB increase when Zn doping increased. When comparing both the apparent rate and TOF results, it can be said that 9.0% Zn-doped Ag NPs can be used as a more active catalyst for MB degradation compared to MO degradation.

With increasing Zn doping, the catalytic activity of the nanoparticles increased in the degradation reactions of both toxic dyes. (Table 3). The increased activity can be attributed to some factors. Firstly, Zn doping alters the surface properties of Ag NPs, leading to changes in their catalytic behavior. This modification can enhance the interaction between the catalyst and the reactants, thereby improving the catalytic activity [66]. Secondly, Zn doping can create additional active sites on the surface of Ag NPs, which are facilitate to catalytic reactions. These new active sites may facilitate the adsorption and activation of reactant molecules, promoting faster reaction rates [65]. Finally, the combination of Ag and Zn in doped nanoparticles can result in synergistic effects, where the presence of Zn enhances the catalytic properties of Ag. This synergistic interaction between Ag and Zn can lead to improved catalytic performance compared to pure Ag nanoparticles [84].

Table 3
Comparison of the rate constant and TOF for the catalytic reduction of MO and MB

Dye	Catalyst	Catalyst amount for 0,8 mL (mg)	% Degradation	Time (min)	Rate constant, k_{app} (min^{-1})	TOF x 10^{-3}, ($mol.g^{-1}$ min^{-1})
Methyl Orange	**Ag NP**	1.12	24.01	30	0.0106	0.91
	1.6%Zn doped Ag NP	1.137	46.87	25	0.0239	1.10
	9.0% Zn doped Ag NP	1.23	96.56	15	0.2199	1.65
Methylene Blue	**Ag NP**	1.12	37.63	35	0.0171	0.79
	1.6% Zn doped Ag NP	1.137	78.36	30	0.0678	0.9
	9.0% Zn doped Ag NP	1.23	98.38	10	0.4445	2.54

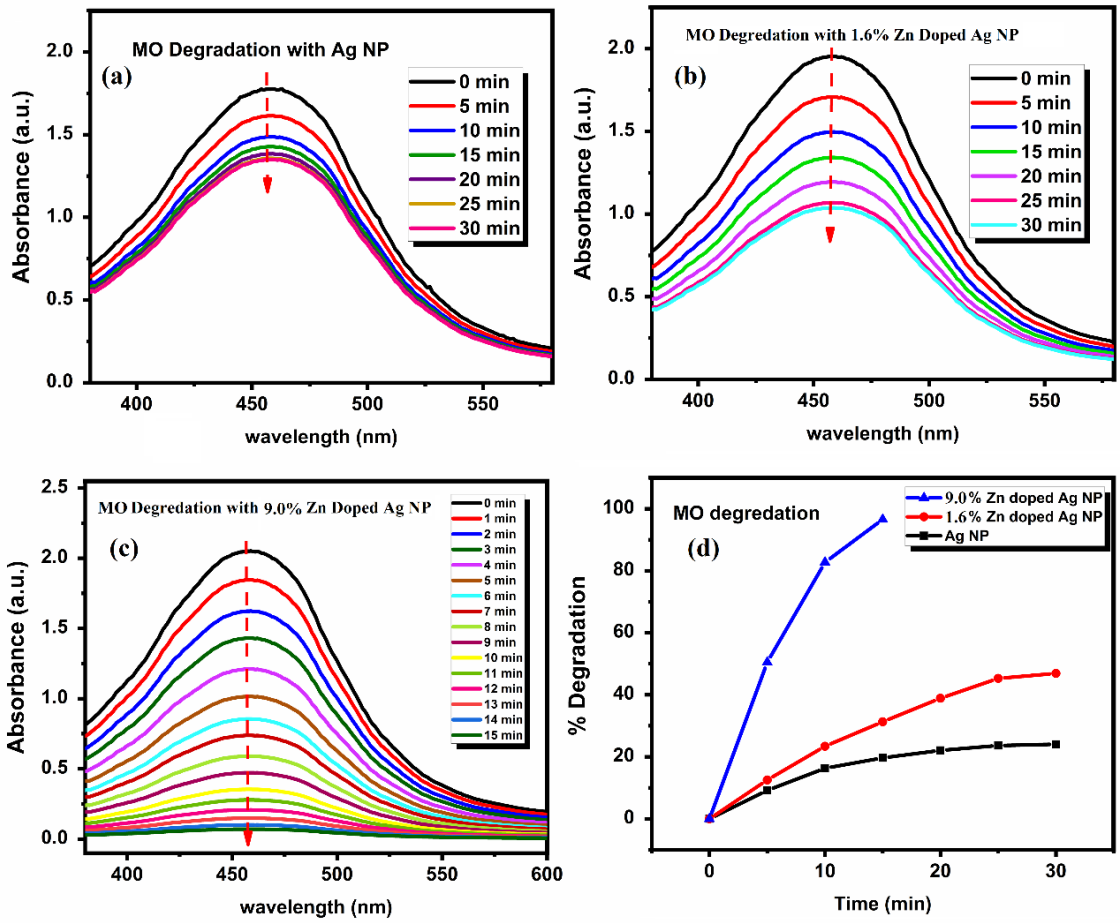

Figure 5
The UV-Vis absorption spectra of MO dye degradation using a) Ag NP, b) 1.6% Zn doped Ag NP, c) 9.0% Zn doped Ag NP and d) degradation percents of MO vs time for three catalysts

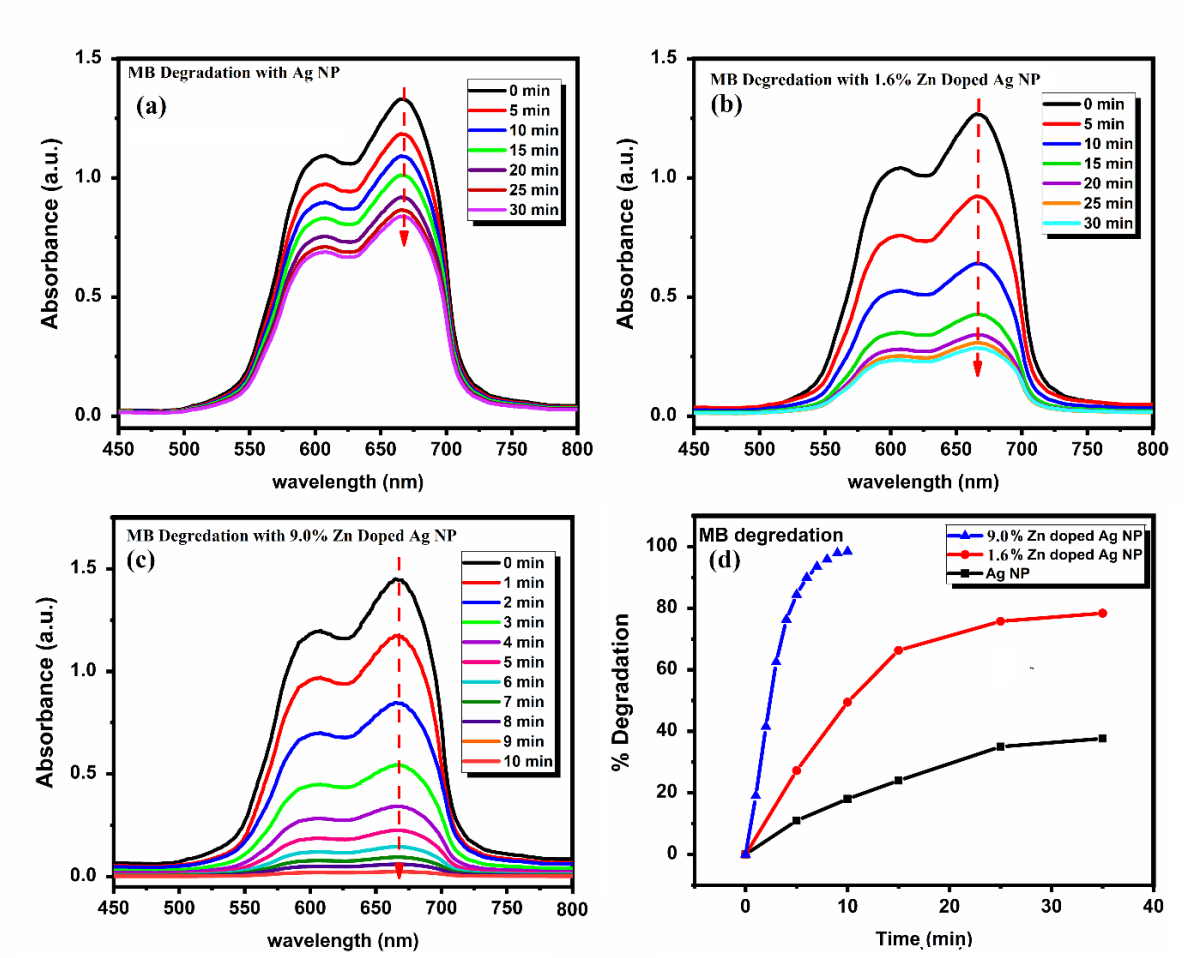

Figure 6

The UV-Vis absorption spectra of MB dye degradation using a) Ag NP, b) 1.6% Zn doped Ag NP, c) 9.0% Zn doped Ag NP and d) degradation percents of MB vs time for three catalysts

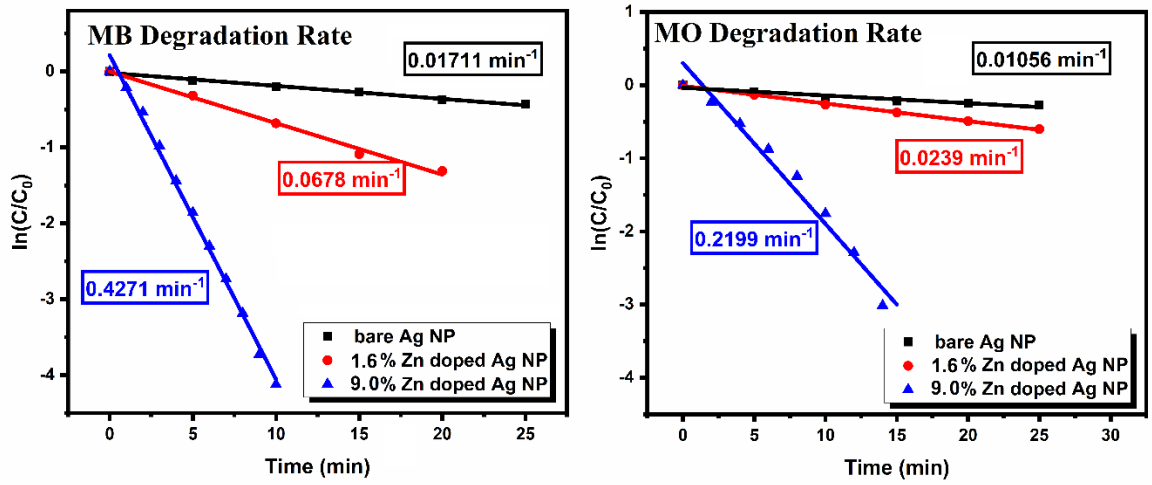

Figure 7

*Plot of ln (C_t/C_0) versus time (min) for the degradation of **a.** MO **b.** MB using Ag NP, 1.6% Zn doped Ag NP, and 9.0% Zn doped Ag NP.*

After determining the activity of 9.0% Zn doped Ag NP, loading density studies were conducted. The amounts of dyes added to the reaction medium and the used amount of $NaBH_4$ were kept constant, and the amounts of 9.0 % Zn doped Ag NP catalyst added to the reaction environment were changed.

0.4, 0.6, 0.8-, and 0.9-mL NP suspensions were separately added to the reaction environments, and percentage degradations were monitored. When 0.9 mL NP suspension was added to reaction instead of 0.8 mL than the percent degradation increases only from 96.56% to 97.02% for MO and from 98.38% to 98.76% for MB. (Table 4) As a result of the studies, it was found that adding 0.8 mL NP suspension yielded optimal results and increasing the added NP amount beyond 0.8 mL did not result in a significant change in the percent degradation of the two dyes. This could be attributed to the saturation of reactants on the catalyst's available surface, where increasing the amount of catalyst did not increase the percent degradation at the same reaction time [85].

Table 4
MO and MB degradation values with the change of 9.0% Zn doped Ag NP catalyst amount

Dye	NP suspension(mL)	% degradation	Time(min)
MO	0.4	87.21	30
	0.6	92.19	25
	0.8	**96.56**	**15**
	0.9	97.02	15
MB	0.4	89.49	30
	0.6	91.69	25
	0.8	**98.38**	**10**
	0.9	98.76	10

Catalytic degradations of MO and MB in the presence of constant catalyst and $NaBH_4$ amount were also evaluated to examine the impact of the dye concentration on the catalytic reaction process. The concentrations of the dyes were changed from 2.5 mg/mL to 7.5 mg/mL while maintaining the 9.0% Zn doped Ag NP catalyst loading (0.8 mL) and $NaBH_4$ concentration (0.1 M) The variation of the percent degradation of dyes at the same time interval was presented in Table 5. It is observed that with the rise of dye concentration the value of percent degradation increased up to a 5 mg/mL concentration after that it decreased with the rise of dye concentration to 7.5 mg/mL. MO degradation firstly increase from 96.09 to 96.56 with the increase of dye concentration from 2.5 to 5 mg/mL. However, when the concentration was increased to 7.5 mg/mL degradation decrease to 90.93%. Similarly, MB degradation first increase from 92.71 to 98.38 with the increase of dye concentration from 2.5 to 5 mg/mL. However, degradation decrease to 97.07% with the increase in the concentration. In the low concentrations of the dyes, the percent degradations were found as low value because most of the catalytic sites were occupied by the borohydride ions. With the increase in the concentrations of dyes, they began to dominate most of the catalytic surface, resulting in the increase in the percent degradation. However, at higher concentrations, a significant portion of the catalytic surface became occupied by the dye molecules due to their high binding capability. This hindered the reaction with BH_4^- ions, consequently reducing the percent degradation values [86].

Table 5
MO and MB degradation with 9.0% Zn doped Ag NP

	Dye amount (mg/mL)	% Degradation	Time(min)
MO	2.5	96.09	30
	5	96.56	15
	7.5	90.93	15
MB	2.5	92.71	30
	5	98.38	10
	7.5	97.07	10

Table 6
Some studies from literature for methylene blue and methyl orange dyes degradation by various biosynthesized Ag nanoparticles with the use of $NaBH_4$.

Nanomaterial	Biosynthesis source	Dye degraded	Time for degradation	Degradation %	Ref.
9.0% Zn doped Ag NP	***Polygonum cognatum***	**Methylene blue**	**10**	**98.38**	**This work**
Ag	*Lathyrus brachypterus*	Methylene blue	6	98	[87]
Ag	*Albizia procera*	Methylene blue	70	99.6	[88]
Ag	*Gmelina arborea*	Methylene blue	7	100	[89]
Ag	*C. paradisi (Paradise citrus)*	Methylene blue	4	93.29	[90]
Ag	*Blumea lacera*	Methylene blue	24	56	[91]
Ag/ZnO nanocomposite	*Valeriana officinalis*	Methylene blue	2	100	[92]
9.0% Zn doped Ag NP	***Polygonum cognatum***	**Methyl orange**	**15**	**96.56**	**This work**
Ag	*Heterotheca subaxillaris*	Methyl orange	11	100	[93]
Ag	*Cassia alata*	Methyl orange	120	98.6	[94]
Ag	*Clitoria ternatea*	Methyl orange	10	100	[95]
Ag	*Hibiscus tiliaceus*	Methyl orange	45	100	[96]
Ag	*S. costus*	Methyl orange	135	72.88	[97]
Ag/ZnO nanocomposite	*Valeriana officinalis*	Methyl orange	4	100	[92]

In recent studies on the degradation of methylene blue (MB) and methyl orange (MO) dyes using green synthesized Ag nanoparticles, a variety of biosynthesis sources and their effectiveness have been explored (Table 6). For instance, NP synthesized using Lathyrus brachypterus extract enabled 98% degradation of MB in just 6 minutes, while that of Albizia procera showed a 99.6% degradation of MB in 70 minutes. NP synthesized using Gmelina arborea demonstrated complete degradation (100%) of MB in 7 minutes. On the other hand, degradation of MO using Ag nanoparticles synthesized from sources like Heterotheca subaxillaris flower and Cassia alata resulted in 100% degradation in 11 and 120 minutes, respectively. When comparing these literature results to our findings using 9.0% Zn-doped Ag nanoparticles, it is evident that our method yields superior results. Our nanoparticles achieved 98.38% degradation of 5 mg/mL MB in just 10 minutes and 96.56% degradation of 5 mg/mL MO in 15 minutes. These results demonstrate that our Zn-doped Ag nanoparticles not only achieve high degradation percentages but also do so in significantly shorter times compared to many biosynthesized Ag nanoparticles reported in the literature. This highlights the potential of our Zn-doped Ag nanoparticles as a highly efficient alternative for dye degradation.

CONCLUSION

In this study, Ag NP and Zn doped Ag NP were successfully synthesized using Polyganum cognatum plant as reducing and stabilizing agent by systematically varying zinc doping ratio (bare Ag NP, 1.6% Zn-doped Ag NP, and 9.0% Zn-doped Ag NP). The catalytic activities of synthesized nanoparticles were studied using the MO and MB dyes degradation reactions using a solution of sodium borohydride ($NaBH_4$) as the reducing agent. Some characterization techniques such as STEM, EDS, XRF, XRD, FTIR and ICP-MS analyses verified the effective incorporation of Zn into the Ag NP matrix, demonstrating the presence of components and structural alterations in the 9.0% Zn doped Ag NPs. UV-Vis spectroscopy was used to observe the process of degradation.

In catalytic experiments, different concentrations of nanoparticle (NP) suspensions (400, 600,

800, and 900 µL) were added to 3 mL cuvettes while the Ag concentration remained constant (1400 ppm) for all types of NPs (bare Ag NP, 1.6% Zn-doped Ag NP, and 9.0% Zn-doped Ag NP). According to catalytic degradation experiments, Zn doping at 9.0% significantly improved the degradation efficiency compared to bare Ag NPs and 1.6% Zn-doped Ag NPs. Specifically, the 9.0% Zn-doped Ag NPs achieved 96.56% degradation of MO in 15 minutes and 98.38% degradation of MB in 10 minutes, with rate constants of 0.2199 min^{-1} and 0.4445 min^{-1}, respectively. Additionally, the turnover frequencies (TOF) for MO and MB were 1.65 x 10^{-3} $mol.g^{-1}$ min^{-1} and 2.54 x 10^{-3} $mol.g^{-1}$ min^{-1}, respectively. Increasing the doping amount of Zn from 1.6% to 9.0% greatly decrease reaction times and improve degradation efficiency with MO degradation improving from 46.87% in 25 minutes (kapp = 0.0239 min^{-1}, TOF = 1.10 x 10^{-3} $mol.g^{-1}$ min^{-1}) to 96.56% in 15 minutes, and MB degradation increasing from 78.36% in 30 minutes (kapp = 0.0678 min^{-1}, TOF = 0.9 x 10^{-3} $mol.g^{-1}$ min^{-1}) to 98.38% in 10 minutes. The optimal NP suspension volume was found to be 0.8 mL, beyond which no significant improvement in degradation was observed. Furthermore, the study found that the optimal dye concentration for degradation was 5 mg/mL, as higher concentrations led to decreased efficiency due to surface saturation of the catalyst. These findings highlight the effectiveness of 9.0% Zn-doped Ag NPs as catalysts for the rapid and efficient degradation of hazardous dyes, presenting a viable solution for wastewater treatment applications.

Author Contributions

Research Design (CRediT 1) M.A. (40%) - T.N.A. (60%)
Data Collection (CRediT 2) M.A. (30%) - Ü.Ü. (20%) - T.N.A. (50%)
Research - Data Analysis - Validation (CRediT 3-4-6-11) M.A. (30%) - Ü.Ü. (20%) - T.N.A. (50%)
Writing the Article (CRediT 12-13) M.A. (50%) - T.N.A. (50%)
Revision and Improvement of the Text (CRediT 14) M.A. (40%) - Ü.Ü. (20%) - T.N.A. (40%)

Financing

Not applicable.

Data availability

The data presented in this study are available on request from the corresponding author.

Conflict of interest

The authors declare that there are no conflicts of interests.

REFERENCES

[1] B. Akgayev, S. Akbayrak, M. Yılmaz, M.S. Büker, V. Unsur, Assessing the feasibility of photovoltaic systems in Türkiye: Technical and economic analysis of on-grid, off-grid, and utility-scale PV ınstallations, *Necmettin Erbakan University Journal of Science and Engineering*. 6(1) (2024), 69-92. doi:10.47112/neufmbd.2024.33

[2] M. Ismail, K. Akhtar, M.I. Khan, T. Kamal, M.A. Khan, M.A. Asiri, S.B. Khan, Pollution, toxicity and carcinogenicity of organic dyes and their catalytic bioremediation, *Current pharmaceutical design*. 25(34) (2019), 3645-3663. doi:10.2174/1381612825666191021142026

[3] M.A. Al-Nuaim, A.A. Alwasiti, Z.Y. Shnain, The photocatalytic process in the treatment of polluted water, *Chemical papers*. 77(2) (2023), 677-701. doi:10.1007/s11696-022-02468-7

[4] M. Priyadarshanee, U. Mahto, S. Das, Mechanism of toxicity and adverse health effects of environmental pollutants, In Microbial biodegradation and bioremediation. (2022), 33-53. Elsevier. doi:10.1016/B978-0-323-85455-9.00024-2

[5] S. Bulbul, E. Ayhan, H. Gökmeşe, Termik santral atığı olan kömür külünün SBR matrisli bileşiklere ilave edilmesinin mekanik özelliklere etkisi, *Necmettin Erbakan University Journal of Science and Engineering*. 5(2) (2023), 96-107. doi:10.47112/neufmbd.2023.14

[6] M.A. Al-Nuaim, A.A. Alwasiti, Z.Y. Shnain, The photocatalytic process in the treatment of polluted water, *Chemical papers*, 77(2) (2023) 677-701. doi:10.1007/s11696-022-02468-7

[7] A. Saravanan, P.S. Kumar, D.V.N. Vo, S. Jeevanantham, S. Karishma, P.R.A. Yaashikaa, review on catalytic-enzyme degradation of toxic environmental pollutants: Microbial enzymes, *Journal of Hazardous Materials*. 419 (2021), 126451. doi:10.1016/j.jhazmat.2021.126451

[8] D. Astruc, Introduction: nanoparticles in catalysis, *Chemical reviews*. 120(2) (2020), 461-463. doi: 10.1021/acs.chemrev.8b00696

[9] A. Dhaka, S.C. Mali, S. Sharma, R.A. Trivedi, review on biological synthesis of silver nanoparticles and their potential applications, *Results in Chemistry*. (2023), 101108. doi:10.1016/j.rechem.2023.101108

[10] B. Mekuye, The Impact of size on the optical properties of silver nanoparticles based on dielectric function, Nanotechnology and Nanomaterials Annual Volume (2023). doi:10.5772/intechopen.113976

[11] W. Lewandowski, M. Fruhnert, J. Mieczkowski, C. Rockstuhl, E. Górecka, Dynamically self-assembled silver nanoparticles as a thermally tunable metamaterial, *Nature communications*. 6(1) (2015), 6590. doi:10.1038/ncomms7590

[12] G. Palani, H. Trilaksana, R.M. Sujatha, K. Kannan, S. Rajendran, K. Korniejenko, M. Uthayakumar, Silver nanoparticles for wastewater management, *Molecules*. 28(8) (2023), 3520. doi:10.3390/molecules28083520

[13] M.A. Kareem, I.T. Bello, H.A. Shittu, P. Sivaprakash, O. Adedokun, S. Arumugam, Synthesis, characterization, and photocatalytic application of silver doped zinc oxide nanoparticles, *Cleaner Materials*. 3 (2022), 100041. doi:10.1016/j.clema.2022.100041

[14] V. Vinitha, M. Preeyanghaa, V. Vinesh, R. Dhanalakshmi, B. Neppolian, V. Sivamurugan, Two is better than one: Catalytic, sensing and optical applications of doped zinc oxide nanostructures, *Emergent Materials*. 4 (2021), 1093-1124. doi:10.1007/s42247-021-00262-x

[15] D. Ntemogiannis, M. Tsarmpopoulou, A. Stamatelatos, S. Grammatikopoulos, V. Karoutsos, D.I. Anyfantis, P. Poulopoulos, ZnO Matrices as a platform for tunable localized surface plasmon resonances of silver nanoparticles, *Coatings*. 14(1) (2024), 69. doi:10.3390/coatings14010069

[16] S. Lv, Y. Du, F. Wu, Y Cai, T. Zhou, Review on LSPR assisted photocatalysis: effects of physical fields and opportunities in multifield decoupling, *Nanoscale Advances*. 4(12) (2022), 2608-2631. doi:10.1039/D2NA00140C

[17] Y. Li, Q. Liao, W. Hou, L. Qin, Silver-based surface plasmon sensors: fabrication and applications, *International Journal of Molecular Sciences*. 24(4) (2023), 4142. doi:10.3390/ijms24044142

[18] E. Vanags, I. Bite, L. Ignatane, R. Ignatans, A. Trausa, C.F. Tipaldi, K. Smits, Zinc Oxide Tetrapods Doped with Silver Nanoparticles as a Promising Substrate for the Detection of Biomolecules via Surface-Enhanced Raman Spectroscopy, *ChemEngineering*. 8(1) (2024), 19. doi:10.3390/chemengineering8010019

[19] S. Raha, M. Ahmaruzzaman, ZnO nanostructured materials and their potential applications: progress, challenges, and perspectives, *Nanoscale Advances*. 4(8) (2022), 1868-1925. doi: 10.1039/D1NA00880C

[20] H. Li, P. Wang, J. Qian, Y. Li, Q. Yuan, L. Du, Y. Chen, Zn-doped MnCe catalyst designed and applied for indoor low concentration formaldehyde removal and simultaneous antibacterial, *Materials Chemistry and Physics*. 305 (2023), 127946. 2023.127946. doi: 10.1016/j.matchemphys

[21] Y. Sun, W. Zhang, Q. Li, H. Liu, X. Wang, Preparations and applications of zinc oxide based photocatalytic materials, *Advanced Sensor and Energy Materials*. (2023), 100069. doi:10.1016/j.asems.2023.100069

[22] J. Schumann, M. Eichelbaum, T. Lunkenbein, N. Thomas, M.C. Alvarez Galvan, R. Schlögl, M. Behrens, Promoting strong metal support interaction: doping ZnO for enhanced activity of Cu/ZnO: M (M= Al, Ga, Mg) catalysts, *ACS catalysis*. 5(6) (2015), 3260-3270. doi:10.1021/acscatal.5b00188

[23] M.L. Sun, Z.P. Hu, H.Y. Wang, Y.J. Suo, Z.Y. Yuan, Design strategies of stable catalysts for propane dehydrogenation to propylene, *ACS Catalysis*. 13(7) (2023), 4719-4741. doi:10.1021/acscatal.3c00103

[24] N.A. Erfan, M.S. Mahmoud, H.Y. Kim, N.A. Barakat, Synergistic doping with Ag, CdO, and ZnO to overcome electron-hole recombination in TiO2 photocatalysis for effective water photo splitting reaction, *Frontiers in Chemistry*. (2023), 11. doi:10.3389/fchem.2023.1301172

[25] T. Mao, M. Liu, L. Lin, Y. Cheng, C.A Fang, study on doping and compound of zinc oxide photocatalysts, *Polymers*. 14(21) (2022), 4484. doi:10.3390/polym14214484

[26] I.H. Ifijen, M. Maliki, B. Anegbe, Synthesis, photocatalytic degradation and antibacterial properties of selenium or silver doped zinc oxide nanoparticles: A detailed review, *OpenNano*. 8 (2022), 100082. doi: 10.1016/j.onano.2022.100082

[27] D. Gupta, A. Boora, A Thakur, T.K. Gupta, Green and sustainable synthesis of nanomaterials: recent advancements and limitations, *Environmental Research*. 231 (2023), 116316. doi:10.1016/j.envres.2023.116316

[28] P. Szczyglewska, A. Feliczak-Guzik, I. Nowak, Nanotechnology–general aspects: A chemical reduction approach to the synthesis of nanoparticles, *Molecules*. 28(13) (2023), 4932. doi:10.3390/molecules28134932

[29] V. Harish, M.M. Ansari, D. Tewari, A.B. Yadav, N. Sharma, S. Bawarig, A. Barhoum, Cutting-edge advances in tailoring size, shape, and functionality of nanoparticles and nanostructures: A review, *Journal of the Taiwan Institute of Chemical Engineers*. 149 (2023), 105010. doi:10.1016/j.jtice.2023.105010

[30] Y. T. Gebreslassie, F.G. Gebremeskel, Green and cost-effective biofabrication of copper oxide nanoparticles: Exploring antimicrobial and anticancer applications, *Biotechnology Reports*. (2024), e00828. doi:10.1016/j.btre.2024.

[31] A.R. Bagheri, N. Aramesh, M.S. Hasnain, A.K. Nayak, R.S. Varma, Greener fabrication of metal nanoparticles using plant materials: A review, *Chemical Physics Impact*. 7 (2023), 100255. doi:10.1016/j.chphi.2023.100255

[32] A.M.E. Shafey, Green synthesis of metal and metal oxide nanoparticles from plant leaf extracts and their applications: A review, *Green Processing and Synthesis.* 9(1) (2020), 304-339. doi:10.1515/gps-2020-0031

[33] N.M. Ishak, S.K. Kamarudin, S.N. Timmiati, Green synthesis of metal and metal oxide nanoparticles via plant extracts: an overview, *Materials Research Express*. 6(11) (2019), 112004. doi:10.1088/2053-1591/ab4458

[34] S. Gözcü, R.A. Uğan, H. Özbek, B. Gündoğdu, Z. Güvenalp, Evaluation of antidiabetic and antioxidant effects of Polygonum cognatum Meisn. and phytochemical analysis of effective extracts, *Biomedical Chromatography*. 38(3) (2024), e5809. doi:10.1002/bmc.5809

[35] N. Eruygur, E. Ucar, M. Ataş, M. Ergul, M. Ergul, F. Sozmen, Determination of biological activity of Tragopogon porrifolius and Polygonum cognatum consumed intensively by people in Sivas, *Toxicology reports*. 7 (2020), 59-66. doi:10.1016/j.toxrep.2019.12.002

[36] F. Demirgül, M. Divriklioğlu-Kundak, O. Sağdiç, Bioactive properties, antibacterial activity, and color features of *Polygonum cognatum*: The effects of frozen storage and cooking process, *Food Science and Technology*. 42 (2022), e00322. doi:10.1590/fst.00322

[37] R. Akpınar, G. Yıldırım Baştemur, B. Bıçak, N.O. Sanli, E. Mertoğlu Kamalı, M. Pekmez, S. Perçin Özkorucuklu, Phytochemical profiling, in vitro biological activities, and in silico (molecular docking and absorption, distribution, metabolism, excretion, toxicity) studies of Polygonum cognatum Meissn, *Journal of Separation Science*. 47(1) (2024), 2300750. doi:10.1002/jssc.202300750

[38] A. Yıldırım, A. Mavi, A. Kara, Antioxidant and antimicrobial activities of Polygonum cognatum Meissn extracts, *Journal of the Science of Food and Agriculture*. 83(1) (2003), 64-69. doi:10.1002/jsfa.1288

[39] M. Pehlivan, H.İ.K. Çöven, B. Çerçi, A. Eldem, T. Öz, N. Savlak, İ. Pirim, The cytotoxic effect of Polygonium cognatum and chemotherapeutic effect of doxorubicin on glioblastoma cells, *European Journal of Therapeutics*. 27(1) (2021), 50-54. doi:10.5152/eurjther.2021.20085

[40] A.Q. Malik, T.U.G.,Mir, D. Kumar, I.A. Mir, A. Rashid, M. Ayoub, S. Shukla, A review on the green synthesis of nanoparticles, their biological applications, and photocatalytic efficiency against environmental toxins, *Environmental Science and Pollution Research*. 30(27) (2023), 69796-69823. doi:10.1007/s11356-023-27437-9

[41] B. Mahesh, A comprehensive review on current trends in greener and sustainable synthesis of ferrite nanoparticles and their promising applications, *Results in Engineering*. (2023), 101702. doi:10.1016/j.rineng.2023.101702

[42] A. Saravanan, P.S. Kumar, S. Karishma, D.V.N. Vo, S. Jeevanantham, P.R. Yaashikaa, C.S. George, A review on biosynthesis of metal nanoparticles and its environmental applications, *Chemosphere*. 264 (2021), 128580. doi:10.1016/j.chemosphere.2020.128580

[43] B. Mahesh, A comprehensive review on current trends in greener and sustainable synthesis of ferrite nanoparticles and their promising applications, *Results in Engineering*. (2023), 101702. doi:10.1016/j.rineng.2023.101702

[44] A.B. Daphedar, S. Kakkalameli, B. Faniband, M. Bilal, R.N. Bhargava, L.F.R. Ferreira, S. I. Mulla, Decolorization of various dyes by microorganisms and green-synthesized nanoparticles: current and future perspective, *Environmental Science and Pollution Research*. 30(60) (2023), 124638-124653. doi:10.1007/s11356-022-21196-9

[45] S.S. Emmanuel, A.A. Adesibikan, O.D. Saliu, E.A. Opatola, Greenly biosynthesized bimetallic nanoparticles for ecofriendly degradation of notorious dye pollutants: A review, *Plant Nano Biology*. 3 (2023), 100024. doi:10.1016/j.plana.2023.100024

[46] N.T. T. Nguyen, L.M. Nguyen, T.T.T. Nguyen, R.K. Liew, D.T.C. Nguyen, T. Van Tran, Recent advances on botanical biosynthesis of nanoparticles for catalytic, water treatment and agricultural

applications: A review, *Science of the Total Environment*. 827 (2022), 154160. doi:10.1016/j.scitotenv.2022.154160

[47] M. Yilmaz, A. Yilmaz, A. Karaman, F. Aysin, O. Aksakal, Monitoring Chemically and Green-Synthesized Silver nanoparticles in maize seedlings via Surface-Enhanced Raman Spectroscopy (SERS) and their phytotoxicity evaluation, *Talanta*. (225) (2021), 121952. doi:10.1016/j.talanta.2020.121952. doi:10.1016/j.talanta.2020.121952

[48] Ö. Kaplan, N. Gökşen Tosun, Biosynthesis of ıron, copper and silver nanoparticles using *Polygonum cognatum* and tragopogon porrifolius extracts and evaluation of their antimicrobial potentials, *Düzce Üniversitesi Bilim ve Teknoloji Dergisi*. 11(4) (2023), 2155–2167. doi:10.29130/dubited.1093468

[49] N. Gürsoy, S. Elagöz, E. Gölge, *Polygonum cognatum* Meissn. ve funguslu ortamda sentezlenen gümüş nanopartiküllerinin (agnp) antimikrobiyal özelliklerinin araştırılması, *Türk Tarım ve Doğa Bilimleri Dergisi*. 7 (1) (2020), 221–230. doi: 10.30910/turkjans.680075

[50] H. Meskher, S.B. Belhaouari, K. Deshmukh, C.M. Hussain, F.A Sharifianjazi, Magnetite composite of molecularly ımprinted polymer and reduced graphene oxide for sensitive and selective electrochemical detection of catechol in water and milk samples: An artificial neural network (ANN) application, *Journal of The Electrochemical Society*. 170(4) (2023), 047502. doi:10.1149/1945-7111/acc97c

[51] M.E. Pekdemir, S. Pekdemir, Ş. İnci, S. Kırbağ, M. Çiftci, Thermal, Magnetic properties and antimicrobial effects of magnetic ıron oxide nanoparticles treated with *Polygonum cognatum*, *Iranian Journal of Science and Technology, Transactions of Civil Engineering*. 45 (5) (2021), 1579–1586. doi:10.1007/s40995-021-01167-4

[52] R. Abaid, M. Malik, M.A. Iqbal, M. Malik, Z. Shahwani, T.Z. Ali, K. Morsy, R.Y. Capangpangan, A.C. Alguno, J.R. Choi, Biosynthesizing *Cassia fistula* extract-mediated silver nanoparticles for MCF-7 cell lines anti-cancer assay, *ACS Omega*. 8(19) (2023), 17317–17326. doi:10.1021/acsomega.3c02225

[53] T.C. Kömürcü, N. Bilgiçli, Yumurtalı ve yumurtasız formüle edilen madımak (*Polygonum cognatum*) tozu ilaveli erişte lerin fonksiyonel içeriği ve duyusal özellikleri, *Necmettin Erbakan University Journal of Science and Engineering.* 6(1), (2024), 124-138. doi:10.47112/neufmbd.2024.37

[54] P.N.V.K. Pallela, S. Ummey, L.K. Ruddaraju, S.V.N. Pammi, S.G Yoon, Ultra Small, mono dispersed green synthesized silver nanoparticles using aqueous extract of Sida cordifolia plant and investigation of antibacterial activity, *Microbial Pathogenesis*. 124 (2018), 63-69. doi:10.1016/j.micpath.2018.08.026

[55] D. Nayak, S. Ashe, P.R. Rauta, M. Kumari, B. Nayak, Bark extract mediated green synthesis of silver nanoparticles: evaluation of antimicrobial activity and antiproliferative response against osteosarcoma, *Materials Science and Engineering:C*. 58 (2016), 44-52. doi:10.1016/j.msec.2015.08.022

[56] J. Jiang, G. Oberdörster, P. Biswas, Characterization of size, surface charge, and agglomeration state of nanoparticle dispersions for toxicological studies, *Journal of Nanoparticle Research*. 11 (2009), 77-89. doi:10.1007/s11051-008-9446-4

[57] X. Yin, W. Que, D. Fei, F. Shen, Q. Guo, Ag nanoparticle/ZnO nanorods nanocomposites derived by a seed-mediated method and their photocatalytic properties, *Journal of Alloys and Compounds*. 524 (2012), 13-21. doi:10.1016/j.jallcom.2012.02.052

[58] N. Bhattacharjee, I. Som, R. Saha, S.A Mondal, critical review on novel eco-friendly green approach to synthesize zinc oxide nanoparticles for photocatalytic degradation of water pollutants, *International Journal of Environmental Analytical Chemistry*. 104(3) (2024), 489-516. doi:10.1080/03067319.2021.2022130

[59] H. Jan, M. Shah, H. Usman, M.A. Khan, M. Zia, C. Hano, B.H. Abbasi, Biogenic synthesis and

characterization of antimicrobial and antiparasitic zinc oxide (ZnO) nanoparticles using aqueous extracts of the Himalayan Columbine (*Aquilegia pubiflora*), *Frontiers in Materials*. 7 (2020), 249. doi:10.3389/fmats.2020.00249

[60] A. Król, P. Pomastowski, K. Rafińska, V. Railean-Plugaru, B. Buszewski, Zinc oxide nanoparticles: Synthesis, antiseptic activity and toxicity mechanism, *Advances in colloid and interface science*. 249 (2017), 37-52. doi:10.1016/j.cis.2017.07.033

[61] M. Bandeira, M. Giovanela, M. Roesch-Ely, D.M. Devine, J. da Silva Crespo, Green synthesis of zinc oxide nanoparticles: A review of the synthesis methodology and mechanism of formation, *Sustainable Chemistry and Pharmacy*. 15 (2020), 100223. doi:10.1016/j.scp.2020.100223

[62] N. Singh, F.Z. Haque, Synthesis of zinc oxide nanoparticles with different pH by aqueous solution growth technique, *Optik*. 127(1) (2016). 174-177. doi:10.1016/j.ijleo.2015.09.024

[63] T. Parsai, A. Kumar, Understanding effect of solution chemistry on heteroaggregation of zinc oxide and copper oxide nanoparticles, *Chemosphere*. 235 (2019), 457-469. doi:10.1016/j.chemosphere.2019.06.171

[64] H. Veisi, S. Azizi, P. Mohammadi, Green synthesis of the silver nanoparticles mediated by *Thymbra spicata* extract and its application as a heterogeneous and recyclable nanocatalyst for catalytic reduction of a variety of dyes in water, *Journal of Cleaner Production*. 170 (2018), 1536-1543. doi:10.1016/j.jclepro.2017.09.265

[65] A. Dandia, S.L. Gupta, A. Indora, P. Saini, V. Parewa, K.S. Rathore, Ag NPs decked GO composite as a competent and reusable catalyst for 'ON WATER'chemoselective synthesis of pyrano [2, 3-c: 6, 5-c′] dipyrazol]-2-ones, *Tetrahedron Letters*. 58(12) (2017), 1170-1175. doi:10.1016/j.tetlet.2017.02.014

[66] S.K. Pandey, M.K. Tripathi, V. Ramanathan, P.K. Mishra, D. Tiwary, Enhanced photocatalytic efficiency of hydrothermally synthesized g-C3N4/NiO heterostructure for mineralization of malachite green dye, *Journal of Materials Research and Technology*. 11 (2021), 970-981. doi:10.1016/j.jmrt.2021.01.059

[67] C.W. Lou, A.P. Chen, T.T Lic, J.H. Lin, Antimicrobial activity of UV-induced chitosan capped silver nanoparticles, *Materials Letters.* 128 (2014), 248-252. doi:10.1016/j.matlet.2014.04.145

[68] M. Zafar, T. Iqbal, Green synthesis of silver and zinc oxide nanoparticles for novel application to enhance shelf life of fruits. *Biomass Conversion and Biorefinery*. 14(4) (2024), 5611-5626. doi:10.1007/s13399-022-02730-8

[69] N. Ahmad, S. Sharma, M.K. Alam, V.N. Singh, S.F. Shamsi, B.R., Mehta, A. Fatma, Rapid synthesis of silver nanoparticles using dried medicinal plant of basil, *Colloids and Surfaces B: Biointerfaces.* 81(1) (2010), 81-86. doi:10.1016/j.colsurfb.2010.06.029

[70] D.R. Mota, W.D.S. Martini, D.S. Pellosi, Influence of Ag size and shape in dye photodegradation using silver nanoparticle/ZnO nanohybrids and polychromatic light, *Environmental Science and Pollution Research*. 30(20) (2023), 57667-57682. doi:10.1007/s11356-023-26580-7

[71] M.U. Rashid, S.J. Shah, S. Attacha, L. Khan, J. Saeed, S.T. Shah, H.I. Mohamed, Green Synthesis and characterization of zinc oxide nanoparticles using *Citrus limetta* peels extract and their antibacterial activity against brown and soft rot pathogens and antioxidant potential, *Waste and Biomass Valorization*. (2024), 1-16. doi:10.1007/s12649-023-02389-w

[72] P. Perumal, N.A. Sathakkathulla, K. Kumaran, R. Ravikumar, J.J. Selvaraj, V. Nagendran, S. Rathinasamy, Green synthesis of zinc oxide nanoparticles using aqueous extract of shilajit and their anticancer activity against HeLa cells, *Scientific Reports*. 14(1) (2024), 2204. doi:10.1038/s41598-024-52217-x

[73] P. Ramesh, A. Rajendran, M. Ashokkumar, Biosynthesis of zinc oxide nanoparticles from *Phyllanthus niruri* plant extract for photocatalytic and antioxidant activities, *International Journal of Environmental Analytical Chemistry*. 104(7) (2024), 1561-1572.

doi:10.1080/03067319.2022.2041004

[74] P.A. Luque, H.E. Garrafa-Gálvez, C.A. García-Maro, C.A. Soto-Robles, Study of the optical properties of ZnO semiconductor nanoparticles using *Origanum vulgare* and its effect in Rhodamine B degradation, *Optik*. 258 (2022), 168937. doi: 10.1016/j.ijleo.2022.168937

[75] Md.R. Khan, S.M. Hoque, K.F.B. Hossain, Md.A.B. Siddique, Md.K. Uddin, Md.M. Rahman, Green synthesis of silver nanoparticles using *Ipomoea aquatica* leaf extract and its cytotoxicity and antibacterial activity assay, *Green Chemistry Letters and Reviews*. 13(4) (2020), 303-315. doi:10.1080/17518253.2020.1839573

[76] K.J. Rao, S. Paria, Green synthesis of silver nanoparticles from aqueous *Aegle marmelos* leaf extract, *Materials Research Bulletin*. 48(2) (2013), 628-634. doi: 10.1016/j.materresbull.2012.11.035

[77] D.A. Kumar, V. Palanichamy, S.M. Roopan, Green synthesis of silver nanoparticles using *Alternanthera dentata* leaf extract at room temperature and their antimicrobial activity, *Spectrochimica Acta Part A: Molecular and Biomolecular Spectroscopy*. 127 (2014), 168-171. doi: 10.1016/j.saa.2014.02.058

[78] J.A. Garibay-Alvarado, M.A. Ruiz-Esparza-Rodríguez, E.A. Zaragoza-Contreras, S.Y. Reyes-López, Ag nanoparticle-decorated SiO2–Al2O3–ZrO2 composites as a low-cost substrate for enhanced signal ınfrared spectroscopy, *ACS Applied Nano Materials*. 7(5) (2024). 4658-4666. doi:10.1021/acsanm.3c03464

[79] L. Gharibshahi, E. Saion, E. Gharibshahi, A.H. Shaari, K.A. Matori, Structural and optical properties of Ag nanoparticles synthesized by thermal treatment method, *Materials*. 10(4) (2017), 402. doi:10.3390/ma10040402

[80] R.B. Patil, A.D. Chougale, Analytical methods for the identification and characterization of silver nanoparticles: A brief review, *Materials Today: Proceedings*. 47 (2021), 5520-5532. doi:10.1016/j.matpr.2021.03.384

[81] S.K. Rout, B.C. Tripathy, P. Padhi, B.R. Kar, K.G. Mishra, A green approach to produce silver nano particles coated agro waste fibers for special applications, *Surfaces and Interfaces*. 7 (2017), 87-98. doi:10.1016/j.surfin.2017.03.004

[82] S. Ahmad, A. Yousaf, M.N. Tahir, A.A. Isab, M. Monim-ul-Mehboob, W. Linert, M. Saleem, Structural characterization and antimicrobial activity of a silver (I) complex of arginine, *Journal of Structural Chemistry*. 56 (2015), 1653-1657. doi:10.1134/S0022476615080302

[83] V.P. Singh, D. Das, C. Rath, Studies on intrinsic defects related to Zn vacancy in ZnO nanoparticles, *Materials Research Bulletin*. 48(2) (2013), 682-686. doi:10.1016/j.materresbull.2012.11.026

[84] A.M. Mostafa Mwafy, A. Eman, A.M. Khalil, A. Toghan, E.A. Alashkar, ZnO/Ag multilayer for enhancing the catalytic activity against 4-Nitrophenol, *Journal of Materials Science: Materials in Electronics*. 34(4) (2023), 300. doi:10.1007/s10854-022-09631-6

[85] Y. Sun, W. Zhang, Q. Li, H. Liu, X. Wang, Preparations and applications of Zinc Oxide based photocatalytic materials, *Advanced Sensor and Energy Materials*. 2(3) (2023), 100069. doi: 10.1016/j.asems.2023.100069

[86] J. Bednář, L. Svoboda, Z. Rybková, R. Dvorský, K. Malachová, T. Stachurová, D. Matýsek, V. Foldyna, Antimicrobial synergistic effect between Ag and Zn in Ag-ZnO·mSiO2 silicate composite with high specific surface area, *Nanomaterials (Basel)*. 9(9) (2019), 1265. doi: 10.3390/nano9091265

[87] M. Şahin, Y. Arslan, F. Tomul, B. Yıldırım, H. Genç, Green synthesis of silver nanoparticles using Lathyrus brachypterus extract for efficient catalytic reduction of methylene blue, methyl orange, methyl red and investigation of a kinetic model, *Reaction Kinetics, Mechanisms and Catalysis*. 135(6) (2022), 3303-3315. doi:10.1007/s11144-022-02299-3

[88] M. Rafique, I. Sadaf, M.B. Tahir, M.S. Rafique, G. Nabi, et al. Novel and facile synthesis of silver nanoparticles using *Albizia procera* leaf extract for dye degradation and antibacterial applications, *Materials Science and Engineering: C.* 99 (2019), 1313–1324. doi:10.1016/j.msec.2019.02.059

[89] H.T. Kahraman, Synthesis of silver nanoparticles using *Alchemilla vulgaris* and Helichrysum arenarium for methylene blue and 4-nitrophenol degradation and antibacterial applications, *Biomass Conversion and Biorefinery*. (2024), 1-12. doi:10.1007/s13399-024-05314-w

[90] K. Naseem, M. Zia Ur Rehman, A. Ahmad, D. Dubal, T.S. AlGarni, Plant extract induced biogenic preparation of silver nanoparticles and their potential as catalyst for degradation of toxic dyes, *Coatings*. 10 (2020), 1235. doi:10.3390/coatings10121235

[91] P.K. Pandey, J. Sarkar, S. Srivastava, Catalytic dye degradation of textile dye methylene blue by using silver nanoparticles fabricated by sustainable approach, *Engineering Proceedings*. 37(1) (2023), 16. doi:10.3390/ECP2023-14684

[92] A. Yeganeh-Faal, M. Bordbar, N. Negahdar, M. Nasrollahzadeh, Green synthesis of the Ag/ZnO nanocomposite using *Valeriana officinalis* L. root extract: application as a reusable catalyst for the reduction of organic dyes in a very short time, *Iet Nanobiotechnology*. 11(6) (2017), 669-676. doi:10.1049/iet-nbt.2016.0198

[93] R. Rajasekar, R. Thanasamy, M. Samuel, T.N.J.I. Edison, N. Raman, Ecofriendly synthesis of silver nanoparticles using *Heterotheca subaxillaris* flower and its catalytic performance on reduction of methyl orange, *Biochemical Engineering Journal*. 187 (2022), 108447. doi:10.1016/j.bej.2022.108447

[94] K. Nagaraj, P. Thangamuniyandi, S. Kamalesu, M. Dixitkumar, A.K. Saini, S.K. Sharma, C. Karuppiah, Silver nanoparticles using *Cassia alata* and its catalytic reduction activities of rhodamine6G, methyl orange and methylene blue dyes, *Inorganic Chemistry Communications*. 155 (2023), 110985. doi:10.1016/j.inoche.2023.110985

[95] D. Khwannimit, R. Maungchang, P. Rattanakit, Green synthesis of silver nanoparticles using Clitoria ternatea flower: an efficient catalyst for removal of methyl orange, *International Journal of Environmental Analytical Chemistry*. 102(17) (2022), 5247-5263. doi:10.1080/03067319.2020.1793974

[96] V.V. Konduri, N.K. Kalagatur, L. Gunti, U.K. Mangamuri, V.R. Kalagadda, S. Poda, S.B.N. Krishna, Green synthesis of silver nanoparticles from *Hibiscus tiliaceus* L. Leaves and their applications in dye degradation, antioxidant, antimicrobial, and anticancer activities, *South African Journal of Botany*. 168 (2024), 476-487. doi:10.1016/j.sajb.2024.03.035

[97] B.U. Hijazi, M. Faraj, R. Mhanna, M.H. El-Dakdouki, Biosynthesis of silver nanoparticles as a reliable alternative for the catalytic degradation of organic dyes and antibacterial applications, *Current Research in Green and Sustainable Chemistry*. 8 (2024), 100408. doi:10.1016/j.crgsc.2024.100408

FEN ve MÜHENDİSLİK BİLİMLERİ DERGİSİ

Vol: 7 No: 1 Year: 2025 | Araştırma Makalesi/Research Article | e-ISSN: 2667-7989

https://doi.org/10.47112/neufmbd.2025.76

Karabiber özütü kullanılarak sentezlenen biyojenik gümüş nanopartiküller ile grafen yapıların kombine antibakteriyel ve antioksidan etkisi

Selim IŞILDAK [1*] Mahfuz ELMASTAŞ [1,2] Behiç Selman ERDOĞDU [3] Meryem ERDOĞDU [4]

[1] Tokat Gaziosmanpaşa University, Graduate School of Natural and Applied Sciences, Department of Chemistry, Tokat, Türkiye
[2] University of Health Sciences, Hamidiye Faculty of Pharmacy, Department of Biochemistry, İstanbul, Türkiye
[3] Necmettin Erbakan University, Faculty of Science, Department of Molecular Biology and Genetics, Konya, Türkiye
[4] Necmettin Erbakan University, Faculty of Dentistry, Department of Prosthetic Dentistry Therapy, Konya, Türkiye

Makale Bilgisi

Geliş Tarihi: 12.11.2024
Kabul Tarihi: 06.01.2025
Yayın Tarihi: 30.04.2025

Anahtar Kelimeler:
Antibakteriyel,
Antioksidan,
Grafen Oksit,
Gümüş nanopartikül.

ÖZET

Nanoteknoloji, malzemelerin nanometre ölçeğinde, özellikle 1 ila 100 nanometre aralığında tasarım ve manipülasyonuna odaklanan öncü bir araştırma alanıdır. Gümüş nanoparçacıkları, antiseptik özellikleri ile bilinir ve genellikle malzemelerin antibakteriyel etkinliğini artırmak amacı ile diş hekimliği gibi alanlarda kullanılır. Son zamanlarda, grafen bazlı malzemeler de antibakteriyel özellikleri nedeniyle önem kazanmıştır. Bu çalışma ile karabiber ekstraktı kullanılarak mikrodalga yöntemi ile sentezlenmiş gümüş nanoparçacıkları ile grafen yapılarının kombinasyonunun antibakteriyel ve antioksidan aktiviteleri incelenmiştir. Sentezlenen malzemeler, UV-Vis spektroskopisi, taramalı elektron mikroskobu (SEM) ve enerji dağıtıcı X-ışını spektroskopisi (EDS) gibi çeşitli analitik yöntemlerle karakterize edilmiştir. Grafen ve gümüş nanoparçacık kompozitlerinin antibakteriyel etkinliği, *Staphylococcus aureus* (*S. aureus*) üzerine agar well difüzyon yöntemi kullanılarak değerlendirilmiştir. Ayrıca, kompozitlerin serbest radikal süpürme aktiviteleri DPPH, FRAP ve ABTS testleri ile test edilmiştir. Sonuçlar, grafen oksit ve gümüş nanoparçacıklarının kombinasyonunun 14.40 mm ile en büyük inhibisyon alanını oluşturduğunu, antioksidan aktivitenin ise genel olarak gümüş nanoparçacıklar için grafen ve kompozit yapılara kıyasla daha üstün olduğunu göstermiştir. Bu sonuçlar, sentezlenen grafenin, biyosentezlenmiş gümüş nanoparçacıkları ile entegrasyonunun antibakteriyel aktiviteyi geliştirebileceği ve biyomedikal alanlarda kullanılabileceğini göstermektedir.

Combined Antibacterial and Antioxidant Effect of Graphene Structures with Biogenic Silver Nanoparticles Synthesized by Using Black Pepper Extract

Article Info

Received: 12.11.2024
Accepted: 06.01.2025
Published: 30.04.2025

Keywords:
Antibacterial,
Antioxidant,
Graphene oxide,
Silver nanoparticle.

ABSTRACT

Nanotechnology is a pioneering research field that focuses on the design and manipulation of materials at the nanoscale, particularly within the range of 1 to 100 nanometers. Silver nanoparticles are known for their antiseptic properties and are commonly used in fields such as dentistry to enhance the antibacterial efficacy of materials Recently, graphene-based materials have also gained importance due to their antibacterial properties. In this study, antibacterial and antioxidant activities of the combination of silver nanoparticles and graphene structures synthesized by microwave method using black pepper extract were investigated. The synthesized materials were characterized by various analytical methods such as UV-Vis spectroscopy, scanning electron microscopy (SEM) and energy dispersive X-ray spectroscopy (EDS). The antibacterial activity of graphene and silver nanoparticle composites was evaluated using agar well diffusion method on *Staphylococcus aureus* (*S. aureus*). In addition, the free radical scavenging activities of the composites were tested by DPPH, FRAP and ABTS assays. The results showed that the combination of graphene oxide and silver nanoparticles produced the largest inhibition area of 14.40 mm, while the antioxidant activity was generally superior for silver nanoparticles compared to graphene and composite structures. These results suggest that the integration of synthesized graphene with biosynthesized silver nanoparticles can improve antibacterial activity and can be used in biomedical fields.

To cite this article:
Işıldak, S., Elmastaş, M., Erdoğdu, B.S. & Erdoğdu, M. (2025). Combined antibacterial and antioxidant effect of graphene structures with biogenic silver nanoparticles synthesized by using black pepper extract. *Necmettin Erbakan University Journal of Science and Engineering, 7*(1), 77-91. https://doi.org/10.47112/neufmbd.2025.76

***Corresponding Author:** Selim Işıldak, *se.isildak@gmail.com*

INTRODUCTION

Nanotechnology is an important and developing field that is utilized in many scientific disciplines and having an impact on human life. It entails creating and working with materials that range in size from 1 to 100 nanometers and have special properties like a high surface area-to-volume ratio, which contribute to their diverse applications and effects [1]. The applications for nanoparticle-based technologies are numerous and include semiconductors, batteries, pharmaceuticals, and industrial catalysis. Fullerenes, liposomes, metal nanoparticles, nanodroplets, and dendrimers are some types of nanomaterials [2]. The synthesis of metallic nanoparticles is primarily conducted through two main methodologies. The first is the "bottom-up" approach, which involves constructing materials from atomic or molecular components. The second is the "top-down" approach, which focuses on breaking down larger bulk materials into nanoscale particles. Nowadays, silver nanoparticles (AgNPs) are one of the most popular materials because they have important antibacterial properties. In addition to their enhanced antibacterial activity, AgNPs have other beneficial properties that make them useful for a variety of applications [3]. The biological synthesis of AgNPs has become increasingly popular in recent years. The use of microorganisms and plant extracts for this synthesis represents a strong alternative to traditional chemical and physical synthesis methods as they are simpler to use, more economical, more environmentally friendly, and easily scalable for high-yield production [4].

AgNPs can effectively inhibit the growth of a variety of bacteria, making them a useful addition to materials such as dental composites and other restorative materials [5,6]. AgNPs have an antibacterial effect because they release silver ions, which are toxic to bacteria and can damage bacterial cell membranes, impairing bacterial cell functions and causing cell lysis [7]. This property is particularly important in some areas such as prosthetic dentistry, where the risk of infection is increased due to the presence of foreign materials in the oral cavity. Without substantially altering their mechanical qualities, AgNPs can be added to a variety of dental materials, including acrylic and composite resins, to increase their antimicrobial efficacy [8,9]. In addition, AgNPs exhibit antioxidant activities due to their ability to scavenge free radicals. This effect is particularly significant in dental applications, as oxidative stress can accelerate the progression of oral diseases and lead to the degradation of dental materials [10,11]. The antioxidant capacity of AgNPs has been shown to be comparable to that of ascorbic acid, indicating their potential role in protecting dental materials from oxidative damage. Additionally, adding AgNPs to dental materials enhances their antibacterial properties while halting oxidative deterioration, which increases the materials' stability and durability [12,13]. Investigating environmentally friendly methods of synthesizing AgNPs, like plant extracts, further increases their appeal for dental applications. Because they still have antimicrobial and antioxidant qualities but are less damaging to human cells, the green synthesized AgNPs are safe for use in dental procedures [14,15]. Nanomaterials have shown significant potential to control bacterial colonization in prosthetic dentistry by highlighting the antibacterial properties of silver nanoparticles (AgNPs), which can effectively inhibit bacterial growth and biofilm formation on prosthetic materials. This capability is crucial for enhancing the longevity and success of dental implants, as bacterial biofilms are a primary cause of implant failure [16].

The antibacterial and antioxidant properties of GO have made it a significant material in various fields. The unique physical and chemical characteristics of GO primarily contribute to its antibacterial effects [17] . Studies have demonstrated that GO can damage bacteria membranes, resulting in cell lysis and death. The bacterial cells suffer physical harm and membrane stress due to the sharp edges of the graphene sheets, which facilitate this mechanism [18,19]. Furthermore, electron transfer interactions between graphene and microbial membranes, which depend on direct physical contact and membrane perturbation rather than just reactive oxygen species (ROS), strengthen the antibacterial effects [20]. GO is a versatile treatment for dental infections because research shows that it has broad-spectrum antimicrobial activity against a variety of bacterial strains, including both Gram-positive and Gram-

negative bacteria [21,22]. In addition, GO has significant antioxidant properties. GO has been shown to be an effective free radical scavenger, outperforming conventional antioxidants such as ascorbic acid and mannitol under certain conditions [23]. This antioxidant activity is critical in prosthodontics, as oxidative stress can degrade dental materials and compromise the integrity of prosthetic devices. Incorporating GO into dental materials can increase their resistance to oxidative degradation, hence extending their useful lifespan [24]. GO has also been shown to increase the activity of antioxidant enzymes in biological systems, including catalase (CAT) and superoxide dismutase (SOD), which are essential for cellular defense against oxidative stress [25].

In this study, we aimed to investigate the synergistic antibacterial and antioxidant properties of green synthesized AgNPs coupled with graphene materials. To achieve this, we characterized the synthesized nanoparticles using various analytical methods. The antimicrobial efficacy of the nanoparticles and graphene structures, both individually and in combination, was evaluated against *Staphylococcus aureus* through the agar well diffusion method. Additionally, we conducted DPPH, FRAP, and $ABTS^{+}$ analyses to assess their antioxidant capacity.

MATERIALS AND METHODS

Chemicals used in the study

All materials used in this study were rinsed with deionized water. The chemicals employed were sourced from various suppliers, including sulfuric acid (H_2SO_4), iron (III) chloride ($FeCl_3$), and ABTS (2,2'-Azino-Bis (3-Ethylbenzothiazoline-6-Sulfonic Acid) from Merck. Additionally, sodium nitrate ($NaNO_3$), potassium permanganate ($KMnO_4$), Müller Hinton agar, hydrogen peroxide (H_2O_2), silver nitrate ($AgNO_3$), DPPH (2,2-Diphenyl-1-picrylhydrazyl), potassium ferricyanide ($K_3Fe(CN)_6$), trichloroacetic acid (TCA), and ammonium acetate (CH_3COONH_4) were obtained from Sigma-Aldrich. The graphene structures were purchased from MediSen (Türkiye) company.

Graphene oxide synthesis

A modified version of the Hummers method was used to synthesize GO from natural graphite. In brief, 1 g of $NaNO_3$ and 46 mL of H_2SO_4 were mixed with 1 g of natural graphite powder, and the mixture was continuously stirred in an ice bath to keep the temperature below 20 °C. Gradually, 6 g of $KMnO_4$ was added while stirring. After 60 min., the mixture was taken out of the ice bath, and the temperature was raised to 35 °C, where it was maintained for an additional 30 min. After that, 70 mL of water was gently added to the mixture, which was agitated for another 15 min. Then, 80 mL of hot water (at 60 °C) and a 30% H_2O_2 solution were added to reduce any remaining $KMnO_4$ until effervescence ceased. The resulting product was washed multiple times to remove any residual salt impurities. After undergoing a thermal reduction process at 200 °C for 3 h, a black powder of GO was obtained.

Synthesis of silver nanoparticles and characterization

The black pepper was subjected to a washing process that included three rinses with distilled water, followed by removal of impurities and subsequent drying. The dried plant materials were then ground into a fine powder. 10 g of this powder was boiled in 100 mL of distilled water to extract plant material. The resulting extracts were centrifuged at 5000 rpm (at 4 °C for 12 min). The obtained supernatant was collected and then filtered with Whatman filter paper (Grade No. 1). 100 mL of distilled water was used to dissolve 0–017 g of AgNO3 to create a 1 mM AgNO3 solution. The extract was then mixed with 80 milliliters of AgNO3 solution to synthesize AgNPs. After that, the mixture was exposed to microwave radiation for 25 min. in a laboratory-grade microwave with a 700-watt power setting. AgNP colloidal suspensions were sonicated for 10 min. at 55% power after the synthesis process. The

resulting pellets were discarded after the suspensions were centrifuged at 4 °C (5000 rpm) for 15 min. The centrifugation process was carried out again for the supernatants. The residual colloidal nanoparticles underwent additional purification through centrifugation using ultra-pure water at 10.000 rpm and 4°C for 15 min. to eliminate any residual plant extract. This washing step was performed twice. Finally, the purified AgNPs were lyophilized and stored at 4°C in a dark container for future applications. The resulting nanoparticles were then characterized by UV-Vis, SEM, DLS and EDS.

Antibacterial activity test using agar well diffusion assay

The *Staphylococcus aureus* strain (ATCC 6538P) was provided in lyophilized form. To evaluate the antibacterial activity, Mueller Hinton agar was prepared. The turbidity of the bacterial suspension intended for testing was calibrated to match the McFarland 0.5 standard. Following the homogenization of the liquid culture through shaking, approximately 100 µL was dispensed onto a Petri dish to evenly moisten the surface, which was then spread using a Drigalski spatula. To assess the antibacterial activity, wells with a diameter of approximately 7 mm were created on the agar surface, into which composite suspensions with nanoparticles and graphene structures were introduced in a final volume of 100 µL. Gentamicin at a concentration of 10 µg/mL served as the positive control. After a pre-incubation period of 1 h at 25 °C, the bacterial isolate was incubated at 37 °C for 24 h. The zones of inhibition surrounding each sample were subsequently measured. Each experimental trial was conducted in triplicate for both the samples and the bacterial isolate.

Free radical (DPPH) scavenging activity

The evaluation of free radical scavenging activity using DPPH (2,2-diphenyl-1-picryl hydrazyl) was conducted following the protocol established by Blois et al. [26]. A 0.26 mM solution of DPPH was prepared in ethanol. A specified quantity of stock solutions containing GO and AgNPs, ranging from 10 to 200 mg/mL, was measured out. To achieve a total volume of 4 mL in the reaction vessel, ethanol was added after adding 1 mL of the DPPH solution (0.26 mM). After that, the mixture was vortexed, and it was left to incubate for 30 min. Following incubation, a spectrophotometer was used to measure each sample's absorbance at a wavelength of 517 nm.

Ferric reducing power (FRAP) activity

The analysis was conducted utilizing the Oyaizu method [27], with modifications as described by Elmastas et al. [27,28]. A stock solution containing 100 µL of GO and AgNPs was prepared by diluting with phosphate buffer (0.2 M, pH 6.6) to a final volume of 1.25 mL. Subsequently, 1.25 mL of 1% $K_3Fe(CN)_6$ was added to the mixture. This combination was incubated at 50 °C for 20 min. After incubation, 1.25 mL of trichloroacetic acid 10% TCA and 0.25 mL of 0.1% FeCl3 were added to the mixture. The absorbance of the final solution was measured at 700 nm.

ABTS radical scavenging activity

This study was conducted following the methodology established by Re et al. [29]. A 0.1 M phosphate buffer solution (pH 7.4) was prepared. Subsequently, a 2 mM ABTS (2,2'-Azino-bis(3-ethylbenzothiazoline-6-sulfonic acid)) solution was prepared using the phosphate buffer, and this was mixed with a 2.45 mM K2S2O8 (potassium persulfate) solution in a 1:2 ratio. The mixture was allowed to stand in the dark for 6 h. After this period, an appropriate volume of stock solutions was taken and diluted with phosphate buffer to a final volume of 3 mL. Then, 1 mL of the ABTS solution was added, and the mixture was vortexed to ensure thorough mixing. The resulting solution was incubated at room temperature for 1 h, after which the absorbance was measured at 734 nm using a spectrophotometer.

RESULTS AND DISCUSSION

The aqueous extract of black pepper was utilized for the synthesis of AgNPs from silver nitrate ($AgNO_3$). The first signs of AgNPs formation were observed almost immediately after 25 min. constant stirring and microwave irradiation. A rapid change in color from the initially colorless reaction mixture to a brownish yellow was the first sign of this formation. UV-Vis spectroscopy was then used to confirm the presence of AgNPs. This technique is effective because the free electrons within the nanoparticles generate surface plasmon resonance [30]. In line with earlier findings in the literature, the samples showed a peak at a wavelength of about 440 nm, according to the UV-Vis analysis [31]. Figure 1 illustrated the UV-Vis spectrum of the synthesized AgNPs.

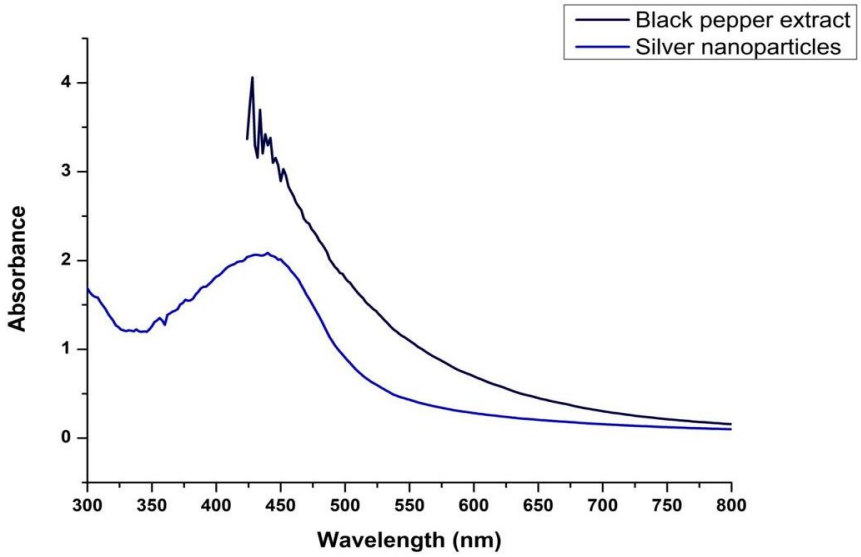

Figure 1
UV-Vis analysis of silver nanoparticles and black pepper extract synthesized by microwave method

Dynamic light scattering (DLS) was used to measure the polydispersity index (PDI), mean particle size, and particle size distribution of AgNPs in the reaction mixtures. The DLS analysis revealed that the average particle size distribution of the nanoparticles in the solution was measured at 60.95 nm, with a polydispersity index of 0.278 (Figure 2).

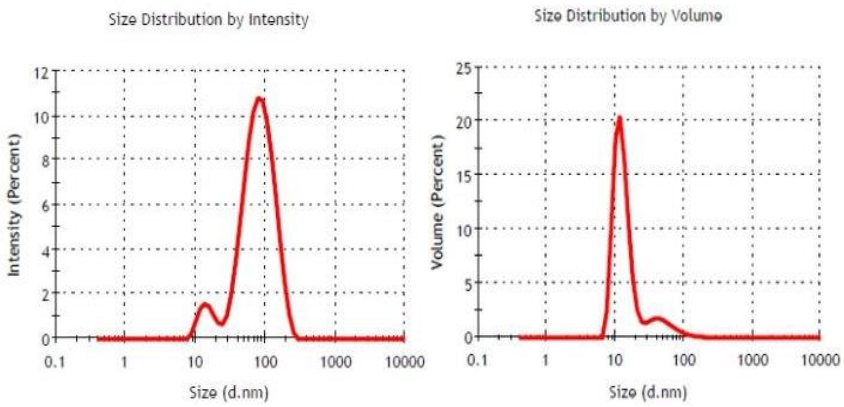

Figure 2
Particle size distribution by density and by volume

Zeta potential is an essential parameter for assessing the stability of nanofluids, which are defined

as liquid mixtures containing water and conductive solid particles with sizes typically below 100 nm [32,33]. Zeta potential is a crucial metric for evaluating the stability of metal nanoparticles in aqueous solutions because it reflects the overall charge present on the nanoparticles. The synthesized AgNPs have a negative charge, as indicated by their zeta potential value of -22.5 mV (Figure 3). This is significant because it implies that the nanoparticles are coated with biomolecules, which increases their stability through electrostatic repulsion. This helps keep the nanoparticles from aggregating and maintains their dispersion in solution [34].

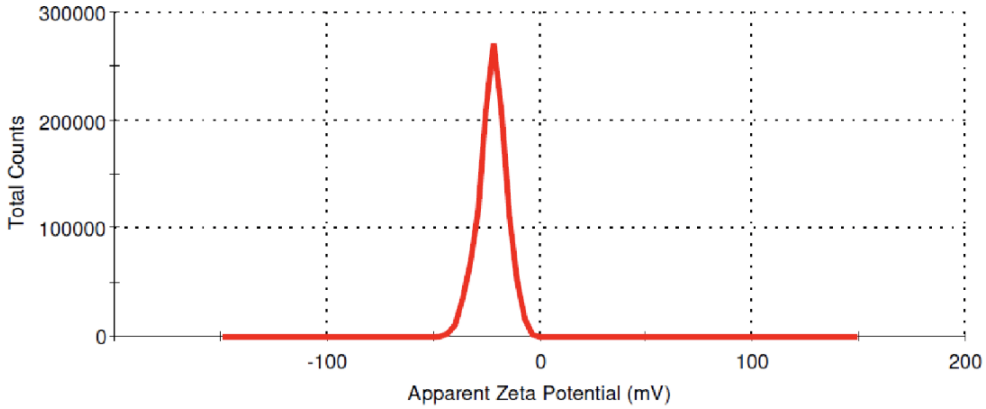

Figure 3
Zeta potential analysis of synthesized nanoparticles.

To investigate the morphology of the synthesized structures of graphene, GO and AgNPs, scanning electron microscopy (SEM) analyzes were carried out (Figure 4 and 6). The SEM examination provided insights into the overall structure of the materials.

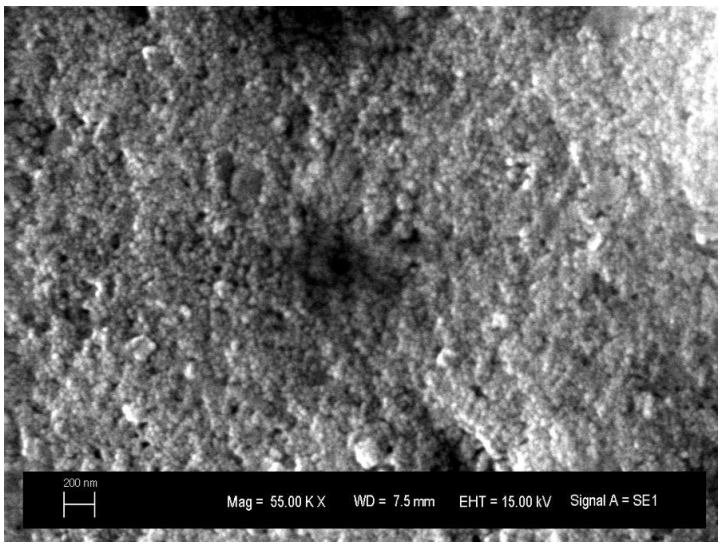

Figure 4
SEM image of silver nanoparticles.

Energy Dispersive Spectroscopy (EDS) analysis provides both qualitative and quantitative insights into the elemental composition of nanoparticles, which is crucial for understanding their formation and stability. The EDS spectrum for the synthesized AgNPs reveals a prominent signal around 3 keV, confirming the presence of silver. This peak is characteristic of metallic silver nanocrystals, which typically exhibit optical absorption peaks due to their surface plasmon resonance (SPR) [35]. Together with other elements, the presence of silver suggests that black pepper extract was used to create

the nanoparticles, where biomolecules might have helped stabilize them.

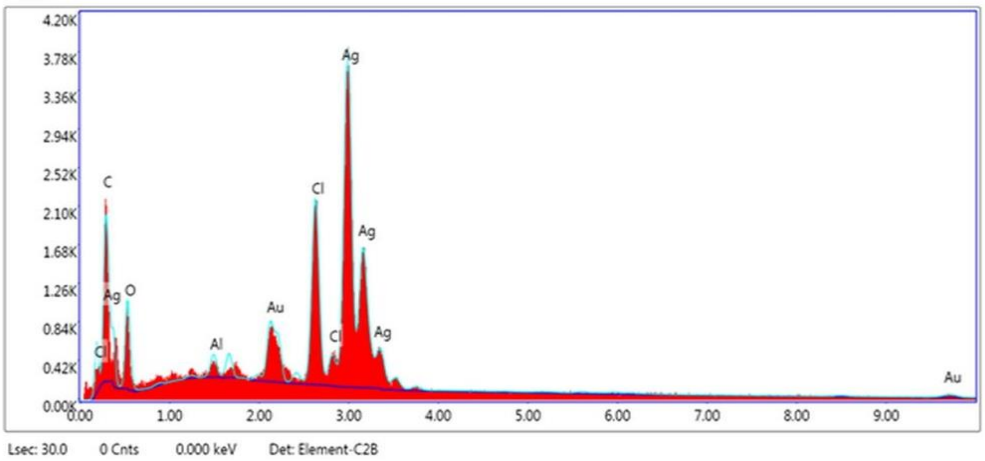

Figure 5

EDS analysis of silver nanoparticles

As shown in Figure 5, silver was the most prevalent element in the EDS analysis, making up roughly 56.2% of the total composition. Cl, O, Al, and Au were among the other elements that were observed with Ag. The coating is responsible for the Au peaks in the spectrum, while plant extract may be the source of other elements. This high silver content is noteworthy because it shows that AgNPs were successfully synthesized.

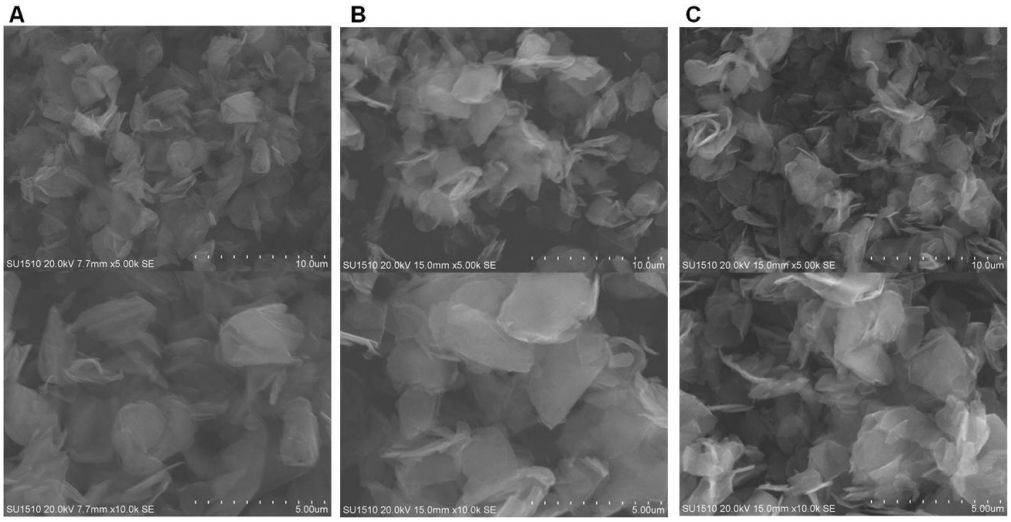

Figure 6

SEM images of A) graphene 1, b) graphene 2 and c) graphene oxide structures

In Figure 6, two distinct structures of graphene and graphene oxide are depicted through scanning electron microscopy (SEM) images. These images illustrate the unique morphological characteristics of each material. The SEM images clearly demonstrated that both graphene oxide and graphene have been effectively exfoliated to form separated thin sheets.

In this study, the antibacterial activities of several structures such as GO, G1, G2, AgNPs, GO+AgNPs, G1+AgNPs and G2+AgNPs against *Staphylococcus aureus* at a concentration of 100 µg/mLwas evaluated. Gentamicin was employed as a positive control in the experiment.

The investigation into the antibacterial properties of GO and AgNPs reveals significant findings

regarding their individual and combined effects. The inhibition zone measured for GO was recorded at 9.90 ± 0.85 mm, while AgNPs exhibited a larger inhibition zone of 12.37 ± 0.75 mm. Notably, when GO and AgNPs were combined in equal proportions and maintained at the same concentration, the resulting inhibition zone increased to 14.40 ± 1.08 mm. This increase suggests a synergistic effect between GO and AgNPs, which is not typically observed with other graphene-based materials (Figure 7 and 8).

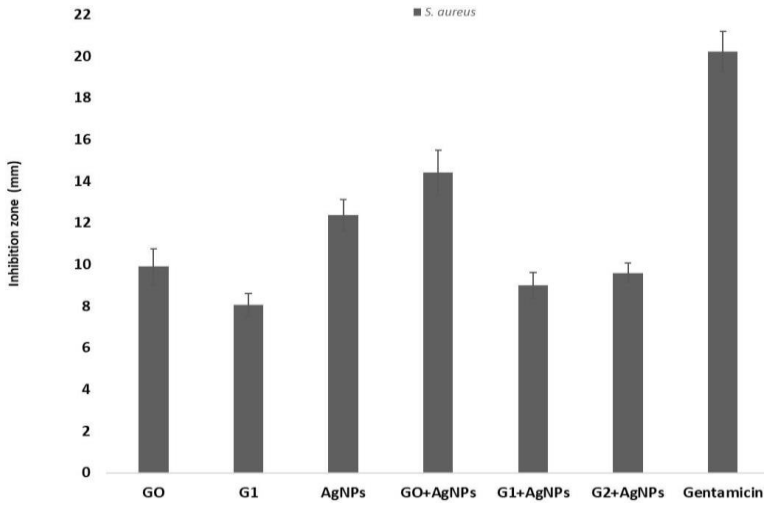

Figure 7
Inhibition zones of the materials used against S. aureus

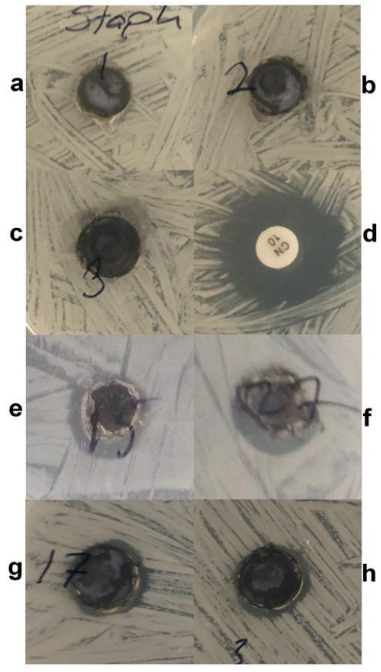

Figure 8
Antibacterial activity of synthesized silver nanoparticles and graphene structures a) GO b)G1 c)G2 d)Gentamicin e)AgNP f)GO+AgNP g) G1+AgNP h) G2+AgNP

The combination of graphite oxide and AgNPs demonstrated strong antibacterial activity, according to the results. Additionally, it was discovered that structures based on graphene have unique antibacterial properties. In recent times, there has been a concerning rise in the resistance of pathogenic bacteria and fungi to commercially available antimicrobial agents, posing a significant global threat. Drug resistance represents one of the most critical and prevalent challenges [36]. The treatment of bacterial infections is becoming increasingly complicated, as pathogens are capable of developing resistance to current antimicrobial agents and antibiotics. Furthermore, resistant pathogens have the potential to disseminate within healthcare settings and communities, leading to broader issues related to infection control [37]. To address this issue, innovative methods and strategies are essential. Promising approaches include the utilization of natural antimicrobials, combination therapies, synergistic treatments, and more recently, the application of metal nanoparticles in composite structures [38]. Numerous studies have confirmed that silver-graphene-based nanocomposites have antimicrobial properties. For example, graphene oxide-silver (GO-Ag) nanocomposites have shown antibacterial qualities against a number of pathogens [39] . Graphene oxide-silver nanoparticles (GO-AgNPs) have been shown to exhibit antibacterial activity due to a synergistic effect rather than just the additive effects of bare GO and AgNPs [40].

Antioxidant substances can neutralize radicals present in the environment. Among them, DPPH radical (2,2-diphenyl-1-picrylhydrazyl) is widely used due to its easy measurement, stability, simplicity and reproducibility in assessing radical scavenging activity by observing discoloration [41]. The DPPH radical provides a tool to measure the antioxidant efficacy of different compounds by assessing their potential to act as hydrogen donors or free radical scavengers. In this study, to determine the radical scavenging activity of the materials, we used the DPPH radical, which has a maximum absorption at 517 nm.

Table 1

Antioxidant activity (DPPH free radical scavenging activity)

	IC50 (µg/mL)
Trolox	5.77±0.11
BHA	4.89±0.15
BHT	7.65±0.16
GO	ND
G1	ND
G2	ND
AgNP	83.51±1.37
GO+ AgNP	161.,33±1.99
G1+ AgNP	183.23±1.23
G2+ AgNP	350.84±3.89

A higher level of antioxidant activity was indicated by a lower IC50 value. AgNPs produced by biosynthesis notably exhibited the highest scavenging activity (83.51 µg/mL) (Table 1). Compared to positive controls, this value was much lower. According to the DPPH scavenging analysis, AgNPs showed significant inhibitory activity compared to common antioxidants such as Trolox, BHA (butylated hydroxyanisole) and BHT (butylated hydroxytoluene), although this activity decreased, especially when graphene-based materials were present. Additionally, graphene structures were found to have no inherent radical scavenging activity.

As indicated in Table 2, the antioxidant effect of graphene materials, measured by their Ferric Reducing Antioxidant Power (FRAP) reduction capacity, was significantly lower compared to the standard antioxidants BHT and BHA.

Table 2
Ferric reducing power (FRAP) activity

	µmol TE/mg sample
BHA	5.36±0.16
BHT	3.96±0.12
GO	0.26±0.03
G1	0.57±0.06
G2	0.62±0.08
AgNP	3.46±0.18
GO+AgNP	2.26±0,21
G1+AgNP	2.38±0.15
G2+AgNP	2.25±0.08

Table 3
ABTS+ Radical Removal Activity

	IC50 (µg/mL)
Trolox	6.54±0.15
BHA	5,87±0.18
BHT	6.12±0.23
GO	139.82±1.23
G1	162.09±2.45
G2	184.74±2.57
AgNP	5.74±0.14
GO+AgNP	23.64±0.15
G1+AgNP	16.12±0.12
G2+AgNP	18.64±0.13

The ABTS assay is a commonly used technique to assess the antioxidant properties of natural substances, particularly by measuring their ability to eliminate the stable radical action ABTS [42]. AgNPs were observed to have a notably high level of activity (Table 3). However, this activity was noticeably reduced when graphene structures were coupled with AgNPs.

Several studies have demonstrated that AgNPs contribute the reduction of ferric ions and stabilizes free radicals, so they increase the overall antioxidant capacity of composite materials [43,44], as correspondence to our findings. Moreover, it was also reported that graphene and AgNPs show a synergistic effect, where graphene matrix aids in the dispersion and stabilization of AgNPs, leading to increased catalytic and antioxidant activities [44,45]. In addition to their antioxidant capabilities, the antibacterial properties of GO-AgNPs further complement their potential applications in medical and environmental fields. The antibacterial action is primarily due to the oxidative stress induced by silver nanoparticles, which can damage bacterial cell walls, while graphene oxide contributes to this effect through its ability to generate reactive oxygen species [46,47]. This dual functionality of GO-AgNPs not only enhances their utility as antioxidant agents but also positions them as effective antimicrobial agents, making them suitable for various biomedical applications, including wound dressings and drug delivery systems [47,48].

CONCLUSION

In this study, composite structures obtained by combining AgNPs biologically synthesized from black pepper extract and GO structures have great potential, especially in terms of antibacterial properties. The study showed that the synergistic combination of AgNPs and GO significantly increased

antibacterial activity against *Staphylococcus aureus*. In this study, the antioxidant capacity of biologically synthesized AgNPs was found to be higher than that of GO structures. However, the combination of AgNPs with GO structures had a negative impact on the antioxidant capacity and a decrease in this capacity was observed. While the combination of AgNPs and GO nanocomposites increases antibacterial effectiveness, reducing antioxidant properties may affect long-term material performance. It is believed that such nanocomposites can contribute to the development of more biocompatible, durable and infection-resistant materials such as dental materials. Combining GO nanocomposites with AgNPs may make it possible to create dental materials that are both mechanically robust and biologically compatible.

Ethical Statement

This study was derived from a part of Master's thesis “Synthesis of grafphene oxide-silver nanoparticle composite structures, investigation of antibacterial and antioxidant properties”, presented by Selim Işıldak under the supervision of Prof. Dr. Mahfuz Elmastaş.

Author Contributions

Research Design (CRediT 1) S.I. (%50) - M.E. (%50)
Data Collection (CRediT 2) S.I. (%50) - M.E. (%30) - B.S.E. (%10) - M.E. (%10)
Research - Data Analysis - Validation (CRediT 3-4-6-11) S.I. (%50) - M.E. (%30) - B.S.E. (%10) - M.E. (%10)
Writing the Article (CRediT 12-13) S.I. (%60) - M.E. (%20) - B.S.E. (%10) - M.E. (%10)
Revision and Improvement of the Text (CRediT 14) S.I. (%40) - M.E. (%40) - B.S.E. (%10) - M.E. (%10)

Financing

This research was not supported by any public, commercial, or non-profit organization.

Conflict of Interest

The authors declare no conflict of interest.

REFERENCES

[1] A. Albanese, P.S. Tang, W.C.W. Chan, The effect of nanoparticle size, shape, and surface chemistry on biological systems, *Annual Review of Biomedical Engineering*. 14 (2012), 1-16.

[2] R. V Bordiwala, Green synthesis and Applications of Metal Nanoparticles.- A Review Article, *Results in Chemistry*. 5 (2023) 100832. doi:https://doi.org/10.1016/j.rechem.2023.100832

[3] X. Li, B. Li, R. Liu, Y. Dong, Y. Zhao, Y. Wu, Development of pH-responsive nanocomposites with remarkably synergistic antibiofilm activities based on ultrasmall silver nanoparticles in combination with aminoglycoside antibiotics, *Colloids and Surfaces B: Biointerfaces*. 208 (2021), 112112. doi:https://doi.org/10.1016/j.colsurfb.2021.112112

[4] F. Erci, R. Cakir-Koc, I. Isildak, Green synthesis of silver nanoparticles using *Thymbra spicata* L. var. *spi*cata (zahter) aqueous leaf extract and evaluation of their morphology-dependent antibacterial and cytotoxic activity, *Artificial Cells, Nanomedicine, and Biotechnology*. 46 (2018), 150-158. doi:10.1080/21691401.2017.1415917

[5] M. Khubchandani, N. Thosar, S. Dangore–Khasbage, R. Srivastava, Applications of silver nanoparticles in pediatric dentistry: An overview, *Cureus*. 14(7) (2022), e26956. doi:10.7759/cureus.26956

[6] C.B. Girón, J.F.H. Sierra, I. DeAlba-Montero, M.A. Urbano-Peña, F. Ruíz, therapeutic use of silver nanoparticles in the prevention and arrest of dental caries, *Bioinorganic Chemistry and Applications*. 2020 (2020), 1-7. doi:10.1155/2020/8882930

[7] I.X. Yin, J. Zhang, I.S. Zhao, M.L. Mei, Q. Li, C.H. Chu, The antibacterial mechanism of silver nanoparticles and ıts application in dentistry, *International Journal of Nanomedicine*. 15 (2020), 2555-2562. doi:10.2147/ijn.s246764

[8] S. Sakhamuri, S.L. Kotha, A.R.G.M. AlAsmari, G.H. AlJefri, F.N. Almotawah, S.K. Mallineni, R. Sajja, Silver nanoparticles in dental applications: A descriptive review, *Bioengineering*. 10 (2023), 327. doi:10.3390/bioengineering10030327

[9] C.B. Girón, J. Mariel-Cárdenas, M. Pierdant-Pérez, J.F. Hernández-Sierra, J.E. Morales-Sánchez, F. Ruíz, Effectiveness of a combined silver nanoparticles/fluoride varnish in dental remineralization in children: ın vivo study, *Superficies Y Vacío*. 30 (2017), 21-24. doi:10.47566/2017_syv30_1-020021

[10] A.-S. Neculai-Valeanu, B.-M. Madescu, I. Porosnicu, A.-M. Ariton, Effect of various environmentally friendly reducing agents on the antioxidant activity of green synthesized silver nanoparticles, *Life Science and Sustainable Development*. 3 (2022), 49-53. doi:10.58509/lssd.v3i2.206

[11] B. Essghaier, R. Dridi, F. Mottola, L. Rocco, M.F. Zid, H. Hannachi, Biosynthesis and characterization of silver nanoparticles from the extremophile plant *Aeonium haworthii* and their antioxidant, antimicrobial and anti-diabetic capacities, *Nanomaterials*. 13 (2022), 100. doi:10.3390/nano13010100

[12] T. Barot, D. Rawtani, P. Kulkarni, Physicochemical and biological assessment of silver nanoparticles ımmobilized halloysite nanotubes-based resin composite for dental applications, *Heliyon*. 6 (2020), e03601. doi:10.1016/j.heliyon.2020.e03601

[13] E.S. Allehyani, Surface Functionalization of polyester textiles for antibacterial and antioxidant properties, *Polymers*. 14 (2022), 5512. doi:10.3390/polym14245512

[14] S. Ghosh, S.D. Patil, M. Ahire, R. Kitture, S.P. Kale, K. Pardesi, S.S. Cameotra, J. Bellare, D.D. Dhavale, A.M. Jabgunde, B.A. Chopade, Synthesis of silver nanoparticles using *Dioscorea bulbifera* tuber extract and evaluation of its synergistic potential in combination with antimicrobial agents, *International Journal of Nanomedicine*. (2012), 483. doi:10.2147/ijn.s24793

[15] F. Hong, P. Chen, Y.U. Xue-fen, Q. Chen, The Application of silver to decontaminate dental unit waterlines—a systematic review, *Biological Trace Element Research*. 200 (2022), 4988-5002. doi:10.1007/s12011-022-03105-w

[16] H.Y.Y. Kuşçu, Utilization of nanomaterials in prosthetic dental treatment, *HRU International Journal of Dentistry and Oral Research*. (2023). doi:10.61139/ijdor.1270852

[17] H. Mohammed, A. Kumar, E. Bekyarova, Y. Al-Hadeethi, X. Zhang, M. Chen, M.S. Ansari, A. Cochis, L. Rimondini, Antimicrobial mechanisms and effectiveness of graphene and graphene-functionalized biomaterials. A scope review, *Frontiers in Bioengineering and Biotechnology*. 8 (2020), 465.

[18] S. Liu, T.H. Zeng, M. Hofmann, E. Burcombe, J. Wei, R. Jiang, J. Kong, Y. Chen, Antibacterial activity of graphite, graphite oxide, graphene oxide, and reduced graphene oxide: Membrane and oxidative stress, *Acs Nano*. 5 (2011), 6971-6980. doi:10.1021/nn202451x

[19] X. Wang, P. Lü, Y. Li, H. Xiao, X. Li, Antibacterial activities and mechanisms of fluorinated graphene and guanidine-modified graphene, *RSC Advances*. 6 (2016), 8763-8772. doi:10.1039/c5ra28030c

[20] J. Li, G. Wang, H. Zhu, M. Zhang, X. Zheng, Z. Di, X. Liu, X. Wang, Antibacterial activity of large-area monolayer graphene film manipulated by charge transfer, *Scientific Reports*. 4 (2014). doi:10.1038/srep04359

[21] V.P. Veeraraghavan, Fabrication, Characterization, Antibacterial and biocompatibility studies of graphene oxide loaded alginate chitosan scaffolds for potential biomedical applications, *Texila International Journal of Public Health*. (2023), 77-85. doi:10.21522/tijph.2013.se.23.01.art009

[22] J. Chen, H. Peng, X. Wang, F. Shao, Z. Yuan, H. Han, Graphene oxide exhibits broad-spectrum antimicrobial activity against bacterial phytopathogens and fungal Conidia by intertwining and membrane perturbation, *Nanoscale*. 6 (2014), 1879-1889. doi:10.1039/c3nr04941h

[23] Y. Qiu, Z. Wang, A.C.E. Owens, I. Külaots, Y. Chen, A.B. Kane, R.H. Hurt, Antioxidant chemistry of graphene-based materials and its role in oxidation protection technology, *Nanoscale*. 6 (2014), 11744-11755. doi:10.1039/c4nr03275f

[24] B. Kaczmarek-Szczepańska, M. Michalska-Sionkowska, P. Binkowski, J.P. Łukaszewicz, P. Kamedulski, 3d-structured and blood-contact-safe graphene materials, *International Journal of Molecular Sciences*. 24 (2023), 3576. doi:10.3390/ijms24043576

[25] Z. Chen, J. Zhao, J. Qiao, W. Li, Z. Guan, Z. Liu, X. Bai, B. Xing, J. Zhang, J. Li, W. Yin, H. Zhu, Graphene-mediated antioxidant enzyme activity and respiration in plant roots, *Acs Agricultural Science & Technology*. 2 (2022), 646-660. doi:10.1021/acsagscitech.2c00074

[26] M.S. Blois, Antioxidant determinations by the use of a stable free radical, *Nature*. 181 (1958), 1199-1200.

[27] M. Oyaizu, Studies on products of browning reaction antioxidative activities of products of browning reaction prepared from glucosamine, *The Japanese Journal of Nutrition and Dietetics*. 44 (1986), 307-315.

[28] M. Elmastaş, I. Gülçin, Ö. Işildak, Ö.İ. Küfrevioğlu, K. İbaoğlu, H.Y. Aboul-Enein, Radical scavenging activity and antioxidant capacity of bay leaf extracts, *Journal of the Iranian Chemical Society*. 3 (2006), 258-266.

[29] R. Re, N. Pellegrini, A. Proteggente, A. Pannala, M. Yang, C. Rice-Evans, Antioxidant activity applying an improved ABTS radical cation decolorization assay, *Free Radical Biology and Medicine*. 26 (1999), 1231-1237.

[30] M.A. Noginov, G. Zhu, M. Bahoura, J. Adegoke, C. Small, B.A. Ritzo, V.P. Drachev, V.M. Shalaev, The effect of gain and absorption on surface plasmons in metal nanoparticles, *Applied Physics B*. 86 (2007), 455-460.

[31] P. Makvandi, U. Josić, M. Delfi, F. Pinelli, V. Jahed, E. Kaya, M. Ashrafizadeh, A. Zarepour, F. Rossi, A. Zarrabi, T. Agarwal, E.N. Zare, M. Ghomi, T.K. Maiti, L. Breschi, F.R. Tay, Drug delivery (nano)platforms for oral and dental applications: Tissue regeneration, ınfection control, and cancer management, *Advanced Science*. 8 (2021). doi:10.1002/advs.202004014

[32] M.M. Sarafraz, F. Hormozi, Scale formation and subcooled flow boiling heat transfer of CuO–water nanofluid inside the vertical annulus, *Experimental Thermal and Fluid Science*. 52 (2014), 205-214.

[33] M.M. Sarafraz, S.M. Peyghambarzadeh, Nucleate pool boiling heat transfer to Al2O3-water and TiO2-water nanofluids on horizontal smooth tubes with dissimilar homogeneous materials, *Chemical and Biochemical Engineering Quarterly*. 26 (2012), 199-206.

[34] A. Ahmad, Y. Wei, F. Syed, K. Tahir, A.U. Rehman, A. Khan, S. Ullah, Q. Yuan, The effects of bacteria-nanoparticles interface on the antibacterial activity of green synthesized silver nanoparticles, *Microbial pathogenesis*. 102 (2017), 133-142.

[35] H.M.M. Ibrahim, Green synthesis and characterization of silver nanoparticles using banana peel extract and their antimicrobial activity against representative microorganisms, *Journal of Radiation Research and Applied Sciences*. 8 (2015), 265-275.

[36] M.M. Stevanović, S.D. Škapin, I. Bračko, M. Milenković, J. Petković, M. Filipič, D.P. Uskoković, Poly (lactide-co-glycolide)/silver nanoparticles: Synthesis, characterization, antimicrobial activity, cytotoxicity assessment and ROS-inducing potential, *Polymer*. 53 (2012), 2818-2828.

[37] F.C. Tenover, Mechanisms of antimicrobial resistance in bacteria, *The American journal of medicine*. 119 (2006), 3-10.

[38] K. He, Z. Zeng, A. Chen, G. Zeng, R. Xiao, P. Xu, Z. Huang, J. Shi, L. Hu, G. Chen, Advancement of Ag–graphene based nanocomposites: an overview of synthesis and its applications, *Small*. 14 (2018), 1800871.

[39] A.C.M. de Moraes, B.A. Lima, A.F. de Faria, M. Brocchi, O.L. Alves, Graphene oxide-silver nanocomposite as a promising biocidal agent against methicillin-resistant *Staphylococcus aureus*, *International Journal of Nanomedicine*. (2015), 6847-6861.

[40] J. Tang, Q. Chen, L. Xu, S. Zhang, L. Feng, L. Cheng, H. Xu, Z. Liu, R. Peng, Graphene oxide–silver nanocomposite as a highly effective antibacterial agent with species-specific mechanisms, *ACS Applied Materials & Interfaces*. 5 (2013), 3867-3874.

[41] İ. Gülçin, Antioxidant properties of resveratrol: A structure–activity insight, *Innovative Food Science & Emerging Technologies*. 11 (2010), 210-218.

[42] C.A. Rice-Evans, N.J. Miller, G. Paganga, Structure-antioxidant activity relationships of flavonoids and phenolic acids, *Free Radical Biology And Medicine*. 20 (1996), 933-956.

[43] N. Anwar, M. Shah, S. Saleem, H. Rahman, Plant mediated synthesis of silver nanoparticles and their biological applications, *Bulletin of the Chemical Society of Ethiopia*. 32 (2018), 469-479. doi:10.4314/bcse.v32i3.6

[44] I. Yaremchuk, T. Bulavinets, P. Stakhira, V. Fitio, Nanocomposite materials based on graphene, graphene oxide, and silver nanoparticles, *Information and Communication Technologies Electronic Engineering*. 3 (2023), 163-169. doi:10.23939/ictee2023.01.163

[45] A. Rahim, V.N. Ratnakaram, M.J.S. Al Musawi, M. Syam Sundar, A. Syed, K. Nitish, J.K. Monditoka, E.G. Grace, H. Subha, C. Basavaiah, B. Hari Babu, D. Ramachandran, Enhanced catalytic, antioxidant, and electrochemical properties of green-synthesized graphene-silver nanocomposite utilizing *Moringa oleifera* leaf extract, *ChemistrySelect*. 9 (2024), e202401848. doi:10.1002/slct.202401848

[46] I. Nasim, M. Shamly, K.K. Jaju, V. Vishnupriya, Z. Jabin, Antioxidant and anti-inflammatory activity of a nanoparticle based intracanal drugs, *Bioinformation*. 18 (2022), 450-454.

[47] M. Wierzbicki, S. Jaworski, E. Sawosz, A. Jung, G. Gielerak, H. Jaremek, W. Łojkowski, B. Woźniak, L. Stobiński, A. Małolepszy, A. Chwalibog, Graphene oxide in a composite with silver nanoparticles reduces the fibroblast and endothelial cell cytotoxicity of an antibacterial nanoplatform, *Nanoscale Research Letters*. 14 (2019). doi:10.1186/s11671-019-3166-9

[48] Y. Bao, C. Tian, H. Yu, J. He, K. Song, J. Guo, X. Zhou, O. Zhuo, S. Liu, In situ green synthesis of graphene oxide-silver nanoparticles composite with using gallic acid, *Frontiers in Chemistry*. 10 (2022). doi:10.3389/fchem.2022.905781

FEN ve MÜHENDİSLİK BİLİMLERİ DERGİSİ

Vol: 7 No: 1 Year: 2025 | Araştırma Makalesi/Research Article | e-ISSN: 2667-7989

https://doi.org/10.47112/neufmbd.2025.77

Yakın-Kızılötesinde Absorplayan, Karboksilik Asit ile Fonksiyonlandırılmış Tiyofen Kaynaşık BODIPY Bileşiklerinin Sentezi ve Özellikleri

Yusuf ÇAKMAK [1,2*]

[1] Necmettin Erbakan University, Faculty of Engineering, Department of Metallurgical and Materials Engineering, Konya, Türkiye

[2] Necmettin Erbakan University, Science and Technology Research and Application Center (BITAM), Konya, Türkiye

Makale Bilgisi

Geliş Tarihi: 02.03.2024
Kabul Tarihi: 31.08.2024
Yayın Tarihi: 30.04.2025

Anahtar Kelimeler:
BODIPY,
Boyar maddeler,
Boya duyarlı güneş pilleri,
Fotodinamik terapi,
Kimyasal sensörler.

ÖZET

Bor dipirrometen boyaları, kimyasal indikatörler, biyolojik etiketleme, fotodinamik terapi ve güneş pilleri gibi çeşitli alanlarda en önemli bileşik türlerinden biridir. Bu boyaların önemli türevlerinden biri de tiyofen ile kaynaşmış BODIPY yapılarıdır. Bu yapılar, yakın IR absorpsiyonu, ağır atomsuz ışığa duyarlılık ve kompakt yapı gibi özel özellikler kazandırır. Oldukça önemli özellikler barındırmalarına rağmen, bu boyar madde türevleri düşük sentetik verimlere sahip olabilmektedirler. Birkaç on yıl içinde, kaynaşmış BODIPY yapılarının çeşitli türevleri yayınlandı. Bununla birlikte, daha fazla özellikten yararlanmak ve sentetik verimi artırmak için bu boyaların sayısını artırmak için daha fazla çalışmaya ihtiyaç vardır. Bu çalışmada, CTFBOD1-2 olarak adlandırılan iki adet yakın kızılötesi bölgeden absorplama yapabilen tiyofen ile kaynaşmış Bodipy bileşikleri tasarlanmış, sentezlenmiş ve çeşitli teknikler kullanılarak karakterize edilmiştir. Her iki bileşik de mezo-4-karboksifenil birimleri ile türevlendirilmiştir, çünkü boya duyarlı güneş pili yapıları için potansiyel bileşik olma durumları vardır. Ve elektron verici yapıları olarak, bir donör-alıcı yapı oluşturmak için 4-metoksifenil ve hegziltiyofen birimleri de ayrıca sübstitüe edilmiştir. Fotofiziksel ve döngüsel voltametri karakterizasyonları da gerçekleştirilmiştir. Hegzil-tiyofen bağlı yapıda (CTFBOD2), muhtemelen tiyofen biriminin daha güçlü elektron itme kabiliyetine bağlı olarak hem absorpsiyon hem de emisyonda daha fazla batokromik kayma gözlemlenmiştir. Bu yapı ile 775 nm'ye kadar absorplama gözlenebilmekte ve güneş hasadı için kompakt yapılarla bu pencereye ulaşmak son derece önemlidir. Bileşiklerin, ışığa duyarlılaştırıcı olarak boya duyarlı güneş pili konsepti gibi çeşitli alanlarda yapı taşları olarak kullanılabileceği gözlemlenmiştir.

Synthesis and Properties of Carboxylic Acid Functionalized Near IR Absorbing Thiophene Fused BODIPY Compounds

Article Info

Received: 02.03.2024
Accepted: 31.08.2024
Published: 30.04.2025

Keywords:
BODIPY,
Chemosensors,
Dyes,
Dye sensitized solar cell,
Photodynamic therapy.

ABSTRACT

Boron dipyrromethene dyes are one of the most important types of compounds in various fields such as chemical indicators, biological labelling, photodynamic therapy, and solar cells. One of the important derivatives of these dyes are the thiophene-fused BODIPY structures. These structures impart special features such as near IR absorption, heavy atom free photosensitization and compact structure. Although having important aspects, these derivatives of dyes suffer from low synthetic yields. In a few decades various derivatives of fused BODIPY structures were published. However, still more studies are needed to increase the number of these dyes in order to exploit more features and increase the synthetic yields. In the current work, two near-infrared absorbing thiophene fused Bodipy compounds, named CTFBOD1-2, were designed, synthesized and characterized using various techniques. Both compounds were substituted with *meso*-4-carboxyphenyl units since we have investigated their potential for dye-sensitized solar cell structures. And as electron donor structures, 4-methoxyphenyl and hexylthiophene units were attached to form a donor-acceptor structure. Photophysical and cyclic voltammetry characterizations were also accomplished. In the hexyl-thiophene attached structure (CTFBOD2) we have observed more bathochromic shift in both absorption and emission probably due to the stronger electron pull ability of the thiophene unit. With this structure up to 775 nm absorption is observed, and it is highly important to reach this window with compact structures for solar harvesting. We have observed that the compounds could have been investigated as building blocks in various fields such as dye-sensitized solar cell concept as a photosensitizer.

To cite this article:
Çakmak, Y. (2025). Synthesis and properties of carboxylic acid functionalized near IR absorbing thiophene fused BODIPY compounds. *Necmettin Erbakan University Journal of Science and Engineering*, *7*(1), 92-102. https://doi.org/10.47112/neufmbd.2025.77

***Corresponding Author:** Yusuf Çakmak, *yusuf.cakmak@erbakan.edu.tr*

INTRODUCTION

The research on BODIPY (boron dipyrromethene) compounds and similar dye structures continue its popularity for a few decades and steadily find more space in literature over the years. Valuable properties of this kind of dye include high molar absorptivity, high fluorescence quantum yield, stability, and moderately easily modifiable structure [1]. A variety of different reactions could be performed on the BODIPY core either post- or pre-modification routes [2]. There have been various efforts to obtain near IR absorbing or fluorescing dyes/fluorophores [3-7]. Xanthene, rhodamine, and fluorescein are some of the important classes of compounds and their derivatives are also made available to work in this region. The dyes working in near IR region have found utilization in organic or bulk heterojunction solar cells [4, 8-10], photodynamic cancer therapy[11-13], or biological labelling [14, 15]. The reason for the utilization of near IR dyes in solar cells is due to a large amount of the solar radiation in this region. Traditional [16] (e.g. silicon-based solar cells) or new generation [17] (e.g. dye-sensitized solar cells) renewable energy sources play important roles to meet the high energy demand in today's world. Also, fluorescence detection methods have been frequently used in various fields such as the authentication of extra virgin olive oils [18].

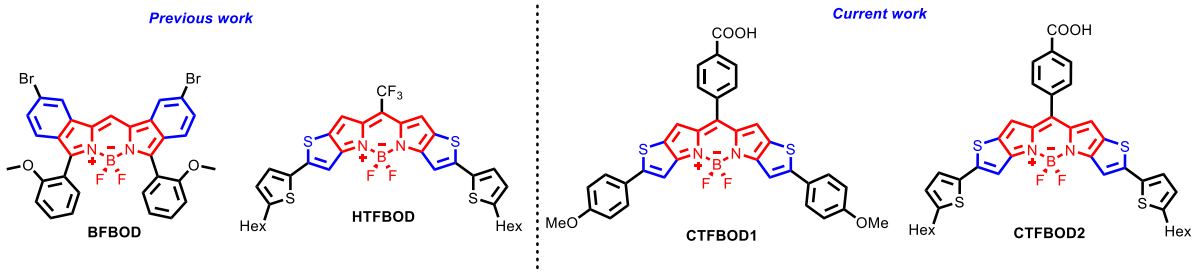

Figure 1

Fused BODIPY structures that were studied by our group previously (left) and in this current work (right). Nomenclature of BODIPY was also shown on BFBOD

BODIPY compounds could be post-modified for their utilization in the near-infrared regions including Knoevenagel condensation to obtain π electron extension from the methyl units, direct substitution with ethynyl units and C=N bond substitution [2]. Pre-modification includes synthesizing benzofused, thiophene-fused or furan-fused pyrroles and then the formation of the BODIPY core using these building blocks has been accomplished [3, 19, 20]. However, there are not many publications regarding the synthesis and applications of these fused structures, although they induce rich properties in the dye core. These properties include a rigid structure, high molar absorptivity and high fluorescence quantum yield. One drawback of these types of structures is their low synthetic yields.

In this work, two new thiophene fused BODIPY structures have been designed and synthesized (Figure 1-right). The structures of our previous efforts on fused BODIPY structures were also shown as a comparison (Figure 1-left) [3, 5]. These compounds have been synthesized with benzocarboxylic acid units arranged to the *meso* position of the BODIPY core for their potential utilization in dye sensitized solar cells concept. Different synthetic pathways have been investigated and the optimum synthetic path was considered to obtain the final compounds. The synthesized structures CTFBOD1 and CTFBOD2 both absorb around 700 nm making them available to be used in applications that necessitate near infrared region absorption or fluorescence. It has also been observed that carboxylic acid unit has an adverse effect on synthetic yields.

MATERIALS AND METHODS

Cyclic Voltammetry Measurements

Cyclic voltammetry was recorded on a Gamry Interface 1010E instrument in a single-component cell under a nitrogen atmosphere. 0.1 M tetrabutylammonium hexafluorophosphate in acetonitrile was used as an electrolyte was purged with nitrogen gas. Ag wire as reference electrode, Pt wire as auxiliary electrode and glassy carbon electrode as working electrode were used. Scanning range was between -1700 mV and +1700 mV and the scanning rate of 200 mV/s was adjusted. BODIPY compounds were dissolved in $CHCl_3$ (1 mg/mL) and they were added to the glassy carbon electrode surface and dried with nitrogen gas. As internal standard ferrocene was used and added to the electrolyte solution. For the calculations of optical bandgap, the equation of $E_g = 1243/\lambda$ (λ = start of the maximum absorbance) was used [21]. For the calculation of the HOMO-LUMO following equations were used [21]:

$$E_{LUMO} = -e.[E_{red}^{onset} + 4.4] \; ; \; E_{HOMO} = -e.[E_{ox}^{onset} + 4.4]$$

Synthesis

Compound 1: This reaction is performed according to the previous report [19]. 5-bromo-2-thiophencarboxaldehyde (1.88 g, 9.86 mmol, 1 eq.) was dissolved in methanol (10 mL) and cooled to 0°C. Methylazidoacetate (3.82 g, 29.6 mmol, 3 eq.) was then added to the flask. Sodium methoxide (1.6 g, 29.6 mmol, 3 eq.) suspension was prepared in methanol (30 mL) and added dropwise to the reaction flask over 20 minutes while keeping the temperature low. It was stirred for another 30 minutes, and brought to room temperature, then stirred for 3 h in this way. Then, the saturated NH_4Cl solution was added dropwise to form the precipitate, and the precipitate was filtered, washed with water, and dried. This substance was dissolved in 30 mL of toluene and refluxed for 1.5 hours. The substance was obtained pure by the removal of the solvent (22% yield). ^{1}H NMR 400 MHz, $CDCl_3$, ppm: (d) 9.25 (br s, 1H), 7.1-6.9 (m, 2H), 3.90 (s, 3H).

Compound 2: This reaction is performed according to the previous report [19]. 4-(Methoxy)phenylboronic acid (0.180 g, 1.18 mmol, 1.1 eq.), compound **1** (0.280 g, 1.08 mmol, 1 eq.) were dissolved in degassed toluene (10 mL) and ethanol (2.5 mL) under inert atmosphere to an oven-dried two-neck flask fitted with a condenser. Tetrakis(triphenylphosphine)-palladium (0.016 g, 0.022 mmol, 0.02 eq) and Na_2CO_3 solution (0.045 g in 2.5 mL H_2O) were added. The mixture was refluxed for 6 hours at 80°C, and then cooled, extracted with diethyl ether, dried over magnesium sulfate and concentrated under reduced pressure. The residue was purified by chromatography (silica gel, DCM) to afford **2** (80 mg, 26 %) as a yellow solid. ^{1}H NMR 400 MHz, $CDCl_3$, ppm: (d) 9.14 (br s, 1H), 7.54 (d, J= 8.6 Hz, 2H), 7.12 (s, 1H), 7.06 (s, 1H), 6.93 (d, J= 8.6 Hz, 2H), 4.36 (q, J= 7.2 Hz, 2H), 3.85 (s, 3H), 1.40 (t, J= 7.1 Hz, 3H).

Compound 3: This reaction is performed by modification of the previous report [22]. **2** (0.380 g, 1.32 mmol, 1 eq.) is dissolved in 22.5 mL of EtOH. Then, NaOH (1.11 g, 21 eq., 27.8 mmol) was dissolved in 11.3 mL of H_2O and added to the flask. The reaction was refluxed and the proceeding of the reaction was monitored using TLC for 1-2 hours. The flask was then cooled to room temperature and the pH was adjusted to 3 through addition of 6 M HCl. Then, the precipitates were filtered and substance **3** was obtained pure (0.336 g, 1.32 mmol, quantitative). ^{1}H NMR 400 MHz, DMSO-d_6, ppm: (d) 12.55 (br s, 1H), 11.97 (br s, 1H), 7.60 (m, 2H), 7.25 (s, 1H), 6.99 (m, 3H), 3.76 (s, 3H).

Compound 4: This reaction is performed by modification of the previous report [22]. Compound **3** (0.336 g, 1.23 mmol) was dissolved in TFA (7 mL, degassed with N_2) under N_2 gas. The reaction was heated to 40°C. After 10 minutes, the reaction was checked with TLC and neutralized with saturated sodium bicarbonate. Then, chloroform was added (10 mL) and the organic phase was washed with water

(3x10 mL). The organic phase was dried, and the solvent was removed. Column chromatography is performed with DCM, resulting in 51.4 mg of pure substance (18% yield). ^{1}H NMR 400 MHz, $CDCl_3$, ppm: (d) 8.25 (br s, 1H), 7.55 (d, J= 8.7 Hz, 2H), 7.1 (s, 1H), 6.97 (m, 1H), 6.92 (d, J=8.7 Hz, 2H), 6.46 (m, 1H), 3.83 (s, 3H). HRMS)$^+$; $(M)^+$ $C_{13}H_{12}NOS^+$ calculated for 230.0634, found 230.0658.

***Compound CTFBOD1*:** Dichloromethane (25 mL) was degassed with N_2 gas for 15 minutes. Then, 4 drops of trifluoroacetic acid (TFA) are added. Compound **4** (0.050 g, 0.22 mmol) and 4-formylbenzoic acid (0.017 g, 0.11 mmol) were added to the flask and left to stir overnight at room temperature. DDQ (0.025 g, 0.11 mmol) was then added to the solution. After stirring for 2 hours at room temperature, 0.3 mL of triethylamine and 0.3 mL of boron trifluoride diethyl ether were added, and the formation of green colour was observed. The reaction was added DCM (20 mL) and washed with water (3x20 mL). The organic layer is collected, dried and evaporated to dryness under reduced pressure. The purification of compound **CTFBOD1** was accomplished using silica gel flash column chromatography (5% MeOH/DCM) and the product was obtained pure in 31% yield (22 mg, dark green color). ^{1}H NMR 400 MHz, $CDCl_3$, ppm: (d) 8.25 (d, J= 6.6 Hz, 2H), 7.8-7.6 (m, 6H), 7.40 (s, 2H), 6.97 (d, J= 8.4 Hz, 4H), 6.76 (s, 2H), 3.87 (s, 6H). HRMS; $(M)^-$ 635. 1088 calculated for $C_{34}H_{22}BF_2N_2O_4S_2^-$, found 635.10540.

Compound 5: This reaction is performed according to the previous report [8]. 2,2'-bitiophene (2.0 g, 12.03 mmol, 1 eq.) was dissolved in 10 mL of benzene and cooled to 0°C. Hexanoyl chloride (1.7 mL, 12.51 mmol, 1.04 eq.) and $SnCl_4$ (1.4 mL; 12.87 mmol; 1.07 eq.) were added to the reaction mixture and stirred at 0°C under N_2 atmosphere for 15 min. Then the reaction was added ice and extracted with DCM. The organic phase was then extracted with $NaHCO_3$. Afterwards, the organic layer was collected, dried with Na_2SO_4, and the solvent was removed under reduced pressure. In the second part of the process 2.74 g (6 eq.; 72.18 mmol) of $LiAlH_4$ and 2.4 g (1.5 eq.; 18.05 mmol) of $AlCl_3$ in Et_2O (30 mL) were dissolved. The dried substance from the first part was dissolved in 12 mL of toluene and two solutions were combined. Then the flask was stirred at RT for 1 hour. Then, 10 mL of EtOAc and 20 mL of 6 M HCl were added to the flask. The organic phase was extracted with Et_2O, collected, dried with Na_2SO_4 and removed under reduced pressure. Compound **5** was used in the next step without any further purification (75% yield) ^{1}H NMR 400 MHz, $CDCl_3$, ppm: d 7.15 (dd, J = 1.1 Hz; 5.1 Hz, 1H), 7.08 (dd, J=1.1 Hz; 3.7 Hz, 1H), 6.95-7.00 (m, 2H), 6.65 (m, 1H), 2.78 (m, 2H), 1.66 (m, 2H), 1.2-1.5 (m, 6H), 0.88 (m, 3H).

Compound 6: This reaction is performed according to the previous report [8]. 1.02 mL (1.2 eq.; 10.89 mmol) of $POCl_3$ was added to 7 mL of DMF at 0 °C. The mixture was stirred for 1 h until it reached to RT. 2.27 g (1 eq.; 9.08 mmol) of 5-Hexyl-2,2'-bitiophene **5** was added to the reaction mixture and stirred overnight at 60°C. Then, 150 mL of ice-water was added to the reaction mixture and the pH value of the reaction was adjusted to around 7 using NaOH solution. Et_2O (30 mL) was added, and the organic layer was washed 3 times with deionized water. Then it was dried with Na_2SO_4, and the solvent was removed under reduced pressure. The crude mixture was then purified using silica gel column chromatography (Petroleum ether: EtOAc, 6/1), and the yield was calculated as 77%. ^{1}H NMR 400 MHz, $CDCl_3$, ppm: δ 9.83 (m, 1H), 7.65 (m, 1H), 7.17 (m, 2H), 6.75 (m, 1H), 2.81 (m, 2H), 1.68 (m, 2H), 1.1-1.5 (m, 6H), 0.88 (t, J= 5.0 Hz, 3H).

Compound 7: 5'-Hexyl-[2,2'-bitiophene]-5-carbaldehyde **6** (1.0 g, 3.58 mmol, 1 eq.) was dissolved in anhydrous ethanol (30 mL, molecular sieve dried) at RT. Ethylazidoacetate (1.85 g, 14.3 mmol, 4 eq.) was added and stirred at 0°C under N_2 atmosphere for 20 min. 0.774 g (4 eq.; 14.3 mmol) of NaOMe (dissolved in 6 mL dry ethanol) was added dropwise at 0°C for 20 min. The reaction mixture was stirred at this temperature for 30 minutes and stirring was continued at RT for 2 hours. The progress of the reaction was monitored using TLC, and 10 mL of saturated NH_4Cl solution was added to the

reaction medium as soon as the starting material did not appear in TLC. The solid substance formed was then filtered and dissolved in 30 mL of toluene and refluxed for 1.5 hours. After evaporating the solvent, the mixture was submitted to silica gel column chromatography (Pet. Ether: EtOAC, 6/1). Compound **7** was then obtained in 56% yield. ^{1}H NMR 400 MHz, $CDCl_3$, ppm: (δ) 9.02 (br s, 1H), 7.07 (m, 1H), 7.03 (m, 1H), 6.96 (m, 1H), 6.70 (m, 1H), 3.90 (s, 3H), 2.81 (m, 2H), 1.67 (m, 2H), 1.1-1.5 (m, 6H), 0.90 (m, 3H).

Compound 8: Compound **7** (0.333 g, 0.958 mmol, 1 eq.) was dissolved in ethanol (16 mL). In another flask NaOH (0.804 g, 20.1 mmol, 21 eq.) was dissolved in 8 mL of water and added to the reaction dropwise, and it was refluxed for 1 hour. After cooling the reaction a few mL of 6 M HCl was added. Resulting solids were filtered and compound **8** was obtained quantitatively. ^{1}H NMR 400 MHz, DMSO-d_6, ppm: (d) 11.6 (br s, 1H), 7.07 (m, 1H), 6.97 (s, 1H), 6.75 (m, 2H), 2.75 (m, 2H), 1.60 (m, 2H), 1.4-1.1 (m, 6H), 0.85 (m, 3H).

Compound 9: Compound **8** (0.250 g, 0.72 mmol) was dissolved in TFA (7 mL) under N_2 atmosphere. Then the reaction was heated to 40 °C and stirred for 10 minutes. The reaction was completed by the addition of saturated $NaHCO_3$ solution (20 mL). Then, ethyl acetate (30 mL) was added, and the organic phase was extracted with water (3x20 mL), filtered, dried, and evaporated under reduced pressure to obtain compound **9** (75% yield). ^{1}H NMR 400 MHz, $CDCl_3$, ppm: (d) 8.2 (br s, 1H), 6.9-7.1 (m, 3H), 6.65 (m, 1H), 6.42 (m, 1H), 2.80 (m, 2H), 1.68 (m, 2H), 1.2-1.5 (m, 6H), 0.90 (m, 3H). HRMS)$^+$; $(M)^+$ $C_{16}H_2ONS_2^+$ calculated for 290.1032, found 290.1060.

Compound CTFBOD2: 25 ml of dichloromethane was degassed with nitrogen gas for 15 minutes and 0.05 g of substance **9** (0.17 mmol) and 0.0125 g of 4-formylbenzoic acid (0.08 mmol) were dissolved in this solvent. Then, 4 drops of trifluoroacetic acid (TFA) were added and left to stir overnight. Subsequently, DDQ (0.019 g, 0.08 mmol, 1 eq.) was added to the solution. After stirring at room temperature for 1 h, 0.25 ml of triethylamine and 0.25 ml of boron trifluoride diethyl ether were added. After 1 h, deionized water (25 mL) was added. The organic phase was washed 3 times with deionized water (3x25 mL) and then dried with Na_2SO_4 and the solvent was removed under reduced pressure. Silica gel column chromatography was performed (MeOH in DCM, 5%) and product **CTFBOD2** was obtained in 44% yield with a dark green colour (0.028 g). ^{1}H NMR 400 MHz, $CDCl_3$, ppm: (d) 8.25 (m, 2H), 7.68 (m, 2H), 7.25 (m, 4H), 6.77 (m, 2H), 6.63 (m, 2H), 2.85 (m, 4H), 1.72 (m, 4H), 1.1-1.5 (m, 12H), 0.92 (m, 3H). HRMS)$^-$; $(M)^-$ $C_{40}H_{38}BF_2N_2O_2S_4$- calculated for 755.1883, found 755.19975.

RESULTS AND DISCUSSION

Synthesis

Compound CTFBOD1 was synthesized in five steps (Figure 2). First, 5-bromo-2-carboxaldehyde was submitted to Hemetsberger-Knittel indolization reaction using ethyl azidoacetate, and sodium methoxide in methanol. Afterwards, a second heating step was applied in toluene and compound 1 was obtained in 22% yield. In the second step, 1 and 4-methoxyphenylboronic acid were reacted according to the Suzuki coupling reaction protocol and 2 was obtained in 13% yield. Later, the methyl ester unit of 2 was hydrolysed in the basic medium in a quantitative yield. Then, thiophene fused pyrrole derivative was reacted with TFA and decarboxylation was achieved to obtain the compound 4. In the final step, compound CTFBOD1 was obtained by utilizing the BODIPY formation procedure, using pyrrole derivative 4 and 4-carboxybenzaldehyde in 31% yield.

The second compound CTFBOD2 was synthesized in six steps (Figure 3). First, 2,2'-bithiophene was alkylated in two steps using tin(IV) chloride and hexanoyl chloride in benzene. Then, the carbonyl group was reduced using $LiAlH_4$ to achieve the compound 5. Then, formylation reaction was applied

according to the Vilsmeier-Haack reaction procedure to obtain the compound 6. Later, 6 was submitted to the Hemetsberger-Knittel indolization reaction to obtain the compound 7 and with this critical reaction thiophene fused pyrrole was obtained. By employing similar steps as compound CTFBOD2, compounds 8, 9 and the final structure CTFBOD2 were obtained. The final three reactions were accomplished with a total yield of 33%.

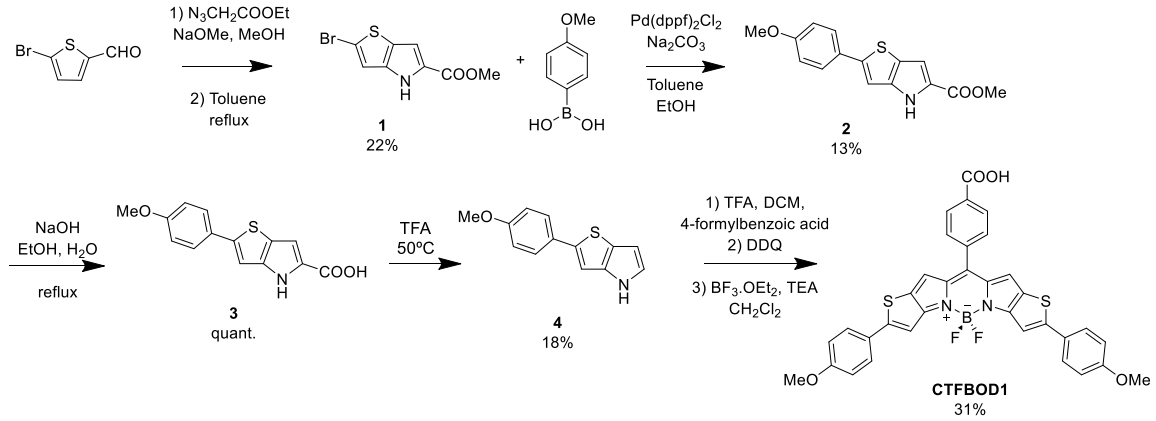

Figure 2
Synthesis scheme for the CTFBOD1 thiophene fused BODIPY structure

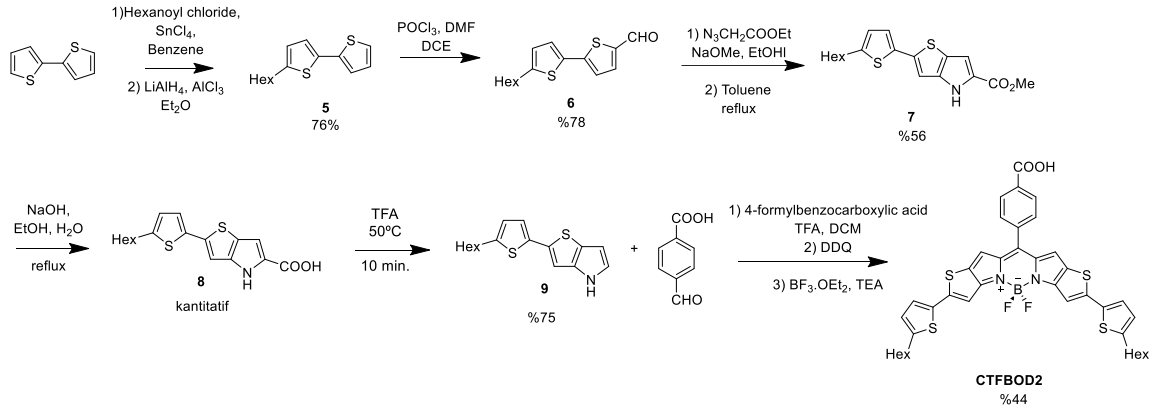

Figure 3
Synthesis scheme for the CTFBOD2 thiophene fused BODIPY structure

Photophysical Characterization and Cyclic Voltammetry Measurements

After synthesis of the compounds, absorption, and fluorescence emission of the compounds in chloroform were obtained (Figure 4). 4-methoxyphenyl substituted structure CTFBOD1 has absorbance and fluorescence maxima at 681 nm and 714 nm, respectively (Table 1). The regular tetramethyl-Bodipy core has absorbance maximum of around 500 nm and a huge shift to the red end of the electromagnetic spectrum of around 200 nm was observed with this thiophene fused structure. For the second structure, CTFBOD2, even more redshift was observed in both spectra. The absorbance maximum was observed at 707 nm and the fluorescence maximum was observed at 735 nm. More, the range of absorption is up to 800 nm, and for the fluorescence it is 850 nm. The difference between absorbance maxima of CTFBOD1 and CTFBOD2 is around 30 nm and this difference can be attributed to the stronger electron donating effect of the additional thiophene unit upon comparison with the methoxyphenyl unit of compound CTFBOD1. Both compounds have 4-carboxyphenyl moiety in the *meso* position of the BODIPY core. Therefore, an effective electron push-pull has been expected from the edges to this carboxy unit. Compound CTFBOD2 has a stronger donor unit and, a more effective electron push-pull

and a smaller HOMO-LUMO bandgap are expected. In our previous work, we have studied a similar dye, hexylbithiophene fused Bodipy structure, HTFBod (Figure 1) [3]. This structure has a stronger electron withdrawing trifluoromethyl unit in the *meso* position of the BODIPY core, then a smaller bandgap and more bathochromic shift were observed. The compound has absorbance and emission maxima at 764 and 788 nm, respectively and around 60 nm difference compared to CTFBOD2 was observed.

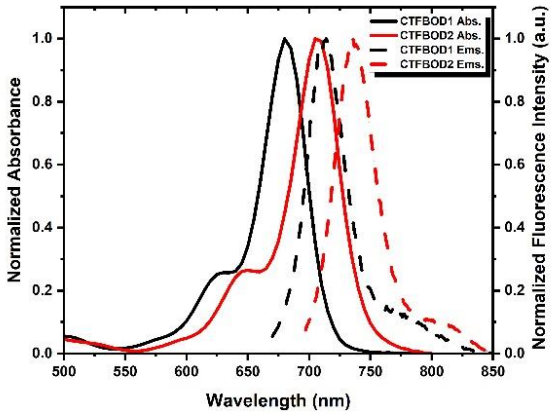

Figure 4
Absorptivity and Fluorescence Spectra of the compounds CTFBOD1 and CTFBOD2

Another fused structure that is similar to the synthesized compounds is the compound BFBOD, which was studied in our previous work (Figure 1) [5]. This compound has 2,3-benzo fused BODIPY structure, rather than the 1,2-thiophene fused structures of the current study. BFBOD has absorbance maxima at 622 nm which corresponds to around 60 nm hypsochromic shift compared to CTFBOD1. Therefore, it would be concluded that for more near IR absorption applications the design of 2,3-thiophene-fused structures is more convenient than 1,2-benzofused structures.

Table 1
Photophysical properties of compounds CTFBOD1 and CTFBOD2

Compounds	$\lambda_{abs,\ max}$ (nm)[1]	$\lambda_{ems,\ max}$ (nm)[1]	ε ($M^{-1}.cm^{-1}$)[1]
CTFBOD1	681	714	96000
CTFBOD2	707	735	92000

[1]In $CHCl_3$

Electrochemical Characterizations

Synthesized near-IR dyes CTFBOD1-2 were examined by cyclic voltammetry (CV) to obtain the oxidation and reduction potentials, the corresponding frontier orbital energy levels (HOMO and LUMO energy levels) and the bandgap (Figure 5a). In these calculations starting points of the first reduction and oxidation peaks were considered. For calculations of the electrochemical bandgap, potential difference between LUMO and HOMO were calculated.

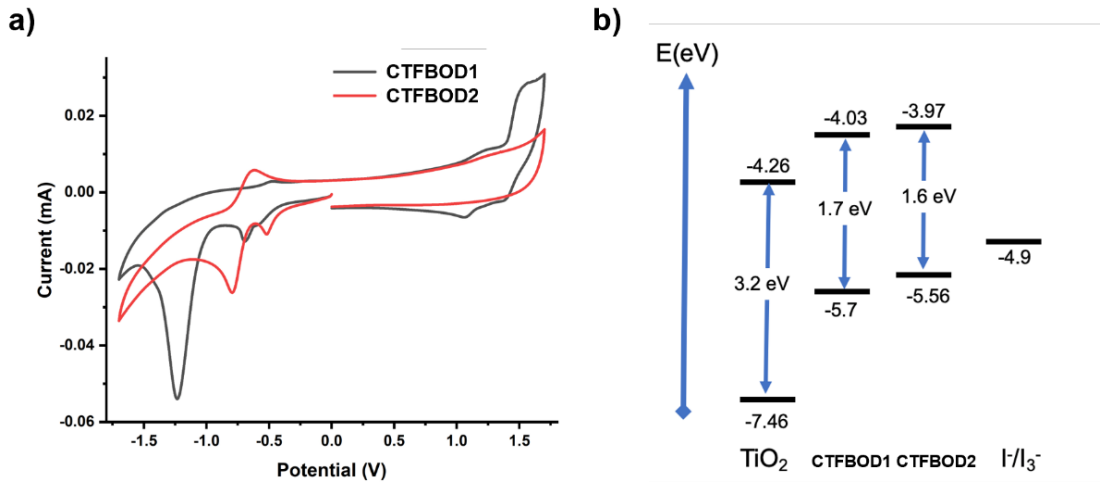

Figure 5

(a) Cyclic voltammograms of the compounds CTFBOD1 and CTFBOD2. (b) Energy levels of synthesized dyes, TiO_2 and iodide-triiodide electrolyte

Table 2

Electrochemical data of the CTFBOD1 and CTFBOD2 compounds based on the CV and spectroscopic measurements

Dye	E_{ox}^{onset} (V)[a]	HOMO (eV)[a]	HOMO (eV)[b]	E_{red}^{onset} (V)[a]	LUMO (eV)[a]	Eg (eV)[a]	Eg (eV)[b]
CTFBOD1	0.98	–5.38	**–5.7**	**–0.38**	**–4.03**	1.36	**1.67**
CTFBOD2	0.98	–5.38	**–5.56**	**–0.43**	**–3.97**	1.41	**1.59**

The results of the calculations are shown in Table 2. When determining the HOMO and LUMO energy levels of compounds CTFBOD1 and CTFBOD2, CV and optical measurements were used, and HOMO energy levels were calculated as –5.7 and –5.56 eV for CTFBOD1 and CTFBOD2, respectively. Corresponding LUMO levels are calculated as –4.03 and –3.97 eV, respectively. While calculating these reduction potentials, optical bandgaps were considered and written in bold in Table 2 since the oxidation peaks in CV were not clear. These calculated data, TiO_2 and iodide/triiodide energy levels were depicted in Figure 5b. According to these data, electron transfer from the LUMO energy levels of CTFBOD1 and CTFBOD2 to the TiO_2 conduction band of –4.26 eV seems probable. In the same way, electron transfer from the electrolyte solution to the HOMO energy levels of the dyes also seems possible.

CONCLUSIONS

In this study, synthesis, and characterization of two novel derivatives of [*b*]-thiophene fused BODIPY structures were investigated. Fused BODIPY structures are one of the fascinating derivatives of this type of dye and have largely been studied in recent decades [19, 22]. These types of structures could be used in applications such as organic photovoltaics, photodynamic therapy, bioimaging and chemosensors. In this current work, for the synthesis of thiophene-fused BODIPY structures, various synthetic routes have been considered, and optimum synthesis routes were accomplished. Hemetsberger-Knittel indolization reaction by using ethylazidoacetate or methylazidoacetate is the critical step where ultimate care is necessary to form the corresponding fused-pyrrole. At the end of the various efforts, we were able to synthesize the compounds CTFBOD1 and CTFBOD2 in moderate yields. During photophysical characterizations near IR absorption and fluorescence of the molecules were achieved. The *meso* position of the BODIPY core was substituted with carboxy-phenyl functionality, rendering them suitable for dye-sensitized solar cell applications. The HOMO-LUMO

energy levels were also determined using cyclic voltammetry studies, and the suitability for electron injection/collection upon use in this type of solar cell was also confirmed. More, the carboxy groups in the molecules could also be investigated in biological studies since they facilitate solubility in aqueous medium. Near IR absorption up to 800 nm is highly desired for these types of applications. Therefore, the derivatives in this study are of great importance in various fields and could be adapted to the growing area of high technological products. Similar studies with these types of novel structures and their investigation in various fields are currently under study in our research group.

Financing
The author thanks TUBITAK (Project No: 216Z015) for financial support.

Ethical Statement
This study is an original research article designed and developed by the author.

Author Contributions
Research Design (CRediT 1) Y.Ç. (%100)
Data Collection (CRediT 2) Y.Ç. (%100)
Research - Data Analysis - Validation (CRediT 3-4-6-11) Y.Ç. (%100)
Writing the Article (CRediT 12-13) Y.Ç. (%100)
Revision and Improvement of the Text (CRediT 14) Y.Ç. (%100)

REFERENCES

[1] P. De Bonfils, L. Péault, P. Nun, V. Coeffard, State of the art of bodipy-based photocatalysts in organic synthesis, *European Journal of Organic Chemistry*. 12 (2021), 1809-1824.

[2] N. Boens, B. Verbelen, W. Dehaen, Postfunctionalization of the BODIPY core: synthesis and spectroscopy. *European Journal of Organic Chemistry*. 30 (2015), 6577-6595.

[3] Y. Cakmak, Synthesis and investigation of a hexyl substituted thieno-fused BODIPY derivative as a versatile near-IR fluorophore, *Turkish Journal of Chemistry*. 46 (2022), 1120-1127.

[4] M. Tok, B. Say, G. Dölek, B. Tatar, D. Özgur, Ç. Kurukavak, M. Kus, Y. Dede, Y. Çakmak, Substitution effects in distyryl BODIPYs for near infrared organic photovoltaics, *Journal of Photochemistry and Photobiology A-Chemistry*. 429 (2022), 113933.

[5] B. Can, Y. Çakmak, Exploration of Two Different Strategies in Near IR Absorbing Boron Dipyrromethene Derivatives for Photodynamic and Bioimaging Purposes, *ChemistrySelect*. 6 (2021), 8855-8860.

[6] O. Buyukcakir, O. Bozdemir, S. Kolemen, S. Erbas, E. Akkaya, Tetrastyryl-Bodipy dyes: Convenient synthesis and characterization of elusive Near IR fluorophores, *Organic Letters*. 11 (2009), 4644-4647.

[7] B. Kukrer, E. U. Akkaya, Red to near IR fluorescent signalling of carbohydrates, *Tetrahedron Letters*. 40 (1999), 9125-9128.

[8] T. Bura, N. Leclerc, S. Fall, P. Lévêque, T. Heiser, P. Retailleau, S. Rihn, A. Mirloup, R. Ziessel, High-performance solution-processed solar cells and ambipolar behavior in organic field-effect transistors with Thienyl-BODIPY Scaffoldings, *Journal of the American Chemical Society*. 134 (2012), 17404-17407.

[9] S. Kolemen, O. A. Bozdemir, Y. Cakmak, G. Barin, S. Erten-Ela, M. Marszalek, J. H. Yum, S. M. Zakeeruddin, M. K. Nazeeruddin, M. Gratzel and E. U. Akkaya, Optimization of distyryl-Bodipy chromophores for efficient panchromatic sensitization in dye sensitized solar cells, *Chemical Science*. 2 (2011), 949-954.

[10] S. Erten-Ela, M. Yilmaz, B. Icli, Y. Dede, S. Icli, E. U. Akkaya, A panchromatic boradiazaindacene (BODIPY) sensitizer for dye-sensitized solar cells, *Organic Letters*. 10 (2008), 3299-3302.

[11] B. Say, B. Tatar, B. Uzulmez, M. Bakirci, G. Gulseren, Y. Cakmak, Caging of Bodipy Photosensitizers through Hydrazone Bond Formation and their Activation Dynamics, *ChemMedChem*. 18(13) (2023), e202300199.

[12] Z. Li, Z. Zhou, Y. Wang, J. Wang, L. Zhou, H. Cheng, J. Yoon, Activatable nano-photosensitizers for precise photodynamic cancer therapy, *Coordination Chemistry Reviews*. 2023, 493.

[13] A. Prieto-Castaneda, F. Garcia-Garrido, C. Diaz-Norambuena, B. Escriche-Navarro, A. Garcia-Fernandez, J. Banuclos, E. Rebollar, I. Garcia-Moreno, R. Martinez-Manez, S. de la Moya, A. Agarrabeitia, M. Ortiz, Development of geometry-controlled all-orthogonal BODIPY trimers for photodynamic therapy and phototheragnosis, *Organic Letters*. 24 (2022), 3636-3641.

[14] L. Zhao, H. Zhou, Q. Zhou, C. Peng, T. Cheng, G. Liu, Biomimetic fluorescent probe for chiral glutamic acid in water and its application in living cell imaging, *Sensors and Actuators B-Chemical*. 320 (2020), 128383.

[15] O. Tsay, K. Lee, D. Churchill, Selective and competitive cysteine chemosensing: resettable fluorescent "turn on" aqueous detection Cu^{2+} displacement and salicylaldimine hydrolysis, *New Journal of Chemistry*. 36 (2012), 1949-1952.

[16] A. O. Özkan, H. B. Demir, Fotovoltaik Panellerde Sıcaklık ve Zenit Açısının Panel Güç Üretimine Etkisi. *Necmettin Erbakan University Journal of Science and Engineering*. 1(1) (2019), 1-9.

[17] M. İ. Özgün, A. B. Batıbay, B. Ünal, Y. R. Eker, A. Terlemez, Investigation of the use of TiO2

obtained from endodontic NiTi Files in dye-sensitized solar cells. *Necmettin Erbakan University Journal of Science and Engineering*. 5(1) (2023), 1-8.

[18] F. N. Arslan, İ. Varlı, Synchronous fluorescence spectroscopy method based on chemometrics: Authentication of extra virgin olive oils harvested in Mut (Mersin) region and refined edible oils. *Necmettin Erbakan University Journal of Science and Engineering*. 5 (2023), 278-287.

[19] Y. Kubota, K. Kimura, J. Jin, K. Manseki, K. Funabiki, M. Matsui, Synthesis of near-infrared absorbing and fluorescing thiophene-fused BODIPY dyes with strong electron-donating groups and their application in dye-sensitised solar cells, *New Journal of Chemistry*. 43 (2019), 1156-1165.

[20] K. Umezawa, A. Matsui, Y. Nakamura, D. Citterio, K. Suzuki, Bright, color-tunable fluorescent dyes in the Vis/NIR region: Establishment of new "Tailor-Made" multicolor fluorophores based on Borondipyrromethene, *Chemistry-A European Journal*. 15 (2009), 1096-1106.

[21] L. Leonat, G. Sbârcea, I. Brânzoi, Cyclic voltammetry for energy levels estimation of organic materials, *University Politehnica of Bucharest Scientific Bulletin Series B-Chemistry and Materials Science*. 75 (2013), 111-118.

[22] K. Umezawa, Y. Nakamura, H. Makino, D. Citterio, K. Suzuki, Bright, color-tunable fluorescent dyes in the visible-near-infrared region, *Journal of the American Chemical Society*. 130 (2008), 1550-1551.

FEN ve MÜHENDİSLİK BİLİMLERİ DERGİSİ

Vol: 7 No: 1 Year: 2025 Araştırma Makalesi/Research Article e-ISSN: 2667-7989

https://doi.org/10.47112/neufmbd.2025.78

H_2O_2'nin SO_3H ile Fonksiyonelleştirilmiş Aktif Karbon/Co-B Nanokompozitleri ile Elektrokimyasal Tespiti

Sümeyye SARIKAYA[1] Görkem TASAR[1] Hasan Hüseyin İPEKCİ[1*] Aytekin UZUNOĞLU[1,2]

[1] Necmettin Erbakan University, Faculty of Engineering, Department of Metallurgical and Material Engineering, Konya, Türkiye

[2] İstanbul Technical University, Faculty of Chemistry- Metallurgical, Department of Metallurgical and Material Engineering, Konya, Türkiye

Makale Bilgisi

Geliş Tarihi: 04.04.2024
Kabul Tarihi: 24.07.2024
Yayın Tarihi: 30.04.2025

Anahtar Kelimeler:
Aktif Karbon,
Elektrokimyasal Sensör,
Hidrojen Peroksit,
Kobalt-bor.

ÖZET

Hidrojen peroksitin farmasötikten klinik ve çevresel uygulamalara ve gıda uygulamalarına kadar çeşitli alanlarda yaygın olarak kullanıldığı göz önüne alındığında, canlı sağlığı üzerindeki zararlı etkileri önemli bir sorundur. Bu nedenle, H_2O_2'nin hızlı, doğru, ucuz ve hassas yöntemlerle tespiti büyük talep görmektedir. Bu çalışmada, oldukça duyarlı H_2O_2 sensörleri oluşturmak için yeni bir katalizör kompozisyonu önerilmiştir. Bu bağlamda, ticari olarak aktifleştirilmiş karbon yüzeyini önce -SO_3H gruplarıyla modifiye edilmiş ve ardından H_2O_2'ye karşı yüksek elektrokatalitik aktivite elde etmek için amorf kobalt-boron fazı kullanılmıştır. Co-B@AC-SO_3H örnekleri SEM, TEM, XPS, XRD ve Raman spektroskopisi kullanılarak karakterize edilmiştir. XRD sonuçlarıyla amorf bir Co-B fazının varlığı doğrulanmış ve XRD ve Raman sonuçlarında karakteristik aktifleştirilmiş karbon tepe noktaları gösterilmiştir. Co-B@AC-SO_3H/GCE tabanlı sensörler, AC/GCE ve AC-SO_3H/GCE tabanlı karşılaştırma yapıldığında çok daha iyi duyarlılık göstermiştir. Sensörler, gerçek örneklerde H_2O_2 tespiti için yüksek depolama stabilitesi ve yüksek güvenilirlik göstermiştir.

Electrochemical Detection of H_2O_2 with SO_3H-functionalized Activated Carbon/Co-B Nanocomposites

Article Info

Received: 04.04.2024
Accepted: 24.07.2024
Published: 30.04.2025

Keywords:
Active Carbon,
Cobalt-Boron,
Electrochemical Sensor,
Hydrogen Peroxide,

ABSTRACT

While hydrogen peroxide has been widely used in various applications ranging from pharmaceutical to clinical and environmental to food applications, its harmful effects on health are an important challenge. Therefore, the detection of H_2O_2 with fast, accurate, cheap, and sensitive methods is in great demand. In this work, we proposed a novel catalyst composition to construct highly sensitive H_2O_2 sensors. In this study, we modified the surface of commercial activated carbon with first -SO_3H groups and then the amorphous cobalt-boron phase to achieve high electrocatalytic activity toward H_2O_2. The Co-B@AC-SO_3H samples were characterized using SEM, TEM, XPS, XRD, and Raman spectroscopy. XRD results confirmed the presence of an amorphous Co-B phase and the characteristic activated carbon peaks were obtained in both XRD and Raman results. The Co-B@AC-SO_3H/GCE-based sensors showed much improved sensitivity compared to AC/GCE and AC-SO_3H/GCE-based counterparts. The sensors showed high storage stability and reliability in detecting H_2O_2 in real samples.

To cite this article:
Sarıkaya, S., Tasar, G., İpekci, H.H. & Uzunoğlu, A. (2025). Electrochemical detection of H_2O_2 with SO_3H-functionalized activated carbon/Co-B nanocomposites. *Necmettin Erbakan University Journal of Science and Engineering, 7*(1), 103-114. https://doi.org/10.47112/neufmbd.2025.78

***Corresponding Author:** Hasan Hüseyin İpekci, *hsnpkc@gmail.com*

INTRODUCTION

The development of electrochemical sensors with high accuracy, good selectivity, wide linear range, and low limit of detection has been a focus of research to enhance the practical applicability of sensors against various analytes including glucose [1], hydrogen peroxide (H_2O_2) [2], dopamine [3], uric acid [4], ascorbic acid [5], and so on. Electrochemical sensors are classified into two main sub-classes: enzymatic and non-enzymatic electrochemical sensors. While enzymatic sensors pose various advantages including high specificity and sensitivity, the denaturation of enzymes depending on the storage conditions is one of the main challenges [6]. In addition, the use of biological enzymes on the electrode surface as the detection layer increases the cost of the electrochemical sensors, which hinders their wide use and practical applications. Therefore, the research focused on the development of novel non-enzymatic electrochemical sensors became a hot topic in electrochemical sensor research. In non-enzymatic sensors, the enzyme layer is replaced by enzyme-mimicking nanomaterials, which in turn enhances the storage stability and lowers the cost of the electrochemical sensors [7]. So far, various carbon-based materials have been implemented in the construction of non-enzymatic electrochemical sensors such as activated carbon [8], carbon nanotubes [9], graphene [10], graphene-related materials, and graphdiyne [11,12]. Among those different carbon allotropes, activated carbon has gained a great focus owing to its low cost, large physical surface area, ease of surface functionalization, high electronic conductivity, and high chemical stability [8]. The reported studies indicated that the modification of carbon surface with nanoparticles is one of the effective ways to achieve high electrochemical activity. This is because carbon itself without defects or nanoparticle decoration shows low electrochemical activity due to its chemical inertness. So far, various noble, non-noble metal and metal oxide nanoparticles have been used to decorate the surface of carbon-based materials to enhance the sensing, mechanical an antifungal performance of the materials [13–15]. On the other hand, especially the use of noble-metal nanoparticles on carbon surfaces increases the cost of sensor fabrication [3].

Hydrogen peroxide has been widely exploited in different applications ranging from pharmaceutical to clinical and environmental to food. Owing to its oxidizing nature, it is also used in disinfectants. While its wide use in various applications, the interaction of H_2O_2 with biological molecules in cells may cause peroxidation of lipids of the cell membrane and proteins, resulting in enzyme denaturation in the cells and damage to DNA. For this reason, the determination of H_2O_2 level with high accuracy, sensitivity, and selectivity in complex media is of great interest to human health. While different conventional analytical tools have been implemented to determine the H_2O_2 level such as chemical titration, fluorescence [16], chemiluminescence [17], spectrophotometry [18], and high-performance liquid chromatography [19]; those methods require a trained person to conduct the experiments, and the experiments are time-consuming and require complex sample preparation steps. Therefore, electrochemical sensors show great promise in detecting H_2O_2 in a cost-effective, fast, and accurate manner.

Among various metal and metal oxide alloy nanoparticles, cobalt-boron-based nanoparticles show improved electrocatalytic performance due to the electron interaction between Co and B atoms by making the Co electroactive sites [20]. While Co-B-based catalysts have been widely used in the hydrolysis of $NaBH_4$ for hydrogen production, their use in electrochemical sensors has not been reported. In the given study, we designed a novel catalyst structure consisting of sulfonate ($-SO_3H$)-functionalized activated carbon-supported Co-B nanoparticles for the detection of H_2O_2. Modifying activated carbon with $-SO_3H$ enables the immobilization of highly dispersed, nanosized metal and metal oxide nanoparticles [1,21,22]. In the given work, we designed a novel catalyst hybrid consisting of cobalt-boron decorated SO_3H-functionalized activated carbon to develop highly sensitive electrochemical H_2O_2 sensors. The catalysts were characterized using X-ray diffraction (XRD), scanning electron microscopy (SEM), transmission electron microscopy (TEM), Raman spectroscopy,

and X-ray photoelectron spectroscopy (XPS). The sensor performance was evaluated using cyclic voltammetry and chronoamperometry methods.

MATERIALS AND METHODS

Sulfonic acid, sodium nitrate, sodium borohydride, cobalt (II) chloride hexahydrate ($CoCl_2.6H_2O$), ethanol, and Nafion® 117 solutions were purchased from Sigma-Aldrich. Active carbon was obtained from Nanografi from Turkey. Sodium hydroxide was purchased from Riedel-de Haën Company.

Preparation of AC-SO_3H Nanoparticles

300 mg of activated carbon (AC) was sonicated in 30 ml DI for 10 minutes using an ultrasonic bath. The suspension was then stirred at 700 rpm in an ice bath using a magnetic stirrer. Sulfonic acid was dissolved in another beaker containing NaOH/DI solution. A certain amount of sodium nitrate was added to the beaker and sonicated for 5 additional minutes in an ultrasonic bath, which was flowed by stirring in an ice bath at 700 rpm using a magnetic stirrer. The obtained mixture was then added to the AC and DI-containing suspension drop by drop. The mixture was stirred for 5 h in an ice bath. The obtained suspension was centrifuged, and the precipitate was washed with DI and ethanol several times, followed by a drying process at 50 ºC.

Preparation of Co NPs@AC-SO_3H

20 mM CoCl2.6H2O and 100 ml DI water were mixed in an ice bath. 100 mg of AC-SO_3H was dispersed in ethanol and then introduced into a Co-containing solution. The resultant solution was stirred at 1300 rpm for 15 h using a magnetic stirrer in an ice bath. Sodium borohydride was added to the mixture drop by drop and left to stir for an additional hour. After this step, the mixture was centrifuged and washed several times with DI and ethanol. The precipitate was dried in a vacuum oven. The synthesized catalysts were named Co-B@AC-SO_3H. The synthesis route is shown schematically in Figure 1.

Figure 1
A schematic showing the synthesis route

Characterization of the Catalysts

The phase analysis and bonding properties of the samples were determined using X-ray diffraction and Raman spectroscopy methods. The surface topography and the 2D nanoscale images were obtained using scanning electron (SEM) and transmission electron microscopy (TEM), respectively. The elemental analysis of AC-SO_3H was carried out using X-ray photoelectron spectroscopy (XPS).

Fabrication of Catalysis Ink and Electrochemical Sensors

A glassy carbon electrode (GCE, 3 mm) was first polished with alumina powder and washed with an ethanol/ water mixture in an ultrasonic bath. The catalyst ink was prepared by mixing Co-B@AC-SO_3H, Nafion, ethanol, and DI. 5 µl of the ink was dropped onto a pre-polished GCE surface and dried for 2 h at room temperature. To form a permselective membrane on the sensor surface, a certain amount of Nafion 117 solution (0.05 wt%) was dropped on the sensor surface. The electroanalytical performance of the sensors was evaluated using cyclic voltammetry (CV) and amperometry (CA) methods using an Ivium Compacstat potentiostat. A three-electrode setup was used, in which the glassy carbon electrode (GCE), Ag/AgCl electrode (3 M NaCl, 0.195 V vs RHE), and the platinum wire were used as the working, reference, and counter electrodes, respectively. All the electrochemical measurements were performed at 0.01 M PBS with a pH of 7.4 at room temperature, and DI water was used in all experiments.

RESULTS AND DISCUSSION

Physical Characterization of the Samples

The SEM images recorded at different magnifications are given in Figure 2a-c. As observed, the Co-B@AC-SO_3H powder showed an agglomerated structure. The images at high magnifications showed the presence of homogeneously distributed carbon agglomerates as expected. The TEM images (Figure 2d-f) indicated the presence of regular carbon-shaped particles. It should be noted that no Co-B nanoparticle was observed on the carbon surface, which is attributed to the small particle size. This is because as discussed earlier, in the presence of -SO_3H on the surface of substrates, fine metal nanoparticles can be immobilized on the surface. Therefore, it is essential to conduct additional tools to reveal the presence of Co-B in the catalysts. The XRD and Raman results discussed below also indicated the presence of Co-B alloy nanoparticles on the activated carbon surface. Therefore, the TEM images revealed that the Co-B nanoparticles were too small to be observed in the TEM images.

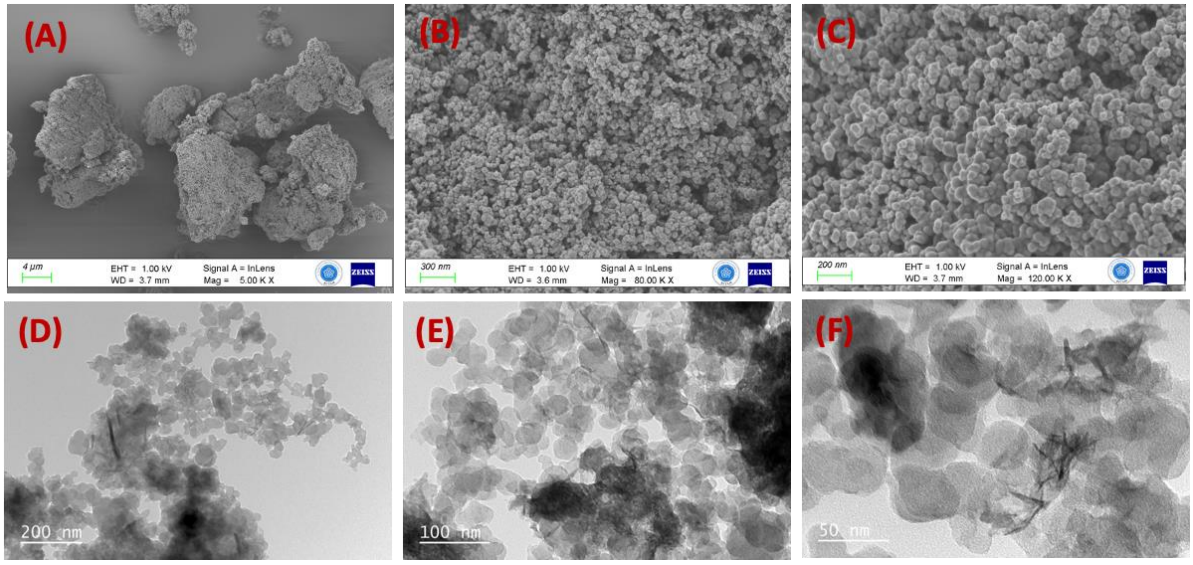

Figure 2
(a-c) SEM and (d-f) TEM images of the samples

The XRD result of Co-B@AC-SO_3H is given in Figure 3a. The characteristic carbon peak was obtained at 25.53°, corresponding to the (002) plane family. In addition, a weak XRD reflection at ca. 43.37° was observed [4]. These results indicated the presence of an amorphous carbon phase. Since Co-B has an amorphous structure, it is not possible to observe the Co-B in the XRD reflection. On the other

hand, XRD reflections with very low intensities located at ca. 44.5° (111) and 51.5° (200) correspond to the crystalline Co nanoparticles (JCPDS #: 15-0806). The presence of diffuse Co reflections indicated the formation of the amorphous Co-B phase in the catalysts. The Raman spectra of the catalyst indicated D and G bands at ca. 1368 and 1603 cm^{-1}, respectively, which are peculiar to the carbon structure. The intensities of the D and G bands (I_D/I_G) were found to be 0.94 and 0.92 for AC-SO_3H and Co-B@AC-SO_3H. Thus, it may be suggested that the decoration of AC-SO_3H with Co-B resulted in a slight recovery in the defect concentration of activated carbon. The Raman reflections observed below 1000 cm^{-1} are ascribed to the Co-containing species.

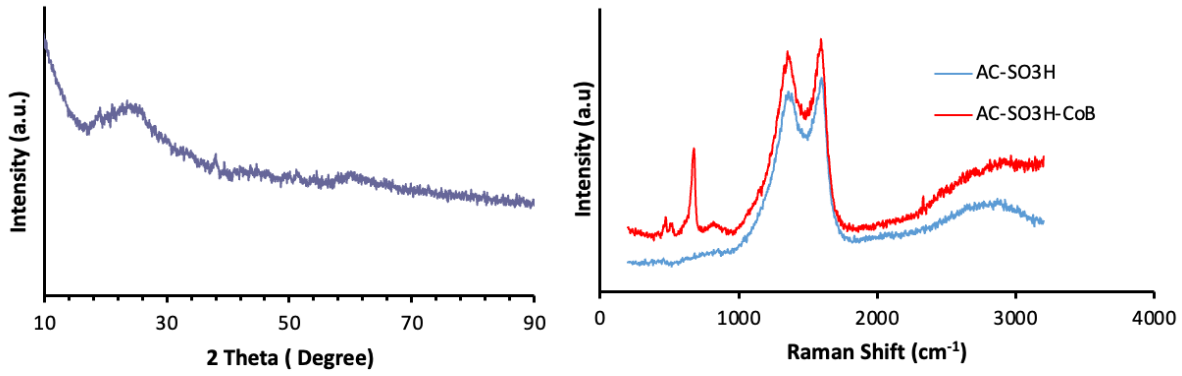

Figure 3
a) XRD and b) Raman Results of the samples

To confirm the -SO_3H modification of activated carbon, AC-SO_3H was analyzed using X-ray photoelectron spectroscopy method. The elemental analysis results indicated that after the sulfonation process, the sample contained S element with 0.25 at.%, indicating the successful modification of the AC surface. The XPS analysis is shown in Figure 4. Figure 4b shows the O1s spectrum with two deconvoluted peaks. The peaks at 532.7 and 534.2 eV correspond to C-O and S=O bonded to organic groups, respectively. The S2p spectrum is deconvoluted into three peaks, S2p 3/2, S2p 1/2, and thiol groups at 168.0 eV, 169.3 eV, and 164.4 eV, respectively (Figure 4c). These results explained that successful sulfonation on the activated carbon surface as SO_3H groups [23,24].

Electrochemical Characterization of the Sensors

The CV behaviors of AC-SO_3H and Co-B@AC-SO_3H-modified GCEs in the absence and presence of H_2O_2 (2 mM) are shown in Figures 5a and b, respectively. While both electrodes did not yield any significant redox peaks in the absence of the analyte, significant reduction peaks were observed with the introduction of H_2O_2, indicating the catalytic activity of the samples. It should be emphasized that the reduction peak current obtained from Co-B@AC-SO_3H was almost twice compared to that obtained from AC-SO_3H, confirming the electrochemical activity of the amorphous Co-B phase in the catalyst layer. The change in the peak current with increasing scan rate is displayed in Figure 5c and the corresponding calibration curve is shown in Figure 5d. As observed, the peak current increased linearly with the square root of the scan rate, indicating that the electrooxidation of H_2O_2 on the sensor surface is a diffusion-controlled reaction [2,25,26].

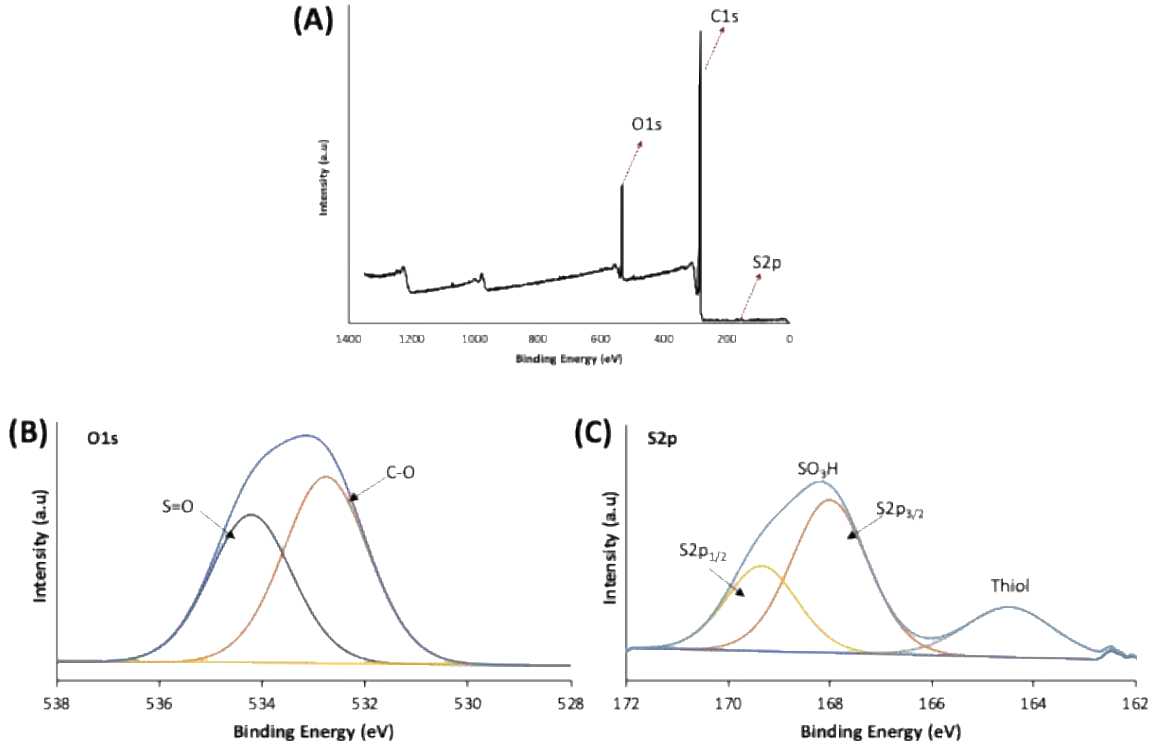

Figure 4

XPS scan a) survey, high resolution for b) O1s, and c) S2p of AC-SO_3H.

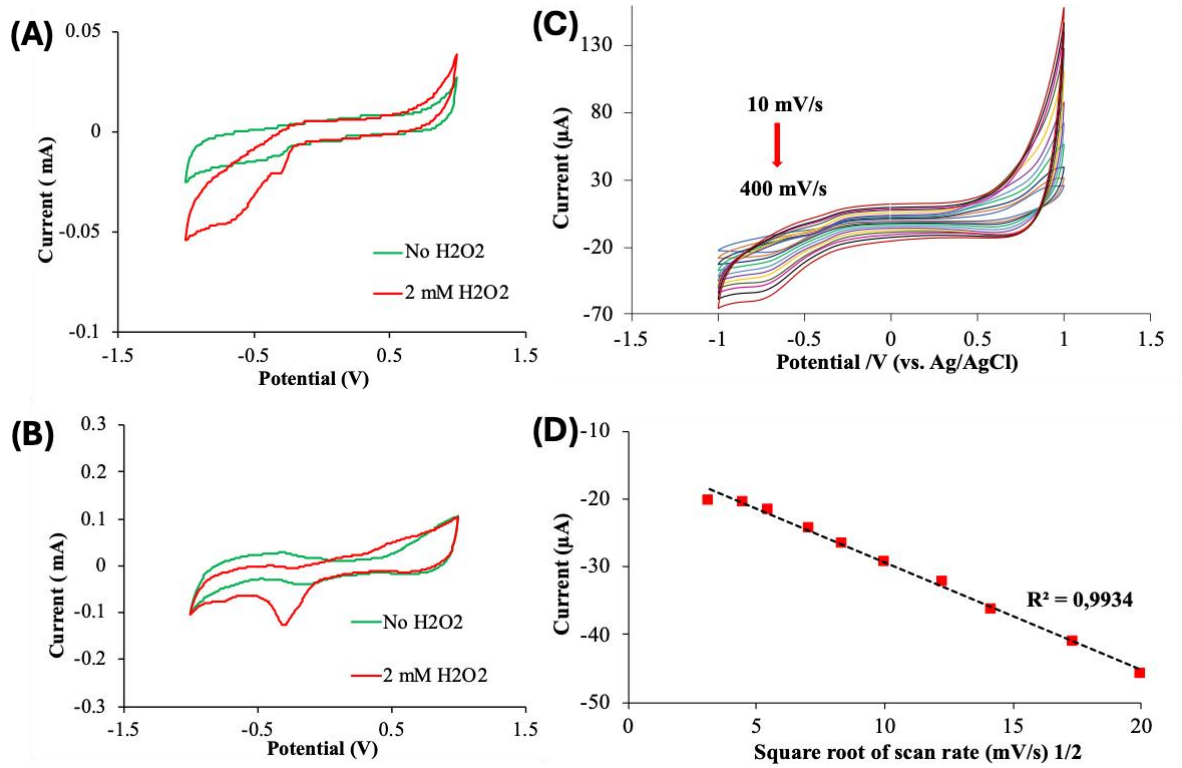

Figure 5

CV curves of a) AC-SO_3H and b) Co-B@AC-SO_3H, c) Effect of scan rate on the peak current of Co-B@AC-SO_3H-based sensors, and d) Corresponding scan rate-peak current graph.

To achieve the highest electrocatalytic performance, the working potential of the sensor was optimized. The calibration (current-concentration) curves obtained from the Co-B@AC-SO_3H/GCE-based sensors at different working potentials are displayed in Figure 6a. The curves showed that the

highest current values were measured at the working potential of 0.6 V. Therefore, further analytical measurements were conducted at that potential. To demonstrate the superior performance of our novel catalyst, we prepared AC/GCE, AC-SO_3H/GCE, and Co-B@AC-SO_3H/GCE-based sensors. The measured current responses toward the successive addition of H_2O_2 are given in Figure 6b. The corresponding calibration curves are displayed in Figure 6c. The highest sensitivity was measured from the Co-B@AC-SO_3H/GCE-based sensors, which is 33.8 and 2.3 times higher than those obtained from AC/GCE and AC-SO_3H/GCE-based sensors, respectively. Therefore, we can allege that the modification of the AC-SO_3H surface with Co-B yielded much higher electrocatalytic activity. The linear ranges of the sensors, however, were almost similar to each other. A high sensitivity of -175.958 ± 7.60 µA $mM^{-1}cm^{-2}$ (RSD%: 4.31, n=3) was achieved from the Co-B@AC-SO_3H/GCE-based sensors. The upper linear range of the sensors was found to be 24 mM. The limit of detection of the Co-B@AC-SO3H/GCE-based sensors was calculated to be 10.8 µM (signal-to-noise ratio of 3). To show the capability of the detection of low H_2O_2 concentrations, H_2O_2 with various concentrations including 10, 30, 50, and 100 µM were introduced and the recorded currents are displayed in Figures 6d and f, which indicate the detection of the analyte with concentrations close to the LOD value. The selectivity of Co-B@AC-SO_3H/GCE-based sensors was studied using glucose (GC), NaCl, ascorbic acid (AA), and uric acid (UA). As displayed in Figure 6e, no significant change in the current response was observed, confirming the high selectivity of the sensors.

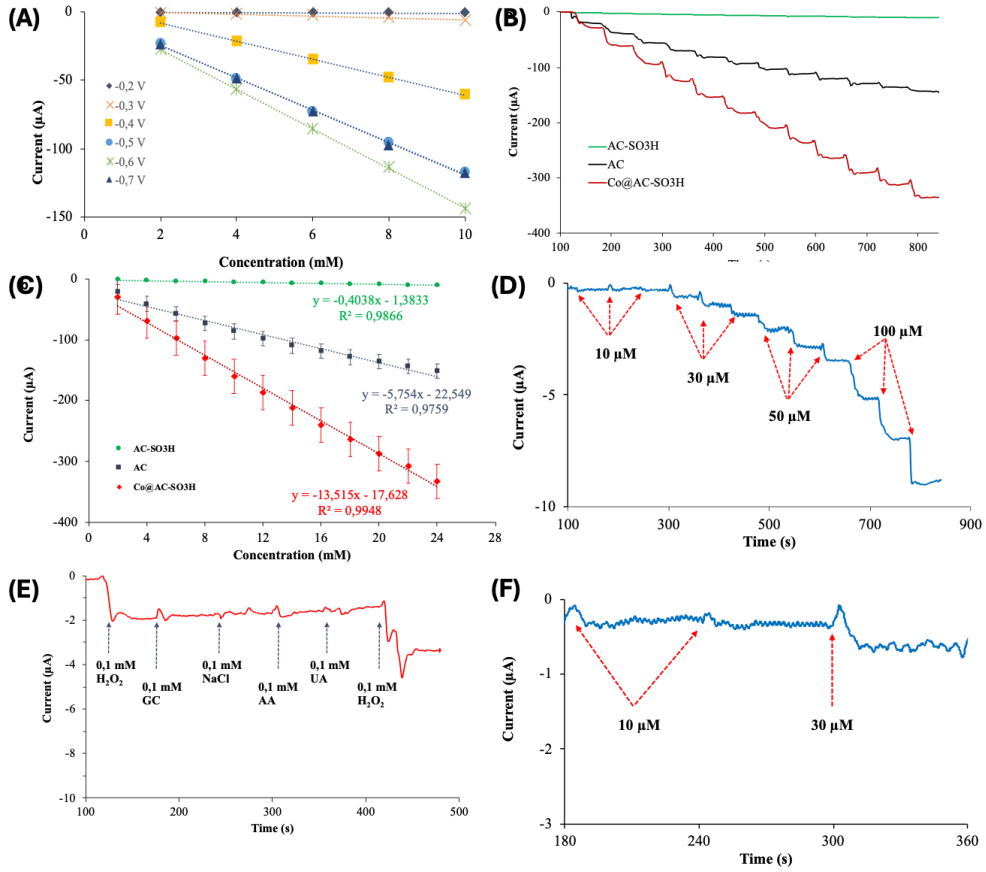

Figure 6

a) Effect of applied voltage on sensor response, b) Chronoamperometry results of AC/GCE, AC- SO_3H/GCE, and Co-B@AC-SO_3H/GCE-based sensors, c) Corresponding calibration curves, d, f) Chronoamperometry results against varying amount of H_2O_2, e) Selectivity of the sensors

The storage stability of the sensors was evaluated by measuring the amperometric response to against 2 mM H_2O_2 for 25 days (n=4). As shown in Figure 7, compared to the initial current (-28.67 ±0.51 µA), after 25 days, the average current response of -29.96 ±0.46 µA was measured. Therefore,

after 25 days, the sensors did not show any drop in current, indicating a high long-term stability. The electrodes were kept at room temperature throughout these experiments.

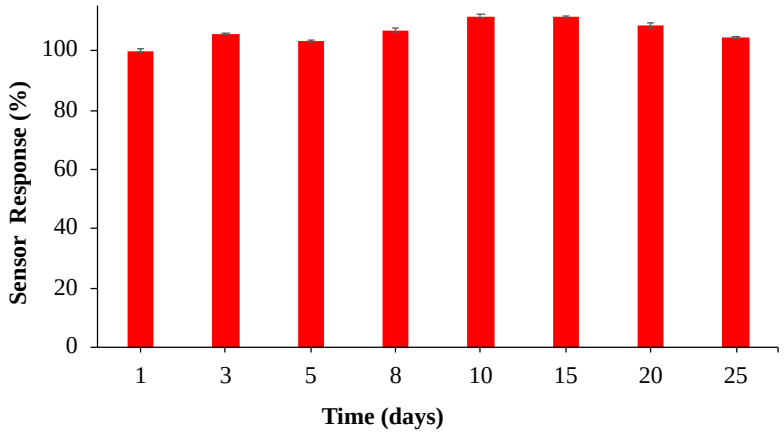

Figure 7
Storage stability of the Co-B@AC-SO_3H/GCE-based sensors (n=4)

Table 1
Comparison of the performance of carbon-based sensors with previously reported sensors

Sensor	Method	Sensitivity ($\mu A\ \mu M^{-1}\ cm^{-2}$)	Linear range (µM)	LOD (µM)	Ref.
rGO/FeNPs/GCE	CA	0.2086	0.1-2150	0.056	[27]
RGO/CNTs-Pt	CA	347 ± 5	0.4-18 10-4x10^3	0.31	[28]
CoHCFNPs/GR/CPE	CA	-	0.6-379.5	0.1	[29]
Co(III)/MWCNT/Nafion	CV	-	0.05-100	0.05	[30]
Vit.B12-NGr	DPV CV	8.775 4.081	2.49-24.5 19.9-167.7	0.02 -	[31]
$CoFe_2O_4$/CNTs/GCE	CA	-	5-50	0.05	[32]
Cu_2O/GNs	CA	-	300-7.8x10^3	20.8	[33]
Au-HS/SO_3H-PMO (Et)	CA	635	0.2-4.3x10^3	0.05	[34]
rGO/CoPc–COOH/GCE	CA	14.5	100–12x10^3	60	[35]
Co-B@AC-SO_3H/GCE	CA	175.958	20-24x10^3	10.8	This work

CoHCFNPs/ GR: Cobalt hexacyanoferrate nanoparticles/graphene, **Vit.B12-NGr:** Vitamin B12 functionalized nitrogen-doped graphene, **$CoFe_2O_4$:** Cobalt ferrite, **Co_3O_4–rGO:** Co_3O_4-reduced graphene oxide, **Cu_2O/GNs:** Cu_2O nanocubes wrapped by graphene nanosheets, **Co_2P/ITO:** Cobalt phosphide/Indium tin oxide, **CoPc–COOH:** Cobalt phthalocyanine tetracarboxylic acid.

Table 2
Detection of H_2O_2 in real samples

Exp. #	Spiked (mM)	Calculated (mM)	Recovery (%)
1	2.0	2.04	102.2
2	4.0	4.07	101.9
3	6.0	6.03	100.5

The performance of the Co-B@AC-SO3H/GCE-based sensors was compared with those reported previously. Some of the recent reports are listed in Table 1. As observed, our novel sensor surface yielded higher performance in terms of linear range and sensitivity. On the other hand, the LOD of our sensor design was higher than those listed in Table 1, suggesting that the LOD of Co-B@AC-SO_3H/GCE-based sensors should be decreased further. The real applicability and the reliability of the sensor response were evaluated by measuring the H_2O_2 concentration in real samples. In this experiment, we evaluated the current response of H_2O_2 in a 3 wt% H_2O_2-containing disinfectant using our sensors. The analytical results were calculated using the measured and calculated H_2O_2 concentrations. Recovery

% values were calculated using calculated and spiked H_2O_2 concentrations based on the equation of Recovery=((calculated/spiked)*100). The calculated value is used to determine the analyte concentration in the spiked sample using the electrochemical method, while spiked refers to the amount of a known analyte concentration containing H_2O_2. As shown in Table 2, the average recoveries are between 100.5% and 102.2%, which indicates that the sensors are effective for the detection of H_2O_2 in practical analysis.

CONCLUSIONS

Herein, we developed a novel catalyst by exploiting the high electrocatalytic activity of the amorphous Co-B phase precipitated on SO_3H-modified activated carbon. The Co-B@AC-SO_3H samples were characterized using SEM, TEM, XPS, XRD, and Raman spectroscopy. The presence of an amorphous Co-B phase was confirmed by XRD results, and the characteristic activated carbon peaks were obtained in both XRD and Raman results. The Co-B@AC-SO_3H/GCE-based sensors showed much improved sensitivity compared with their AC/GCE and AC-SO_3H/GCE-based counterparts. The sensors showed high storage stability and high reliability in detecting H_2O_2 in real samples. Electrochemical sensors have been proven to detect hydrogen peroxide with electrochemical sensors in environmental monitoring applications in a wide range of fields such as food safety, pharmaceuticals, and water treatment. Their high sensitivity, specificity, and real-time analysis capabilities make them ideal for applications requiring accurate and rapid detection. As technology advances, the development of more sophisticated and robust electrochemical sensors will further enhance their use and expand their applications, contributing to safety and quality improvement in many industries.

Ethical Statement

This study is derived from a undergratude thesis entitled ‘Preparation of Active Carbon Based Sensor for Hydrogen Peroxide Determination’ submitted under the supervision of Aytekin Uzunoglu on July 2020.

Author Contributions

Research Design (CRediT 1) H.H.İ. (50%) - A.U. (50%)
Data Collection (CRediT 2) S.S. (50%) - G.T. (50%)
Research - Data Analysis - Validation (CRediT 3-4-6-11) S.S. (30%) - G.T. (20%)-H.H.İ. (%50)
Writing the Article (CRediT 12-13) H.H.İ. (70%) - A.U. (30%)
Revision and Improvement of the Text (CRediT 14) H.H.İ. (70%) - A.U. (30%)

Financing

This study was supported by the Necmettin Erbakan University, Scientific Research Projects Coordination Unit institution with project number 191219009.

Conflict of Interest

The authors declare no conflict of interest.

REFERENCES

[1] M. Dilsen, H.H. Ipekci, A. Uzunoglu, Inkjet printing of Pd/SO3H-modified graphene on different polymeric substrates to construct flexible electrochemical sensors, *Journal of Materials Research*. 38 (2023), 3572-3584. doi:10.1557/S43578-023-01086-7/METRICS

[2] A. Uzunoglu, H.H. Ipekci, The use of CeO2-modified Pt/C catalyst inks for the construction of high-performance enzyme-free H2O2 sensors, *Journal of Electroanalytical Chemistry*. 848 (2019), 113302. doi:10.1016/J.JELECHEM.2019.113302

[3] H.H. Ipekci, Electrochemical Dopamine Detection Using Palladium/Carbon Nano Onion Hybrids, *Hittite Journal of Science and Engineering*. 10 (2023), 201-209. doi:10.17350/HJSE19030000308

[4] H.H. Ipekci, Holey MoS2-based electrochemical sensors for simultaneous dopamine and uric acid detection, *Analytical Methods*. 15 (2023), 2989-2996. doi:10.1039/D3AY00573A

[5] P. Deng, J. Feng, J. Xiao, Y. Wei, X. Liu, J. Li, Q. He, Application of a simple and sensitive electrochemical sensor in simultaneous determination of paracetamol and ascorbic acid, *Journal of The Electrochemical Society*. 168 (2021,) 096501. doi:10.1149/1945-7111/ac1e59

[6] J. Baranwal, B. Barse, G. Gatto, G. Broncova, A. Kumar, Electrochemical sensors and their applications: A review, *Chemosensors*. 10 (2022). doi:10.3390/chemosensors10090363

[7] C. Revathi, R.T. Rajendra kumar, Chapter 7 - Enzymatic and Nonenzymatic Electrochemical Biosensors, içinde: M. Hywel, C.S. Rout, D.J.B.T.-F. and S.A. of 2D M. Late (Ed.), *Woodhead Publishing Series in Electronic and Optical Materials*, *Woodhead Publishing*, 2019: ss. 259-300. doi:10.1016/B978-0-08-102577-2.00007-5

[8] J. Wang, H. Kong, J. Zhang, Y. Hao, Z. Shao, F. Ciucci, Carbon-based electrocatalysts for sustainable energy applications, *Progress in Materials Science*. 116 (2021), 100717. doi:10.1016/j.pmatsci.2020.100717

[9] C.B. Jacobs, M.J. Peairs, B.J. Venton, Review: Carbon nanotube based electrochemical sensors for biomolecules, *Analytica Chimica Acta*. 662 (2010), 105-127. doi:10.1016/j.aca.2010.01.009

[10] Y. Wang, Y. Shao, D.W. Matson, J. Li, Y. Lin, Nitrogen-doped graphene and its application in electrochemical biosensing, *ACS Nano*. 4 (2010), 1790-1798. doi:10.1021/nn100315s

[11] X. Sun, M. Duan, R. Li, Y. Meng, Q. Bai, L. Wang, M. Liu, Z. Yang, Z. Zhu, N. Sui, Ultrathin graphdiyne/graphene heterostructure as a robust electrochemical sensing platform, *Analytical Chemistry*. 94 (2022), 13598-13606. doi:10.1021/acs.analchem.2c03387

[12] E. Ceylan, O. Ozoglu, H.H. Ipekci, A. Tor, A. Uzunoglu, Non-enzymatic detection of methyl parathion in water using CeO2-CuO-decorated reduced graphene oxide, *Microchemical Journal.* 199 (2024), 110261. doi: 10.1016/j.microc.2024.110261

[13] S. Bulbul, E. Ayhan, H. Gökmeşe, Effect on mechanical properties of addition of coal ash as thermal power plant waste to SBR Matrix Compounds, *Necmettin Erbakan University Journal of Science and Engineering*. 5 (2023), 135-146. doi:10.47112/neufmbd.2023.14

[14] İ. Akın, E. Zor, H. Bingöl, Preparation and characterization of GO/Fe3O4 doped polymeric composite membranes, *Necmettin Erbakan University Journal of Science and Engineering*. 5 (2023), 38-52. doi:10.47112/neufmbd.2023.8

[15] K. Çetin, K. Şarkaya, B. Kavakcıoğlu Yardımcı, Antifungal activities of copper (II) ion and histidine incorporated polymers on yeast *Saccharomyces cerevisiae*, *Necmettin Erbakan University Journal of Science and Engineering*. 5 (2023), 267-277. doi:10.47112/neufmbd.2023.24

[16] Y. Zuo, Y. Jiao, C. Ma, C. Duan, A novel fluorescent probe for hydrogen peroxide and its application in bio-imaging, *Molecules*. 26 (2021). doi:10.3390/MOLECULES26113352

[17] W.J. Cooper, J.K. Moegling, R.J. Kieber, J.J. Kiddle, A chemiluminescence method for the analysis of H2O2 in natural waters, *Marine Chemistry*. 70 (2000), 191-200. doi:10.1016/S0304-4203(00)00025-6

[18] K. Sunil, B. Narayana, Spectrophotometric determination of hydrogen peroxide in water and cream samples, *Bulletin of Environmental Contamination and Toxicology*. 81 (2008), 422-426. doi:10.1007/S00128-008-9477-7

[19] P. Gimeno, C. Bousquet, N. Lassu, A.-F. Maggio, C. Civade, C. Brenier, L. Lempereur, High-performance liquid chromatography method for the determination of hydrogen peroxide present or released in teeth bleaching kits and hair cosmetic products, *Journal of Pharmaceutical and Biomedical Analysis*. 107 (2015), 386-393. doi:10.1016/j.jpba.2015.01.018

[20] B. Long, J. Chen, S.W. Sharshir, L. Ibrahim, W. Zhou, C. Wang, L. Wang, Z. Yuan, The mechanism and challenges of cobalt-boron-based catalysts in the hydrolysis of sodium borohydride, *Journal of Materials Chemistry A*. 12 (2024), 5606-5625. doi:10.1039/D3TA07308D

[21] L. Xin, F. Yang, Y. Qiu, A. Uzunoglu, T. Rockward, R.L. Borup, L.A. Stanciu, W. Li, J. Xie, Polybenzimidazole (PBI) functionalized nanographene as highly stable catalyst support for polymer electrolyte membrane fuel cells (PEMFCs), *Journal of The Electrochemical Society*. 163 (2016), F1228-F1236. doi:10.1149/2.0921610JES/XML

[22] L. Xin, F. Yang, S. Rasouli, Y. Qiu, Z.F. Li, A. Uzunoglu, C.J. Sun, Y. Liu, P. Ferreira, W. Li, Y. Ren, L.A. Stanciu, J. Xie, Understanding Pt nanoparticle anchoring on graphene supports through surface functionalization, *ACS Catalysis*. 6 (2016), 2642-2653. doi:10.1021/ACSCATAL.5B02722/ASSET/IMAGES/MEDIUM/CS-2015-02722X_0010.GIF

[23] U.I. Nda-Umar, I. Ramli, E.N. Muhamad, N. Azri, Y.H. Taufiq-Yap, Optimization and characterization of mesoporous sulfonated carbon catalyst and its application in modeling and optimization of acetin production, *Molecules.* 25 (2020), 5221. doi:10.3390/molecules25225221

[24] C.B. Rodella, D.H. Barrett, S.F. Moya, S.J.A. Figueroa, M.T.B. Pimenta, A.A.S. Curvelo, V.T. Silva, Pyhsical and chemical studies of tungsten carbide catalysts: effects of Ni promotion and sulphonated carbon, *RSC Advances.* 5 (2015), 23874. doi:10.1039/c5ra03252k

[25] A. Uzunoglu, S. Song, L.A. Stanciu, A sensitive electrochemical H2O2 sensor based on PdAg-decorated reduced graphene oxide nanocomposites , *Journal of The Electrochemical Society*. 163 (2016), B379-B384. doi:10.1149/2.1201607JES/XML

[26] A. Uzunoglu, A.D. Scherbarth, L.A. Stanciu, Bimetallic PdCu/SPCE non-enzymatic hydrogen peroxide sensors, *Sensors and Actuators B: Chemical*. 220 (2015), 968-976. doi:10.1016/J.SNB.2015.06.033

[27] B. Amanulla, S. Palanisamy, S.M. Chen, V. Velusamy, T.W. Chiu, T.W. Chen, S.K. Ramaraj, A non-enzymatic amperometric hydrogen peroxide sensor based on iron nanoparticles decorated reduced graphene oxide nanocomposite, *Journal of Colloid and Interface Science*. 487 (2017), 370-377. doi:10.1016/J.JCIS.2016.10.050

[28] Y. Zhang, Q. Cao, F. Zhu, H. Xu, Y. Zhang, W. Xu, X. Liao, An amperometric hydrogen peroxide sensor based on reduced graphene oxide/carbon nanotubes/Pt NPs modified glassy carbon electrode, *International Journal of Electrochemical Science*. 15 (2020), 8771-8785. doi:10.20964/2020.09.62

[29] S. Yang, G. Li, G. Wang, J. Zhao, M. Hu, L. Qu, A novel nonenzymatic H2O2 sensor based on cobalt hexacyanoferrate nanoparticles and graphene composite modified electrode, *Sensors and Actuators B: Chemical*. 208 (2015), 593-599. doi:10.1016/J.SNB.2014.11.055

[30] C.M. Parnell, F. Watanabe, U.B. Nasini, B.C. Berry, T. Mitchell, A.U. Shaikh, A. Ghosh, Electrochemical sensing of hydrogen peroxide using a cobalt(III) complex supported on carbonaceous nanomaterials, *Journal of Electroanalytical Chemistry*. 740 (2015), 37-44. doi:10.1016/J.JELECHEM.2014.12.022

[31] S.A. Bhat, N. Rashid, M.A. Rather, S.A. Pandit, P.P. Ingole, M.A. Bhat, Vitamin B12 functionalized N-Doped graphene: A promising electro-catalyst for hydrogen evolution and electro-oxidative sensing of H2O2, *Electrochimica Acta*. 337 (2020), 135730. doi:10.1016/J.ELECTACTA.2020.135730

[32] S. Sahoo, P.K. Sahoo, S. Manna, A.K. Satpati, A novel low cost nonenzymatic hydrogen peroxide sensor based on CoFe2O4/CNTs nanocomposite modified electrode, *Journal of Electroanalytical Chemistry*. 876 (2020), 114504. doi:10.1016/J.JELECHEM.2020.114504

[33] M. Liu, R. Liu, W. Chen, Graphene wrapped Cu2O nanocubes: Non-enzymatic electrochemical sensors for the detection of glucose and hydrogen peroxide with enhanced stability, *Biosensors and Bioelectronics*. 45 (2013), 206-212. doi:10.1016/J.BIOS.2013.02.010

[34] F. Jia, H. Zhong, F. Zhu, X. Li, Y. Wang, Z. Cheng, L. Zhang, Z. Sheng, L. Guo, Nonenzymatic hydrogen peroxide electrochemical sensor based on Au-HS/SO3H-PMO (Et) nanocomposite, *Electroanalysis*. 26 (2014), 2244-2251. doi:10.1002/ELAN.201400318

[35] I.S. Hosu, Q. Wang, A. Vasilescu, S.F. Peteu, V. Raditoiu, S. Railian, V. Zaitsev, K. Turcheniuk, Q. Wang, M. Li, R. Boukherroub, S. Szunerits, Cobalt phthalocyanine tetracarboxylic acid modified reduced graphene oxide: a sensitive matrix for the electrocatalytic detection of peroxynitrite and hydrogen peroxide, *RSC Advances*. 5 (2014), 1474-1484. doi:10.1039/C4RA09781E

FEN ve MÜHENDİSLİK BİLİMLERİ DERGİSİ

Vol: 7 No: 1 Yıl: 2025 | Araştırma Makalesi/Research Article | e-ISSN: 2667-7989

https://doi.org/10.47112/neufmbd.2025.79

Examining the Energy Saving Potential of a Dairy Enterprise Based on an Energy Audit

Fatih AKKURT[1*] İsmail Buğrahan ÖZSAN[2]

[1] Necmettin Erbakan University, Faculty of Engineering, Department of Energy Systems Engineering, Konya, Türkiye

[2] Necmettin Erbakan University, Graduate School of Natural and Applied Science, Department of Energy Systems Engineering, Konya, Türkiye

Makale Bilgisi

Makale Geçmişi

Geliş Tarihi: 23.06.2024
Kabul Tarihi: 20.11.2024
Yayın Tarihi: 30.04.2025

Keywords:
Süt Tesisi
Enerji Etüdü
Enerji Tasarruf Potansiyeli,
Enerji Tasarruf Projeleri.

ÖZET

Süt ve ürünlerinin gıda sektöründe enerji tüketimindeki payı oldukça yüksektir. Bu nedenle enerji tasarrufu bu sektörde gerçekten önemlidir. Bu çalışmada bir süt işletmesinin enerji denetimine dayalı enerji tasarruf potansiyeli incelenmiştir. Öncelikle işletmenin mevcut enerji tüketimine göre oluşturulan standart ve hedef denklemlerle enerji tasarruf potansiyeli belirlenmiştir. Enerji tüketen cihazlarda bazı ölçümler yapılmıştır. Ölçümlerle verimli çalışmayan cihazlar ve enerji kaçağı olan noktalar belirlenmiştir. Enerji tasarrufu için bazı projeler önerilmiştir. Önerilen projeler sayesinde yıllık 332,51 TEP (ton eşdeğer petrol) enerji tasarrufu sağlanacağı belirlenmiştir. Ayrıca oluşturulan sonuç denklemiyle önerilen projelerin enerji tasarrufunda faydalı olabilmesi için işletmenin üretiminin 3810 Ton/Ay altına düşmemesi gerektiği anlaşılmıştır.

Examining the Energy Saving Potential of a Dairy Enterprise Based on an Energy Audit

Article Info

Article History

Received: 23.06.2024
Accepted: 20.11.2024
Published: 30.04.2025

Keywords:
Dairy Enterprise,
Energy Audit,
Energy Saving Potential,
Energy Saving Projects.

ABSTRACT

The share of milk and its products in terms of energy consumption in the food sector is quite high. Therefore, energy saving is really important in this sector. In this study, the energy saving potential of a dairy enterprise was examined based on energy audit. First, energy saving potential was determined with standard and target equations that were generated according to the current energy consumption of enterprise. Some measurements were made on energy-consuming devices. The devices that do not work efficiently and points with energy leakage have been determined with the measurements. Some projects were suggested for energy saving. It was determined that 332.51 TOE (tons of oil equivalent) of energy would be saved annually thanks to the suggested projects. It was also understood, with the result equation generated, that the production of the enterprise should not fall below 3810 Tons/Month in order the suggested projects to be useful in energy saving.

To cite this article:

Akkurt, F., & Özsan, İ.B. (2025). Examining the energy saving potential of a dairy enterprise based on an energy audit. *Necmettin Erbakan University Journal of Science and Engineering*, *7*(1), 115-125. https://doi.org/10.47112/neufmbd.2025.79

***Corresponding Author:** Fatih Akkurt, *fakkurt@erbakan.edu.tr*

INTRODUCTION

For centuries, energy has been one of the indispensables of humanity. Energy has a large share of all our needs and its use is increasing day by day. That's why generating energy with the least harm to our environment and using it in the most efficient way has become the subject of very different scientific disciplines. For example, while the reuse of coal waste in energy generation is a subject of materials engineering, designing buildings according to minimum energy needs is a subject of architecture [1,2].

Energy audit is one of the most popular methods to examine the efficient use of energy. It has a large scale of application for residences, hotels, hospitals and factories etc. Energy audits have become mandatory in many countries in businesses with high energy consumption. According to the law prepared by the Ministry of Energy and Natural Resources in Turkey, in the industrial facilities with an average energy consumption value of 1000 TOE (tons of oil equivalent) or more for the last three years or with a total construction area more than 20,000 m², in the commercial enterprises with an energy consumption above 500 TOE or with a total construction area more than10,000 m², in the public buildings with an energy consumption of 250 TOE and in the facilities generates electricity above 100 MW is mandatory to appoint an energy manager. [3].

According to the Food and Agriculture Organization (FAO) reports, world milk production in 2023 is approximately 950 million tons [4]. Turkey is one of the leading countries in milk production. It is the 8th largest milk producer in the world and the 3rd largest milk producer in Europe. Total milk production in 2021 is determined as 23.2 million tons [5]. Therefore, it is important to reduce the energy consumption of dairies by researching energy saving methods in that sector.

A high amount of energy is used in dairy and other food industries processing, manufacture and storage of various products [6-7]. So, the use of energy and its saving is one of the important subjects of the dairy sector. The energy audit and analysis of energy saving potential in the dairy sector have been carried out by some researchers. Of these, Altan and Kayışoğlu [8] conducted an energy audit in a raw milk production enterprise in Tekirdağ province and identified energy saving opportunities by making cost analyzes of efficiency-increasing projects. They determined that there will be an energy saving potential of 16 kW through the implementation of some energy saving projects. Josijević et al [9] conducted a case study for a medium dairy production company from Central Serbia. They determined that the proposed energy conservation measures can ensure 11-15% energy savings for electricity and 20-23% of heat energy annually. Boutaghriout et al [10] carried out the energy use and cost analysis of three dairies in Algerian that their main energy sources were electricity and natural gas. They suggested the possibilities of replacing old pumps with high-efficiency ones and integrating solar thermal energy into the system. Söğüt et al [11] developed energy consumption equations for a tomato paste factory based on its production and energy consumption data. They calculated that the energy saving potential of the enterprise at a rate of 10.13% depending on the specific energy consumption. Işık and Akan [12] carried out the energy saving study of the industrial double face sheepskins manufacturing plant. They calculated that the energy saving potential of the enterprise can be realized as 9.9%, that is, 36,168 TOE per year. Aydın and Çankaya [13] examined energy consumption of an enterprise with an annual energy consumption of over thousand TOE in the food sector. They determined 128 TOE annual energy savings thanks to some proposed solutions.

In this study, the energy saving potential of a dairy enterprise with an annual energy consumption above 1000 TOE was examined based on energy audit. Within this scope, energy consumption data of the enterprise was obtained and its energy saving potential was determined with standard and target equations that were generated according to the current energy consumption of enterprise. By making some measurements on energy consuming devices, the inefficient devices and points where energy leaks were determined. Some projects were suggested for energy saving. According to the projects to be

implemented, the annual energy saving amount of the business and how much of the energy saving potential of the business can be achieved have been determined.

MATERIALS AND METHODS

The enterprise where energy audit was conducted is a dairy facility with a daily milk processing capacity of 900 tons and the primary product group being milk powder, as well as producing cheese, kashar, butter, clarified butter, cream, yoghurt and derivatives. Natural gas and electrical energy are used as energy sources in the facility. Within the scope of the energy audit, first, the energy consumption amounts of the enterprise in the last three years were determined. Subsequently, the energy consumption points of the enterprise were determined, and their energy performances were measured with some devices such as energy analyzer, compressed air flow meter, thermal camera, flue gas analyzer, ultrasonic liquid flow meter, air quality probe, ultrasonic leak detector, pitot tube and propeller speed probe. The brands and intended uses of the measurement devices used in the energy audit are presented in Table 1.

Table 1
The brands and intended uses of the measurement devices

	Purpose of the measurement	Device	Brand of the device
Boilers	Determination of heat losses	Thermal camera	Testo 883-2
	Determination of flue gas components	Flue gas analyzer	Nova Plus
	Determination of linear velocity of fluid	Speed Probe	Testo/440 dP
Insulation	Determination of liquid temperature	Immersion Temperature Probe	Testo 435
	Determination of heat losses	Thermal camera	Testo 883-2
	Determination of surface temperature	Surface Temperature Probe	Testo 435
Compressors	Determination of air flow rate	Compressed air flow meter	VP Instruments/VPS
	Determination of compressed air leakage	Ultrasonic leak detector	UE Systems /UP3000SL
Electric Motors	Determination of energy consumption, harmonics and power factor	Energy analyzer	Fluke / 1732
	Determination of power consumption	Clamp ammeter	Unit Clamp Ammeter
Pumps	Determination of energy consumption, harmonics and power factor	Energy analyzer	Fluke / 1732
	Flow measurements	Ultrasonic liquid flowmeter	GE Transport / PT 878
Cooling	Determination of energy consumption	Energy analyzer	Fluke / 1732
	Flow measurements	Ultrasonic liquid flowmeter	GE Transport / PT 878
Fans	Determination of linear velocity of fluid	Speed Probe	Testo/440 dP
Lightings	Determination of lightening	Luxmeter	UNIT Luxmeter

Energy Saving Projects

Depending on the measurements, the energy audit study was evaluated under eight main projects in the inefficient devices and points where energy leaks were determined.

Boilers

There are two natural gas-fired steam boilers in the enterprise: Selnikel boiler and Theta boiler. The efficiencies and waste heat potentials of the boilers were determined according to the measurements.

To determine the efficiency of the boiler system, flue gas content and temperature were measured with a flue gas analyzer in the boiler chimneys. The linear velocity must be known to determine the flue gas flow rate. Dynamic pressure was measured with a pitot tube to determine the linear velocity. Chimney dimensions were also measured. The surface temperatures of the boiler were measured with a probe to determine the thermal losses on the surfaces. The boiler efficiencies were calculated with the following equation:

$$\mu_b = \frac{m_b * i_b - m_s * i_s}{B * H_u} \quad (1)$$

$\boldsymbol{\mu_b}$: Boiler efficiency, $\boldsymbol{m_b}$: Steam flow rate (kg/h), $\boldsymbol{m_s}$: Water flow rate (kg/h), $\boldsymbol{i_b}$**:** Steam enthalpy (kcal/kg), $\boldsymbol{i_s}$: Feed water enthalpy (kcal/kg), **B**: Fuel flow rate (kg/h), $\boldsymbol{H_u}$: Fuel lower heating value (kcal/kg)

The waste heat amount of the boilers was calculated with the following equation:

$$Q = m * (c_1 * T_1 - c_2 * T_2) \quad (2)$$

Q: Waste heat amount (kcal), $\boldsymbol{m}$: Air/Water flow rate (kg/h), $\mathbf{c_1}$**,** $\mathbf{c_2}$: Air/Water specific heat (kcal/Nm^3°C), $\mathbf{T_1}$ **,** $\mathbf{T_2}$: Heat transfer fluid temperatures (°C)

As a result, it was concluded that it was necessary to apply combustion adjustment to the Theta steam boiler, to apply an economizer to the Selnikel boiler and to operate the Theta steam boiler as the primary boiler.

Insulation

Energy leaks in the prosses were measured with a thermal camera and surface temperature probe. The heat losses were calculated with the following basic heat transfer equations. The target surface temperature intended to be at 50ºC after insulation. According to the calculations, some insulation applications were suggested for valves, hot lines and surfaces in order to prevent heat losses.

$$Q_C = U * (T_1 - T_1) \quad (3)$$

$$Q_R = \varepsilon * \sigma * (T_1^4 - T_3^4) \quad (4)$$

$\boldsymbol{Q_C}$: Heat flow density by conduction and convection (W/m²), $\boldsymbol{Q_R}$: Heat transfer by radiation (W), $\mathbf{T_1}$: Surface temperature (K), $\mathbf{T_2}$: Ambient Temperature (K), **U**: Heat transfer coefficient by conduction and convection (W/m²K), **σ**: Boltzmann's constant (5,67 x 10^{-8} W/m²K⁴), **ε**: Emission Coefficient (0< ε<1), $\mathbf{T_3}$: Ambient wall temperature (K)

Compressors

There are three compressors in the enterprise: two active and one spare. Electrical and mechanical measurements were conducted for compressors and air lines. Electrical measurements included measurements of electric motors that drive the compressors. Mechanical measurements included measurements of pressure, temperature values, air flow rates and air leaks of compressors. The amount of electricity consumed in the compressors was measured with an energy analyzer. The amount of air leaks and power loss of compressors were calculated with the following equation. Periodic inspection and maintenance are recommended to prevent air leaks.

The amount of leakage is determined with the following equation:

$$\dot{L} = \frac{\dot{C} * t_1}{t_1 + t} \quad (5)$$

L̇: The amount of air leakage (lt/s), **Ċ**: Compressor Capacity (lt/s), $\mathbf{t_1}$: Compressor loaded working time (s), **t**: Compressor unloaded working time (s)

The power loss in compressor was calculated with the following equation:

$$P = \frac{\dot{L}}{3}(kW) \quad (6)$$

Electric Motors

The power of electric motors was measured with an energy analyzer from the electrical supply panels. Annual energy consumption was determined with the following equations. In measurements, the number of motors, label value, power consumption, efficiency and operating hours were taken into consideration. As a result, it was recommended to replace the existing electric motors with high-efficiency electric motors.

$$P_{m,n} = A * V * 1{,}73 * LF \quad (7)$$

$$P_{m,i} = \frac{P_{m,n}}{\mu_m} * 100 \quad (8)$$

$$AC = P_{e,i} \times h_a \quad (9)$$

$\mathbf{P_m}$: Nominal motor power (kW), **LF**: Load factor, $\mathbf{P_{m,i}}$: Instantaneous motor power (kW), $\boldsymbol{\mu_m}$: Motor efficiency, $\mathbf{h_a}$: Annual working hours, **AC**: Annual energy consumption (kWh)

Pumps

Flow rates, fluid pressures, fluid temperatures and active power values of the pumps were determined with flow meters, manometers, thermometers and electrical supply panels to determine their efficiency with the following equations. As a result of measurements, it was recommended to replace low-efficiency pumps in the system with more efficient pumps.

$$P_P = \frac{\rho * g * Q * H}{1000 * \mu_p} \quad (10)$$

$\mathbf{P_P}$: Pump shaft power (kW), **ρ**: Density of fluid (kg/m^3), **g**: Gravitational acceleration, **Q**: Flow rate (m^3/s), **H**: Total differential height (m), $\boldsymbol{\mu_p}$: Pump efficiency

Cooling

The cooling load and COP (coefficient of performance) of the chillers were determined according to the measurements. It has been determined that the cooling load and COP value of chillers was slightly below the ideal levels. So, no project was recommended for cooling units.

$$COP = \frac{\dot{m} * (i_o - i_i)}{P_{chill}} \quad (11)$$

$\boldsymbol{\dot{m}_b}$: Refrigerant flow rate (kg/s), $\boldsymbol{i_i}$: Refrigerant evaporator inlet enthalpy (kcal/kg), $\boldsymbol{i_o}$**:** Refrigerant evaporator outlet enthalpy (kcal/kg), $\mathbf{P_{chill}}$: Chiller power (kW)

Fans

There were five tower units in the enterprise that produced milk powder and whey powder. There was a chimney fan in each tower. Mechanical and electrical measurements were carried out to examine the operating regime of the fans and determine their total efficiency. The efficiency of fans was determined with the following equations. The results were compared with higher efficiency fans. Then, it was suggested to replace the fans with more efficient fans.

$$\mu_{total} = \mu_f * \mu_{ds} * \mu_{em} \quad (12)$$

$$P_f = \frac{\Delta p * V * A}{3.600 * 102} \quad (13)$$

$$\mu_f = \frac{P_f}{P_s} \quad (14)$$

$$\mu_{ss} = \frac{P_s}{P_{em}} \quad (15)$$

$$\mu_{em} = \frac{P_{em}}{P_e} \quad (16)$$

$\boldsymbol{\mu_{total}}$: Total efficiency (%), $\mathbf{P_f}$: Fan power (kW), **V**: Velocity (m/s), **A**: Cross Section Area (m²), **ΔP**: Pressure Difference (mmSS), $\mathbf{P_s}$: Shaft power power (kW), $\boldsymbol{\mu_f}$: Fan efficiency (%), $\mathbf{P_{em}}$: Elektrik motoru gücü (kW), $\boldsymbol{\mu_{ss}}$: Shaft system efficiency (%), $\mathbf{P_e}$: Power from the grid (kW), $\boldsymbol{\mu_{em}}$: Electric motor efficiency (%)

Lighting

There were 280 lighting armatures with 2x18 W power in the enterprise. It is recommended to replace old types with LEDs that can provide the same function with less energy consumption. Annual energy saving was determined with the following equation:

$$E_{a,s,l} = (P_{led} - P_{std}) * t_{a,lig} \quad (17)$$

$\mathbf{E_{a,s,l}}$: Annual lighting saving(kWh), $\mathbf{P_{LED}}$: LED lighting armature power (W), $\mathbf{P_{std}}$: Standard lighting armature power (W), $\mathbf{t_{a,lig}}$: Annual lighting time (h)

Determination of Energy Saving Potential

First, the standard and the target equations and lines were created according to current monthly production and energy consumption amounts. Then, the annual energy saving of the enterprise to be achieved through the implementation of the projects was determined. The projects result equation and line were created according to annual energy saving values. Lastly, it was evaluated how close to the targeted energy saving could be achieved with the help of target and projects result lines.

RESULTS AND DISCUSSIONS

The monthly average production and energy consumption data of the enterprise for the last three years were determined within the scope of energy audit. The average monthly production and energy consumption values of the enterprise for three years were presented in Table 2. The annual average production of enterprise was 44378 tons. The total energy consumption of the business was 5666 TEP, including 1453 TEP electricity and 4243 TEP natural gas. The distribution of the energy types used in the enterprise is given in Figure 1. It was determined that 74.9% of the energy consumption was natural gas while 25.1% was electricity.

Table 2

The production and energy consumption values of enterprise

Months	Production TON	Electricity TOE	Natural Gas TOE	Total TOE
January	3690	116	478	594
February	3732	107	404	511
March	4065	117	450	567
April	4410	114	445	560
May	3968	126	374	500
June	3960	128	365	493
July	3751	144	259	402
August	3541	140	228	368
September	3424	126	251	377
October	3315	101	288	390
November	3202	92	345	437
December	3319	112	355	467
TOTAL	44378	1423	4243	5666

Energy Saving Projects

Depending on the measurements, the energy audit study was evaluated under eight main projects in the inefficient devices and points where energy leaks were determined

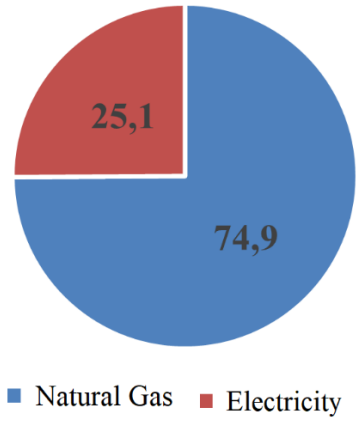

Figure 1
Distribution of energy consumption types

The annual energy saving values to be achieved by the implementation of the projects were presented collectively in Table 3. It was calculated that with the proposed projects, 332.51 TOE can be saved annually from natural gas energy and 133.69 TOE from electricity. It has been determined that by realizing these projects, a profit of $654460 can be saved as a result of an investment cost of $545082. It was seen that the highest energy gain among the projects will be with the application of economizer to the Selnikel steam boiler with 199.96 TOE. Although this application has an investment cost of $81382 it has been recommended that it should be a priority project with a very short payback period of 0.4 years. The change of compressors can be postponed due to its low energy savings and long payback periods. In general, a ranking can be made in the implementation of projects by taking into account the payback periods.

The energy consumption values of the current, targeted and after the project's situations depending on the monthly production amounts were presented in Table 4. The sum of annual energy consumption in the current situation by natural gas and electricity was determined as 5666 TOE. The standard equation has been created according to the monthly production and energy consumption amounts in the current situation. The standard equation was found to be y=0.1408x-48.676 with the regression compatibility coefficient of R^2=0.42. The target equation relation was obtained as y=0.1858x-258.72 by using the points under the standard line. The target line was created by applying all monthly production values to the target equation. The target line expresses the amount of ideal energy consumption depending on the monthly production. The annual energy saving that corresponds to 9.2% of annual energy consumption was determined as 525 TOE according to the target equation. The monthly energy consumption values after the implementation of projects were determined by subtracting the monthly saving from the current energy consumption values. It has been determined that as a result of the implementation of the projects 466.2 TOE annually and 38.85 TOE monthly energy savings will be achieved. The projects result equation was determined as y=0.1408x-87.526. Standard, target and projects result lines and equations are presented in Figure 2-4 depending on monthly production and energy consumption values. The energy saving after the projects was determined to be 8.2% of annual energy consumption.

Table 3
Total results of the energy savings projects

	Projects	Annual Energy Saving Potential (TOE)		Benefit and Investment Cost of the Project ($)		Payback Period (Year)
		Natural Gas	Electricity	Benefit	Investment Cost	
Boilers	Applying Combustion Adjustment to Theta Steam Boiler	39.43		40969	1595	0.04
	Economizer Application to Selnikel Steam Boiler	199.96	-	206962	81382	0.40
	Application of Operating Theta Steam Boiler as Primary Boiler	59.92	-	62265	-	-
Insulation	Insulation on Valves, Lines and Surfaces	33.20	-	34495	18771	1.65
Compressors	Replacement of Compressors	-	31.77	74287	239866	6.45
	Elimination of Losses and Leaks in Compressed Air Lines	-	26.29	61469	-	-
Electric Motors	Replacement of Electric Motors	-	41.86	96308	57527	0.60
Pumps	Replacement of Electric Pumps	-	18.29	42072	62223	4.85
Cooling Fans	No project was suggested.					
	Replacement of Fans	-	11.84	27256	71069	13.67
Lightings	Replacement of Armatures	-	3.64	8377	12649	1.51
	TOTAL	332.51	133.69	654460	545082	

Table 4
The energy consumptions of the current, targeted and projects result situations

	Current		Targeted		Projects Results	
	Production	Consumption	Consumption	Saving Potential	Consumption	Saving
	TON	TOE	TOE	TOE	TOE	TOE
January	3690	594	427	167	555	38.85
February	3732	511	435	77	472	38.85
March	4065	567	497	70	528	38.85
April	4410	560	561	-1	521	38.85
May	3968	500	479	22	462	38.85
June	3960	493	477	16	454	38.85
July	3751	402	438	-36	364	38.85
August	3541	368	399	-31	329	38.85
September	3424	377	377	-1	338	38.85
October	3315	390	357	32	351	38.85
November	3202	437	336	101	398	38.85
December	3319	467	358	109	428	38.85
TOTAL	44378	5666	5141	525	5200	466.2
PERCENTAGE				9.2%		8.2%

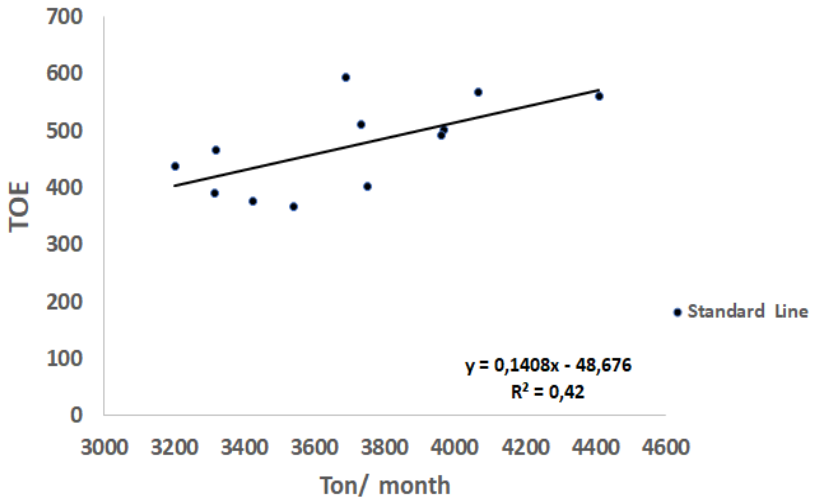

Figure 2
The standard equation and line

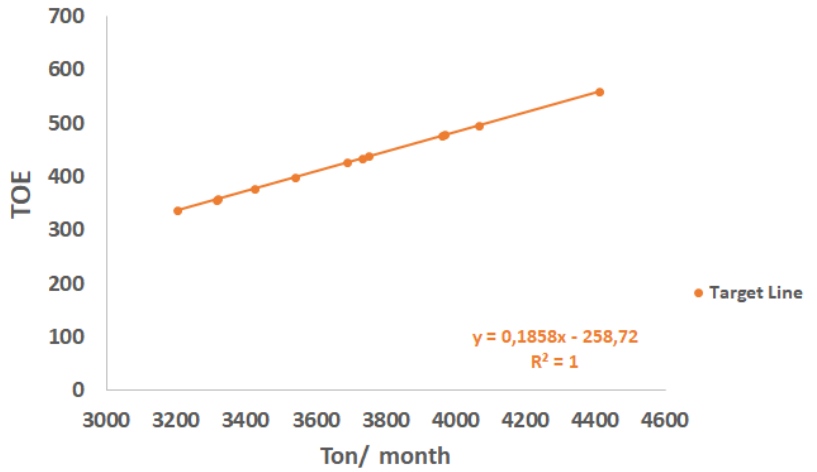

Figure 3
The target equation and line

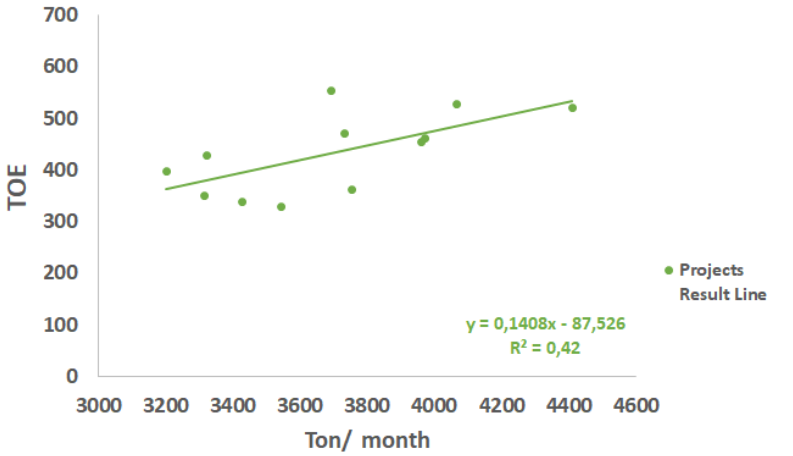

Figure 4
The Projects result equation and line

As a result of the energy audit study, it was determined that the targeted annual energy saving was 525 TOE as 9% of annual energy consumption. It has been calculated that the energy savings of the enterprise will be 466.2 TOE as 8.2% of annual energy consumption according to implementation of the projects. That means that the targeted energy saving is near to be approached. In addition, the combination of the standard, target and projects result equations and lines are presented in Figure 5.

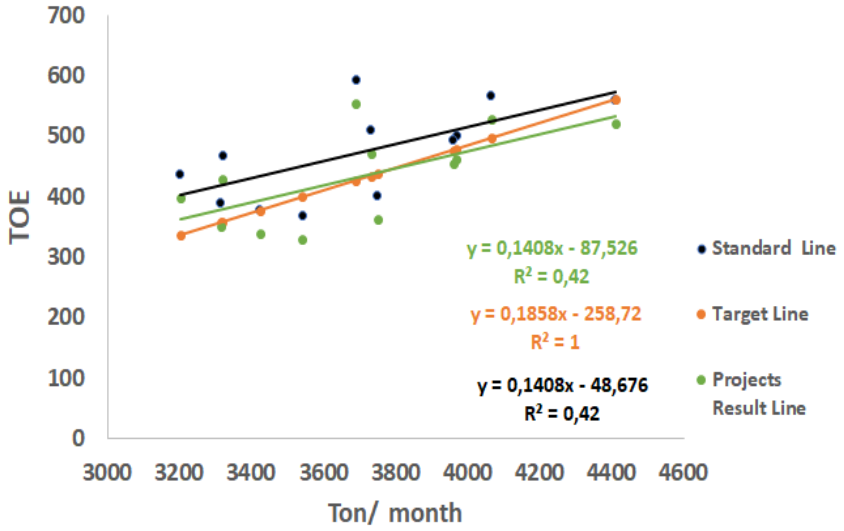

Figure 5
Combination of the standard, target and projects result equations and lines

A monthly production value was determined as 3810 Tons/Month at the intersection of the target and the project's result lines. That means that the proposed projects do not provide the targeted energy savings below that production amount, however they cause them to exceed the targeted energy saving above that amount. In this case, to reduce the effect of constant energy consumptions, independent of the production amount, the monthly milk process should not be less than the mentioned amount. In addition to the eight projects proposed to improve the current situation in the enterprise, additional energy input can be provided by installing solar energy systems that produce both heat and electricity. In this case, it will be possible to exceed the targeted savings values.

Ethical Statement
This study is derived from a master's thesis entitled "ENERGY AUDIT OF A MILK PROCESSING PLANT" by İsmail Buğrahan ÖZSAN, submitted under the supervision of Assistant Professor Dr. Fatih AKKURT in January 2024.

Author Contributions
Research Design (CRediT 1) F.A. (%50) – İ.B.Ö. (%50)
Data Collection (CRediT 2) F.A. (%20) – İ.B.Ö. (%80)
Research - Data Analysis - Validation (CRediT 3-4-6-11) F.A. (%20) – İ.B.Ö. (%80)
Writing the Article (CRediT 12-13) F.A. (%90) – İ.B.Ö. (%10)
Revision and Improvement of the Text (CRediT 14) F.A. (%90) – İ.B.Ö. (%10)

Financing
This article was not funded by any public, commercial or non-profit organization.

REFERENCES

[1] Ş. Bülbül, E. Ayhan, H. Gökmeşe, Effect on Mechanical Properties of Addition of Coal Ash as Thermal Power Plant Waste to SBR Matrix Compounds, *Necmettin Erbakan University Journal of Science and Engineering*, 5(2) (2023), 135-146. doi: 10.47112/neufmbd.2023.14.

[2] H.D. Arslan, S.M. Acar Bilgili, S. Doğan, Natural Ventilation Analysis of TOKİ Type Houses on Different Climate Regions, *Necmettin Erbakan University Journal of Science and Engineering*, 6(1) (2024), 21-39. doi:10.47112/neufmbd.2024.30.

[3] İ.B. Özsan, Energy Audit of a Milk Processing Plant, MS Thesis, *Necmettin Erbakan University Institute of Science*, Department of Energy Systems Engineering, Konya, 2024.

[4] Food and Agriculture Organizations of the United Nations, (2023). https://openknowledge.fao.org/home. (erişim 20 Mayıs 2023).

[5] Turkish National Dairy Council (TNDC). (2023). http:// ulusalsutkonseyi.org.tr/en/. (erişim 15 Mayıs 2023).

[6] M. Janzekovic, B. Mursec, P. Vindis, F. Cus, Energy saving in milk processing, *Journal of Achievements in Materials and Manufacturing Engineering.* 33 (2) (2009), 197-203.

[7] Charan, R. and Prasad S. (1993). Energy Conservation in Milk Spray-Drying Plant. *Journal of Food Engineering* 18, 247-258. doi:10.1016/0260-8774(93)90089-3

[8] A.D. Altan, B. Kayışoğlu, Integration of Projects Enhancing Productivity Based on Energy Audit Data in Raw Milk Production Sector—a Case Study in Turkey, *Digitizing Production Systems: Selected Papers from ISPR2021*. (2021), 107-120. doi: 10.1007/978-3-030-90421-0_9.

[9] M.M. Josijević, V.M. Šušteršič, D.R. Gordić, Ranking energy performance opportunities obtained with energy audit in dairies, *Thermal Science*. 24 (2020), 2865-2878. doi: 10.2298/TSCI1911251000J.

[10] S. Bhardwaj, R. Prakash, S. Malik, V.K. Singh, Energy auditing in a dairy farm, school and temple complex in Hisar district, Haryana, India, *India. Indian Journal of Health and Well-being Wellbeing*. 9 (2018), 886-891.

[11] Z .Söğüt, N. İlten Z. Oktay, Examination of Energy Saving Potantial Depending on Energy Audit in Tomato Paste factory. *6th İnternational Advanced Technologies Symposium.* (2011), *Elazığ, Turkey*.

[12] N.O. Işık, A.E. Akan, Investigation of Energy Saving Potential of a Double Face Sheepskins Production Plant by Specific Energy Consumption Method, *European Journal of Science and Technology*. 11 (2018), 22-26.

[13] F. Aydın, B. Çankaya, Investigation of the Energy Audit Annual Consumption of 1.000 TOE, *Ereğli Journal of Agricultural Sciences,* 3 (2023), 59-67. doi: 10.54498/ETBD.2023.23.

FEN ve MÜHENDİSLİK BİLİMLERİ DERGİSİ

Vol: 7 No: 1 Year: 2025 | Araştırma Makalesi/Research Article | e-ISSN: 2667-7989

https://doi.org/10.47112/neufmbd.2025.80

s-Triazin İçeren Çok Dişli Schiff Bazlarının Sentezi ve Karakterizasyonu: Bazı Geçiş Metali Komplekslerinin Araştırılması

Erdem BÜYÜKASLAN [1] Ahmed Hamdi MİRGHANİ [1] Şaban UYSAL [1*]

[1] Karabük University, Faculty of Science, Department of Chemistry, Karabük, Türkiye

Makale Bilgisi

Geliş Tarihi: 08.08.2024
Kabul Tarihi: 24.11.2024
Yayın Tarihi: 30.04.2025

Anahtar Kelimeler:
Çok dişli ligand,
s-Triazin,
Salen,
Saloph.

ÖZET

Bu çalışmada ilk olarak sırasıyla siyanürik klorür ve hidrokinon veya 1,4-fenilendiaminin reaksiyona sokulmasıyla iki bazik ara ürün elde edildi. Bu bileşiklerin 4-hidroksibenzaldehit ile reaksiyonundan EBA1 ve EBA2 elde edildi. Bu bileşiklerin sırasıyla 4-aminobenzoik asit ve 5-aminoizoftalik asit ile reaksiyona sokulmasıyla EBL1-EBL4 olarak kodlanan dört hedef ligand elde edildi. Elde edilen bu ligandlar, FTIR, elementel analiz, ^{1}H ve ^{13}C NMR yöntemleriyle karakterize edildi. Elde edilen hedef ligandların $[M(Salen/Saloph)]_2O$ (M= Cr^{3+} ve Fe^{3+}) ile reaksiyonu sonucu [M(Salen/Saloph)] başlıklı kompleksler elde edildi. Bu kompleksler elementel analiz ve FTIR kullanılarak karakterize edildi. Komplekslerin manyetik özellikleri araştırıldı. Komplekslerin termal dayanıklılığı TGA tekniği kullanılarak belirlendi. Çalışmanın sonunda termal olarak kararlı ve paramanyetik özelliklere sahip 6 adet tetrapodal ligand ve 16 adet tetrapodal kompleks sentezlenmiş ve karakterize edilmiştir.

Synthesis and Characterization of Multidentate Schiff Bases Containing s-Triazine: Investigation of Their Some Transition Metal Complexes

Article Info

Received: 08.08.2024
Accepted: 24.11.2024
Published: 30.04.2025

Keywords:
Polydentate ligand,
s-Triazine,
Salen,
Saloph.

ABSTRACT

In this paper, two basic mid-products were obtained by reacting cyanuric chloride and hydroquinone or 1,4-phenylendiamine, respectively. EBA1 and EBA2 were obtained from the reaction of these compounds and 4-hydroxybenzaldehyde. Four target ligands encoded as EBL1-EBL4 were obtained by reacting these compounds with 4-aminobenzoic acid and 5-aminoisophthalic acid, respectively. These obtained ligands were characterized by FTIR, elemental analysis, ^{1}H and ^{13}C NMR and methods. The obtained target ligands were reacted with $[M(Salen/Saloph)]_2O$ (M= Cr^{3+} and Fe^{3+}) to obtain [M(Salen/Saloph)] capped complexes. These complexes were characterized using elemental analysis, and FTIR. The magnetic properties of the complexes were investigated. The thermal endurance of the complexes was determined using the TGA technique. At the end of the study, 6 tetrapodal ligands and 16 tetrapodal complexes, which are thermally stable with paramagnetic properties, were synthesized and characterized.

To cite this article:
Büyükaslan, E., Almahdi, A.H.M. & Uysal, Ş. (2025). Synthesis and characterization of multidentate schiff bases containing s-Triazine: Investigation of their some transition metal complexes. *Necmettin Erbakan University Journal of Science and Engineering*, *7*(1), 126-140. https://doi.org/10.47112/neufmbd.2025.80

***Sorumlu Yazar:** Şaban Uysal, sabanuysal@karabuk.edu.tr

INTRODUCTION

Schiff bases are defined as compounds formed as a result of the condensation reaction between primary amines and aldehydes or ketones, containing a carbon-nitrogen double bond (C=N) in their structure. This synthesis was first performed by German chemist Hugo Schiff in 1869. In the 1930s, Pfeiffer later utilized them as ligands. Schiff bases are also known as azomethines or imines [1]. The formation of Schiff bases from the reaction between primary amines and carbonyl compounds (aldehydes or ketones) occurs in two main steps. In the first step, a condensation reaction occurs between the primary amine and the carbonyl group, resulting in the formation of a carbinolamine intermediate. In the second step, this intermediate undergoes dehydration to produce the Schiff base [2]. Schiff bases exhibit different properties depending on the substituents attached to the imine group in their structure. Electronegative substituents on the nitrogen atom enhance the stability of azomethine. Schiff bases are more stable against alkali-containing groups, but they undergo hydrolysis in a low pH range. Upon hydrolysis, they convert to carbonyl and amine compounds. If there is an electronegative amine with an unshared electron on the nitrogen, the reaction is completed entirely. In this case, they are isolated with high efficiency since hydrolysis does not occur. The inductive effect is another factor affecting the stability of azomethines [3]. Schiff bases are preferred due to their low cost, ease of synthesis, and their highly stable chemical and thermal properties. They are used in the cosmetic industry, plastic industry, pesticides, chemotherapy in medicine, dye industry, electronics, analytical chemistry, polymer synthesis, as photographic chemicals, and for corrosion prevention in metals [4-6]. Medicines and many natural compounds consist of heterocyclic ring structures. In the field of chemistry, especially in inorganic and organic chemistry, there is a greater need for heterocyclic compounds, and they play an effective role in most synthesized compounds. Heterocyclic compounds are obtained as a result of the substitution of carbon atoms in the structure with heteroatoms such as sulfur, nitrogen, and oxygen. s-Triazines are also compounds with heterocyclic structures. s-Triazine compounds are formed by the substitution of three carbon atoms in the benzene ring with nitrogen atoms [7, 8]. 1,3,5-Triazine stands out as a captivating chemical scaffold in medicinal chemistry endeavors, owing to its diverse array of biological roles, including antimicrobial, antifungal, antimalarial, carbonic anhydrase inhibition, and anticancer properties [9-11]. Schiff bases with an s-triazine core demonstrate a range of biological activities, including anticancer, antimycobacterial, antibacterial, antidepressant, analgesic effects, and enzyme inhibition. Additionally, derivatives of 1,3,5-triazine have demonstrated the ability to bind to and regulate estrogen receptor alpha (ERα) and estrogen receptor beta (ERβ) [12,13].

In this study, we aimed to increase the thermal and electrical properties of such compounds to a higher level by synthesizing s-triazine-based supramolecular Schiff base ligands. For this reason, salen/saloph compounds have been used because they can coordinate well with other ligands. Starting from 2,4,6-trichloro-1,3,5-triazine, tetrapodal s-triazine-based Schiff base compounds containing carboxyl groups were synthesized. Salen/saloph initial complexes and capping complexes were obtained from these synthesized compounds, and the magnetic and thermal behaviors of the resulting complexes were examined.

EXPERIMENTAL

Apparatus and reagents

The ^{1}H and ^{13}C NMR analyses of the ligands were performed using a Bruker AvanceCore NMR spectrometer operating at 400 MHz. The ^{1}H and ^{13}C NMR spectra of the ligands were recorded in DMSO-d_6. Elemental analyses (C, H, N) of the compounds were carried out using a LECO 932 CHNS analyzer. The FTIR spectra of the synthesized complexes were recorded using a Thermo Nicolet iS5 FTIR spectrometer equipped with an ID7 ATR accessory. The metal contents of each complex were determined on a Varian, Vista AX CCD Simultaneous Model Inductively Coupled Plasma Atomic

Emission Spectrophotometer (ICP-AES). Magnetic susceptibility measurements of the complexes were performed using the Gouy method on a Sherwood Scientific MX Gouy device, with Hg[Co(SCN)4] as the calibrant. The effective magnetic moments, μ_{eff}, per metal atom were calculated from the expression: $\mu_{eff} = 2.84\sqrt{X_M}T$ B.M., where X_M is the molar susceptibility. TGA analyses of the compounds were conducted using a HITACHI STA7300 Thermal Analysis System.

Cyanuric chloride (Merck), 4-hydroxybenzaldehyde (Sigma), p-phenylenediamine (Sigma), 5-amino isophthalic acid (Sigma), 4-aminobenzoic acid (Sigma), hydroquinone (Sigma), potassium carbonate (Sigma), sodium carbonate (Sigma), sodium sulfate (Sigma), and solvents including acetone (Merck), benzene (Merck), ethyl acetate (Merck), ethanol (Sigma), methanol (Sigma), 1,4-Dioxane (Merck), N,N-dimethylformamide (Merck) were purchased from the mentioned companies. [(MSalen/Saloph)$_2$O] (M = Cr^{3+} and Fe^{3+}) initial complexes, which are used in complex formation reactions and called ligand complexes, were synthesized and used according to the literature [14].

Synthesis of 4,4',4'',4'''-(((1,4-phenylenebis(oxy))bis(1,3,5-triazine-6,2,4-triyl))tetrakis(oxy))tetrabenzaldehyde (EBA1) and 4,4',4'',4'''-(((1,4-phenylenebis(azanediyl)) bis(1,3,5-triazine-6,2,4-triyl))tetrakis(oxy))tetrabenzaldehyde (EBA2)

EBS1 (2.03 g, 5.00 mmol) or EBS2 (2.02 g, 5.00 mmol) and 4-hydroxybenzaldehyde (2.69 g, 22.00 mmol) were weighed and placed into a 100 mL flask. Approximately 5.00 g of Na_2CO_3 and 50 mL of benzene were added. The mixture was stirred at 70°C under reflux for 24 hours. Then, the solid sodium carbonate residue was filtered under vacuum through filter paper. 20 mL of hot ethyl acetate was added twice, and the solid residue was discarded. The remaining liquid portion was washed twice with a 10% sodium carbonate solution and twice with distilled water. Sodium sulfate was added and the mixture was left overnight. The sodium sulfate was filtered out, and the organic solvent was evaporated. The resulting solid was recrystallized from ethanol. Compound EBA1 was elucidated using FTIR, ^{1}H, and ^{13}C NMR spectroscopy and elemental analysis method.

EBA1: Yellow solid; Yield: 78%; M.P.: 265-268°C; FTIR (ATR, cm^{-1}): 1698 (C=O), 1585 (C=N_{trz}), 1500, 1424 (C-C_{arom}), 1296 (C-O_{phen}); ^{1}H NMR δ (ppm): 9.87 (s, 4H), 7.84 (d, 8H), 7.15 (d, 8H), 7.07 (d, 4H); ^{13}C NMR δ (ppm): 192.10 (C9), 184.90 (C4), 177.50 (C3), 161.10 (C5), 150.01 (C2), 132.50 (C7), 123.30 (C1), 121.80 (C6), 116.10 (C8); Calculated/Found Analysis: C: 64.17/64.13, H: 3.23/3.21, N: 11.23/11.22, O: 21.37/21.33

EBA2: Yellow solid; Yield: 73%; M.P.: 184-187°C; FTIR (ATR, cm^{-1}): 3205 (N-H_{str}), 3069 (C-H_{arom}), 1694 (C=O), 1591 (N-H_{bend}), 1562 (C=N_{trz}), 1510, 1499, 1456, 1418 (C-C_{arom}), 1295 (C-O_{phen}), 1205 (C-N_{str}); ^{1}H NMR δ (ppm): 9.87 (s, 4H), 7.85 (d, 8H), 7.15 (d, 8H), 6.40 (d, 4H), 4.74 (s, 2H); ^{13}C NMR δ (ppm): 192.10 (C9), 184.90 (C4), 171.90 (C3), 161.20 (C5), 133.20 (C8), 131.50 (C7), 128.80 (C2), 122.00 (C6), 118.70 (C1); Calculated/Found Analysis: C: 64.34/64.33, H: 3.51/3.49, N: 15.01/15.00, O: 17.14/17.12.

General synthesis of target ligands (EBL1-EBL4)

A mixture of EBA1 or EBA2 (1.25 mmol) with 4-aminobenzoic acid or 5-aminoisophthalic acid (5.00 mmol) was dissolved in 50 mL of ethanol and 25 mL of DMF (N,N-dimethylformamide). The solution was then heated under reflux at a temperature of 85-90°C for 24 hours, while the reaction progress was monitored using thin-layer chromatography. Upon completion, the excess solvent was removed by evaporation, and the resulting solid product was collected by filtration. This crude product was further purified by recrystallization from an ethanol-DMF mixture. The final compound, labeled as EBL1, was characterized using elemental analysis, FTIR, and both ^{1}H and ^{13}C NMR spectroscopy.

EBL1: Yellow solid; Yield: 72%; M.P.: 334-336°C; FTIR (ATR, cm^{-1}): 1682 (C=O), 1592 (C=N_{im}),

1564 (C=N_{trz}), 1359 (COO^-), 1285 (C-O_{phen}); ^{1}H NMR δ (ppm): 10.60 (s, 4H), 8.69 (s, 4H), 8.24 (d, 8H), 7.79 (d, 8H), 7.60 (d, 8H), 7.08 (d, 8H), 7.01 (d, 4H); ^{13}C NMR δ (ppm): 184.90 (C4), 176.20 (C3), 168.90 (C14), 160.01 (C9), 157.50 (C10), 155.90 (C5), 149.10 (C2), 132.50 (C8), 131.50 (C12), 130.01 (C7), 128.50 (C13), 123.50 (C1), 121.50 (C11), 121.20 (C6); Anal. Calculated/Found: C:66.66/66.64, H:3.62/3.58, N:11.43/11.40, O: 18.28/18.26

EBL2: Red solid; Yield: 79%; M.P.: 202-204°C; FTIR (ATR, cm-1): 3069 (C-H_{arom}), 1702 (C=O), 1644 (C=N_{im}), 1575 (C=N_{trz}), 1498, 1447, 1418 (C-C_{arom}), 1382 (COO^-), 1296 (C-O_{phen}); ^{1}H NMR δ (ppm): 11.16 (s, 8H), 8.69 (s, 4H), 8.51 (s, 4H), 8.02 (s, 8H), 7.65 (d, 8H), 7.01 (d, 8H), 6.56 (d, 4H); ^{13}C NMR δ (ppm): 185.00 (C4), 176.50 (C3), 168.80 (C14), 160.00 (C9), 154.90 (C10), 156.00 (C5), 149.90 (C2), 133.50 (C8), 131.50 (C12), 129.90 (C7), 129.50 (C13), 123.90 (C1), 129.00 (C11), 120.90 (C6); Calculated/Found Analysis: C: 61.72/61.69 H: 3.17/3.16, N: 10.00/9.98, O: 25.12/25.10.

EBL3: Yellow, solid; Yield: 70%; M.P.: 330-332 °C; FTIR (ATR, cm^{-1}): 3286 (N-H_{str}), 1688 (C=O_{str}), 1651 (C=N_{im}), 1625 (N-H_{str}), 1557 (C=N_{trz}), 1496, 1409 (C-C_{arom}), 1361 (COO-), 1315 (C-O_{phen}); ^{1}H NMR δ (ppm): 11.17 (s, 4H), 8.69 (s, 4H), 7.98 (d, 8H), 7.76 (d, 8H), 7.49 (d, 8H), 6.96 (d, 4H), 6.84 (d, 8H), 4.89 (s, 2H); ^{13}C NMR δ (ppm): 169.50 (C4), 172.00 (C3), 169.00 (C14), 160.00 (C9), 157.50 (C10), 155.80 (C5), 132.60 (C8), 131.50 (C12), 130.02 (C7), 129.00 (C2), 128.20 (C13), 121.40 (C11), 121.20 (C6), 118.50 (C1); Anal. Calculated/Found: C: 66.77/66.72, H: 3.79/3.77, N: 13.74/13.72, O: 15.70/15.67.

EBL4: Yellow, solid; Yield: 74%; M.P.: 363°C (dec.); FTIR (ATR, cm^{-1}): 1693 (C=O_{acid}), 1567 (C=N $_{trz\text{-}broad}$), 1504, 1410 (C-C_{arom}), 1359 (COO^-), 1297 (C-O_{phen}); ^{1}H NMR δ (ppm): 11.19 (s, 8H), 8.68 (s, 4H), 8.52 (s, 4H), 8.01 (s, 8H), 7.61 (d, 8H), 6.98 (d, 4H), 6.85 (d, 8H), 4.85 (s, 2H); ^{13}C NMR δ (ppm): 179.00 (C4), 172.50 (C3), 168.90 (C14), 160.00 (C9), 153.80 (C10), 156.00 (C5), 132.50 (C8), 131.40 (C12), 130.70 (C7), 129.10 (C2), 129.50 (C13), 128.90 (C11), 120.90 (C6), 118.50 (C1); Anal. Calculated/Found: C: 61.81/61.79, H: 3.31/3.28, N: 12.01/12.00, O: 22.87/22.85.

The General synthesis of [Cr/FeSalen/Saloph)$_4$] capped complexes (EBC1-EBC16) of target ligands

EBL1, EBL2, EBL3 or EBL4 (0.75 mmol) and [(MSalen/Saloph)$_2$O] (M: Cr^{3+} or Fe^{3+}) [1.50 mmol (for EBL1 and EBL3) or 3.00 mmol (for EBL2 and EBL4)] were weighed and dissolved in 50 mL of methanol. The mixture was stirred under reflux for 3 hours at 75°C. Then the solvent was evaporated, and the solid product was recrystallized from methanol.

EBC1: Green solid; Yield: 70%; M.P.: 246-248 °C (dec.); μ_{eff} (B.M.): 3.83, FTIR (ATR, cm^{-1}): 3050, 3022, 3015 (C-H_{arom}), 2899 (C-C_{aliph}), 1696 (C=O), 1617 (C=N_{imine}), 1597 (C=N_{trz}), 1530,1458, 1440 (C-C_{arom}), 1380 (COO^-), 1290 (C-O_{phen}); Calculated/Found Analysis: C: 63.56/63.55, H: 3.88/3.85, Cr: 8.34/8.32, N: 10.11/10.09, O: 14.11/14.09.

EBC2: Green solid; Yield: 72%; M.P.: 244-247 °C (dec.); μ_{eff} (B.M.): 3.85, FTIR (ATR, cm^{-1}): 3045, 3020, 3010 (C-H_{arom}), 1699 (C=O), 1626 (C=N_{im}), 1592 (C=N_{trz}), 1532,1461,1440 (C-C_{arom}), 1380 (COO^-), 1297 (C-O_{phen}); Calculated/Found Analysis: C: 66.17/66.15, H: 3.60/358, N: 9.38/9.36, O: 13.10/13.07, Cr: 7.74/7.73,

EBC3: Brown solid; Yield: 77%; M.P.: 247-249 °C (dec.); μ_{eff} (B.M.): 1.72, FTIR (ATR, cm^{-1}): 3051,3027,3013 (C-C_{arom}), 2896 (C-C_{aliph}), 1698 (C=O), 1621 (C=N_{im}), 1595 (C=N_{trz}), 1537, 1465, 1440 (C-C_{arom}), 1382 (COO^-), 1296 (C-O_{phen}); Calculated /Found Analysis: C: 63.17/63.15, H: 3.86/3.82, N: 10.05/10.03, O: 14.02/14.01, Fe: 8.90/8.86.

EBC4: Brown solid; Yield: 76%; M.P.: 246-248 °C (dec.); μ_{eff} (B.M.): 1.71, FTIR (ATR, cm^{-1}): 3049, 3035, 3020 (C-H_{arom}), 1695 (C=O), 1618 (C=N_{im}), 1597 (C=N_{trz}), 1530, 1462, 1445 (C-C_{arom}), 1380

(COO^-), 1292 (C-O_{phen}); Calculated /Found Analysis: C: 65.79/65.77, H: 3.58/3.55, N: 9.33/9.31, O: 13.03/13.01, Fe: 8.27/8.25.

EBC5: Green solid; Yield: 80%; M.P.: 346°C (dec.); μ_{eff} (B.M.): 3.84, FTIR (ATR, cm^{-1}): 3045, 3021, 3012 (C-H_{arom}), 2895 (C-H_{aliph}), 1721, 1702 (C=O), 1624 (C=Nim), 1596 (C=N_{trz}), 1535, 1462, 1440 (C-C_{arom}), 1385 (COO^-), 1291 (C-O_{phen}); Analytical Calculated/Found: C: 60.98/60.96, H: 3.79/3.77, N: 9.24/9.22, O: 15.43/15.40, Cr: 10.56/10.53.

EBC6: Green solid; Yield: 74%; M.P.: 341°C (dec.); μ_{eff} (B.M.): 3.83, FTIR (ATR, cm^{-1}): 3041, 3025, 3013 (C-H_{arom}), 1721, 1704 (C=O), 1622 (C=N_{im}), 1597 (C=N_{trz}), 1533, 1466, 1441 (C-C_{arom}), 1388 (COO^-), 1295 (C-O_{phen}); Analytical Calculated/Found: C: 64.45/64.43, H: 3.45/3.42, N: 8.42/8.41, O: 14.06/14.03, Cr: 9.62/9.60.

EBC7: Dark Brown solid; Yield: 81%; M.P.: >300°C (dec.); μ_{eff} (B.M.): 1.70, FTIR (ATR, cm^{-1}): 3047, 3027, 3015 (C-H_{arom}), 2896 (C-H_{aliph}), 1722, 1700 (C=O), 1621 (C=N_{im}), 1595 (C=N_{trz}), 1537, 1465, 1441 (C-C_{arom}), 1382 (COO^-), 1294 (C-O_{phen}); Analytical Calculated/Found: C: 60.50/60.45, H: 3.76/3.74, N: 9.17/9.16, O: 15.31/15.29, Fe: 11.25/11.23.

EBC8: Red solid; Yield: 78%; M.P.: 290°C (dec.); μ_{eff} (B.M.): 1.71, FTIR (ATR, cm^{-1}): 3078, 3045, 3011 (C-H_{arom}), 1721 (C=O), 1602 (C=N_{im}), 1577 (C=N_{trz}), 1531, 1487, 1459, 1443, 1435 (C-C_{arom}), 1376, (COO^-), 1311 (C-O_{phen}); Analytical Calculated/Found: C: 63.99/63.96, H: 3.43/3.39, N: 8.36/8.34, O: 13.96/13.95, Fe: 10.26/10.23.

EBC9: Dark green solid; Yield: 79%; M.P.: 358 °C (dec.); μ_{eff} (B.M.): 3.86, FTIR (ATR, cm^{-1}): 3011 (C-H_{arom}), 1685 (C=O_{acid}), 1620 (C=N_{im}), 1594 (N-H_{bend}), 1565 (C=N_{trz}), 1542, 1496, 1470, 1441 (C-C_{arom}), 1385 (COO^-), 1286 (C-O_{phen}); Calculated/Found Analysis: C: 63.61/63.59, H: 3.96/3.93, N: 11.24/11.21, O: 12.84/12.83, Cr: 8.34/8.32.

EBC10: Dark green solid; Yield: 75%; M.P.: 352 °C (dec.); μ_{eff} (B.M.): 3.84, FTIR (ATR, cm^{-1}): 3016 (C-H_{arom}), 1688 (C=O_{acid}), 1620 (C=N_{im}), 1596 (N-H_{bend}), 1565 (C=N_{trz}), 1542, 1496, 1470, 1442 (C-C_{arom}), 1385 (COO^-), 1290 (C-O_{phen}); Calculated/Found Analysis: C: 66.22/66.20, H: 3.68/3.65, N: 10.44/10.43, O: 11.92/11.90, Cr: 7.75/7.73.

EBC11: Brown solid; Yield: 82%; M.P.: 250 °C (dec.); μ_{eff} (B.M.): 1.72, FTIR (ATR, cm^{-1}): 3014 (C-H_{arom}), 1687 (C=O_{acid}), 1619 (C=N_{im}), 1597 (N-H_{bend}), 1564 (C=N_{trz}), 1543, 1495, 1469, 1443 (C-C_{arom}), 1386 (COO^-), 1289 (C-O_{phen}); Calculated/Found Analysis: C: 63.22/63.19, H: 3.94/3.93, N: 11.17/11.13, O: 12.76/12.74, Fe: 8.91/8.89.

EBC12: Brown solid; Yield: 80%; M.P.: 262 °C (dec.); μ_{eff} (B.M.): 1.73, FTIR (ATR, cm^{-1}): 3416 (N-H_{str}), 3288 (C-H_{arom}), 3045, 3013 (C-H_{aliph}), 1688 (C=O_{acid}), 1602 (C=N_{im}), 1575 (C=N_{trz}), 1532, 1493, 1459, 1435 (C-C_{arom}), 1376 (COO^-), 1312 (C-O_{phen}); Calculated/Found Analysis: C: 65.84/65.82, H: 3.66/3.63, N: 10.38/10.36, O: 11.85/11.82, Fe: 8.27/8.26.

EBC13: Green solid; Yield: 79%; M.P.: 350°C (dec.); μ_{eff} (B.M.): 3.82; FTIR (ATR, cm^{-1}): 3386 (N-H_{str}), 3050, 3021 (C-H_{arom}), 2915, 2848 (C-H_{aliph}), 1696 (C=O_{acid}), 1616 (C=N im), 1596 (N-H_{bend}), 1568 (C=N_{trz}), 1541, 1503, 1467, 1440 (C-C_{arom}), 1358 (COO^-), 1287 (C-Ophen); Analytical Calculated/Found: C: 61.01/61.00, H: 3.84/3.82, N: 9.96/9.93, O: 14.63/14.61, Cr: 10.56/10.53.

EBC14: Green solid; Yield: 71%; M.P.: 354°C (dec.); μ_{eff} (B.M.): 3.84; FTIR (ATR, cm^{-1}): 3396 (N-H_{str}), 3017 (C-H_{arom}), 1699 (C=O_{acid}), 1620 (C=N_{im}), 1600 (N-H_{bend}), 1574 (C=N_{trz}), 1544, 1508, 1468, 1440 (C-C_{arom}), 1388 (COO^-), 1292 (C-O_{phen}); Analytical Calculated/Found: C: 64.48/64.45, H: 3.50/3.47, N: 9.07/9.04, O: 13.33/13.32, Cr: 9.62/9.60.

EBC15: Dark brown solid; Yield: 76%; M.P.: 243°C (dec.); μ_{eff} (B.M.): 1.72; FTIR (ATR, cm^{-1}): 3388

($N\text{-}H_{str}$), 3051, 3023 ($C\text{-}H_{arom}$), 2917, 2851 ($C\text{-}H_{aliph}$), 1698 ($C{=}O_{acid}$), 1618 ($C{=}N_{im}$), 1597 ($N\text{-}H_{bend}$), 1568 ($C{=}N_{trz}$), 1542, 1504, 1468, 1443 ($C\text{-}C_{arom}$), 1360 (COO^{-}), 1288 ($C\text{-}O_{phen}$); Analytical Calculated/Found: C: 60.53/60.51, H: 3.81/3.80, N: 9.88/9.87, O: 14.51/14.50, Fe: 11.26/11.23.

EBC16: Dark brown solid; Yield: 77%; M.P.: 250°C (dec.); μ_{eff} (B.M.): 1.73; FTIR (ATR, cm^{-1}): 3394 ($N\text{-}H_{str}$), 3019 ($C\text{-}H_{arom}$), 1698 ($C{=}O_{acid}$), 1618 ($C{=}N_{im}$), 1598 ($N\text{-}H_{bend}$), 1572 ($C{=}N_{trz}$), 1541, 1505, 1466, 1443 ($C\text{-}C_{arom}$), 1385 (COO^{-}), 1290 ($C\text{-}O_{phen}$); Analytical Calculated/Found: C: 64.02/64.00, H: 3.47/3.45, N: 9.01/9.00, O: 13.23/13.21, Fe: 10.26/10.23.

RESULTS AND DISCUSSION

This study focuses on synthesizing ligands based on cyanuric chloride (CC) and employing hydroquinone (HQ) and p-phenylenediamine (PFDA) as central units. The reactions between **HQ** and **CC**, as well as **PFDA** and **CC**, resulted in the formation of specific compounds, **EBS1** and **EBS2**, respectively. These compounds were further reacted with p-hydroxybenzaldehyde (PHBA) to produce EBA1 and EBA2. Subsequent reactions of **EBA1** with p-aminobenzoic acid (PABAc) and 5-aminoisophthalic acid (5AIPA) yielded target ligands **EBL1** and **EBL2**, while similar reactions with **EBA2** produced **EBL3** and **EBL4**, respectively. The structures of these ligands were characterized using various analytical and spectroscopic techniques. Additionally, reactions with $[Cr/Fe(Salen/Saloph)]_2O$ initial complexes yielded capped complexes, with the structures determined through analytical and spectroscopic methods (**Scheme 1**).

Interpretation of ^{1}H NMR and ^{13}C NMR spectra

When examining the ^{1}H NMR spectra of the intermediate compound coded as **EBS1** and **EBS2**, the singlet signal observed at 4.85 ppm for an aromatic-NH group for **EBS2**, and the singlet signal observed at 6.56 ppm and 7.61 ppm confirms the successful synthesis of this compound, respectively. Similarly, upon inspection of the ^{13}C NMR spectrum of these compounds, signals corresponding to two carbons were observed at 187.0 ppm, four carbons were observed at 170.0 ppm, and in the aromatic region, signals were observed at 150.4 ppm for two carbons, and at 115.8 ppm for four carbons for **EBS1** and 169.0 ppm, four carbons were observed at 163.8 ppm, and in the aromatic region, signals were observed at 133.9 ppm for two carbons, and at 122.3 ppm for four carbons for **EBS1**, further substantiate the successful synthesis of this compound (**Figure 1** and **Figure 2**), (**Figure S1, S2, S9, and S10**, Supporting information) [15-17].

When we examined the ^{1}H NMR spectrum of the intermediate products labeled as **EBA1** and **EBA2**, singlets (4H) observed at 9.87 ppm for the HC=O group, doublets (8H) at 7.84-7.85 ppm, doublets (8H) at 7.15 ppm, and doublet signals (4H) at 7.07-6.40 ppm, have successfully proven the synthesis of these compounds. Upon examining the ^{13}C NMR spectra of these compounds, signals at 192.1 ppm for 4 carbon C_9, at 178.9-184.9 ppm for 4 carbons C_4, at 171.9-177.5 ppm for 2 carbons C_3, at 161.1-161.2 ppm for 4 carbons C_5, at 128.8/150.01 ppm for 2 carbons C_2, at 131.5-132.5 ppm for 8 carbons C_7, at 118.7-123.3 ppm for 4 carbons C_1, and at 121.8-122.0 ppm for 8 carbons C_6, as well as signals at 116.1/133.2 ppm for 4 carbons C_8, provide further evidence of the successful synthesis of these compounds (Figure 3 and Figure 4), (Figure S3, S4, S11, and S12, Supporting information) [18, 19].

Analysis of the ^{1}H NMR spectrum revealed that ligands labeled **EBL1** and **EBL3**, weak signals observed at 10.60-11.17 ppm correspond to acidic protons, singlets observed at 8.69 ppm correspond to four hydrogens (HC=N), doublets (8H) at 7.98-8.24 ppm, doublets (8H) at 7.76-7.79 ppm, doublets (8H) at 7.49-7.60 ppm, doublets (8H) at 6.96-7.08 ppm, and doublets (4H) at 6.84-7.01 ppm. These signals successfully prove the synthesis of these compounds.

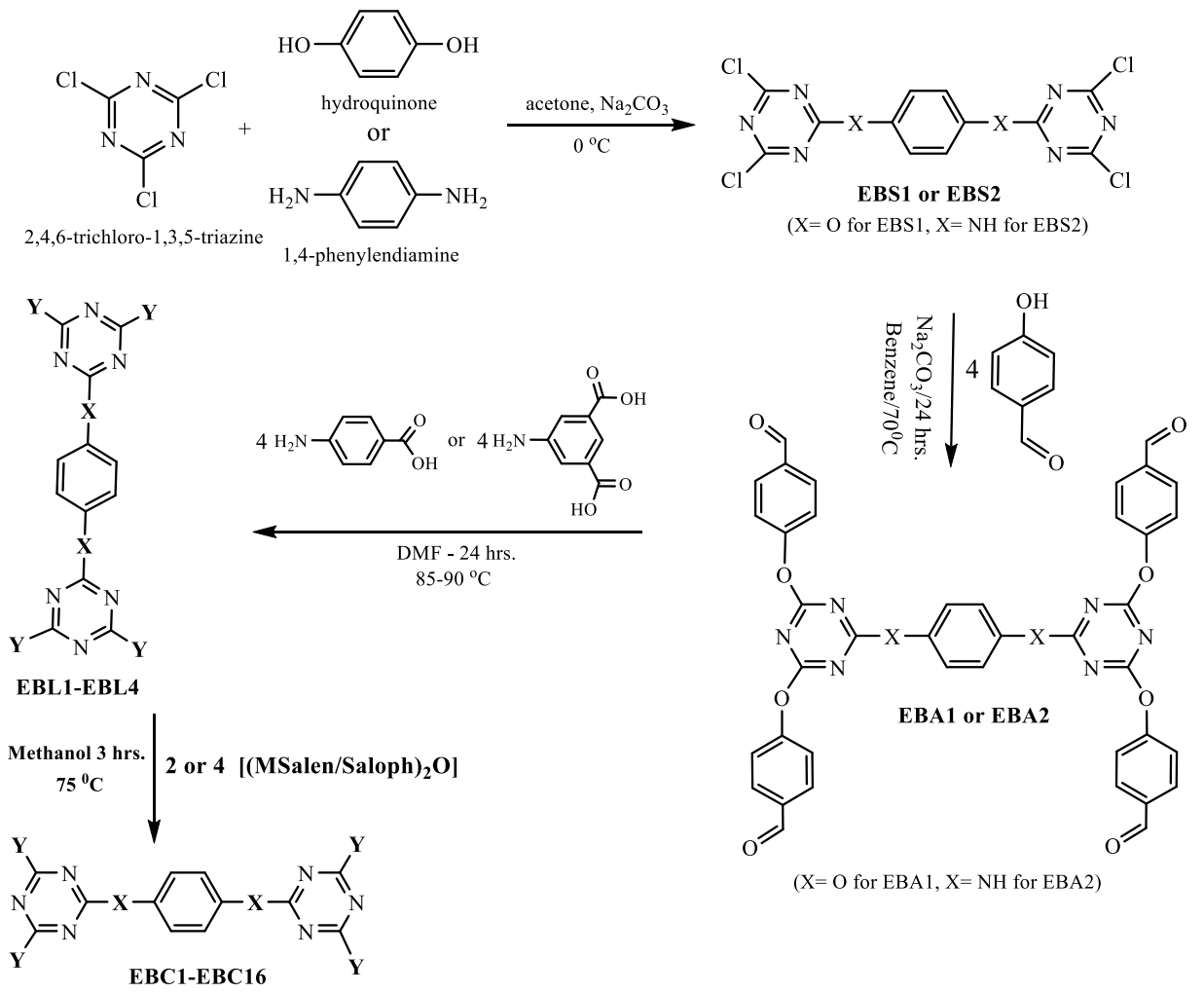

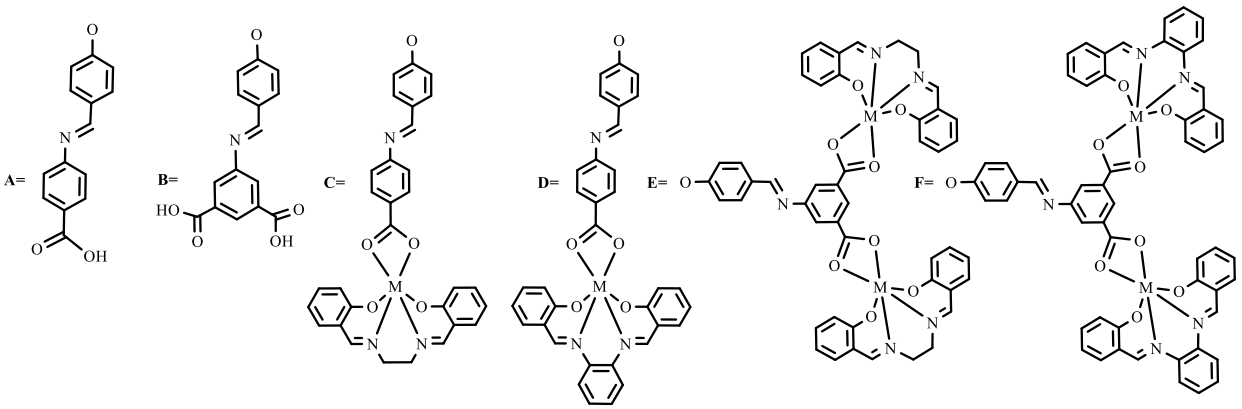

Comp.	X	Y	Comp.	X	Y	M	Comp.	X	Y	M	Comp.	X	Y	M	Comp.	X	Y	M
EBL1	O	A	**EBC1**	O	C	Cr(III)	**EBC5**	O	E	Cr(III)	**EBC9**	NH	C	Cr(III)	**EBC13**	NH	E	Cr(III)
EBL2	O	B	**EBC2**	O	D	Cr(III)	**EBC6**	O	F	Cr(III)	**EBC10**	NH	D	Cr(III)	**EBC14**	NH	F	Cr(III)
EBL3	NH	A	**EBC3**	O	C	Fe(III)	**EBC7**	O	E	Fe(III)	**EBC11**	NH	C	Fe(III)	**EBC15**	NH	E	Fe(III)
EBL4	NH	B	**EBC4**	O	D	Fe(III)	**EBC8**	O	F	Fe(III)	**EBC12**	NH	D	Fe(III)	**EBC16**	NH	F	Fe(III)

Scheme 1

Synthetic route of ligand and complexes

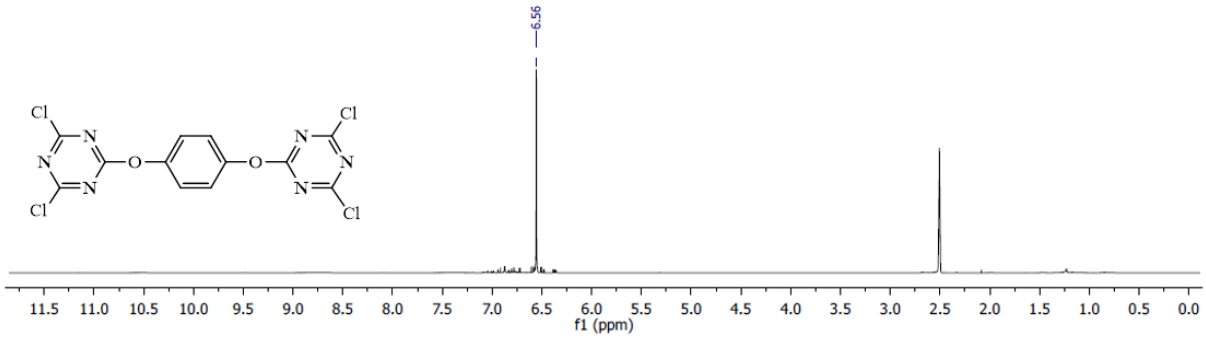

Figure 1

^{1}H NMR spectrum of EBS1.

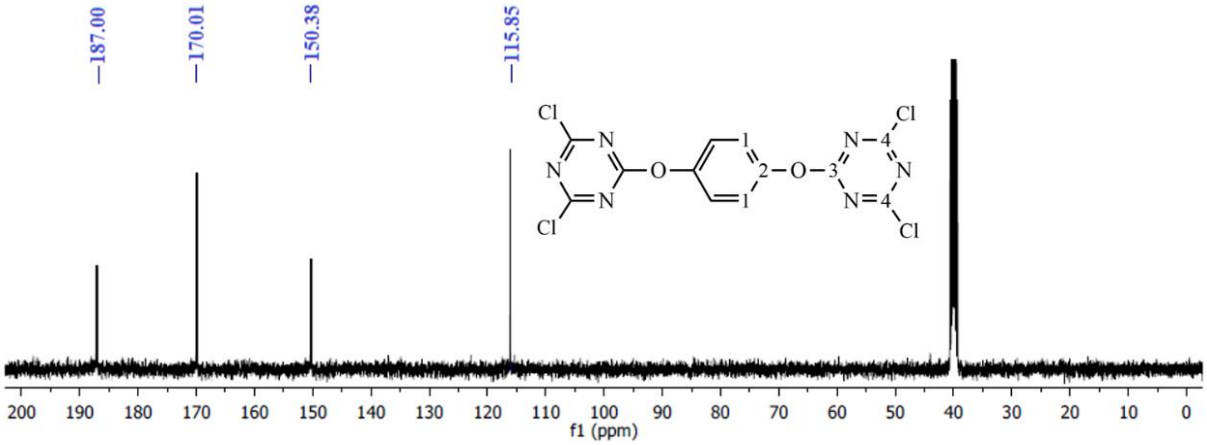

Figure 2

^{13}C NMR spectrum of EBS1

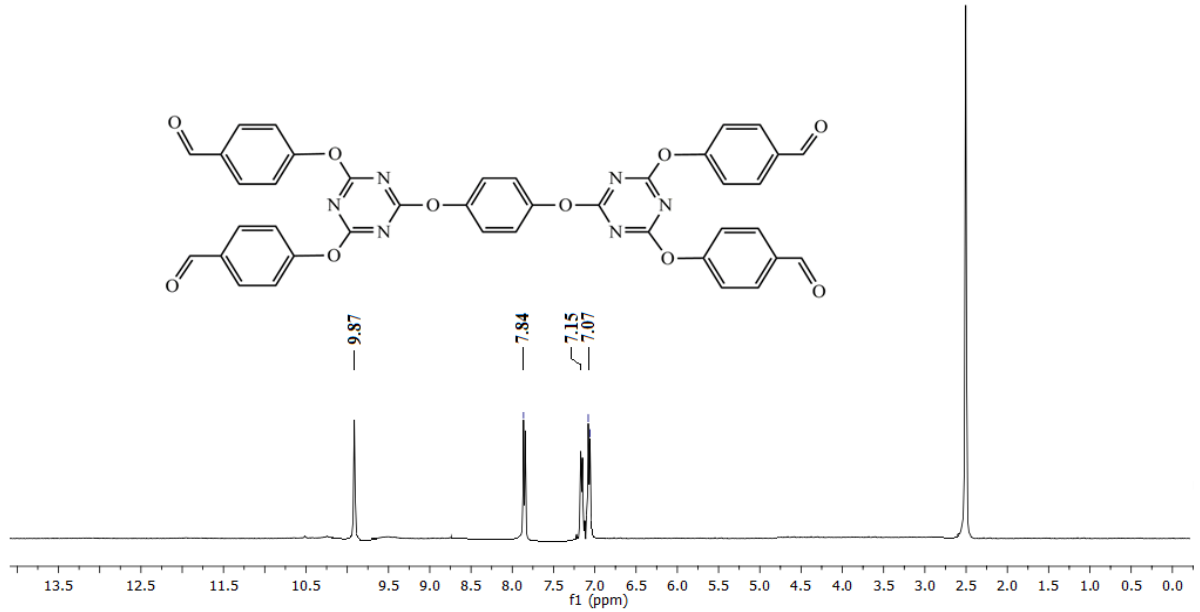

Figure 3

^{1}H NMR spectrum of EBA1

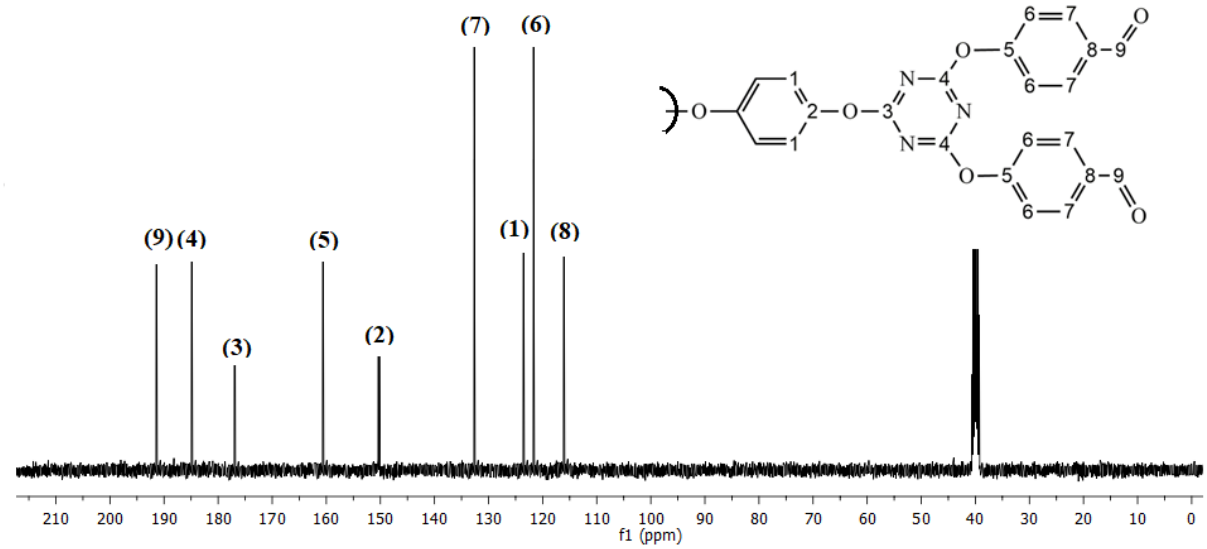

Figure 4

^{13}C NMR spectrum of EBA1

Similarly, when we examine the ^{1}H NMR spectrum of ligands labeled **EBL2** and **EBL4**, weak signals observed at 11.16-11.19 ppm correspond to acidic protons, singlets observed at 8.68-8.69 ppm correspond to four hydrogens (HC=N), singlets (4H) at 8.51-8.52 ppm, singlets (8H) at 8.01-8.02 ppm, doublets (8H) at 7.61-7.65 ppm, doublets (8H) at 6.98-7.01 ppm, doublets (8H) at 6.56-6.84 ppm, and a weak singlet signal (2H) observed at 4.85 ppm in the spectrum of **EBL4**. These signals also prove the successful synthesis of these compounds. Additionally, ^{13}C NMR signals were observed at 184.9/169.5 ppm for 4 carbons C_4, at 172.0-176.2 ppm for 2 carbons C_3, at 168.9-179.5 ppm for 4 carbons C_{14}, at 160.0 ppm for 4 carbons C_9, at 157.5 ppm for 4 carbons C_{10}, at 155.8-155.9 ppm for 4 carbons C_5, 149.1 and 129.0 ppm for 2 carbons C_2, at 132.5-132.6 ppm for 4 carbons C_8, at 131.5 ppm for 8 carbons C_{12}, at 130.0 ppm for 8 carbons C_7, at 128.2-128.5 ppm for 4 carbons C_{13}, at 123.5 and 118.5 ppm for 4 carbons C_1, at 121.4-121.5 ppm for 8 carbons C_{11}, and at 121.2 ppm for 8 carbons C_6 also serve as evidence for the successful synthesis of these compounds, respectively. To examine the ^{13}C NMR spectrum of **EBL2** and **EBL4** codded ligands, signals observed at 185.0 and 179.0 ppm for 4 carbons C_4, at 172.5-176.5 ppm for 2 carbons C_3, at 168.8-168.9 ppm for 8 carbons C_{14}, at 160.0 ppm for 4 carbons C_9, at 153.8-156.0 ppm for 4 carbons C_{10}, at 154.9-156.0 ppm for 4 carbons C_5, at 140.9 and 129.1 ppm for 2 carbons C_2, at 132.5-133.5 ppm for 4 carbons C_8, at 131.4-131.5 ppm for 8 carbons C_{12}, at 139.9 and 130.7 ppm for 8 carbons C_7, at 129.5 ppm for 4 carbons C_{13}, at 129.0 and 118.5 ppm for 4 carbons C_1, at 123.9 and 128.9 ppm for 8 carbons C_{11}, and at 120.9 ppm for 8 carbons C_6 further confirm the successful synthesis of these compounds (Figure 5 and Figure 6), (Figure S5, S6, S7, S8, S13, S14, S15, and S16, Supporting information) [20].

Interpretation of FTIR spectra

In our study, FTIR spectra were obtained to determine the functional groups of the intermediate compounds, target ligands, and target complexes synthesized. Accordingly, when examining the FTIR spectra of the intermediate products coded as **EBS1** and **EBS2**, stretching bands corresponding to s-triazine rings were observed at 1551 cm^{-1} and 1539 cm^{-1}, respectively. Additionally, in the spectrum of **EBS2**, stretching bands for N-H at 3375 cm^{-1} and 3362 cm^{-1}, bending bands for N-H at 1605 cm^{-1}, and stretching bands for C-Car in the aromatic region (1504 cm^{-1}, 1500 cm^{-1}, and 1431 cm^{-1}) were observed. These observations, as illustrated in **Figure S17 and Figure S18**, confirm the successful synthesis of these compounds. When examining the FTIR spectra of the intermediate products coded as EBA1 and EBA2, the observation of C=O stretching bands at 1698 and 1694 cm^{-1}, respectively, stretching bands of s-triazine rings at 1585 cm^{-1} and 1562 cm^{-1}, and specific bands in the aromatic region proved that the

compounds were successfully synthesized (**Figure S19 and Figure S20,** Supplementary Information**)**.

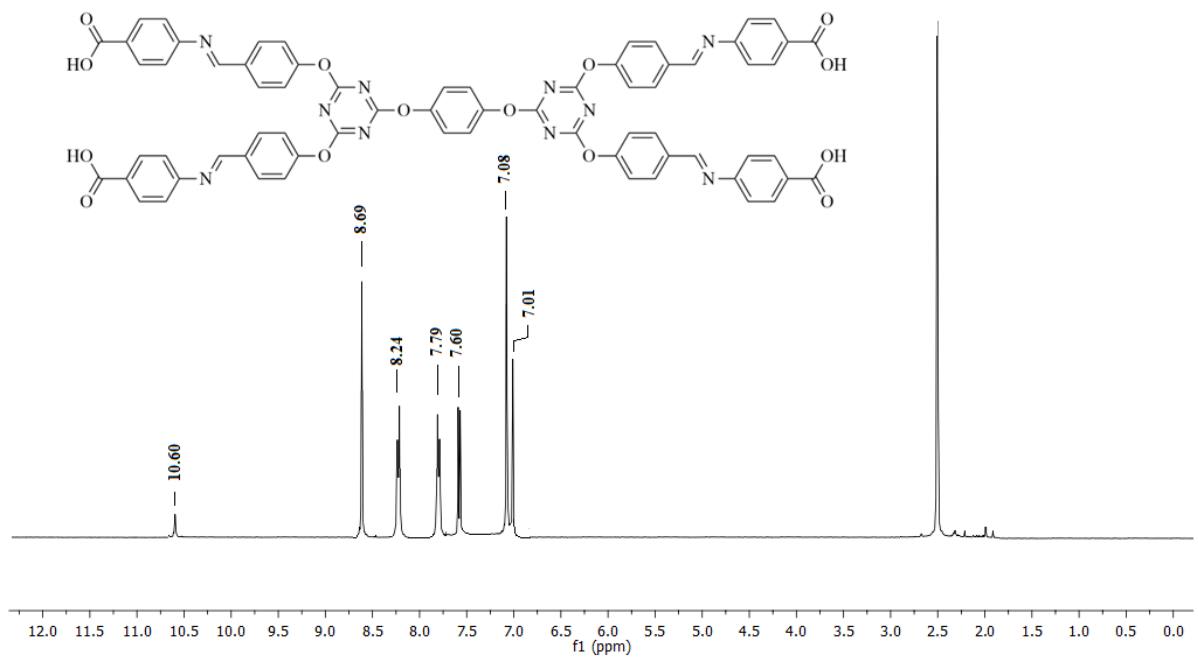

Figure 5
^{1}H NMR spectrum of EBL1

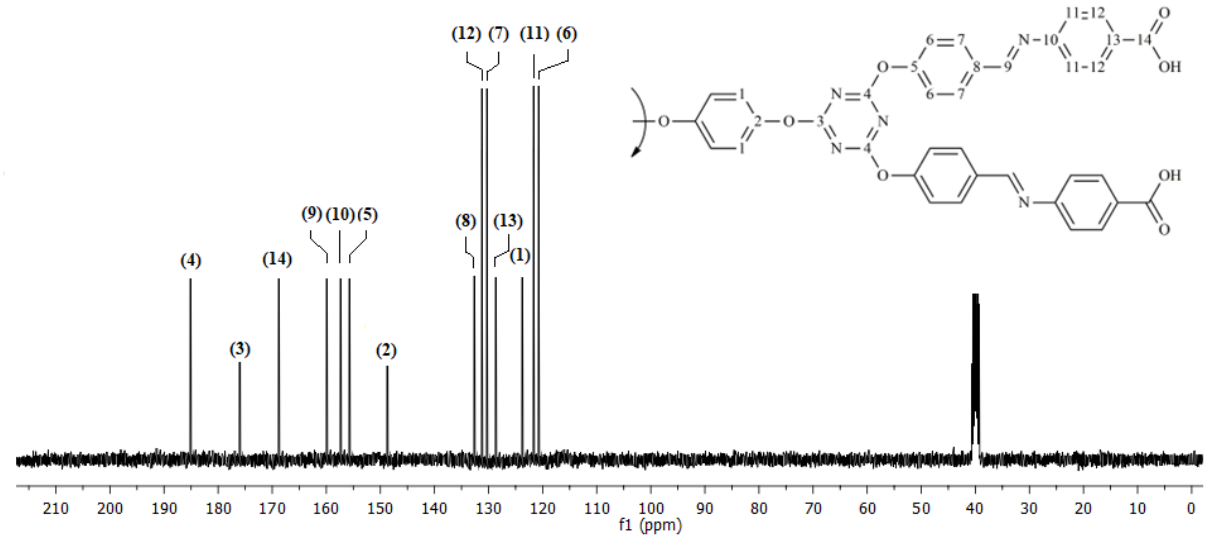

Figure 6
^{13}C NMR spectrum of EBL1

When we examine the FTIR spectra of **EBL1**, **EBL2**, **EBL3,** and **EBL4** target ligands, the C=O stretching bands observed at 1698 and 1694 cm^{-1} in the previous compounds disappear, and instead of them, $C=O_{acid}$ stretching bands appear in the range of 1682-1702 cm^{-1}, and COOH bending bands appear in the range of 1359-1382 cm^{-1} proved that these compounds were successfully synthesized (**Figure S21-Figure S24,** Supplementary Information**)**. When we examine the FTIR spectra of the target complexes coded **EBC1-EBC16**, that the $C=O_{acid}$ stretching bands observed in the range of 1682-1702 cm^{-1} for the ligands shift to higher frequencies (1682-1721 cm^{-1}), and the COO^{-} bending bands in the range of 1359-1382 cm^{-1} shift to higher frequencies (1358-1388 cm^{-1}) showed that these complexes were synthesized, successfully (**Table S1, Table S2** and **Figure S25-Figure S31,** Supplementary

Information**)**. While the FTIR spectra of all synthesized ligands as well as complexes are attached to supplementary information [17, 21-23].

Evaluation of TGA results of some complexes

Thermal gravimetric analysis (TGA) was conducted on certain complexes obtained in our study, namely **EBC3**, **EBC7**, **EBC11** and **EBL15**, to determine their thermal stabilities. The TGA analyses were performed under an N_2 atmosphere with a heating rate of 10 °C/min in the temperature range of 50-800 °C. **Figure 7**, below shows the TGA graph of the **EBC3** complex, while TGA graphs of the other complexes are attached to the supplementary information.

Examination of the TGA plot of the complexes **EBC3**, **EBC7**, **EBC11,** and **EBC15** revealed three stages of decomposition. In the first stage, mass losses of 6.75-8.75 % occurred as the CO_2 group detached from the molecule in the range of 125-205 °C, resulting in the detachment of the FeSalen caps from the main structure. Theoretical mass losses at this stage were calculated as 7.01-8.87 %. In the second stage, mass losses of 21.97-35.10 % occurred as the organic structure attached to the cyanuric chloride centers, excluding the Fe(Salen/Saloph) caps, separated from the structure in the range of 290-440 °C. Theoretical mass loss at this stage was 22.24-35.42%. In the final stage, mass losses of 34.22-46.35% indicated the decomposition of the salen caps in the range of 525-640 °C, with a theoretical mass loss of 37.34-47.23%. Since the heating process was carried out up to 800 °C, no further mass losses were observed beyond this point. FTIR and ICP-AES analyses of the remaining materials after TGA revealed that the residual materials were cyanuric chloride centers and Fe_2O_3 resulting from decomposition. Theoretical data are in good harmony with the experimental data, and consistent with other spectroscopic data (**Figure S32-Figure S35,** Supplementary Information**)** [17, 21-26].

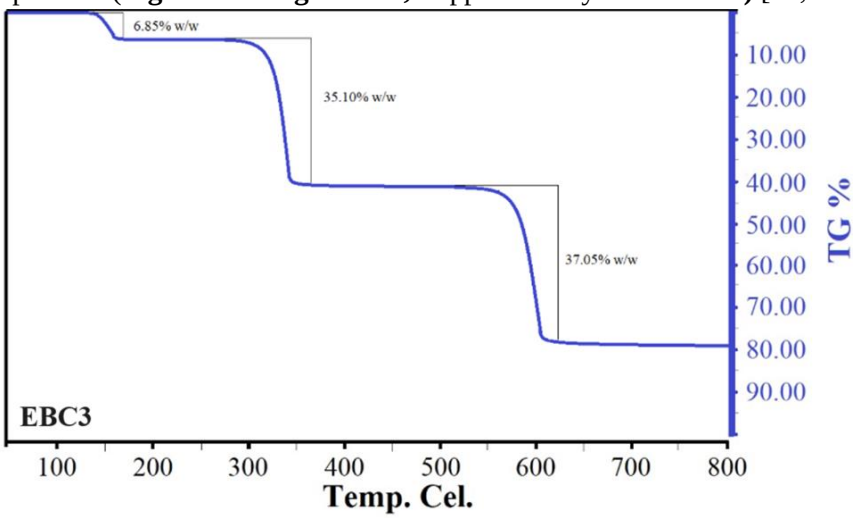

Figure 7
TGA graph of EBC3

Interpretation of magnetic susceptibility measurements

In our study, magnetic susceptibility values of the complexes synthesized were measured at room temperature using a Gouy balance. The molar magnetic susceptibility (μeff) values of all complexes in terms of Bohr magneton (B.M.) are provided in experimental detail.

All synthesized ligands, **EBC1**, **EBC2**, **EBC5**, **EBC6**, **EBC9**, **EBC1**0, **EBC13** and **EBC14** coded complexes, possessing a d^3 electron configuration, were measured paramagnetically. Each Cr^{3+} ion exhibited values of 3.83, 3.85, 3.84, 3.83, 3.86, 3.84, 3.82, and 3.84 B.M. respectively, with a $t_{2g}^3e_g^0$ electron configuration. Similarly, complexes coded as **EBC3**, **EBC4**, **EBC7**, **EBC8**, **EBC11**, **EBC12**, **EBC15** and **EBC16**, possessing a d^5 electron configuration, were measured paramagnetically. Each Fe^{3+}

ion exhibited values of 1.72, 1.71, 1.70, 1.71, 1.72, 1.73, 1.72, and 1.73 B.M. respectively, with a low spin $t_{2g}^5e_g^0$ electron configuration. Literature review indicates that [Fe(Salen/Saloph)$_2$O] complexes possess a $t_{2g}^3e_g^2$ electron configuration and are high-spin and five-coordinate complexes. These complexes, capable of coordinating with another ligand, are termed ligand complexes. When these ligand complexes coordinate with another monodentate ligand, their coordination numbers remain unchanged, and their electronic configurations remain the same. However, when they coordinate with a bidentate ligand using both of its arms, they transition to a low-spin hexacoordinate electron configuration. Considering all the complexes synthesized in our study, denoted as [Cr/Fe(Salen/Saloph)], were measured as low-spin, we evaluate their geometries as distorted octahedral [17, 23, 27-30].

CONCLUSIONS

In this work, four new original ligands (EBL1-EBL4) were synthesized. These ligands were characterized by using elemental analysis, FTIR, ^{1}H and ^{13}C NMR, and ICP-AES spectroscopies. The [MSalen/Saloph] (M = Cr^{3+}, Fe^{3+}) capped complexes were obtained from the reaction of these ligands and ligand complexes ([M(Salen/Saloph)]$_2$O). The structure of these complexes determined as paramagnetic was characterized by using elemental analysis, Magnetic Susceptibility, FTIR, and TGA methods. Complexes (EBC1, EBC2, EBC5, EBC6, EBC9, EBC10, EBC13 and EBC14) showed good harmony with the d^3 (S = 3/2) Cr^{3+} ions, and the other complexes (EBC3, EBC4, EBC7, EBC8, EBC11, EBC12, EBC15 and EBC16) showed good harmony with the low spin d^5 (S = 1/2) Fe^{3+} ions. That is, all Cr^{3+} and Fe^{3+} complexes are in distorted octahedral structure with $t_{2g}^3e_g^0$ and $t_{2g}^5e_g^0$ electronic configuration, respectively. The findings indicated that the carboxylate groups were coordinated to the metal center through both oxygen atoms. Thermogravimetric analysis was performed on selected complexes coded as EBC3, EBC7, EBC11, and EBC15, revealing that they possessed high thermal stability, making them suitable for use in chemical reactions and other applications.

Ethical Statement

This study is derived from a master's thesis entitled “s-Triazin kullanılarak çok dişli Schiff bazlarının sentezi, karakterizasyonu ve bazı geçiş metali komplekslerinin incelenmesi”, submitted under the supervision of Prof. Dr. Şaban UYSAL on 24/08/2023 date.

Author Contributions

Research Design (CRediT 1) E.B. (%40) - A.H.M. (%30) - Ş.U. (%30)
Data Collection (CRediT 2) E.B. (%45) - A.H.M. (%30) - Ş.U. (%25)
Research - Data Analysis - Validation (CRediT 3-4-6-11) E.B. (%40) - A.H.M. (%30) - Ş.U. (%30)
Writing the Article (CRediT 12-13) E.B. (%20) - A.H.M. (%50) - Ş.U. (%30)
Revision and Improvement of the Text (CRediT 14) E.B. (%20) - A.H.M. (%50) - Ş.U. (%30)

Financing

This study was financially supported by the Karabuk University Scientific Research Projects Coordinatorship (Project No: KBUBAP-21-YL-081).

Conflict of interest

The authors declare no conflict of interest for the present study.

Data availability

Data will be made available on request.

Sustainable Development Goals (SDG)

Sustainable Development Goals: Not supported.

REFERENCES

[1] A.A. Mahmood, Green synthesis of Schiff bases: a review study, *Iraqi Journal of Pharmacy*. 18(2) (2022), 180–193. doi:10.33899/iphr.2022.170406

[2] R. Mazzoni, F. Roncaglia, L. Rigamonti, When the metal makes the difference: Template syntheses of tridentate and tetradentate salen-type schiff base ligands and related complexes, *Crystals*. 11(5) (2021), 483. doi:10.3390/cryst11050483

[3] S.J. Swamy, K. Suresh, P. Someshwar, D. Nagaraju. Synthesis of novel Schiff's bases containing pyridine rings, *Synthetic Communications.* 34(10) (2004), 1847–1853. doi:10.1081/SCC-120034167

[4] O. Santoro, X. Zhang, C. Redshaw, Synthesis of biodegradable polymers: a review on the use of schiff-base metal complexes as catalysts for the ring opening polymerization (ROP) of cyclic esters, *Catalysts*. 10(7) (2020), 800. doi:10.3390/catal10070800

[5] Y.M. Ahmed, W.H. Mahmoud, M.M. Omar, G.G. Mohamed, Synthesis, characterization and biological activity of transition metals schiff base complexes derived from 4,6-Diacetylresorcinol and 1,8-Naphthalenediamine, *Journal of Inorganic and Organometallic Polymers and Materials*. 31 (2021), 2339–2359. doi:10.1007/s10904-020-01867-1

[6] H.M. Junaid, M. Batool, F.W. Harun, M.S. Akhter, N. Shabbir, Naked eye chemosensing of anions by Schiff bases, *Critical Reviews in Analytical Chemistry*. 52 (2020), 463–480. doi:10.1080/10408347.2020.1806703

[7] A. El-Faham, A. Sharma, M. Farooq, Z. Almarhoon, R.A. Alhameed, M.A.M. Wadaan, B.G. De La Torre, F. Albericio, Protocol for synthesis of di- and tri-substituted s-triazine derivatives, *MethodsX*. 7 (2020), 100825. doi:10.1016/j.mex.2020.100825

[8] A.H. Cleveland, G.H. Imler, C.J. Snyder, D.E. Chavez, D.A. Parrish, Synthesis of a new 1,2,4-triazine derived azidoxime. *Propellants, Explosives, Pyrotechnics*, 47(10) (2022), e202200138. doi: 10.1002/prep.202200138

[9] X. Ma, S.-T. Tan, C.-L. Khoo, H.-M. Sim, L.-W. Chan, W.-K. Chui, Synthesis and antimicrobial activity of N1-benzyl or N1-benzyloxy-1,6-dihydro-1,3,5-triazine-2,4-diamines, *Bioorganic & Medicinal Chemistry Letters*. 21 (2011), 5428–5431. doi:10.1016/j.bmcl.2011.06.125

[10] A. Sharma, S. Singh, D. Utreja, Recent advances in synthesis and antifungal activity of 1,3,5-triazines, *Current Organic Synthesis*. 13 (2015), 484–503. doi:10.2174/1570179412666150905002356

[11] S. Manohar, S.I. Khan, D.S. Rawat, 4-aminoquinoline-triazine-based hybrids with improved in vitro antimalarial activity against CQ-sensitive and CQ-resistant strains of *Plasmodium falciparum*, *Chemical Biology & Drug Design*. 81 (2013), 625–630. doi:10.1111/cbdd.12108

[12] A. El-Faham, S.M. Soliman, H.A. Ghabbour, Y.A. Elnakady, T.A. Mohaya, M.R.H. Siddiqui, F. Albericio, Ultrasonic promoted synthesis of novel s -triazine-Schiff base derivatives; molecular structure, spectroscopic studies and their preliminary anti-proliferative activities, *Journal of Molecular Structure*. 1125 (2016), 121–135. doi:10.1016/j.molstruc.2016.06.061

[13] A. Barakat, F.F. El-Senduny, Z. Almarhoon, H.H. Al-Rasheed, F.A. Badria, A.M. Al-Majid, H.A. Ghabbour, A. El-Faham, Synthesis, X-Ray crystal structures, and preliminary antiproliferative activities of new S-Triazine-hydroxybenzylidene hydrazone derivatives, *Journal of Chemistry*. 2019 (2019) 1–10. doi:10.1155/2019/9403908

[14] P. Kopel, Z. Sindelar, R. Klicka, Complexes of iron(III) salen and saloph Schiff bases with bridging dicarboxylic and tricarboxylic acids, *Transition Metal Chemistry*. 23(2) (1998), 139–142. doi:10.1023/A:1006990925318

[15] Ş. Uysal, Z.E. Koç, Synthesis and characterization of dendrimeric melamine cored [salen/salophFe(III)] and [salen/salophCr(III)] capped complexes and their magnetic behaviors, *Journal of Hazardous Materials*. 175 (2009), 532–539.

doi:10.1016/j.jhazmat.2009.10.038

[16] K. Kiymaz, S. Uysal, The synthesis and characterization of pyridine cored dentrimeric s-Triazine Schiff bases: Investigation of their [MSalen/Salophen] (M= Cr^{3+}, Fe^{3+}, Co^{3+} and Zr^{4+}) capped complexes, *Journal of Molecular Structure*. 1271 (2022), 134029. doi:10.1016/j.molstruc.2022.134029

[17] Z.E. Koç, Ş. Uysal, Synthesis and characterization of dendrimeric bridged Salen/Saloph complexes and investigation of their magnetic and thermal behaviors, *Helvetica Chimica Acta*. 93 (2010), 910–919. doi:10.1002/hlca.200900294

[18] S.M. Khalil, A.A. Emara, Asymmetric Schiff base (N_2O_3) complexes as ligands towards Mn(II), Fe(III) and Co(II), synthesis and characterization, *Journal of Coordination Chemistry*. 55 (2002), 17–32. doi:10.1080/00958970211871

[19] U.J. Al-Hamdani, A.M. Jassem, A.M. Dhumad, S.A. Al-Shlshat, Synthesis, mesomorphic properties, and theoretical study of benzothiazole-aromatic molecules with ester- and azomethine-linking groups, *Liquid Crystals*. 48 (2021), 2164–2177. doi:10.1080/02678292.2021.1934742

[20] Q. Fang, X. Ding, X. Wu, L. Jiang, Synthesis and characterization of a novel functional monomer containing two allylphenoxy groups and one S-triazine ring and the properties of its copolymer with 4,4′-bismaleimidodiphenylmethane (BMDPM), *Polymer*. 42 (2001), 7595–7602. doi:10.1016/s0032-3861(01)00274-9

[21] B.N. Figgis, R.S. Nyholm, 61. Magnetochemistry. Part II. The temperature-dependence of the magnetic susceptibility of bivalent cobalt compounds, *Journal of the Chemical Society (Resumed)*. (1959), 338. doi:10.1039/jr9590000338

[22] J.S. Griffith, L.E. Orgel, The residual paramagnetism and nuclear magnetic resonance spectra of cobaltic complexes, *Transactions of the Faraday Society*. 53 (1957), 601. doi:10.1039/tf9575300601

[23] Ş. Uysal, H.İ. Uçan, The synthesis and characterization of melamine based Schiff bases and its trinuclear [salen/salophenFe(III)] and [salen/salophenCr(III)] capped complexes, *Journal of Inclusion Phenomena and Molecular Recognition in Chemistry*. 65 (2009), 299–304. doi:10.1007/s10847-009-9581-2.

[24] Z. Cimerman, N. Galic, B. Bosner, The Schiff bases of salicylaldehyde and aminopyridines as highly sensitive analytical reagents, *Analytica Chimica Acta*. 343 (1997), 145–153. doi:10.1016/s0003-2670(96)00587-9.

[25] A.Z. El-Sonbati, W.H. Mahmoud, G.G. Mohamed, M.A. Diab, Sh.M. Morgan, S.Y. Abbas, Synthesis, characterization of Schiff base metal complexes and their biological investigation, *Applied Organometallic Chemistry*. 33 (2019). doi:10.1002/aoc.5048

[26] P. Ghanghas, A. Choudhary, D. Kumar, K. Poonia, Coordination metal complexes with Schiff bases: Useful pharmacophores with comprehensive biological applications, *Inorganic Chemistry Communications*. 130 (2021), 108710. doi:10.1016/j.inoche.2021.108710

[27] I.M. Aouled, S. Uysal, Investigation of thermal and magnetic properties of [MSalen/Saloph] (M = Cr^{3+}, Fe^{3+} or Co^{3+}) capped dinuclear complexes of two novel tetraoxocalix[2]arene[2]triazine ligands, *Journal of Molecular Structure*. 1280 (2023), 135084. doi:10.1016/j.molstruc.2023.135084

[28] I.M. Aouled, S. Uysal, Investigation of [MSalen/salophen] (M = Cr^{3+}, Fe^{3+} or Co^{3+}) capped dinuclear complexes of two novel tetraoxocalix[2](m-hydroxymethyl)arene[2]triazine compounds, *Synthetic Communications*. 51 (2021), 3642–3655. doi:10.1080/00397911.2021.1988107

[29] Ş. Uysal, Z.E. Koç, The synthesis and characterization of (MSalen/salophen/saldeta/salpy) [M=Fe(III) or Cr(III)] capped heteromultinuclear schiff bases-dioxime Ni(II) complexes: Their thermal and magnetic behaviours, *Journal of Molecular Structure*. 1165 (2018), 14–22.

doi:10.1016/j.molstruc.2018.03.101.

[30] Ş. Uysal, M. Er, H. Tahtaci, Synthesis and characterization of tetra-armed-thiosemicarbazone and its salen/salophen capped transition metal complexes: Investigation of their thermal and magnetic properties, *Synthetic Communications*. 46 (2016), 1820–1832. doi:10.1080/00397911.2016.1229791.

FEN ve MÜHENDİSLİK BİLİMLERİ DERGİSİ

Vol: 7 No: 1 Year: 2025 Araştırma Makalesi/Research Article e-ISSN: 2667-7989

https://doi.org/10.47112/neufmbd.2025.81

Artırılmış Biyoaktivite için Bazı Flavonoid Karışımlarının Elektroeğirme Tekniği Kullanılarak Enkapsülasyonu ve Kontrollü Salım Çalışmaları

Deniz Tuğçe ALGAN [1*] Erdal KOCABAŞ [2]

[1] Necmettin Erbakan University, Graduate School of Natural and Applied Sciences, Department of Chemistry, Konya, Türkiye

[2] Necmettin Erbakan University, Faculty of Science, Department of Biotechnology, Konya, Türkiye

Makale Bilgisi

Geliş Tarihi: 25.09.2024
Kabul Tarihi: 01.11.2024
Yayın Tarihi: 30.04.2025

Anahtar Kelimeler:
Antibakteriyel etki,
Elektroeğirme,
Flavonoid,
Hesperidin,
in vitro ilaç salım,
Naringin,
Rutin hidrat.

ÖZET

Narenciye meyvelerinden elde edilen biyoaktif bileşikler olan rutin hidrat, naringin ve hesperidin kullanılarak polimer bazlı elektroeğirme fiberleri hazırlanmıştır. Bu flavonoidlerin antioksidan, anti-inflamatuar ve anti-kanser gibi çeşitli biyolojik aktiviteleri bulunmaktadır. Elektroeğirme tekniği sayesinde, flavonoidlerin biyolojik kullanılabilirliği artırılarak, ilaç taşıma sistemleri, gıda ambalajları ve kozmetik ürünler gibi farklı alanlarda potansiyel uygulamalar geliştirilmesi amaçlanmıştır. Elde edilen fiberlerin morfolojik ve kimyasal ve karakterizasyonları ile flavonoidlerin fiber matris içerisindeki dağılımı ve salım davranışları belirlenmiştir. Aynı zamanda, nanofiberlerin *Staphylococcus aureus* (*S. aureus*) bakterisine karşı antibakteriyel aktivitesi değerlendirildi. Yapılan çalışmanın sonucunda bağırsak pH'ında (pH 7,4) yapılan dissolüsyon analizinde PLA-MIX fiberi etken maddeleri %20-25 oranında, PCL- MIX fiberi etken maddeleri %21-28 oranında salındı. Antibakteriyel sonuçlar nanofiberlerin %45 oranında PLA karışımında daha fazla bakteriyel inhibisyona neden olduğunu gösterdi. Bu çalışma, narenciye atıklarının değerlendirilmesi ve yeni nesil biyomalzemelerin geliştirilmesi açısından önemli bir katkı sağlamaktadır.

Encapsulation of Some Flavonoid Mixtures Using Electrospinning Technique for Enhanced Bioactivity and Controlled Release Studies

Article Info

Received: 25.09.2024
Accepted: 01.11.2024
Published: 30.04.2025

Keywords:
Antibacterial effect,
Electrospinning,
Flavonoid,
Hesperidin,
in vitro drug release,
Naringin,
Rutin hydrate.

ABSTRACT

Polymer-based electrospun fibers were prepared using bioactive compounds derived from citrus fruits such as rutin hydrate, naringin and hesperidin. These flavonoids have various biological activities such as antioxidant, anti-inflammatory and anticancer. By increasing the bioavailability of flavonoids through the electrospinning technique, it is aimed to develop potential applications in different areas such as drug delivery systems, food packaging and cosmetic products. The distribution and release behaviors of flavonoids in the fiber matrix were determined by morphological and chemical characterization of the obtained fibers. At the same time, the antibacterial activity of nanofibers against *Staphylococcus aureus (S. aureus)* bacteria was evaluated. As a result of the study, in the dissolution analysis performed at intestinal pH (pH 7.4), the active ingredients of PLA-MIX fiber were released at a rate of 20-25% and PCL-MIX fiber at a rate of 21-28%. Antibacterial results showed that nanofibers caused more bacterial inhibition in a 45% PLA mixture. This study provides an important contribution to the evaluation of citrus wastes and the development of new-generation biomaterials.

To cite this article:
Algan, D.T. & Kocabaş, E. (2025). Encapsulation of some flavonoid mixtures using electrospinning technique for enhanced bioactivity and controlled release studies. *Necmettin Erbakan University Journal of Science and Engineering*, *7*(1), 141-152. https://doi.org/10.47112/neufmbd.2025.81

***Sorumlu Yazar:** Deniz Tuğçe Algan, *dtalgan92@gmail.com*

INTRODUCTION

Controlled drug delivery offers numerous advantages as it reduces premature degradation, improves drug uptake, maintains drug concentrations within the therapeutic window, and reduces side effects. Over the last decade, recent advances in genomics and nanotechnologies have made it possible to achieve drug delivery by using specifically designed nanoparticle carriers, particularly in anticancer therapy, vaccines, and theranostic imaging [1].

One popular technique for encapsulating active nutraceutical ingredients into fibers is to combine them with the polymer solution and spin the mixture. The encapsulation of bioactive compounds for ultimate incorporation in food plays a major role in food processing. Capsules constructed of polymers based on lipids, proteins, and carbohydrates coat or encapsulate active components, such as food-bioactive chemicals or living cells, inside micro- or nanoscale-sized particles. Encapsulated bioactive compounds have enhanced stability, bioavailability, and physicochemical properties while being shielded from external stresses. Electrospinning is a feasible method for encapsulating food bioactive substances, as it effectively produces dry, food-grade, nano-scaled materials with good encapsulation efficiencies [2-4].

PLA is FDA-approved for direct contact with biological fluids. One of the key features that makes PLA advantageous for drug carriers is its biodegradability. PLA can easily dissolve in extracellular environments, and its degradation rate can be modulated to achieve the desired effect. For drug carrier systems in particular, the kinetics of this degradation can be extended to maintain the sustained release of medicinal agents. This provides sufficient time for the drug to exert its effect, which is crucial since this therapeutic strategy can potentially be diminished by metabolic processes [5].

Polycaprolactone (PCL) is a highly valued polymer for wound dressing applications due to its exceptional mechanical strength, biocompatibility, and biodegradability. PCL is a commonly utilized polymer in the electrospinning process because of its easy spinnability. Due to its biocompatible and biodegradable properties, PCL is a semi-crystalline polyester that has received FDA approval and has promise for usage in biomedical applications like wound dressing applications and delivery systems. One of the most popular biopolymers for skin regeneration is also easily processed into a variety of forms, including films, mats, membranes, and fibers [6-7].

Rutin is gaining significant attention due to its wide pharmacological potential and non-toxic nature. It also has antioxidant, anti-inflammatory, and anticancer activities thanks to its radical sweeping activity. However, its utility in clinical applications is limited by its poor stability and bioavailability. A bioactive compound's pharmacodynamics and pharmacokinetics may be improved by novel drug delivery methods. For this reason, employing a novel drug distribution mechanism can get around regular restrictions [8,10].

Fruits including oranges, lemons, tomatoes, mandarins, and grapefruit peel contain naringin, which has a low solubility in water and a poor absorption rate in the digestive system. Therefore, encapsulation techniques and release mechanisms can increase its formulation, absorption, and stability. This phytochemical has heart-protective, antimicrobial, anticancer, and antioxidant properties [11].

The most common flavonoid in oranges and lemons is hesperidin, a cheap and abundant byproduct of the citrus family. Its benefits include lowering cholesterol, antioxidant, edema-reducing, hypolipidemic, and vascular protection. Hesperidin has a low solubility in water and limited bioavailability [9].

Studies have demonstrated the high multifunctional bioactivities of flavonoids, including antiviral, antioxidant, antibacterial, anti-inflammatory, and anti-tumor properties. Using the

electrospinning technology, the goal of this work was to encapsulate flavonoid combinations for use in the nutraceutical supplement market as a controlled release mechanism [2-4].

MATERIALS AND METHOD

Materials

Rutin hydrate, naringin, and hesperidin were purchased from Merck, Germany. Polylactic acid (PLA) (Mw~ 60,000), polycaprolactone (PCL) (Mn 80,000), hexafluoro-2-propanol (HFIP), methanol (MeOH), chloroform and hydrochloric acid (HCl) were supplied by Sigma- Aldrich, Germany. Gelatin was bought from SelJel Gelatin, Türkiye. pH 1.2 and pH 7.4 buffer solutions were made in laboratory conditions.

Method

Preparing Electrospun Fibers

Three different flavonoids—rutin, naringin, and hesperidin—along with two different polymers—PCL and PLA—were chosen. The three flavonoids were mixed and the was mixture added to the solution at a rate of 10% PLA after PLA (2.5%) and gelatin (7.5%) were dissolved in 20 mL of HFIP. To prepare the PCL-containing electrospinning solution, 80000 kDa PCL (10%) was dissolved in a 40:60 methanol to chloroform mixture before adding mixed active components. For electrospinning, the resultant solution was put into a 5 mL syringe. With a voltage of 18 kV, a flow rate of 1 mL/h, and a tip-to-collector distance of 15 cm, fibers were created by electrospinning [12-13].

Drug Content, Encapsulation Efficiency and in vitro Drug Release

Nanofibers were cut into small pieces, weighted around 100-120 mg, and transferred into 50 mL falcon tubes. Fibers were dissolved with 1 mL chloroform, 1 ml HCl solution (1% v/v), and 3 ml MetOH mixture, centrifuged at 4000 rpm for 20 min, and sonicated for 5 minutes. Solutions were filtered through a 0.45 µm PTFE filter and analyzed by UV-Vis spectroscopy at the suitable wavelength. The results are shown in Table 1 [14-16].

$$EE\% = \frac{Encapsulated\ API}{Total\ API\ content} \quad (1)\ [16]$$

In vitro drug release was carried out by USP <711>. Two distinct pH ranges will be used in the investigation throughout the dissolution phase. The pH 1.2 and pH 7.4 ranges were determined as these. The right buffer solutions were made, and the dissolving process was induced in various parts of the stomach and intestine. Samples were obtained from the stomach environment every 15 minutes from 0 to 2 hours, and every hour from 2 to 3 hours. Samples were obtained from the intestinal environment every 30 minutes between 0 and 2 hours, and every hour between 2 and 5 hours. The HPLC-PDA was used to analyze the samples. The results are shown in Figures 1-4 [17].

Characterization of Fibers

The ZEISS GeminiSEM 500 scanning electron microscope was used to examine the diameter and morphology of the electrospun fibers. A small piece of the fiber mat was gold-sputter-coated (4.35 nm) and placed on the SEM sample holder. A voltage of 20 kV was used to acquire SEM pictures [18].

Shimadzu IR Tracer-100 Fourier Transform Infrared Spectroscopy was used to examine the fiber's chemical content. Active pharmaceutical ingredients (rutin hydrate, naringin and hesperidin), PLA, gelatin, PCL, and two fibers (PLA-MIX and PCL-MIX) were examined in the mid-IR range (4000-400 cm^{-1}) by 16 scans [18].

Antibacterial Activity Assay

The colony counting method was used to evaluate the antibacterial activity of nanofibers against the *Staphylococcus aureus (S. aureus)* ATCC6538 bacterial strain. Each nanofiber, approximately 1 X 1 cm in diameter, was covered with a sterile film after 100 µL of bacterial solution containing 1.5 × 107 colony-forming units (CFU/mL) was added to its surface. The nanofibers were incubated in the incubator at 37°C for 24 hours. After incubation, the films were washed with 1 mL of PBS solution, and 100 µL was taken and inoculated into blank Nutrient agar media. The number of viable bacterial colonies was determined after a 24-hour incubation period at 37°C. The decrease in the number of bacteria was calculated using the following formula:

$$R(\%) = \frac{(B - A)}{B} * 100 \qquad (2)\ [19]$$

R: %inhibition, **A:** the colonies in the control samples, **B:** the colonies in the nanofiber samples

RESULTS

Encapsulation Efficiency and in vitro Drug Release

Active pharmaceutical ingredient (API) amount determination and encapsulation efficiency were calculated. Encapsulation efficiency is calculated by Equation 1.

Table 1
Encapsulation efficiency of API in PLA and PCL electrospun fibers

API	PLA (%)	PCL (%)
RTN	29.80	15.88
HSP	38.41	25.24
NAR	5.09	1.30

According to the dissolution analysis results, the release percentages in the stomach and intestinal environments for the fiber mat produced using PLA-gelatin were similar. In the fiber mat made with the PCL polymer, the release was greater in the intestinal environment compared to the stomach environment.

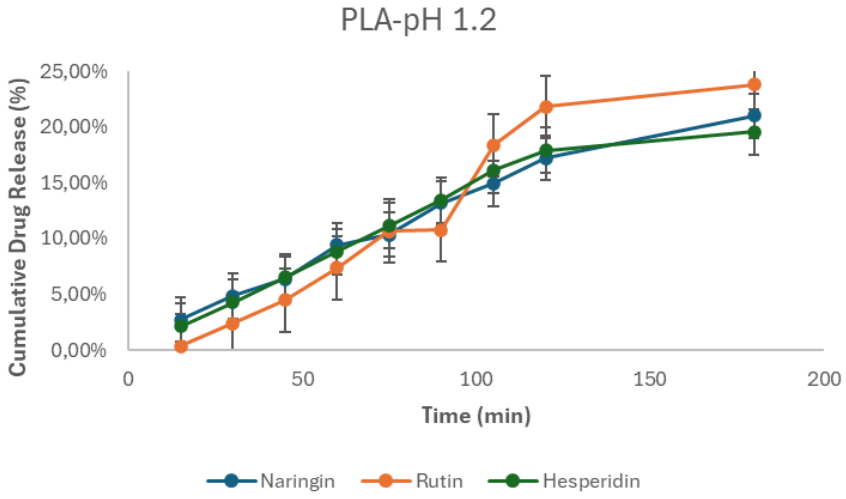

Figure 1
Cumulative drug release of API's from PLA fiber at pH 1.2

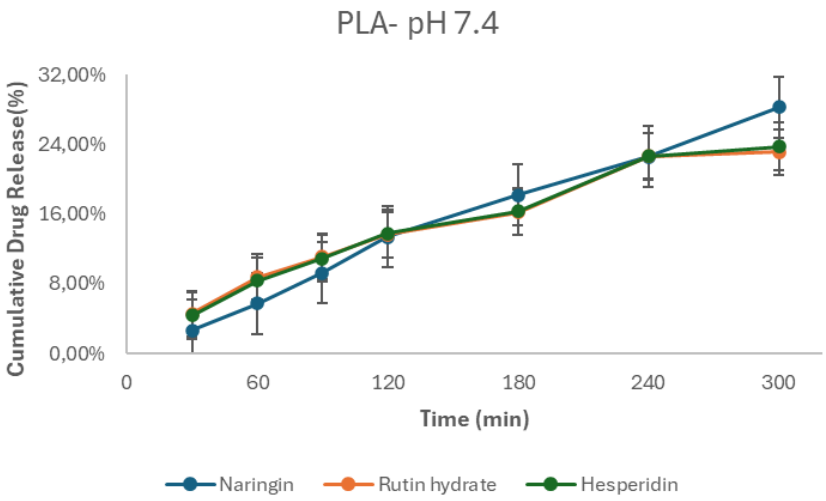

Figure 2
Cumulative drug release of API's from PLA fiber at pH 7.4

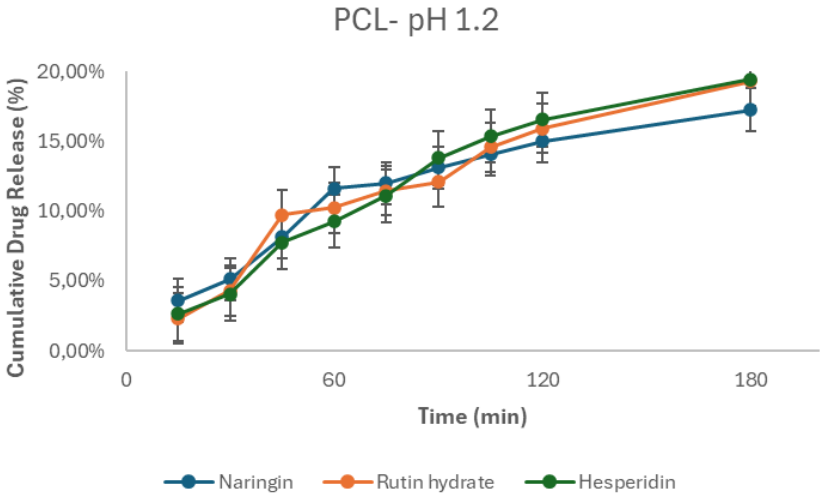

Figure 3
Cumulative drug release of API's from PCL fiber at pH 1.2

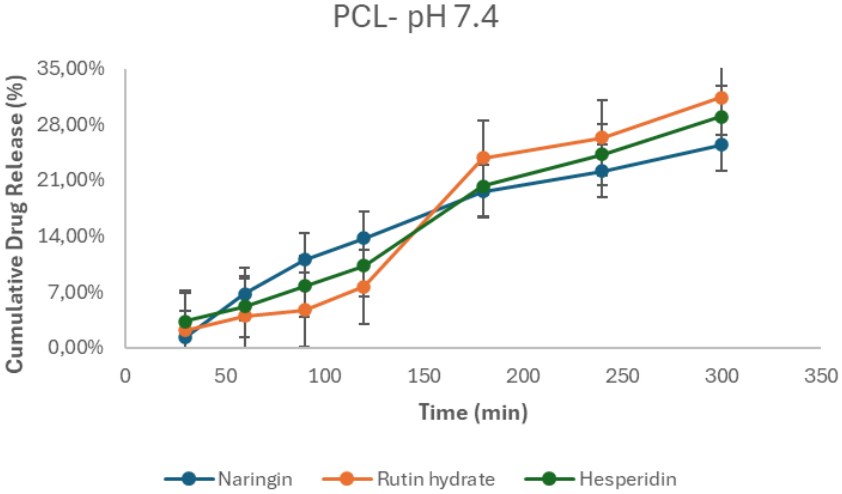

Figure 4
Cumulative drug release of API's from PCL fiber at pH 7.4

FESEM Imaging

In the FE-SEM images of the PCL-MIX mat (Fig. 5), it was seen that the fibers were smooth, and no bead formation was observed. The fiber diameter average thickness is over 800 nm. In the FE-SEM images of the PLA-MIX mat (Fig. 6), it was seen that the fibers were smooth, and no bead formation was observed. The fiber diameter average thickness is over 400 nm.

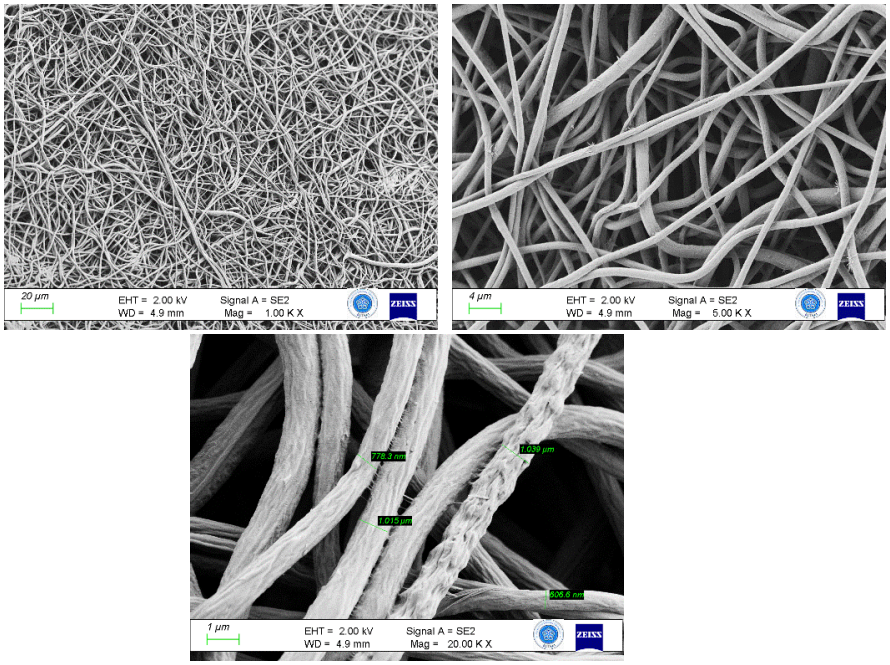

Figure 5
PCL-MIX FESEM images

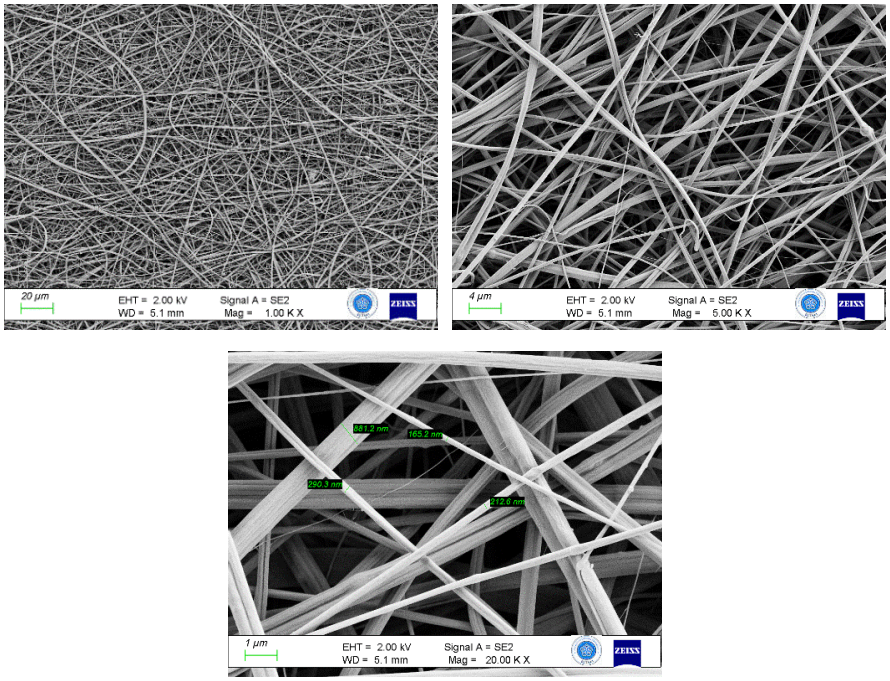

Figure 6
PLA-MIX FESEM images

FT-IR Spectroscopy

In Figure 7, the spectrum of electrospun fibers prepared with PCL polymer, the peak observed at 3500-3300 cm^{-1} was the hydroxyl (-OH) peak. The peak belonging to the alkene group (C=C) was observed at 3000-2900 cm^{-1}. Alkyl (C-H) was observed at 2900-2800 cm^{-1}. The C=O bond was observed at 1760 cm^{-1}. It was called the aromatic ring around 1700-1650 cm^{-1}. There was a carbonyl group and O-C-O structure at 1200-1150 cm^{-1} [20-23].

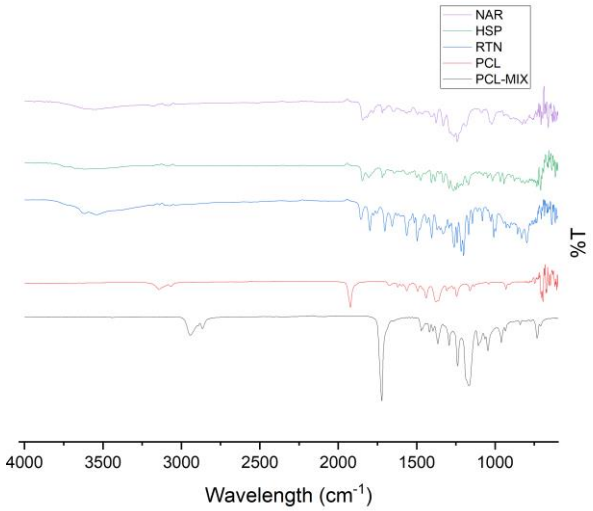

Figure 7
FT-IR spectra of citrus flavonoids, PCL and PCL-MIX fiber

In Figure 8, spectrum of electrospun fibers prepared with PLA-Gelatin polymer, the peak observed at 3500-3300 cm^{-1} is the hydroxyl (-OH) peak. The peak observed at 3000 cm^{-1} indicates the alkene group (C=C). The peak observed at 2900-2800 cm^{-1} belongs to the alkyl (C-H) group. The peaks observed at 1750 and 1700 cm^{-1} are due to carboxyl and ester bonds, respectively. The peak observed at 1650 cm^{-1} is the amide (C=O) group. The peak observed at 1550 cm^{-1} is the stretching vibration of C-N bonds. The peak observed at 1260 cm^{-1} is due to C-O-C bonds. [20-23].

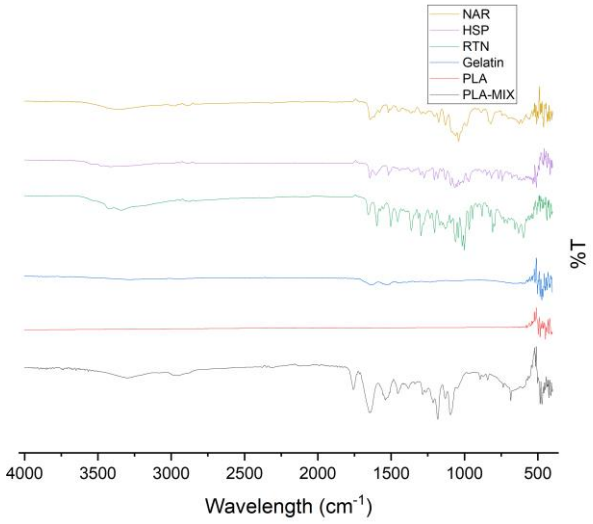

Figure 8
FT-IR spectra of citrus flavonoids, PLA, Gelatin and PLA-MIX fiber

Antibacterial Assay

It has been demonstrated that rutin hydrate has significant antibacterial properties. Rutin's strong antibacterial action was demonstrated by a study that found that at 1.87 mg/mL and 25 °C, it could suppress the growth of Staphylococcus aureus by up to 100%. Moreover, rutin has been shown to amplify the antibacterial properties of other substances, indicating a synergistic potential that may be helpful in fighting resistant bacterial strains. This is especially important when it comes to methicillin-resistant *Staphylococcus aureus* (MRSA), since rutin's capacity to stop bacterial growth may help develop more potent treatment plans [24-25].

Another flavonoid that is mostly present in citrus fruits, naringin, has likewise shown strong antibacterial qualities. Studies have demonstrated that naringin is an efficient means of inhibiting the growth of Staphylococcus aureus, especially in diseases that mirror infections, including osteomyelitis. Naringin works by perhaps rupturing the membranes surrounding bacterial cells or by blocking particular metabolic processes, which stops the growth of bacteria. Furthermore, naringin's involvement in improving the efficacy of other antimicrobial drugs emphasizes its potential as a valuable component in medicinal formulations against bacterial infections [26-27].

Like naringin, hesperidin is a flavonoid that is present in citrus peels and has been linked to several health advantages, including antibacterial action. Studies have revealed that hesperidin can suppress biofilm formation by Staphylococcus aureus, which plays a significant role in the persistence and resistance of bacterial infections. Hesperidin's capacity to prevent the formation of biofilms implies that it may be used with other antibiotics to increase their efficacy in treating infections linked to biofilms. Furthermore, as oxidative stress is known to play a role in bacterial survival and virulence, hesperidin's antioxidant qualities may also contribute to its antibacterial actions [28-29].

In the antibacterial studies, no inhibition zone was observed, but bacterial inhibition percentages were measured as 30.04±3.15% and 45.94±4.6% for PCL and PLA, respectively.

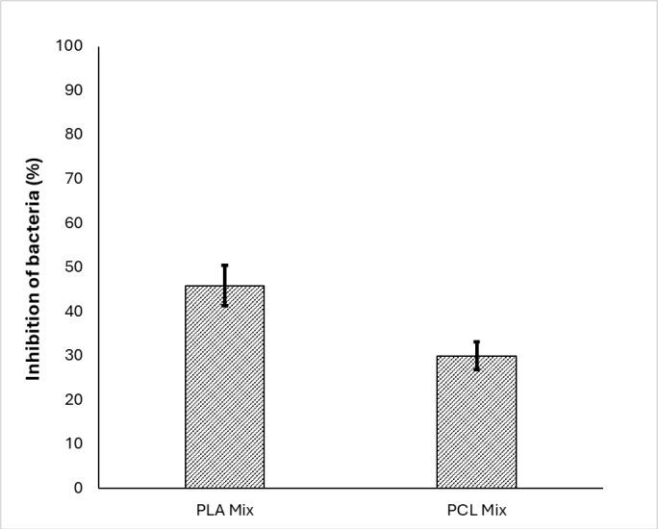

Figure 9
Inhibition of Staphylococcus aureus bacteria in PLA-MIX and PCL-MIX

DISCUSSION AND CONCLUSION

In the study, PLA and PCL electrospun fibers loaded with a flavonoid mixture were analyzed. No bead formation was observed in both produced fibers, and the fiber mats were produced smoothly. Dissolution analysis was performed at stomach pH for 3 hours and at intestinal pH for 5 hours, and it

was observed that the cumulative drug release was above 20% in both environments. In the FE-SEM images of the PCL-MIX fiber mat, it was observed that the fibers were dispersed, and no bead formation was observed. The fiber diameters were 800 nm on average. In the FESEM images of the PLA-MIX fiber mat, it was observed that the fibers were more uniformly placed, and no bead formation was observed. The fiber diameters were 200 nm on average. In the FT-IR spectra of the PCL-MIX fiber, PCL, and flavonoids compared, it was observed that the flavonoids peaked in the PCL-MIX fiber mat. Likewise, in the FT-IR spectra comparing PLA-MIX fiber, PLA, and flavonoids, it was observed that flavonoids peaked in the PLA-MIX fiber mat. *Staphylococcus aureus* is a Gram-positive, aerobic, highly pathogenic bacteria that produces toxins. It is one of the primary microbial food contaminants that cause a variety of ailments in both humans and animals. The bacterial inhibition percentage in the PCL-MIX fiber mat was measured as 30.04±3.15%. While the bacterial inhibition percentage in the PLA-MIX fiber mat was measured as 45.94±4.6%. These results showed that rutin hydrate- hesperidin-naringin-loaded PLA fiber mats can be used to gather antibacterial surfaces for different applications. While cumulative release of substances from PCL nanofiber mats is higher than the release of substances from PLA nanofiber mats, the antibacterial activities of PLA-MIX can cause by nanofiber morphologies and diameters [30-31].

Acknowledgements

We would like to thank Assoc. Prof. Dr. Fatih Erci and MSc student Hala Boubaker, members of the Biotechnology Department of the Faculty of Science at Necmettin Erbakan University, for antibacterial activity assay experiments. We would like to thank the Consolidating the Expertise of Necmettin Erbakan University Towards the Development of Biofibers for Wound Healing and Tissue Regeneration (REGENEU) project, which gave me the idea for this study and enriched my work with the training received.

Ethical Statement

This article is the revised and developed version of the unpublished conference presentation entitled "Polymer-Based Encapsulation of Flavonoids via Electrospinning for Nutraceutical Applications", presented as a poster at the 6th International Congress on Biosensors.

Author Contributions

Research Design (CRediT 1) D.T.A. (%70) - E.K. (%30)
Data Collection (CRediT 2) D.T.A. (%90) - E.K. (%10)
Research - Data Analysis - Validation (CRediT 3-4-6-11) D.T.A. (%80) - E.K. (%20)
Writing the Article (CRediT 12-13) Author 1 D.T.A. (%80) - E.K. (%20)
Revision and Improvement of the Text (CRediT 14) D.T.A. (%50) - E.K. (%50)

Financing

This study was supported by the TÜBİTAK 2244 Industry University Pre-Competition Cooperation project coded 119C100 and the Necmettin Erbakan University Scientific Researcher Project Coordinatorship project coded NEÜBAP-221415002.

Conflict of interest

The authors declare no conflict of interest for the present study.

Sustainable Development Goals (SDG)

Sustainable Development Goals: 3 Good Health and Well-Being

REFERENCES

[1] B. Tyler, D. Gullotti, A. Mangraviti, T. Utsuki, and H. Brem, Polylactic acid (PLA) controlled delivery carriers for biomedical applications, *Advanced Drug Delivery Reviews*. 107 (2016), 163–175. doi:10.1016/j.addr.2016.06.018

[2] B.L. Bachelor, X. Yang, Rutin-loaded cellulose acetate/poly(ethylene oxide) fiber membrane fabricated by electrospinning: A bioactive material, *Materials Science and Engineering: C*. 109(2020), 1–8.

[3] A. İnce Yardımcı, Ö. Tarhan, Electrospun Protein Nanofibers and Their Food Applications. *Mugla Journal of Science and Technology*. 6 (2) (2020), 52–62.

[4] B. Ghorani, N. Tucker, Fundamentals of electrospinning as a novel delivery vehicle for bioactive compounds in food nanotechnology, *Food Hydrocolloids*. 51 (2015), 227–240.

[5] V. DeStefano, S. Khan, A, Tabada, Applications of PLA in modern medicine, *Engineered Regeneration*. 1 (2020), 76–87. doi:10.1016/j.engreg.2020.08.002

[6] R. Ramamoorthy, S. Andra, S. K. Balu, F. Damiri, G. Grishnan N, M., Andiappan, M. Muthalagu, M. Berrada, Flavonoids, phenolics, and tannins loaded polycaprolactone nanofibers (NF) for Wound Dressing Applications, *Results in Materials*. 18 (2023), 100407. doi:10.1016/j.rinma.2023.100407

[7] A. C. de Figueiredo J. M. Anaya- Mancipe, A. O. De Silva de Barros, R. Santa- Oliveira, M. L. Dias, R. M. Da Silva Moreira Thire, Nanostructured Electrospun polycaprolactone—propolis mats composed of different morphologies for potential use in wound healing, *Molecules*. 27 (16) (2022), 5351. doi:10.3390/molecules27165351

[8] R. Semwal, S. K. Joshi, R. B. Semwal, D. K. Semwal, Health benefits and limitations of Rutin - a natural flavonoid with high nutraceutical value, *Phytochemistry Letters*. 46 (2021), 119–128. doi:10.1016/j.phytol.2021.10.006

[9] I. Dammak, P. José do Amaral Sobral, Formulation optimization of lecithin-enhanced Pickering emulsions stabilized by chitosan nanoparticles for hesperidin encapsulation, *Journal of Food Engineering*. 229 (2018), 2–11. doi:10.1016/j.jfoodeng.2017.11.001

[10] I. Dammak, P. J. do Amaral Sobral, Investigation into the physicochemical stability and rheological properties of rutin emulsions stabilized by chitosan and lecithin, *Journal of Food Engineering*. 229 (2018), 12–20. doi:10.1016/j.jfoodeng.2017.09.022

[11] B. Salehi, P. V. T. Fokou, M. Sharifi- Rad, P. Zucca, R. Pezzani, N. Martins, J. Sharifi- Rad, The therapeutic potential of naringenin: A review of clinical trials, *Pharmaceuticals*. 12 (1) (2019),11. doi:10.3390/ph12010011

[12] A. Bogdanova, E. Pavlova, a. Polyanskaya, M. Volkova, E. Biryukova, G. Filkov, A. Trofimenko, M. Durymanov, D. Klinov. D. Bagrov, Acceleration of electrospun PLA degradation by addition of gelatin, *International Journal of Molecular Sciences*. 24 (4) (2023), 3535. doi:10.3390/ijms24043535

[13] S. Ravichandran, J. Radhakrishnan, P. Jayabal, G. D. Venkatasubbu, Antibacterial screening studies of Electrospun polycaprolactone nano fibrous mat containing Clerodendrum phlomidis leaves extract, *Applied Surface Science*. 484 (2019), 676–687. doi:10.1016/j.apsusc.2019.04.150

[14] M. K. Haidar, S. S. Timur, G. M. Demirbolat, E. Nemutlu, R. N. Gürsoy, K. Ulubayram, L. Öner, H. Eroğlu, Electrospun nanofibers for dual and local delivery of neuroprotective drugs, *Fibers and Polymers*. 22 (2) (2021), 334–344. doi:10.1007/s12221-021-0228-2

[15] D. L. Galata, Z, Könyves, B. Nagy, m. Novak, L. A. Meszaros, E. Szabo, A. Farkas, G. Marosi, Z. K. Nagy, Real-time release testing of dissolution based on surrogate models developed by machine learning algorithms using NIR spectra, compression force and particle size distribution as input data, *International Journal of Pharmaceutics*. 597 (2021), 120338.

doi:10.1016/j.ijpharm.2021.120338

[16] C. Bommes, A. Pajic, U. Bindrich, V. Heinz, V. Lammers, Release Kinetics and encapsulation efficiency of embedded active ingredients in fat-based matrices using cold extrusion, *Innovative Food Science Emerging Technologies*. 82 (2022), 103187. doi:10.1016/j.ifset.2022.103187

[17] United States Pharmacopeia, General Chapter, ⟨711⟩ Dissolution. USP-NF. *Rockville, MD: United States Pharmacopeia*. 2023. https://doi.org/10.31003/USPNF_M99470_02_01

[18] B. M. Razavizadeh, R. Niazmand, Characterization of polyamide-6/ propolis blended electrospun fibers, *Heliyon*. 6 (8) (2020). doi:10.1016/j.heliyon.2020.e04784

[19] R. A. Wardhani, L. A. T. W. Asri, H. Rachmawati, K. Khairurrijal, B. S. Purwasasmita, Physical–chemical crosslinked electrospun colocasia esculenta tuber protein–chitosan–poly(ethylene oxide) nanofibers with antibacterial activity and cytocompatibility, *International Journal of Nanomedicine*. 15 (2020), 6433–6449. doi:10.2147/ijn.s261483

[20] Y. Wang, Y. Guo, L. Zhang, M. Yuan, L. Zhao, C. Bai, D. J. McClements, Impacts of hesperidin on whey protein functionality: Interacting mechanism, antioxidant capacity, and emulsion stabilizing effects, *Frontiers in Nutrition*. 9 (2023). doi:10.3389/fnut.2022.1043095

[21] S. Wang, T. Xue, B. Niu, L. Wei, H. Wang, Preparation, characterization and antibacterial property of naringin loaded PLGA nanospheres, *Progress in Natural Science: Materials International*. 32(4) (2022), 498–503. doi:10.1016/j.pnsc.2022.08.001

[22] D. Tang, C. Zhu, S. Zhong, M. Zhou, Extraction of naringin from Pomelo peels as Dihydrochalcone's precursor, *Journal of Separation Science*. 34(1) (2010), 113–117. doi:10.1002/jssc.201000475

[23] N. Stoyanova, M. Spasova, N. Manolova, I. Rashkov, M. Kamenova Nacheva, P. Staleva, M. Tavlinova- Kiriova, Electrospun Pla-based biomaterials loaded with Melissa officinalis extract with strong antioxidant activity, *Polymers*. 15(5) (2023), 1070. doi:10.3390/polym15051070

[24] M. A. C. Augusco, D. A. Sarri, J. F. Panontin, M. A. M. Rodrigues, R. de Moura Nunes Fernandes, J. F. M. da silva, C. A. L. Cardoso, M. K. D. Rambo, E. Scapin, Extracts from the leaf of *Couroupita guianensis* (Aubl.): phytochemical, toxicological analysis and evaluation of antioxidant and antimicrobial activities against oral microorganisms, *Plants*. 12 (2023), 1–17. doi:10.3390/plants12122327

[25] M. U. Amin, M. Khurram, B. Khattak, J. Khan, Antibiotic additive and synergistic action of rutin, morin and quercetin against methicillin resistant Staphylococcus aureus, *BMC Complementary and Alternative Medicine*. 15 (2015), 1–12. doi:10.1186/s12906-015-0580-0

[26] R. Wang, N. Wu, D. Zhan, F. Chen, Naringin exerts antibacterial and anti-inflammatory effects on mice with Staphylococcus aureus–induced osteomyelitis, *Journal of Biochemical and Molecular Toxicology*. 38 (2024), 1–12. doi:10.1002/jbt.23753

[27] Z. Yang, L. Li, C. H. Chen, Y. Y. Zhang, Y. Yang, P. Zhang, G. H. Bao, Chemical composition and antibacterial activity of 12 medicinal plant ethyl acetate extracts using LC–MS feature-based molecular networking, *Photochemical Analysis*. 33(3) (2022), 473-489. doi:10.1002/pca.3103

[28] L.A.A. Lopes, J. B. dos Santos Rodrigues, M. Magnani, E. L. de Souza, J. P. de Siqueira- Junior, Inhibitory effects of flavonoids on biofilm formation by *Staphylococcus aureus* that overexpresses efflux protein genes, *Microbial Pathogenesis.* 102 (2017), 193-197. doi:10.1016/j.micpath.2017.03.033

[29] H. M. Fathy, A. A. Abd-el- Maksoud, W. Cheng, F. M. F. Elshaghabee, Value-added utilization of Citrus peels in improving functional properties and probiotic viability of *Acidophilus-bifidus-thermophilus* (ABT)-Type synbiotic yoghurt during cold storage, *Foods.* 11 (2022), 2677. doi:10.3390/foods11172677

[30] F. Erci, E. Torlak, Antimicrobial and antibiofilm activity of green synthesized silver nanoparticles by using aqueous leaf extract of thymus serpyllum, *Sakarya University Journal of Science*. 23 (3)

(2019), 333–339. doi:10.16984/saufenbilder.445146

[31] A. G. Veiko, E. Olchowik- Grabarek, S. Sekowski, A. Roszkowska, E. A. Lapshina, I, Dobrzynska, M. Zamaraeva, I. B. Zavodnik, Antimicrobial activity of quercetin, naringenin and Catechin: Flavonoids inhibit *Staphylococcus aureus*-induced hemolysis and modify membranes of bacteria and erythrocytes, *Molecules*. 28 (3) (2023), 1252. doi:10.3390/molecules28031252

FEN ve MÜHENDİSLİK BİLİMLERİ DERGİSİ

Cilt/Vol: 7 Sayı/No: 1 Yıl/Year: 2025 Araştırma Makalesi/Research Article e-ISSN: 2667-7989

https://doi.org/10.47112/neufmbd.2025.82

Kaptopril Molekülünün Nükleer Manyetik Rezonans ve Elektron Paramanyetik Rezonans Parametrelerinin Hesaplanması

Halil Uğur TAŞDEMİR [1*] Ercan TÜRKKAN [1]

[1] Necmettin Erbakan Üniversitesi, Ahmet Keleşoğlu Eğitim Fakültesi, Matematik ve Fen Bilimleri Eğitimi Bölümü, Fizik Eğitimi Anabilim Dalı, Konya, Türkiye

Makale Bilgisi

Geliş Tarihi: 05.04.2024
Kabul Tarihi: 20.10.2024
Yayın Tarihi: 30.04.2025

Anahtar Kelimeler:
Kaptopril,
Nükleer manyetik rezonans parametreleri,
Elektron paramanyetik rezonans parametreleri.

ÖZET

Bu çalışmada ACE inhibitörü olan ve yüksek tansiyon hastalarının tedavisinde kullanılan Kaptopril ilaç etken maddesi incelenmiştir. Öncelikle Kaptopril molekülünün moleküler yapısını açığa çıkarmak için optimizasyon ve frekans hesaplaması B3LYP fonksiyoneli ve /6-31+G(d) baz seti kullanılarak gerçekleştirilmiştir. Moleküler yapı kullanılarak Kaptopril molekülünün ^{1}H kimyasal kayma değerleri GIAO metodu ve B3LYP/6-31+G(d) fonksiyoneli ve baz seti kullanılarak hesaplanmıştır. Kaptopril molekülünün moleküler yapısı kullanılarak altı olası radikal B3LYP/6-31+G(d) metot baz seti kombinasyonu yardımıyla modellenmiştir. Modellenen olası radikallere ait Elektron Paramanyetik Rezonans parametreleri (aşırı ince yapı sabiti ve g değerleri) yine aynı metot ve baz seti kombinasyonu kullanılarak hesaplanmıştır. Böylece Kaptopril molekülünün deneysel radikal çalışmaları için gelecekte yapılacak araştırmalara yardımcı olabilecek parametreler literatüre sunulmuştur.

Calculation of Nuclear Magnetic Resonance and Electron Paramagnetic Resonance Parameters of Captopril Molecule

Article Info

Received: 05.04.2024
Accepted: 20.10.2024
Published: 30.04.2025

Keywords:
Captopril,
Nuclear magnetic resonance parameters,
Electron paramagnetic resonance parameters.

ABSTRACT

In this study, the active ingredient Captopril, which is an ACE inhibitor and used in the treatment of high blood pressure patients, was examined. First of all, optimization and frequency calculation were performed using the B3LYP functional and /6-31+G(d) basis set to reveal the molecular structure of the Captopril molecule. Using the molecular structure, the ^{1}H chemical shift values of the Captopril molecule were calculated using the GIAO method and the B3LYP/6-31+G(d) functional and basis set. Using the molecular structure of the captopril molecule, six possible radicals were modeled with the help of the B3LYP/6-31+G(d) method basis set combination. Electron Paramagnetic Resonance parameters (g and hyperfine coupling constant values) of the modeled possible radicals were calculated using the same calculation method. Thus, parameters that may assist future research on experimental radical studies of the Captopril molecule have been presented to the literature.

To cite this article:
Taşdemir, H.U. & Türkkan, E. (2025). Kaptopril molekülünün nükleer manyetik rezonans ve elektron paramanyetik rezonans parametrelerinin hesaplanması. *Necmettin Erbakan Üniversitesi Fen ve Mühendislik Bilimleri Dergisi, 7*(1), 153-160. https://doi.org/10.47112/neufmbd.2025.82

***Sorumlu Yazar:** Halil Uğur Taşdemir, *halilugurtasdemir@gmail.com*

GİRİŞ (INTRODUCTION)

İlaçların yan etkilerinden ve yeni yeni ortaya çıkan virüs ve bakterilerden dolayı bütün dünyada yeni ilaçlara ihtiyaç duyulmaktadır. Bu ihtiyaç tüm dünyada yeni ilaç etken maddelerinin sentezlenmesi ya da var olan ilaç etken maddelerinin geliştirilmesi şeklinde uygulanmaktadır. Mevcut ilaç etken maddelerinin geliştirilmesinde bu maddelerin özeliklerinin tam olarak bilinmesi önemlidir. Spektroskopik çalışmalar maddelerin yapıları ve diğer özelliklerini açığa çıkarmak için kullanılan yöntemlerden biridir. Spektroskopik özelliklerin doğru belirlenebilmesi için moleküler yapının hassas bir şekilde tespit edilmiş olması gereklidir. Spektroskopik yöntemler ile sadece moleküler yapı tespiti yapılmaz aynı zamanda moleküllerin diğer özellikleri de tespit edilebilir [1-3]. Bir molekülün moleküler yapısı spektroskopik yöntemler ile ya da teorik hesaplama yöntemleri yardımıyla açığa çıkarılabilir. Moleküler yapıyı tespit etmek için kullanılan metotlarının başında X-ray spektroskopisi gelmektedir. Ancak X-ray spektroskopisinin kullanılamadığı moleküller için Nükleer Manyetik Rezonans (NMR) spektroskopisi, Infrared Rezonans spektroskopisi, Raman spektroskopisi gibi spektroskopik yöntemlerden yararlanılır. Moleküler yapıyı açığa çıkarmada kullanılan yaygın bir hesaplama metodu da Yoğunluk Fonksiyonelleri Teorisi (Density Functional Theory,DFT) yöntemidir [4-8]. DFT metodu moleküler yapıyı tespit etmekte başarılı olduğu kadar NMR, İnfrared ve Raman spektrumlarına ait parametrelerin hesaplanmasında da oldukça başarılı sonuçlar vermektedir.

Bir ilaç etken maddesinin reaksiyon mekanizmasının bilinmesi ilacın nasıl etki edeceği ile ilgili bir fikir oluşturur. Reaksiyon mekanizmaları genelde etken maddelerin indirgenme ya da yükseltgenmeleri üzerinden gerçekleşir. Bir molekülde eşleşmemiş elektron(lar) bulunursa bu tür yapılara radikal ismi verilir. İlaç etken maddesinin indirgenme ya da yükseltgenme mekanizması sonucunda radikalik yapı oluşur. Moleküllerde ki radikalik yapıları tespit etmek için Elektron Paramanyetik Rezonans (EPR) spektroskopisi kullanılır.

Bir moleküldeki radikal, EPR parametreleri olan aşırı ince yapı sabiti (hyperfine coupling constants, hfccs) ve g değerleri yardımıyla deneysel spektrumdan tayin edilebilir. g ve hfccs değerleri EPR spektrumundan elde edilebileceği gibi DFT hesaplama metodu ile de başarılı bir şekilde hesaplanabilir. İlaçlar sterilizasyon amaçlı, bazen de kazara radyasyona maruz kalabilmektedirler. Böyle bir durumda da ilaç içerisinde radikal oluşabilir. Radyasyona maruz kalmış bir ilaçta radikal oluşup oluşmadığını tespit etmek önemlidir.

Bu çalışmada ilaç etken maddesi olan Kaptopril molekülünün, ki bu molekül ACE inhibitörü olarak bilinen yüksek tansiyon hastalığı ve kalp yetmezliği tedavisi için kullanılır, moleküler yapısı NMR parametre hesaplamaları (^{1}H kimyasal kayma değerleri) ve olası radikalleri modellenmiştir. [9-11]. Modellenen olası radikallere ait EPR parametreleri hesaplanmıştır.

MATERYAL VE METOT (MATERIALS AND METHOD)

Kaptopril molekülünün başlangıç yapısı Gaussian 03 programı kullanılarak oluşturuldu [12]. Oluşturulan bu başlangıç yapısı için DFT metodunda B3LYP fonksiyoneli ve 6-31+ G(d) baz seti yardımıyla optimizasyon-frekans hesabı gerçekleştirildi [13-15]. Böylece Kaptopril molekülünün moleküler yapısı açığa çıkarıldı. Kaptopril molekülünün en kararlı yapısı kullanılarak NMR parametresi olan ^{1}H kimyasal kayma değerleri, DFT metodunda B3LYP/6-31+G(d) fonksiyoneli ve baz seti yardımıyla hesaplandı. ^{1}H kimyasal kayma değerlerinin hesaplamaları Tetra Metil Silan molekülü referans alınarak DMSO-d_6 çözeltisi içinde gerçekleştirildi. Kaptopril molekülünün hesaplama sonucunda bulunan en kararlı yapısı kullanılarak olası altı radikal modellenmiştir. Modellenen olası altı radikalin g ve hfccs değerleri B3LYP/6-31+G(d) metot-baz seti kombinasyonu ile hesaplanmıştır.

BULGULAR (RESULTS)

Optimizasyon ve frekans hesaplaması sonucunda bulunan en kararlı yapı Şekil 1'de görülmektedir.

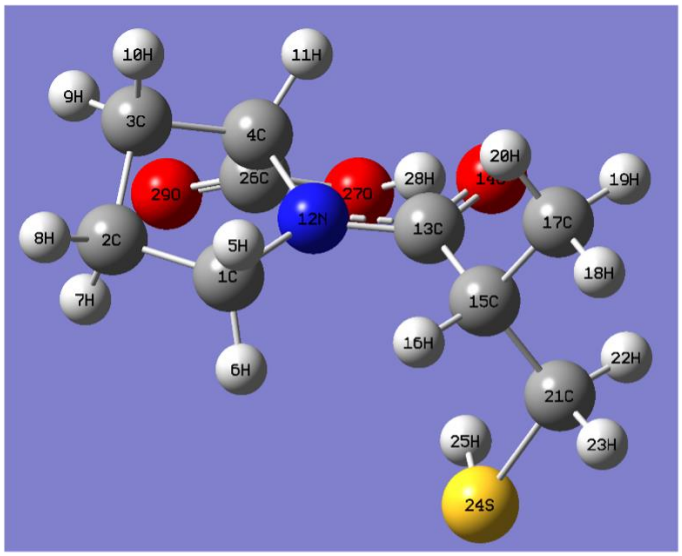

Şekil 1
Kaptopril molekülünün en kararlı yapısı

Şekil 1'de gösterilen en kararlı yapı kullanılarak hesaplanan ve literatürde mevcut olan deneysel ^{1}H kimyasal kayma değerleri Tablo1'de verilmiştir.

Tablo 1
Deneysel ve Hesaplanan ^{1}H Kimyasal Kayma Değerleri

	Teorik Hesaplanan ^{1}H kimyasal kayma değerleri (ppm)	**Deneysel^{1}H kimyasal kayma değerleri (ppm) [16]**
H5-H6	3.43	3.63
H7-H8	1.71	2.03
H9-H10	1.83	2.07
H11	4.37	4.60
H16	2.61	2.44
H18-H19-H20	0.90	1.17
H22-H23	2.33	2.82
H25	1.59	1.53
H28	10.44	9.81

Kaptopril molekülünün en kararlı yapısı kullanılarak modellenen altı olası radikal Şekil 2'de verilmiştir. Şekil 2'de verilen altı olası radikal modellenirken; R1 radikali için 5 numaralı H atomu, R2 radikali için 11 numaralı H atomu, R3 radikali için 18 numaralı H atomu, R4 radikali için 22 numaralı H atomu, R5 radikali için 25 numaralı H atomu ve R6 radikali içinde 28 numaralı H atomlarının Kaptopril molekülünden kopmuş olduğu dikkate alınmıştır.

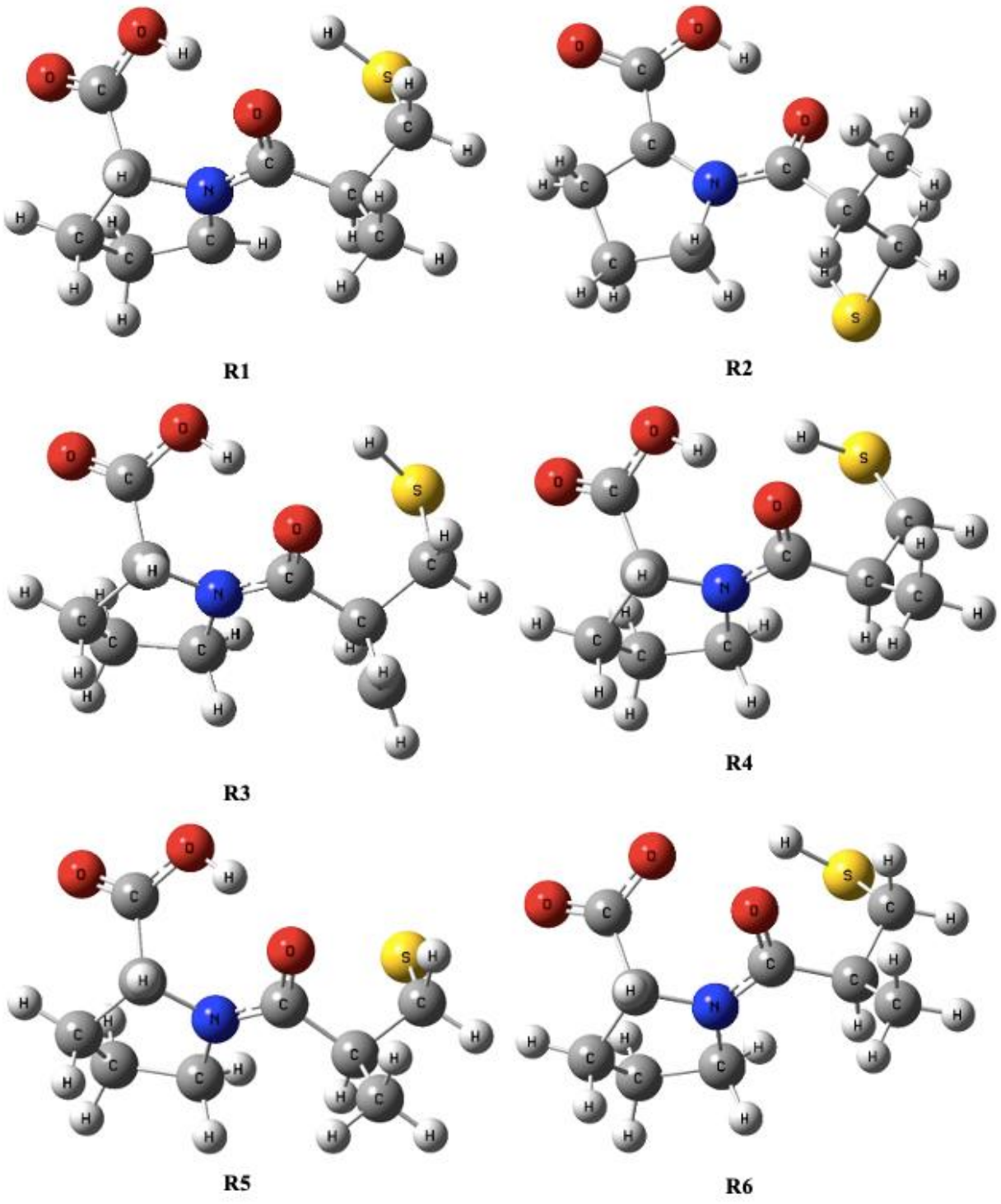

Şekil 2
Kaptopril molekülünün modellenen olası radikalleri

Modellenen olası alt radikale için B3LYP fonksiyoneli ve 631+G(d) baz seti ile hesaplanan g ve hfccs değerleri Tablo 2'de verilmiştir.

Tablo 2
Modellenen Altı Olası Radikalin Hesaplanan EPR Parametreleri

(Gauss)	R1	R2	R3	R4	R5	R6
H5	-	1.6		-		1.7
H6	15.7	-		-		1.2
H7	37.4	-		-		
H8	20.0	-		-		
H9	-	16.6		-		
H10	-	29.6		-		2.8
N12	1.2			-		
H16	-	-	3.7	34.4		1.2
H19	-	-	23.2	-		
H20	-	-	23.5	-		
H22	-	-	1.2	-	27.9	
H23	-	-	-	22.9	24.6	
H25	-	-	-	11.2		
O27						24.3
$\mathbf{g_{iso}}$	2.0030	2.0036	2.0027	2.0039	2.1303	2.0074

TARTIŞMA VE SONUÇLAR (DISCUSSION AND CONCLUSIONS)

Kaptopril molekülünün en kararlı yapısı Şekil 1'de verilmiştir. Şekil 1'deki yapı incelediğinde molekülde azot atomunun bulunduğu halkanın düzlemsel olmadığı görülmektedir. Ayrıca 28 numaralı H atomu ile 14 numaralı O atomu arasındaki bağ mesafesi 1.709 Å. Bu mesafe hidrojen bağı mertebesindedir. Dolayısıyla molekülde H28 ile O14 arasında bir molekül içi hidrojen bağı olduğu söylenebilir. Kaptopril molekülünün en kararlı yapısı kullanılarak hesaplanan ^{1}H kimyasal kayma değerleri Tablo 1 de verilmiştir. Tablo 1 incelendiğinde 28 numaralı H atomunun kimyasal kayma değeri diğer hidrojenlerin kimyasal kayma değerinden büyüktür. Bu durum 28 numaralı H atomunu hidrojen bağı yaptığını gösterir. Deneysel ^{1}H kimyasal kayma değerleri [16] ile hesaplanan değerlerin birbirleriyle uyumlu olduğu Tablo 1'den görülmektedir. Spektroskopik özellikler moleküler yapıya bağlı olduğundan hesaplama sonucunda elde edilen Şekil 1'deki moleküler yapının hesaplamalar için kullanılabileceği anlaşılmıştır. Şekil 2'deki moleküler yapı kullanılarak oluşturulan altı olası radikalin hesaplanan EPR parametreleri Tablo 2 de verilmiştir. R1, R2, R3 ve R4 model radikalleri alkil tipi radikallerdir. Yani karbon merkezli radikallerdir. R6 model radikali ise Oksijen merkezli alkoksi tipi radikaldir [17-18]. R1 model radikalinde eşleşmemiş elektronun H6, H7, H8 atomları ile etkileştiği Tablo 2'den görülmektedir. Buna göre R1 model radikali için eşleşmemiş elektronun azot atomunun bulunduğu halka üzerinde lokalize olduğu söylenebilir. R2 model radikali içinse eşleşmemiş elektronun H9, H10 ve H5 atomları ile etkileştiği Tablo 2'den görülmektedir. R2 model radikalinde de eşleşmemiş elektron azot atomunun bulunduğu halka da lokalize olmuştur. R3 model radikali için eşleşmemiş elektron H16, H19, H20, H22 atomları ile etkileşmiştir. Eşleşmemiş elektronun özellikle H19 ve H20 atomları ile etkileşimi büyüktür. Eşleşmemiş elektron kükürt atomunun bağlı olduğu C21 karbon atomu ile C17 karbon atomu arasında lokalize olmuştur. R4 model radikalinde eşleşmemiş elektron C15 numaralı karbon atomu ile S24 numaralı kükürt atomu arasında lokalize olmuştur. R5 model radikalinde S24 numaralı kükürt atomunun bağlı olduğu kol üzerinde lokalize olmuştur. R5 model radikalinin modellenen R1, R2, R3, R4 radikallerine göre g değeri büyük çıkmıştır. R1, R2, R3 ve R4 model radikallerinin g değerleri organik moleküllerde oluşan radikallerin g değerlerine yakınken R5 model radikalinin g değeri bu aralığa girmemektedir. R6 model radikalinde ise eşleşmemiş elektron O27 ile büyük bir etkileşim gösterirken, H5, H6, H10 ve H16 atomları ile küçük etkileşimler gösterdiği Tablo 2'den görülmektedir. Yani R6 model radikali için eşleşmemiş elektron O27 atomu üzerinde lokalizedir.

R6 model radikali alkoksi tipi bir radikaldir. Yani oksijen merkezli bir radikaldir. Alkoksi tipi radikallerin g değeri Karbon merkezli bir radikal tipi olan Alkil radikallerinden genelde büyüktür. Bu hesaplamada alkil tipi radikaller R1, R2, R3 ve R4 model radikalleridir. R6 model radikali için 27 numaralı Oksijen atomunda hfccs değeri Tablo 2 de görülse de bunun deneysel olarak ölçülmesi pek mümkün değildir. Çünkü hfccs çekirdek spini sıfırdan farklı olan bir çekirdek ile eşleşmemiş elektronun etkileşmesinin bir ölçüsüdür. Oksijen atomunun çekirdek spini sıfırdan farklı olan izotopunun doğada bulunma olasılığı % de 0.038 dir. Bundan dolayı oksijen atomu için deneysel olarak hfccs ölçümü yapmak çok zordur.

Bu çalışmada tansiyon ilacı olarak kullanılan Kaptopril molekülünün moleküler yapısı DFT metodu ile açığa çıkarılmıştır. Kaptopril molekülünün ^{1}H kimyasal kayma değerleri de yine DFT metodu yardımıyla hesaplanmıştır. Hesaplanan ^{1}H kimyasal kayma değerleri ile deneysel değerler birbirleri ile karşılaştırılmıştır. Kaptopril molekülünün en kararlı yapısı kullanılarak altı tane olası radikal modellenmiştir. Altı radikalin EPR parametreleri olan g ve hfccs değerleri DFT metodu yardımıyla hesaplanmıştır. Böylece Kaptopril molekülünde oluşabilecek radikallere ait EPR parametreleri literatüre kazandırılmıştır. Hesaplanan EPR parametreleri Kaptopril molekülünde oluşabilecek radikal çalışmaları için gelecekte yapılacak deneylere yol göstermiş olacaktır.

Etik Beyan (Ethical Declaration)

Bu çalışma, 7. Uluslararası Moleküler Biyoloji ve Biyoteknoloji Kongresinde poster bildirisi özeti şeklinde sunulmuştur.

Yazar Katkıları (Authors Credit)

Araştırma Tasarımı (CRediT 1) H.U.T (%80) – E.T. (%20)
Veri Toplama (CRediT 2) H.U.T. (%60) – E.T. (%40)
Araştırma - Veri Analizi - Doğrulama (CRediT 3-4-6-11) H.U.T (%50) – E.T. (%50)
Makalenin Yazımı (CRediT 12-13) H.U.T (%60) – E.T. (%40)
Metnin Tashihi ve Geliştirilmesi (CRediT 14) H.U.T (%40) – E.T. (%60)

Finansman (Funding)

Bu çalışma kapsamında herhangi bir kurum/kuruluştan finansal destek alınmamıştır.

Çıkar Çatışması (Conflict of Interest)

Yazarların bu çalışma için beyan ettiği herhangi bir çıkar çatışması yoktur. (The authors have no conflicts of interest to disclose for this study.)

Sürdürülebilir Kalkınma Amaçları (SDG)

Sürdürülebilir Kalkınma Amaçları 3: Sağlık ve Kaliteli yaşam

KAYNAKÇA (REFERENCES)

[1] F. N. Aslan, İ. Varlı, Synchronous fluorescence spectroscopy method based on chemometrics: authentication of extra virgin olive oils harvested in Mut (Mersin) region and refined edible oils, *Necmettin Erbakan Üniversitesi Fen ve Mühendislik Bilimleri Dergisi*. 5(2) (2023), 278–287. doi:10.47112/neufmbd.2023.25

[2] M. İ. Özgün, A.B. Batıbay, B. Ünal, Y. R. Eker, A. Terlemez, Investigation of the use of TiO2 obtained from endodontic NiTi Files in dye-sensitized solar cells, *Necmettin Erbakan Üniversitesi Fen ve Mühendislik Bilimleri Dergisi*. 5(1) (2023), 1–8. doi:10.47112/neufmbd.2023.4

[3] K. Çetin, K. Şarkaya, B. Kavakcıoğlu Yardımcı, Bakır (II) iyonu ve histidin içeren polimerlerin *Saccharomyces cerevisiae* mayası üzerindeki antifungal etkileri, *Necmettin Erbakan Üniversitesi Fen ve Mühendislik Bilimleri Dergisi*. 5(2) (2023). doi:10.47112/neufmbd.2023.24

[4] E. Ece, H. U.Tasdemir, R. Biyik, A. Ozmen, U. Sayin, Paramagnetic characterization and dosimetric properties of Airfix drug and its ingredients (Montelukast sodium, Sorbitol): An EPR and DFT study, *Radiaiton Physics and Chemistry*. 195(2022), 110082. doi:10.1016/j.radphyschem.2022.110082

[5] H. U. Tasdemir, Efects of intramolecular hydrogen bonding on nuclear magnetic resonance, electron paramagnetic resonance and molecular docking studies: Mexiletine molecule, *Journal of Molecular Modeling*. 30(41) (2024). doi:10.1007/s00894-024-05838-y

[6] W.J. Hehre, L. Radom, P.V.R. Schleyer, J. Pople, AB INITIO Molecular Orbital Theory, *John Wiley & sons Ltd.*, New York, United States of America, 1986.

[7] V.G. Malkin, O.L. Malkina, L.A. Eriksson, D.R. Salahub, The calculation of NMR and ESR spectroscopy parameters using density functional theory, in: *Theoretical and computational chemistry*, 1995: pp. 273–347. doi:10.1016/s1380-7323(05)80039-1

[8] H. U. Tasdemir, E. Turkkan, U. Sayin, A. Ozmen, EPR study of gamma-irradiated 2-Bromo-4′-methoxyacetophenone single crystals, *Radiation Effect and Defect in Solids*. 171 (2016), 214–222. doi:10.1080/10420150.2016.1170017

[9] M.A. Ondetti, B. Rubin, D.W. Cushman, Design of specific inhibitors of Angiotensin-Converting enzyme: new class of orally active antihypertensive agents, *Science*. 196 (1977), 441–444. doi:10.1126/science.191908.

[10] D.W. Cushman, H.S. Cheung, E.F. Sabo, M.A. Ondetti, Design of potent competitive inhibitors of angiotensin-converting enzyme. Carboxyalkanoyl and mercaptoalkanoyl amino acids, *Biochemistry*. 16 (1977), 5484–5491. doi:10.1021/bi00644a014

[11] N.S. Akhtar, A.A. Isab, A.R. Al-Arfaj, ^{13}C and ^{15}N NMR studies of the ınteraction of gold(I) captopril with selenocyanate, selenourea and thiourea in aqueous solution, *Journal of Inorganic Biochemistry*. 3(1997), 197–205. doi:10.1016/S0162-0134(96)00205-X

[12] M.J. Frisch, G.W. Trucks, H.B. Schlegel, v.d., Gaussian 03, Revision E.01. Gaussian Inc., Pittsburg PA, 2003.

[13] C. Lee, W. Yang, R.G. Parr, Development of the Colle-Salvetti correlation-energy formula into a functional of the electron density, *Physical Review. B, Condensed Matter*. 37 (1988), 785–789. doi:10.1103/physrevb.37.785

[14] A.D. Becke, Density-functional thermochemistry. III. The role of exact exchange, *The Journal of Chemical Physics*. 98 (1993), 5648–5652. doi:10.1063/1.464913

[15] P.J. Stephens, F.J. Devlin, C.F. Chabalowski, M.J. Frisch, Ab initio calculation of vibrational absorption and circular dichroism spectra using density functional force fields, *The Journal of Physical Chemistry*. 98 (1994), 11623–11627. doi:10.1021/j100096a001

[16] H. Kadin, Captopril, in: *Analytical profiles of drug substances*, 1982: pp. 79–137. doi:10.1016/s0099-5428(08)60261-0

[17] W. A. Bernhard, D. M. Close, J. Huttermann, H. Zehner, The alkoxy radical, RCH2O, as a free radical product in x-irradiated single crystals of nucleosides and nucleotides, *The Journal of Chemical Physics*. 67(3) (1977), 1211-1219. doi:10.1063/1.434931

[18] H. U. Tasdemir, U. Sayin, E. Turkkan, A. Ozmen, EPR investigation of gamma irradiated single crystal guaifenesin: A combined experimental and computational study, *Radiation Physics and Chemistry*. 121 (2016), 61–68. doi:10.1016/j.radphyschem.2015.12.016

FEN ve MÜHENDİSLİK BİLİMLERİ DERGİSİ

Vol: 7 No: 1 Year: 2025 | Araştırma Makalesi/Research Article | e-ISSN: 2667-7989

https://doi.org/10.47112/neufmbd.2024.83

Yüksek Hızlı 3B Yazıcıda Basılmış PLA, PETG ve ABS Numunelerin Mekanik Özellikleri

Mürsel EKREM [1] **Musa YILMAZ** [1,2*]

[1] Necmettin Erbakan University, Faculty of Engineering, Department of Mechanical Engineering, Konya, Türkiye

[2] Yozgat Bozok University, Sorgun Vocational School, Department of Transportation Services, Yozgat, Türkiye

Makale Bilgisi

Geliş Tarihi: 16.07.2024
Kabul Tarihi: 27.09.2024
Yayın Tarihi: 30.04.2025

Anahtar Kelimeler:
3B Yazıcı,
Fonksiyonel dereceli malzeme,
ABS, PLA, PETG.

ÖZET

Malzemenin katmanlar halinde biriktirilmesi ile yeni bileşenlerin oluşturulmasında en popüler yöntemlerden biri olan 3B baskı başta havacılık ve tıp olmak üzere birçok alanda geniş bir ürün yelpazesi için kullanılmaktadır. 3B baskı özellikle termoplastik malzemelere odaklanmakta ve fonksiyonel dereceli ürünler kolaylıkla üretilebilmektedir. 3B baskıda kullanılan üretim parametreleri, basılan ürünlerin mekanik özelliklerini önemli ölçüde etkileyecek şekilde değişiklik gösterir. Bu çalışmada, PLA, PETG ve ABS numuneleri, ASTM standartlarına uygun olarak yüksek hızlı bir 3D yazıcı kullanılarak basılmıştır. Üretilen numunelerin malzeme özelliklerini belirlemek amacıyla çekme, sertlik, yüzey pürüzlülüğü ve su emilimi testleri yapılmıştır. Sonuçlar, en çok tercih edilen termoplastik malzemelerin (PLA, PETG ve ABS) karşılaştırmalı bir analizini sunmakta ve yüksek hızlı baskı için bir üretim kılavuzu görevi görmektedir. PETG numuneleri için maksimum gerilme 51,3 MPa olarak bulunurken, PLA için bu değer 48 MPa ve ABS numuneleri için 42,8 MPa olmuştur. Ayrıca, PETG numunesinin üst yüzeyinin ortalama sertliği 76 Shore A ile en yüksek olarak belirlenmiş, PLA ve ABS numuneleri için ise sırasıyla 69 Shore A ve 63 Shore A değerleri gözlemlenmiştir. Son olarak, işlem görmemiş haliyle en pürüzlü yüzey 9,441 Ra ile ABS numunelerinde elde edilmiştir ve zımparalama işlemleri ile yüzey kalitesinde önemli iyileşmeler gözlemlenmiştir.

Mechanical Properties of PLA, PETG, and ABS Samples Printed on a High-Speed 3D Printer

Article Info

Received: 16.07.2024
Accepted: 27.09.2024
Published: 30.04.2025

Keywords:
3D Printer,
Functional graded material,
ABS, PLA, PETG.

ABSTRACT

3D printing, one of the most popular methods for creating new components through the deposition of material in layers, is used across a wide range of products, particularly in the aerospace and medical fields. 3D printing focuses especially on thermoplastic materials, allowing for the easy production of functionally graded products. The manufacturing parameters used in 3D printing vary, significantly affecting the mechanical properties of the printed items. In this study, PLA, PETG and ABS samples were printed using a high-speed 3D printer in accordance with ASTM standards. Tensile, hardness, surface roughness and water absorption tests were performed to determine the material properties of the produced samples. The results provide a comparative analysis of the most preferred thermoplastic materials (PLA, PETG and ABS) and serve as a production guide for high-speed printing. The maximum stress for PETG specimens was found to be 51.3 MPa, while for PLA it was 48 MPa and for ABS specimens 42.8 MPa. In addition, the average hardness of the top surface of the PETG sample was found to be the highest with 76 Shore A, while 69 Shore A and 63 Shore A values were observed for PLA and ABS samples, respectively. Finally, the roughest surface in the untreated state was obtained in ABS samples with 9.441 Ra and significant improvements in surface quality were observed with sanding processes.

To cite this article:
Ekrem, M. & Yılmaz, M. (2025). Mechanical properties of PLA, PETG, and ABS samples printed on a high-speed 3D printer. *Necmettin Erbakan University Journal of Science and Engineering*, *7*(1), 161-174. https://doi.org/10.47112/neufmbd.2024.83

***Corresponding Author:** Musa Yılmaz, *musa.yilmaz@bozok.edu.tr*

INTRODUCTION

Three-dimensional printing is an innovative manufacturing method that enables the rapid and cost-effective creation of complex parts by adding layers. [1]. This technology begins with the creation of a digital model using computer-aided design (CAD) software. This digital model is then transferred to a 3D printer, enabling the production of 3D objects using different materials. This method is frequently preferred in various fields such as automotive, aerospace, and biomedical [2] for purposes such as prototyping, customized products, and R&D [3].

Despite providing many benefits, 3D printing also comes with some disadvantages. Firstly, in certain industrial applications, the production processes can be longer compared to traditional manufacturing methods. Considering the time and material required for the production of large parts, the cost of 3D printing can increase. Additionally, the surface roughness of parts produced by 3D printing is generally high, which can lead to undesirable results in certain applications. Material options are sometimes limited, and suitable options may not be available for specific applications. Lastly, the efficiency of 3D printing for mass production is lower compared to traditional manufacturing methods [4].

The materials used in this method vary widely based on the needs of the printing process, the intended use of the final product, and the desired properties. Various types of materials, including plastics, metal alloys, ceramics, biological materials, and hybrid materials [5], can be used in 3D printing. Plastics are generally the most commonly used type of material and can be divided into many subcategories with different properties; these include thermoplastics, thermosets, elastomers, and biodegradable plastics [6].

Among the most used polymer materials in 3D printing are PLA, PETG, and ABS. These materials have a wide range of applications in various industrial and personal uses and are frequently preferred by the 3D printing community [7].

Polylactic acid (PLA) is a thermoplastic monomer typically derived from organic, renewable sources such as sugarcane or corn starch. PLA is considered an environmentally friendly option as it is biodegradable and sourced from renewable resources. Some of its many advantages include ease of production, recyclability, biocompatibility, and minimal or no carcinogenic effects. PLA is frequently used in both food and medical applications. The absence of smoke or unpleasant odors during printing, along with its ease of sanding, painting, or other finishing processes, increases its preference for 3D printing [8].

PETG (Polyethylene Terephthalate Glycol) is a thermoplastic material widely used in various fields such as 3D printing, packaging, and medical devices. Its advantages include high impact resistance and flexibility, low shrinkage tendency, chemical resistance, and ease of processing. PETG also offers high transparency and glossy surface quality, making it aesthetically appealing. Its recyclability is an environmental benefit. However, it also has disadvantages. PETG tends to soften at high temperatures, which can limit its performance in certain applications. Additionally, it can be more expensive compared to some other thermoplastics. Adhesion issues and moisture absorption capacity can also be drawbacks for some users [9].

ABS (Acrylonitrile Butadiene Styrene) is a widely used thermoplastic favored in various fields such as automotive parts, toys (e.g., LEGO), electronic housing, and 3D printing. Its advantages include high impact resistance, rigidity, durability, good heat resistance, and excellent processability. ABS has good flow properties, allowing to produce complex shapes, and it can be painted and coated, making it suitable for various aesthetic applications. Additionally, it is relatively cost-effective and available in a wide range of colors. However, ABS also has disadvantages. It can emit an unpleasant odor during

production and typically requires high temperatures during 3D printing, which can lead to warping issues. Moreover, it has low resistance to UV radiation and environmental stress cracking, making it less ideal for outdoor applications. Furthermore, recycling ABS is more challenging compared to some other plastics, and it can have a more significant negative environmental impact [10].

Many researchers are conducting studies to optimize the printing process parameters used in the production of 3D parts. A detailed analysis of the mechanical properties of 3D printed parts helps manufacturers predict the mechanical behaviour of the printed part; this demonstrates the necessity of effectively adjusting process parameters to obtain parts of desired quality [2].

This study examined the hardness, surface roughness, tensile strength, and water absorption properties of ABS, PETG, and PLA 3D printing samples. The tensile properties of the samples were evaluated using ASTM D638 standard, while water absorption properties were tested by conditioning in pure water at 25%, 50%, 75%, and 100% saturation levels followed by mass measurements. Surface roughness analysis was conducted by abrading the samples with three different sandpapers (220, 400, and 800 grit) and then measuring with the Surface Roughness Tester TR200 device. Hardness tests were performed using the Shore D version of the Shore NOVOTEST TS-A device, suitable for thermoplastic materials and compliant with ASTM D2240 standard.

MATERIALS AND METHODS

Supply of 3D Printer and Materials

The 3D printer used in the study is shown in Figure 1.

Figure 1
Creality brand 3D printer (while printing tensile specimens with PLA filament material)

After conducting the research, PETG filament was purchased from Elas 3D, PLA filament from Microzey, and ABS filament from Porimo. All filaments have a diameter of 1.75 mm and are in 1 kg spools. The specifications provided by the companies for the purchased filaments are detailed in Table 1.

Table 1
Properties of materials used in 3D printing

Print Specifications	PLA	PETG	ABS
Extrusion Temperature (°C)	190-230	230-250	220-260
Bed Platform Temperature (°C)	25-80	60-80	80-110
Density (g/cm³)	1.24	1.32	1.04
Recycling	Yes	Yes	Yes
Biodegradability	Yes	No	No
Smoke Toxicity	Low	Low	Medium

Additionally, 5 liters of distilled water and three different types of sandpaper (220, 400, and 800 grit) were purchased for use in the tests.

Production of 3D Parts

As part of the project, sample sizes were determined in accordance with relevant ASTM standards or literature. The geometry of the samples was modeled using SolidWorks and saved in STL format. Subsequently, the models were simulated for 3D printing and necessary parameters were adjusted using Creality Print software (Figure 2).

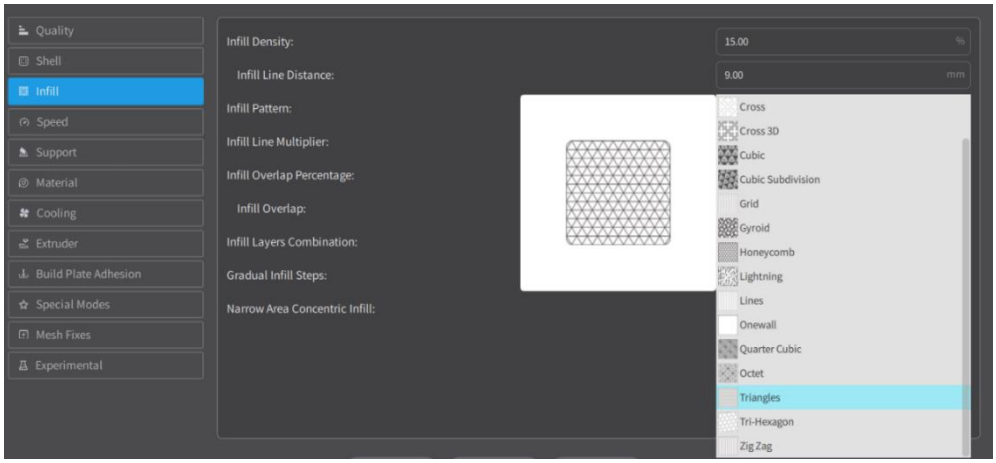

Figure 2
Interface used when setting printing parameters with Creality Print software

The basic parameters used for printing the parts are provided in Table 2.

Table 2
Basic printing parameters of 3D parts

Process Parameters	PLA	PETG	ABS
Layer Thickness (mm)	0,2	0.2	0.2
Initial Layer Thickness (mm)	0.2	0.2	0.2
Number of Wall Lines	2	2	2
Number of Upper and Lower Lines	4	4	4
Raster Angle	45°/-45°	45°/-45°	45°/-45°
Filling Pattern	Triangles	Triangles	Triangles
Filling Speed (mm/s)	300	300	300
Printing Temperature (°C)	230	250	260
Nozzle Diameter (mm)	0.4	0.4	0.4
Room Temperature (°C)	25±1	25±1	25±1
Relative Humidity (%RH)	50±5	50±5	50±5

Tensile Test

The samples designed in SolidWorks program for determining tensile strength in accordance with ASTM D638 standard geometry are shown in Figure 3.

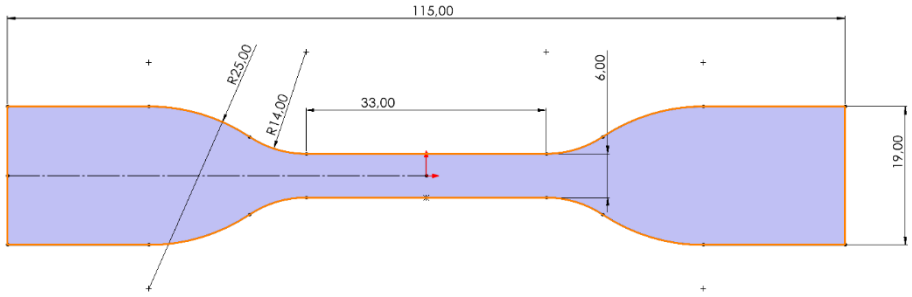

Figure 3
Geometry of specimens used in tensile tests

The tensile specimens designed in SolidWorks were saved in STL format, edited using Creality Print software, and transferred to the printer (Figure 4).

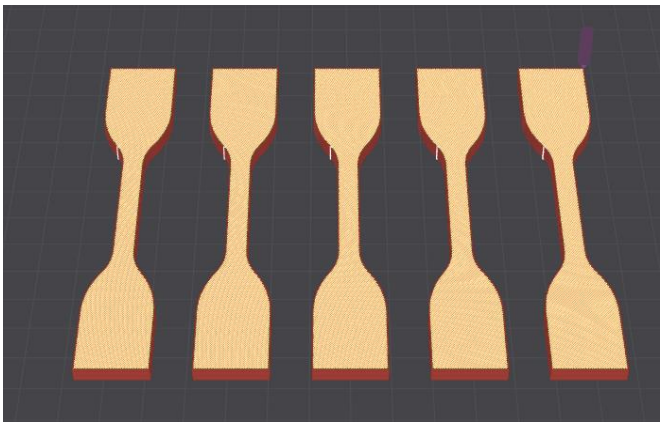

Figure 4
Preparation of tensile samples for printing in Creality Print software

The produced samples (Figure 5) were tested using the Shimadzu Tensile Testing Machine located in the Mechanical Laboratory of Necmettin Erbakan University, Department of Mechanical Engineering.

Figure 5
Tensile samples produced by 3D printer (yellow colour ABS filament material, black colour PETG filament material)

Hardness Test

To determine the hardness of the materials, the Shore Durometer NOVOTEST TS-A device was used (Figure 6). This testing device is typically used to measure the hardness of elastomers, rubber,

plastics, and other soft materials. It operates using the Shore A scale, which measures how much deformation a material undergoes under a specified pressure applied to its surface [11].

Figure 6
a) Shore Durometer NOVOTEST TS-A hardness tester, b) zeroing the load scale

Surface Rouhgness

To enhance the aesthetic appearance of 3D parts, various surface treatments such as sanding, filling, painting, or chemical processes are employed. Therefore, the response of filament materials to sanding is crucial. In this project, samples made from three different materials (PLA, PETG, and ABS) were sanded at three different grades (220, 400, and 800 grit) to investigate surface quality. The sanding process progressed stepwise to higher grits; for example, 220 and 400 grit sanding were performed before using 800 grit sandpaper. Sanding was conducted in a wet environment and continued in one direction until the marks underneath disappeared (Figure 7).

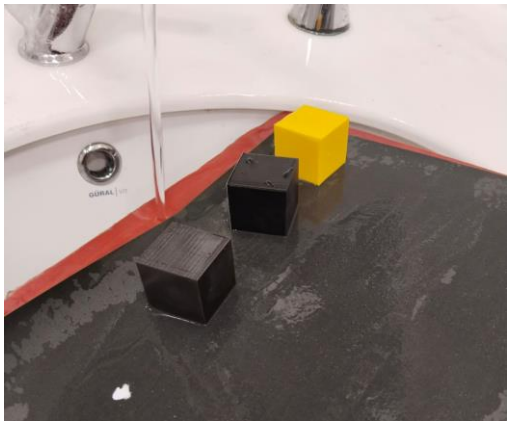

Figure 7
Gradual sanding of the samples in aqueous medium

The Surface Roughness Tester TR200 was used to determine the surface roughness of the samples (Figure 8). Surface roughness was measured in two different angular directions, 0° and 90°, and expressed as the arithmetic average value known as Ra.

Figure 8
Surface roughness tester TR200

Water Absorption Behaviour

As part of the study, cubic parts measuring 3x3x3 cm were produced at 25%, 50%, 75%, and 100% infill densities using three different filament materials (PLA, PETG, and ABS) (Figure 9).

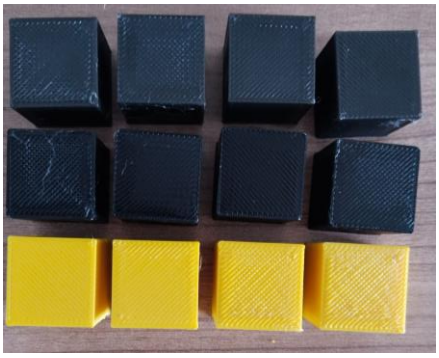

Figure 9
PETG (top), PLA (middle) and ABS (bottom) filament material specimens of different fillings produced to determine water absorption behavior

These parts were fully immersed in distilled water and regular daily mass measurements were taken (Figure 10).

Figure 10
Weighing the samples by keeping them in pure water

Thus, the aim was to determine both the water absorption levels of the samples based on infill density and filament material, as well as any dimensional changes that may occur over time.

RESULTS

The results of the study conducted in the project were analyzed in four parts: tensile test analyses, hardness test analyses, surface roughness analyses, and water absorption behavior analyses.

Tensile Test Analyses

The samples were tested using the Shimadzu Tensile Testing Machine according to ASTM D638 standard, at a crosshead speed of 5 mm/min, at 23°C room temperature, and with 5 repetitions. The data obtained from the tests were analyzed using Excel software and shown in Figure 11. Upon examining the graph, it is observed that in terms of the slope in the elastic region, PLA filament material has the highest modulus of elasticity, while PETG material has the lowest modulus. Additionally, the area under the curves represents the energy required to fracture the material, indicating its toughness. In this context, PETG material exhibits the highest toughness, whereas PLA material shows the lowest toughness.

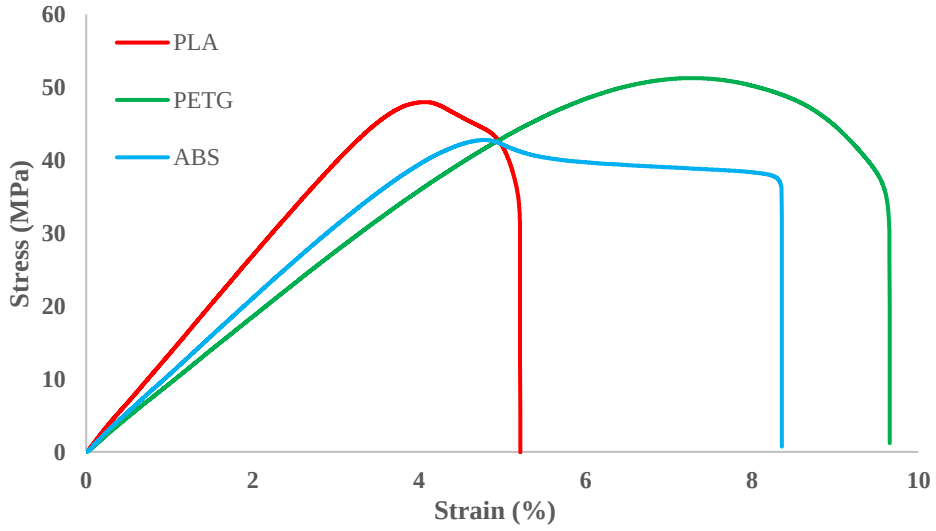

Figure 11
Stress strain graph

The equations used in the calculations are as follows:

$\sigma = F / A$ ……. (Equation 1)

Here, σ represents the stress value; F denotes the tensile force obtained by the testing machine. A represents the cross-sectional area (4x6=24mm^2) of the tensile specimen.

$\varepsilon = (\Delta L / L0).100$……..... (Equation 2)

Here, ε represents the percentage elongation (% strain), ΔL denotes the amount of elongation that occurred, and L0 represents the initial gauge length.

$E = \sigma / \varepsilon$ ……... (Equation 3)

Here, E represents the slope of the linear region of the stress-strain diagram, which is the elastic modulus.

$\int_0^{\varepsilon_k} \sigma . d\varepsilon$ …… (Equation 4)

The value obtained from Equation 4 represents the area under the stress-strain curve, indicating the toughness of the specimen. The results of the calculations and analyses are comprehensively presented in Table 3.

Table 3
Mechanical properties of specimens

Mechanical Properties	PLA	PETG	ABS
Elastic Modulus (MPa)	1346.4±20	905.6±10	1030.0±15
Max. Stress (MPa)	48.0±2	51.3±2	42.8±1
Max. Strain (%)	5.22±0.1	9.65±0.1	8.36±0.1
Toughness (kJ/m³)	159.2±5	334.4±8	256.7±7

When examining Table 3, the maximum tensile strength is achieved in PETG samples up to 51.3 MPa, while PLA and ABS samples yielded 48 MPa and 42.8 MPa, respectively. Additionally, the elastic modulus, an important parameter in material characterization, was highest in PLA samples at 1346.4 MPa, followed by PETG at 905.6 MPa and ABS at 1030 MPa.

The differences in tensile properties between PLA, PETG and ABS materials are related to their molecular structure and thermal behaviour. Although PLA offers high tensile strength, it lacks flexibility due to its crystalline structure, which can cause the material to be brittle under stress. PETG is a PET copolymer that combines the stiffness of PLA with improved flexibility and impact resistance. Its molecular structure provides better adhesion between layers during 3D printing, increasing the overall durability of the material. On the other hand, ABS allows more deformation thanks to its more amorphous structure, making it a suitable option for applications subjected to high mechanical stress or impacts [12,13]. The data obtained in this context are consistent with the findings obtained from other studies in the literature [14].

Hardness Test Analyses

The hardness tests were conducted using the Shore Durometer NOVOTEST TS-A device, with repeated tests at 5 different points on each sample. The test samples were at 100% infill, and both the top and side surfaces of the samples were tested. The data obtained from the tests are presented in Table 4.

Table 4
Hardness analysis of the samples (Unit: Shore A - 50 Shore A medium hardness, 30 Shore A softer flexible material, 90 Shore A hard plastic)

PLA- Top	PLA- Side	PETG- Top	PETG- Side	ABS- Top	ABS- Side
72	50	77	66	64	72
68	46	87	52	63	73
68	53	79	56	62	65
67	48	62	64	63	75
70	51	75	61	64	74

When examining Table 4, differences in hardness values between the top and side surfaces of the samples can be observed. The average hardness on the top surface of the PETG sample reaches the highest value at 76 Shore A, whereas for PLA and ABS samples, it is calculated as 69 Shore A and 63 Shore A, respectively. In terms of side surfaces, the highest hardness is obtained in the ABS sample with an average value of 72 Shore A, while for PLA and PETG samples, values of 50 Shore A and 60 Shore A, respectively, are calculated. In light of all this data, it is evident that all examined samples are moderately hard polymer samples, with no significant characteristic differences among the values.

PLA has a more brittle structure compared to other materials, with relatively low tensile strength

and impact resistance. Its rigid and crystalline structure can show brittleness without allowing significant deformation and therefore its stiffness is lower. ABS, on the other hand, is known for its high strength and durability as a petroleum-based thermoplastic. It has high impact strength, can withstand higher temperatures and provides higher elongation at break than PLA, making it more resistant to bending and deformation and increasing its stiffness. PETG is a thermoplastic that combines the advantages of PLA and ABS. Offering moderate tensile strength, PETG excels in impact resistance and layer adhesion. Thanks to its ability to withstand deformation without cracking, PETG's stiffness is higher than that of PLA, making it a suitable choice for applications requiring both strength and flexibility [15]. As a result, hardness differences between these materials are due to the unique components and mechanical properties of each material. Furthermore, variable parameters in 3D printing processes can lead to variations in these hardness properties [16].

Surface Roughness Analyses

Surface roughness was measured in two different angular directions, 0° and 90°, using the Surface roughness tester TR200, and expressed as the arithmetic average value of the surface roughness parameter Ra. The obtained data are presented in Table 5.

Table 5
Surface roughness values of the samples (Unit Ra)

	Top Surface	Side Surface (0°)	Side Surface (90°)	220 grid top surface	220 grid side surface	400 grid top surface	400 grid side surface	800 grid top Surface	800 grid side surface
PLA	6.603	0.502	11.207	2.195	1.338	1.623	1.173	1.054	0.654
PETG	6.166	0.645	11.506	1.828	1.323	1.148	1.146	0.687	0.763
ABS	9.441	0.792	11.519	2.865	1.222	2.005	0.995	1.363	0.861

When Table 5 is analysed, it is seen that there are differences in surface roughness depending on the material and printing wool. According to the data, it is seen that the roughest top surface is obtained in ABS specimens with 9.441 Ra in the untreated state. On the side surfaces, the surface roughness varies considerably depending on the printing direction and the material difference does not create a characteristic. In addition, the surface quality is greatly improved with the sanding processes and the values are very close to each other in the last step.

Studies show that the surface roughness of PLA is approximately 7% less than PETG and 50% less than ABS. This smoothness is attributed to its low tendency to deform during printing and excellent layer adhesion [17]. However, it is stated that the surface quality decreases with the increase of the printing speed and PLA samples have the highest decrease among the specified materials [18]. ABS typically results in the roughest surface finish of these materials. Surface roughness is affected by factors such as warping and delamination during high-speed printing. The inherent brittleness of ABS leads to more pronounced layer lines and imperfections compared to PLA and PETG [19].

Water Absorption Analysis of 3D Parts

The samples produced from PLA, PETG and ABS filament materials with 25%, 50%, 75% and 100% filling were kept in pure water and weighed every day. Thus, it was possible to analyses the relationship between the water absorption of the specimens and the material and occupancy. The data obtained as a result of the measurements are given in Table 6.

When examining Table 6, it is observed that the material that absorbs the most water is the PLA filament. Additionally, the mass percentage change increases with the increase in void content and the filling of these voids with water. When comparing the samples with full infill, the changes in the masses

of PLA, PETG, and ABS samples after 30 days of conditioning were calculated as 1.04%, 0.3%, and 0.96%, respectively.

PLA has a high-water absorption capacity over time due to its organic structure and hygroscopic properties, which causes the material to show significant changes as it encounters water. PETG, on the other hand, exhibits moderate water absorption and provides better structural integrity than PLA when in contact with moisture. ABS has the lowest water absorption rate of the three materials and is therefore less susceptible to degradation from moisture; however, it can still be affected by high humidity environments [20].

Table 6
Changes in the masses of the samples produced with PLA, PETG and ABS filament material at 4 different filling levels (25%, 50%, 75% and 100%) after standing in water - A:PLA, B:PETG and C:ABS (values in grams)

DAYS	A100	A75	A50	A25	B100	B75	B50	B25	C100	C75	C50	C25
1	9.65	8.01	6.08	4.14	9.94	8.23	6.37	4.58	8.33	7.36	5.93	4.31
2	9.68	8.05	6.09	4.17	9.94	8.23	6.38	4.61	8.35	7.37	5.95	4.32
3	9.69	8.06	6.11	4.29	9.95	8.24	6.39	4.62	8.36	7.39	5.95	4.32
4	9.69	8.08	6.16	4.34	9.95	8.25	6.41	4.68	8.36	7.39	5.95	4.33
5	9.70	8.10	6.21	4.39	9.95	8.26	6.42	4.74	8.37	7.39	5.95	4.33
6	9.70	8.11	6.22	4.39	9.95	8.27	6.43	4.74	8.37	7.39	5.96	4.34
7	9.70	8.12	6.22	4.39	9.95	8.27	6.43	4.74	8.37	7.39	5.96	4.34
8	9.71	8.12	6.22	4.39	9.95	8.27	6.43	4.75	8.38	7.39	5.96	4.34
9	9.72	8.13	6.22	4.39	9.96	8.27	6.43	4.75	8.38	7.40	5.97	4.34
10	9.72	8.13	6.22	4.39	9.96	8.27	6.43	4.75	8.38	7.40	5.97	4.34
11	9.72	8.14	6.22	4.39	9.96	8.27	6.43	4.76	8.38	7.40	5.97	4.34
12	9.72	8.14	6.22	4.39	9.96	8.27	6.43	4.76	8.39	7.40	5.97	4.35
13	9.72	8.14	6.22	4.39	9.96	8.27	6.43	4.76	8.39	7.40	5.97	4.35
14	9.72	8.15	6.22	4.39	9.96	8.27	6.43	4.76	8.39	7.41	5.97	4.35
15	9.73	8.15	6.23	4.39	9.96	8.27	6.43	4.77	8.39	7.41	5.97	4.35
16	9.73	8.15	6.25	4.39	9.96	8.28	6.43	4.78	8.39	7.41	5.97	4.35
17	9.73	8.15	6.25	4.39	9.97	8.28	6.43	4.78	8.39	7.41	5.97	4.35
18	9.73	8.15	6.25	4.39	9.97	8.28	6.43	4.79	8.40	7.41	5.97	4.35
19	9.73	8.15	6.26	4.39	9.97	8.28	6.43	4.79	8.40	7.42	5.97	4.35
20	9.74	8.15	6.26	4.39	9.97	8.28	6.43	4.80	8.40	7.42	5.97	4.35
21	9.74	8.16	6.27	4.39	9.97	8.28	6.43	4.80	8.40	7.42	5.98	4.35
22	9.74	8.16	6.27	4.39	9.97	8.28	6.43	4.80	8.40	7.42	5.98	4.35
23	9.74	8.16	6.28	4.39	9.97	8.28	6.43	4.80	8.40	7.42	5.98	4.35
24	9.74	8.17	6.28	4.39	9.97	8.29	6.43	4.80	8.40	7.42	5.98	4.35
25	9.74	8.17	6.29	4.39	9.97	8.29	6.43	4.80	8.41	7.42	5.98	4.35
26	9.75	8.17	6.29	4.39	9.97	8.29	6.43	4.80	8.41	7.43	5.98	4.35
27	9.75	8.18	6.30	4.39	9.97	8.29	6.43	4.80	8.41	7.43	5.98	4.35
28	9.75	8.18	6.30	4.39	9.97	8.29	6.43	4.80	8.41	7.43	5.98	4.35
29	9.75	8.18	6.31	4.39	9.97	8.29	6.43	4.80	8.41	7.43	5.98	4.35
30	9.75	8.18	6.31	4.39	9.97	8.29	6.43	4.80	8.41	7.43	5.98	4.35
Increase (%)	**1.04**	**2.12**	**3.78**	**6.04**	**0.30**	**0.73**	**0.94**	**4.80**	**0.96**	**0.95**	**0.84**	**0.93**

Considering the obtained data, it is understood that the water absorption amounts of the samples are quite limited and negligible. Furthermore, the obtained data are consistent with other studies in the literature. Thus, it was possible to analyses the relationship between the water absorption of the specimens and the material and occupancy [21].

DISCUSSION AND CONCLUSIONS

In this study, samples were produced and experiments were conducted in accordance with ASTM standards to examine the hardness, surface roughness, tensile strength, and water absorption properties of ABS, PETG, and PLA 3D printed samples. The main results are as follows:

- As a result of the tensile tests, the maximum stress was obtained in PETG samples with 51.3 MPa, while it was 48 MPa and 42.8 MPa in PLA and ABS samples, respectively. Additionally, the modulus of elasticity, which is an important parameter in material characteristics, was highest in PLA samples with 1346.4 MPa, and in PETG and ABS samples, it was 905.6 MPa and 1030 MPa, respectively.
- The average hardness on the top surface of the PETG sample was the highest with 76 Shore A, while it was 69 Shore A and 63 Shore A for PLA and ABS samples, respectively. Considering the obtained data, it is understood that all the examined samples are medium-hardness polymer samples.
- Differences in surface roughness were observed depending on the type of material and the printing direction. According to the data, the roughest top surface, in its untreated state, was obtained in ABS samples with 9.441 Ra. For the side surfaces, surface roughness varied significantly depending on the printing direction, and the sanding processes greatly improved the surface quality, bringing the values quite close to each other in the final step.

It was determined that the material absorbing the most water was the PLA filament. Additionally, the mass percentage change increased with the increase in void content and the filling of these voids with water. When comparing the samples with full infill, the changes in the masses of PLA, PETG, and ABS samples after 30 days of conditioning were calculated as 1.04%, 0.3%, and 0.96%, respectively.

Ethical Statement
This study is an original research article designed and developed by the authors.

Ethics Committee Approval
This study does not require any ethics committee approval.

Author Contributions
Research Design (CRediT 1) M.Y. (%75) – M.E. (%25)
Data Collection (CRediT 2) M.Y. (%75) – M.E. (%25)
Research - Data Analysis – Validation (CRediT 3-4-6-11) M.Y. (%75) – M.E. (%25)
Writing the Article (CRediT 12-13) M.Y. (%75) – M.E. (%25)
Revision and Improvement of the Text (CRediT 14) M.Y. (%75) – M.E. (%25)

Financing
This study was supported by TÜBİTAK under Project Number 1919B012309138 within the scope of the 2209 Program.

Conflict of Interest
The authors declare no conflict of interest.

Sustainable Development Goals (SDG)
Sustainable Development Goals: 9: Industry, Innovation, and Infrastructure

REFERENCES

[1] A. Bhatia, A.K. Sehgal, Additive manufacturing materials, methods and applications: A review, *Materials Today: Proceedings*. 81 (2023), 1060-1067

[2] M.U. Erdaş, B.S. Yıldız, A.R. Yıldız, Experimental analysis of the effects of different production directions on the mechanical characteristics of ABS, PLA, and PETG materials produced by FDM, *Materials Testing*. 66 (2024), 198-206. doi:10.1515/mt-2023-0206

[3] H. Hegab, N. Khanna, N. Monib, A. Salem, Design for sustainable additive manufacturing: A review, *Sustainable Materials and Technologies*. 35 (2023), e00576

[4] S. Kumar, Advantage and Disadvantage, içinde: *Additive Manufacturing Advantage*, *Springer Nature Switzerland*, Cham, 2023: ss. 1-60. doi:10.1007/978-3-031-34563-0_1

[5] E. Madenci, Fonksiyonel derecelendirilmiş malzeme plakların statik analizinde mikro-mekanik modellerin katkısı, *Necmettin Erbakan Üniversitesi Fen ve Mühendislik Bilimleri Dergisi*. 5 (2023), 23-37.

[6] S.F. Iftekar, A. Aabid, A. Amir, M. Baig, Advancements and limitations in 3D printing materials and technologies: a critical review, *Polymers*. 15 (2023), 2519.

[7] K.D. Rajesh, N. Ganesh, S.Y.K. Reddy, H. Mishra, T.M.T. Naidu, Experimental research on the mechanical characteristics of fused deposition modelled ABS, PLA and PETG specimens printed in 3D, *Materials Today: Proceedings*. (2023). doi:10.1016/j.matpr.2023.06.343

[8] K.Q. Nguyen, P.Y. Vuillaume, L. Hu, J. López-Beceiro, P. Cousin, S. Elkoun, M. Robert, Recycled, bio-based, and blended composite materials for 3D printing filament: Pros and cons—A Review, *Materials Sciences and Applications*. 14 (2023), 148-185.

[9] D. Gregor-Svetec, Polymers in printing filaments, içinde: *Polymers for 3D printing*, *Elsevier*, 2022: ss. 155-269. doi: 10.1016/B978-0-12-818311-3.00002-1

[10] A. Dey, I.N.R. Eagle, N. Yodo, A review on filament materials for fused filament fabrication. ournal Manufacturing and Materials Processing 5(3) (2021), 69. doi:10.3390/jmmp5030069

[11] A.B. Vlasov, S.V. Vlasova, Features of thermal ageing of cables with different type of insulation, *IOP Conference Series: Materials Science and Engineering*, *IOP Publishing*, 2019: s. 012132. doi:10.1088/1757-899X/560/1/012132

[12] I. Khan, M. Tariq, M. Abas, M. Shakeel, F. Hira, A.A. Rashid, M. Koç, Parametric investigation and optimisation of mechanical properties of thick tri-material based composite of PLA-PETG-ABS 3D-printed using fused filament fabrication, *Composites Part C: Open Access*.12 (2023), 100392. doi: 10.1016/j.jcomc.2023.100392

[13] R. Kumar, H. Sharma, C. Saran, T.S. Tripathy, K.S. Sangwan, C. Herrmann, A comparative study on the life cycle assessment of a 3d printed product with pla, abs & petg materials, *Procedia CIRP*. 107 (2022). doi: 10.1016/j.procir.2022.04.003

[14] S. Prajapati, J.K. Sharma, S. Kumar, S. Pandey, M.K. Pandey, A review on comparison of physical and mechanical properties of PLA, ABS, TPU, and PETG manufactured engineering components by using fused deposition modelling, *Materials Today: Proceedings*. (2024). doi: 10.1016/j.matpr.2024.05.018

[15] S. Bhandari, R.A.L. Anido, D.J. Gardner, Enhancing the interlayer tensile strength of 3D printed short carbon fiber reinforced PETG and PLA composites via annealing, *Additive Manufacturing*. 30 (2019), 100922. doi: 10.1016/j.addma.2019.100922

[16] A. Nazir, J.-Y. Jeng, A high-speed additive manufacturing approach for achieving high printing speed and accuracy, *Proceedings of the Institution of Mechanical Engineers, Part C: Journal of Mechanical Engineering Science*. 234 (2020), 2741-2749. doi:10.1177/0954406219861664

[17] Y. Kuruoğlu, M. Akgün, H. Demir, FDM yöntemiyle üretilen ABS, PLA VE PETG numunelerin

yüzey pürüzlülüğü ve çekme dayanımının modellenmesi ve optimizasyonu, *International Journal of 3D Printing Technologies and Digital Industry*. 6 (2022), 358-369. doi:10.46519/ij3dptdi.1148923

[18] F. Kartal, A. Kaptan, Response of PLA material to 3D printing speeds: A comprehensive examination on mechanical properties and production quality, *European Mechanical Science*. 8 (2024) 137-144. doi:10.26701/ems.1395362

[19] Y. Kuruoğlu, M. Akgün, H. Demir, Modellıng and optımızatıon of surface roughness and tensıle strength of ABS, PLA AND PETG samples produced by FDM method, *International Journal of 3D Printing Technologies and Digital Industry*. 6 (2022). doi:10.46519/ij3dptdi.1148923.

[20] B. Chaudhary, H. Li, H. Matos, Long-term mechanical performance of 3D printed thermoplastics in seawater environments, *Results in Materials*. 17 (2023), 100381. doi:10.1016/j.rinma.2023.100381.

[21] D. Moreno Nieto, M. Alonso-García, M.-A. Pardo-Vicente, L. Rodríguez-Parada, Product design by additive manufacturing for water environments: Study of degradation and absorption behavior of pla and petg, *Polymers*. 13 (2021), 1036. doi: 10.3390/polym13071036

FEN ve MÜHENDİSLİK BİLİMLERİ DERGİSİ

Cilt/Vol: 7 Sayı/No: 1 Yıl/Year: 2025 Derleme/Review e-ISSN: 2667-7989

https://doi.org/10.47112/neufmbd.2024.84

Ultrason İşleminin Farklı Gıda Prosesleri ile Kombine Kullanım Olanakları

Yavuz YÜKSEL [1*] Berre ÇETİN [1]

[1] Balıkesir Üniversitesi, Mühendislik Fakültesi, Gıda Mühendisliği Bölümü, Balıkesir, Türkiye

Makale Bilgisi

Geliş Tarihi: 15.07.2024
Kabul Tarihi: 06.11.2024
Yayın Tarihi: 30.04.2025

Anahtar Kelimeler:
Ultrason,
Gıda teknolojisi,
Yeni gıda prosesleri.

ÖZET

Gıda endüstrisinde günümüzde taze, uzun raf ömrüne sahip, koruyucu katkılar içermeyen, güvenilir, kaliteli gıdaya olan talepte bir artış söz konusudur. Bu sebeple, son yıllarda gelişen teknolojiyle birlikte ısıl işlem uygulamaları yaygınlaşmıştır. Bununla birlikte, geleneksel ısıl işlem uygulamaları üründe bileşik kayıplarına, tazelik, tekstür ve verimin azalmasına sebep olabilmektedir. Aynı zamanda ısıya duyarlı olan gıdalarda renk ve tat kayıplarına da sebep olabilmektedir. Bu sorunları ortadan kaldırmak ve kaliteli, iyi özelliklere sahip ürün elde edebilmek için yeni ısıl olmayan teknolojiler iyi bir alternatif olmaktadır. Yüksek basınç, darbeli elektrik alanları, manyetik alan ve ultrason gibi uygulamaları içeren bu yeni teknoloji sayesinde çevre dostu, yeşil, kaliteli, uygun maliyetli bir ürün elde ederek, tüketicinin beklentisinin karşılanmasını sağlanmaktadır. Bu uygulamalar arasından ultrason, kirletici olarak kabul edilmeyen bir akustik enerji türüdür. Aynı zamanda ultrason tekniğinin önümüzdeki yıllarda farklı gıda teknolojilerinde işleme alanlarında da kullanılabileceği öngörülmektedir. Bu çalışmada gıda endüstrisinde ultrason uygulamalarının geleneksel ve yeni teknolojilerle kombine kullanımları derlenmiştir.

Possibilities of Combining Ultrasound Processing with Different Food Processes

Article Info

Received: 15.07.2024
Accepted: 06.11.2024
Published: 30.04.2025

Keywords:
Ultrasound,
Food technology,
New food processes.

ABSTRACT

The food industry has a growing demand for fresh, reliable, long-shelf-life, high-quality, and preservative-free food. In response to this, heat treatment applications have become widespread as a consequence of recent advances in technology. Traditional heat treatment methods, however, may result in compound losses in the product as well as a decline in yield, freshness, and texture. It can also cause color and taste loss in foods that are sensitive to heat. New non-thermal technologies are a good alternative to eliminate these problems and obtain quality products with good features. Thanks to this new technology, which includes applications such as high pressure, pulsed electric fields, magnetic field and ultrasound, the consumer's expectations are met by obtaining an environmentally friendly, green, high quality, cost-effective product. Among these applications, ultrasound is a type of acoustic energy that is not considered a pollutant. At the same time, it is anticipated that the ultrasound technique will be used in processing areas in different food technologies in the coming years. In this study, ultrasound applications in the food industry and their combined use with traditional or emerging technologies were tried to be examined.

To cite this article:
Yüksel, Y. & Çetin, B. (2025). Ultrason işleminin farklı gıda prosesleri ile kombine kullanım olanakları. *Necmettin Erbakan Üniversitesi Fen ve Mühendislik Bilimleri Dergisi, 7*(1), 175-188. https://doi.org/10.47112/neufmbd.2024.84

***Sorumlu Yazar:** Yavuz Yüksel, *yavuzyuksel@balikesir.edu.tr*

GİRİŞ (INTRODUCTION)

Günümüzde tüketicilerin taze veya taze benzeri gıdaların, raf ömrünün uzatılmasına yönelik talebin artması nedeniyle araştırmacılar minimal gıda işleme tekniklerine ilgi duymaktadır [1]. Bugüne kadar ısı uygulaması, mikroorganizmaları öldürme ve enzimleri etkisiz hale getirme yeteneğinden dolayı gıda işlemede en yaygın kullanılan yöntemdir. Ayrıca son yıllarda yaşanan önemli teknolojik gelişmeler ve kullanılan ekipmanların yönetiminin kolaylaşması ısıl işlemin kullanımını yaygınlaştırmıştır. Bununla birlikte, ısıl işlem özellikle ağır koşullar altında organoleptik özellikleri bozan ve bazı besin maddelerinin içeriğini veya biyoyararlılığını azaltan kimyasal ve fiziksel değişikliklere neden olabilir [2].

Isıl işleme uygun olmayan, viral veya bakteriyel kaynaklı gıda zehirlenmelerine duyarlı fazla sayıda gıda maddesi vardır. Dolayısıyla bu gıda maddeleri ısıl işleme maruz kaldığında tat, renk ve doku değişiklikleri dahil olmak üzere kimyasal, fiziksel ve mikrobiyal düzeyde değişikliklere uğrayabilmektedir. Bu, teknolojilerin optimize edilmesi ve yaratıcı ve etkili alternatif tekniklerin geliştirilmesi için geniş kapsamlı araştırma ve geliştirme talebine yol açmaktadır [3]. Bu anlamda, günümüzde gıdaların raf ömürlerinin uzatılmasında faydalanılan, sadece yüksek kalitedeki gıdaları elde etmek için değil, aynı zamanda işlevsel olarak da geliştirilmiş gıdaları sağlamak için yüksek basınç, vurgulu elektrik ve manyetik alan gibi yeni teknolojilere yönelmiştir. Ortaya çıkan bu teknolojilerde son zamanlarda ultrason yöntemine artan bir ilgi söz konusudur [4].

Ultrason, bir yayılma ortamında salınan moleküler hareketlerden kaynaklanan mekanik ses dalgalarından oluşur [5]. Ultrason, insan kulağının (1618 kHz) duyulabildiği maksimum frekanstan daha yüksek bir frekansta katı veya akışkan içinde bir mekanik titreşim enerjisidir [1]. Bu titreşimler, ses kaynağı adı verilen ve ortamın mekanik özellikleri sayesinde hareketini komşu parçacıklara ileten belirli bir nesne tarafından üretilir. Salınım başladığında, parçacıklar hareketlerini komşu parçacıklara iletir ve bu parçacıklar da hareketlerini diğerlerine ileterek basınçta yerel bir değişime sebep olur; bu nedenle basit bir titreşim hareketi, bir ses dalgası veya akustik dalga üretmek için mekanik olarak yayılır.

Mekanik dalgalardan oluşan ultrason, bir ortamda parçacıkların değil enerjinin aktarımı yoluyla yayılır; ikincisi aslında enerjinin bir parçacıktan diğerine aktarılmasıyla kendi denge konumu etrafında salınır. Salınım, ortamda çeşitli yönlerde yayılır ve bu nedenle boyuna dalgalar ve enine dalgalar olarak ayrılır [6]. Boyuna dalgalarda parçacıkların iletim ortamındaki salınım hareketi yayılma yönüne paralel, enine dalgalarda ise hareket diktir. Boyuna (veya sıkıştırma) dalgalar herhangi bir ortamda yayılırken, enine dalgalar yalnızca katı ortamda yayılır [7].

Gıda işleme uygulamalarında ultrasonla oluşan kavitasyon (sıvı içerinde oluşan kabarcıkların büyümesi ve içe doğru sönmesi ile yüksek şiddetle patlaması olayı) önemlidir. Sıvı moleküllerin hızlı hareketi, düşük basınçlı bir kabarcıkla biten bir girdap oluşturmaktadır. Sonikasyona tabi tutulan sıvılardaki moleküllerin hızlı hareketi nedeniyle bu tür binlerce kabarcık oluşur. Bu kabarcıklar, kavitasyon ve artan kütle transferi, sonikasyon tarafından oluşturulan hedefleri etkilemektedir [8].

Ultrason kullanımı düşük güçlü ultrason ve yüksek güçlü ultrason olmak üzere iki farklı grupta incelenmektedir. Düşük enerjili ultrason uygulamaları, 1 Wcm^{-2}'nin altındaki yoğunluklarda 100 kHz'den yüksek frekansların kullanımını içerir. Düşük yoğunluklu ultrason o kadar ufak bir güç seviyesi kullanır ki, ultrasonik dalgalar, dalganın içinden geçtiği malzemenin özelliklerinde hiçbir kimyasal veya fiziksel değişikliğe sebep olmaz, yani genellikle tahribatsızdır. Gıda süreçlerinin müdahalesiz izlenmesinde başarıyla kullanılırlar. Düşük yoğunluklu ultrasonun gıda endüstrisindeki en yaygın uygulaması, gıdaların bileşimi, yapısı ve fiziksel durumu gibi fizikokimyasal özellikleri hakkında bilgi veren analitik bir tekniktir [8,9].

Ultrasonun uygulamalarının geleneksel analitik tekniklere göre avantajları vardır çünkü ölçümler

hızlıdır, tahribatsızdır, hassastır, tam otomatiktir. Yüksek enerjili grup ise 18 ile100 kHz arasındaki frekanslarda 1 W·cm-2'den (tipik olarak 10-1000 Wcm^{-2} aralığında) daha yüksek mertebedeki yoğunluklarda kullanan ultrasondur. Bu aralıkta bulunan ultrasonik dalgalar mekanik, kimyasal veya fiziksel etkileri malzeme özelliklerini değiştirme özelliğine sahiptir (örneğin, fiziksel bozulma, belirli kimyasal reaksiyonların hızlanması). Yüksek enerjili ultrason, emülsiyonlar oluşturmak, hücreleri parçalamak ve toplanmış malzemeleri dağıtmak için uzun yıllardan beri kullanılmaktadır. Daha yakın zamanlarda, gelecekteki gelişim için daha büyük potansiyele sahip çeşitli alanlar belirlenmiştir; kristalizasyon işlemlerinin modifikasyonu ve kontrolü, sıvı gıdaların gazının alınması, enzimlerin inaktivasyonu, geliştirilmiş kurutma ve filtreleme ve oksidasyon reaksiyonlarının başlatılması gibi örnekler verilebilir [9].

ULTRASONUN UYGULAMA ALANLARI (APPLICATION AREAS OF ULTRASOUND)

Ultrason, gıda işlemede ekstraksiyon, kurutma, filtrasyon, emülsifikasyon, rehidrasyon vb. gibi çeşitli işlemler için kullanılabilir.

Filtrasyon (Filtration)

Farklı gıda ünitesi operasyonlarıyla kullanıldığında ultrasonun prosesleri iyileştirdiği bulunmuştur. Filtrasyon, katıların ana likör veya sıvı işleme yoluyla verimli bir şekilde ayrılması için etkili bir yöntem olarak uzun süredir kullanılmaktadır. Ana proses maddesi olarak membran yüzeyinin üzerinde biriken filtratlar veya kek filtre nedeniyle oluşan konsantrasyonda kirlenme veya polarizasyonla ilgili zorluklar oluşmaktadır. Bu sorun filtreleme verimliliğinde azalmaya sebep olmuştur. Ultrason enerjisi bu sebeple bu tür bir soruna karşı başarılıdır [10].

Filtrasyon işlemi sırasında ultrason işlemi uygulandığında, membran katmanının üzerinde tutucu katmanların birikmesi meydana gelir ve bu da polarizasyona neden olur. Konsantrasyonu bozulur, ancak içsel membran geçirgenliği bozulmadan kalır. Bunlar akışın artmasına ve dirençli akışın azalmasına sebep olur [11]. Filtrelerle birleştirilen ultrason, membranın topaklanmasını ve tıkanmasını önleyerek filtrenin ömrünü uzatır ve filtre yüzeyi çevresinde boşluğun devam etmesini sağlar. Ultrason yönteminin tek başına uygulanması yerine membran filtre ile uygulanan ultrasonda daha etkili olduğu gözlemlenmiştir [12].

Kurutma (Dehydration)

Gıda maddelerinin kurutulması, ürünü stabil hale getirmek için en çok kullanılan ve umut verici yöntemdir. Geleneksel kurutma teknikleri, büzülme, renk bozulması ve vitaminlerin oksidasyonu gibi olumsuz etkilere sebep olur. Ek olarak, artan enerji maliyetleri, azalan besin kayıpları ile artan kalite gereksinimleri ve olumsuz çevresel etkiler, modern gıda kurutma teknolojilerinin geliştirilmesine olan ilginin artmasına neden olmuştur [13,14].

Ultrason kullanımı çok fazla sıcaklık değişimine neden olmadan kurutma işlemini hızlandırır. Yüksek enerjili ultrason kullanılarak kütle taşıma kinetiğinin artırılabileceği öne sürülmüştür. Ayrıca ultrason, sınır katmanını azaltabilir ve böylece kurutma işlemi için gereken kütle transferine karşı dirençte bir azalmaya neden olabilir [15].

Yapılan bir araştırmaya göre üzüm ve eriklerin konvektif kurutma aşamasından önce ses dalgaları ile ön kurutmanın, ürünün niteliğini iyileştirmenin yanı sıra, dehidrasyon miktarını ve kuruma kinetiğini arttırdığını belirtilmiştir. Ultrasonun, kütle transferini arttırması nedeniyle kurutma sayısını azaltmada etkili olduğu da kanıtlanmıştır. Dolayısıyla güç kullanımını azaltarak etkili kurutma aynı zamanda nemin yayılımını da arttırmaktadır [5].

Ekstraksiyon (Extraction)

Ultrason destekli ekstraksiyon (UAE) ve enzim destekli ekstraksiyon (EAE) gibi yeni teknikler geleneksel ekstraksiyon uygulamasından daha verimlidir. Yüksek miktarlarda polisakkarit üretebilirken aynı zamanda çevre dostudur ve geleneksel tekniklere ideal alternatifler olarak ortaya çıkmaktadır [12]. Ultrasonla geliştirilmiş ekstraksiyon genellikle nispeten düşük bir sıcaklıkta gerçekleştirilir. Biyoaktif ve biyoaktif olmayan bileşenler ve termal olarak bozulabilen diğer bileşenlere gelince, ekstraksiyon sırasında biyoaktivitelerini ve değerlerini korumak için düşük bir sıcaklık faydalıdır [1].

Kesme (Cutting)

Yüksek doğruluk, mükemmel kesim yüzeyleri, daha az miktarda bulaşma, düşük ürün kaybı, daha az deformasyon, kırılgan ürünler için daha az parçalanma eğilimi ve yapışkan veya kırılgan gıdaları işleme yeteneği ile gelişmiş kalitede gıda kesme işlemlerine yönelik artan talep nedeniyle, ultrasonik kesim giderek daha önemli hale gelmektedir [5,16].

Ultrasonik kesme, ürünün kesme verimliliğini ve kalitesini artırmak için geleneksel bıçak hareketi ile üst üste gelen ultrasonun titreşim enerjisini kullanan boyut küçültme işlemidir. Ultrasonik kesme teknolojisi ağırlıklı olarak peynir, unlu mamuller ve şekerleme ürünleri ile pürüzsüz dokuya sahip gıdalar için uygulanmaktadır. Ultrasonik olarak kesilen gıda, kontrole kıyasla numunelerin parlak ve pürüzsüz bir yüzey görünümü sergilemektedir [17].

Emülsifikasyon (Emulsification)

Dispersiyonlar ve emülsiyonlar genellikle stabilizasyon amacıyla yüzey aktif maddeler içerir. Yüzey aktif maddeler, dağılmış maddenin sıvı faz içinde toplanması süresini geciktirir. Böylece yüzey aktif maddeler, her parçacığın etrafında ek bir katman oluşturur. Her ne kadar benzer yüzey aktif maddeler büyük ölçüde stabilize edilmiş olsa da sıvı aşamaların içinde asılı duran gaz halindeki kabarcığı kapsüller. Bu şekilde tüketilen sürfaktan, hatalı partikül boyutu ölçümlerinin elde edilmesiyle emülsiyon veya dispersiyon kalitesi düşer [18].

Ultrason cihazları, sistemdeki hava kabarcıklarının oluşması ve çökmesi anlamına gelen akustik kavitasyon üretebilir. Hava kabarcıklarının çökmesi, kimyasal reaksiyonları teşvik eden reaktif radikallerin salınmasını kolaylaştırabilir [19,20]. Birbiri içinde karışmayan sıvılar arasındaki kavitasyon kabarcığının temas yüzeyi düzlemince çökmesi, daha düşük enerjide de olsa daha yüksek kararlı bir emülsiyon oluşturur [21,22].

Ayrılma (Seperation)

Bu yöntem, parçacık ayırmayla ilgili yeni bir prensibe dayanmaktadır; ultrason dalgalarında (<30 kHz) düşük frekanslı bir emülsiyona uygulanan enerjideki artış, karışımı su ve yağ bölümlerine ayırmak için kullanılmaktadır [23,24]. Süt ürünleri alanında, protein toplama/bölme için kullanılan dokuların temizlenmesi, zarın gözenekliliğini ve farklılaşmasını korumak ve bakteriyolojik kirlilik tehlikesini azaltmak ve uygun ürünler üretmek için bitkinin doğal boyutlarına geri döndürülmesi açısından çok önemli bir prosedürdür [25].

Yapılan araştırmalara göre ultrasonik destekli ayırma (UAS) yöntemi geleneksel ayırma yöntemleriyle karşılaştırıldığında buğday ununun fiziksel olarak ayrılması için yeni bir yol sağladığı gözlemlenmiştir. Buğday unu üretiminde özellikle hammadde ve su kaynaklarına ilişkin kaynak israfını azaltmak amacıyla, bu çevre dostu ve verimli ayırma yöntemi iyi bir alternatif yöntem olmuştur [26].

Rehidrasyon (Rehydration)

Muhafaza için kurutulan gıda maddeleri, kullanımdan önce ılık sıvılara daldırılarak rehidre edilir. Rehidrasyon süreci, geri kazanılan özelliklerle işlev yenilenmesine yönelik öğelerin belirlenmesine

yardımcı olur. Rehidrasyon yöntemi yaklaşık 3 ardışık prosedürden oluşur: suyun emilmesi, ürünün süzülerek şişmesi ve çözünür katılardır [27]. Bu, dehidrasyon sürecinin neden olduğu herhangi bir hasar veya bozulmanın bir göstergesi olarak kullanılır [28]. Rehidrasyon seviyesinin, dehidrasyon sebebiyle gıda maddesinin içindeki yapı veya hücre hasarı düzeyinin önemli ölçüde değiştiği belgelenmiştir. Böylece ürün özelliklerini arttıran büzülmeyi azaltmak için rehidrasyon işleminden önce ön işlem uygulanarak ve verimli bir optimizasyon sağlanmıştır [29].

Yapılan bir araştırmada kurutmadan önce kabakta ultrason ön işlemini kullandığında; burada rehidrasyon kinetiği, rehidrasyon oranında kesin bir iyileşme sağladığı; bu, rehidrasyon ön işleminin kılcal ile oluşturulan boşluktan kaynaklanabileceği anlamına gelebilmektedir. Ultrasonun rehidrasyon sürelerinin azalmasına neden olduğu ve aynı zamanda kurutulmuş gıda tanelerinin rehidrasyonu için de kullanıldığı gözlemlenmiştir [30].

ULTRASON İŞLEMİNİN FARKLI GIDA PROSESLERİ İLE KOMBİNE KULLANIMI (COMBINED USE OF ULTRASOUND WITH DIFFERENT FOOD PROCESSES)

Ultrason uygulamalarının gıda sanayinde farklı proseslerle birlikte kullanımına yönelik çalışmalar devam etmektedir. Diğer teknolojik işlemlerin etkinliklerini artırdığına yönelik birçok araştırma sonucuna ulaşılmıştır. Aşağıda ultrason teknolojisinin farklı proseslerle kombine olarak kullanımı hakkında çalışma sonuçları verilmiştir.

Mikrodalga Teknolojisi ile Birleştirilmiş Ultrason (Ultrasound Combined with Microwave Technology)

Mikrodalgalar gıda endüstrisinde kurutma, pastörizasyon, sterilizasyon, eritme, temperleme, pişirme vb. amaçlarla çok sık kullanılmaktadır. Mikrodalga sistemlerinin frekansı 300 MHz-300 GHz arasında değişebilen, elektromanyetik dalgalardır. Evsel mikrodalga cihazları genel olarak 2,45 GHz frekansında çalışırken, endüstriyel mikrodalga sistemleri 915 MHz ve 2,45 GHz frekanslarında çalışmaktadır. Mikrodalga ısıtma, malzemelerin mikrodalga enerjisini absorbe etme ve onu ısıya dönüştürme yeteneğinden kaynaklanır. Gıda maddelerinin mikrodalga ile ısıtılması temel olarak dipolar ve iyonik mekanizmalar nedeniyle meydana gelir. Nem veya suyun varlığı, suyun dipolar yapısından dolayı dielektrik ısınmaya neden olur. Su molekülleri üzerine salınan bir elektrik alanı çarptığında, kalıcı olarak polarize olmuş dipolar moleküller, elektrik alanı yönünde yeniden hizalanmaya çalışırlar [31,32].

Yapılan bir araştırmaya göre ısıl nem işlemlerinin (ultrason-mikrodalga ve mikrodalga-ultrason) mısır nişastasının fizikokimyasal özelliklerine etkisi araştırılmıştır. Mısır nişastası 90, 180, 360 ve 600 W mikrodalga gücü kullanılarak 1, 2, 3 dakika boyunca ve ultrason kullanılarak 35 °C sabit sıcaklıkta 20, 30, 40 dakika süreyle tahriş edilmiştir. Ultrason destekli modifikasyon yönteminde sıcaklık ve zamanın, mikrodalga destekli modifikasyon yönteminde ise mikrodalga gücü ve süresinin ürünün morfolojisi ve yapısal özelliklerine etkisi araştırılmıştır. Ultrason modifikasyon süresinin arttırılmasının modifikasyon verimliliğini arttırdığı belirlenmiştir. Nişasta granüllerindeki en büyük değişiklik 360 W mikrodalga gücü ve 30-40 dakika ultrasonik koşullar altında gözlemlenmiştir. Doğal mısır nişastası modifikasyonunda ultrason ve mikrodalga kombinasyonunun etkili, hızlı ve çevre dostu bir yöntem olduğu sonucuna varılmıştır. Gelecekteki çalışmalarda mikrodalga modifikasyonunun diğer modifikasyon yöntemleriyle birleştirilmesi mısır ve diğer nişasta türlerinin modifikasyonu için araştırılabilir [33].

Mikrodalga işleminin daha düşük ekipman yüzey sıcaklığı, enerji verimliliği, hızlı hacimsel ısıtma, tekdüze ısıtma ve gıda kalitesinin olası korunması gibi avantajları vardır ve bu da onu geleneksel ısıtmaya göre daha verimli hale getirir. Ultrason ve mikrodalga gücünün kullanıldığı kombine bir işlem, pastörizasyona iyi bir alternatif olabilir [34,35].

Yüksek Basınç ile Birleştirilmiş Ultrason (Ultrasound Combined with High Pressure)

Oda sıcaklığında yaklaşık 100-1000 MPa aralığında uygulanan basınç, yüksek basınçlı işleme (high hydrostatic pressure -HPP) oluşturur [36,37]. Esas olarak bitkisel mikroplar, küfler dahil mayalar ile birlikte patojenlerin deaktivasyonu için kullanılır, ancak basınç tedavisi tek başına sporların kayda değer inaktivasyonunu ve bazı enzimlerin enzimatik aktivitesinin düşürülmesini sağlayamaz. Basıncın çevre sıcaklıklarıyla birlikte kullanılması durumunda, adyabatik ısıtma nedeniyle, 3 ile 9 °C/100 MPa'lık bir sıcaklık artışı meydana gelir [38]. Akışkan malzemeye zorlandığında, yüksek yoğunluklu ultrason, ısı üretimini harekete geçirir. Bu şekilde ultrason uygulamaları 5–8 °C işlem sıcaklığında tasarlanmış bir HHP ön işlemi olarak planlanmış olup, ultrason tedavisi nedeniyle sıcaklık dalgalanmalarının minimum düzeyde tutulması gerekmektedir.

Yapılan bir araştırmada ultra yüksek basınç ve ultrasonun (UHP-US) kombine ön işleminin, vakumla dondurularak kurutulmuş çilek dilimlerinin özellikleri üzerindeki etkisini, tek başına UHP-US ön işlemine kıyasla incelenmiştir. Sonuçlar, UHP-US işleminin kurutma süresini ve enerji tüketimini azalttığını, aynı zamanda kaliteyi daha belirgin şekilde artırdığını göstermektedir [39].

Soxhlet Ekstraksiyonuyla Birleştirilmiş Ultrason (Ultrasound Combined with Soxhlet Extraction)

Soxhlet ekstraksiyonu geleneksel olarak katı ve sıvı yağları matrislerinden çıkarmak için kullanılmaktır. Isıtılmış bir solventten, genellikle n-heksandan yoğunlaşmış buharlara yinelemeli olarak nüfuz ettiği için fikri genel olarak basittir. Ayrıca, soxhlet ekstraksiyonunun uzun çalışma süresi, çok miktarda solvent, buharlaşma ve ekstraksiyonun sonuna doğru temel bir konsantrasyon adımı gibi birkaç dezavantajı vardır. Teoride yalnızca birkaç form, katı ve sıvı yağların ekstraksiyonunu hızlandırmak için soxhlet ekstraksiyonunun ultrason gibi gelişmiş stratejilerle birleştirilmesini gözlemlenmiştir [40].

Ultrason ve Soxhlet yöntemleri birlikte kullanılmak suretiyle soxhlet döngülerinin sayısı, işlem süresi, sıcaklığı ve solvent tüketimini azaltmak için her iki tekniğin olumlu etkisinin gözlemlendiği bir sistem geliştirilmiştir [40]. Yapılan bir araştırmada yer fıstığı yağının Soxhlet işleminden önceki ön işlemi olarak uygulanan ultrasonun, 10 dakika içinde %51,50 ekstraksiyon verimi ile birlikte yağ asidi bileşiminde hafif değişikliklere neden olduğu, oleik asit içeriğinin ise 30 dakika sonra %57.10'dan %56.69'a azaldığı gözlemlenmiştir [41].

Ozmotik Dehidrasyon ile Birlikte Ultrason (Ultrasound with Osmotic Dehydration)

Ozmotik dehidrasyon ile ses dalgalarının kullanılması, daha yüksek su israfına ve daha düşük çözelti sıcaklığında çözünen madde kazanımına neden olur. Tat, renk ve sıcaklığa duyarlı besinler gibi özellikleri de korumuş olur [42,43]. Bunun nedeni genellikle su ve çözünen madde taşınmasını artıran küçük kanalların bir sonucu olarak hücre duvarının gözenekliliğinin artmasıdır. Yapılan bir araştırmada elmaları ozmotik olarak kurutmak için ultrason kullanımının, "su çıkışı" ve "çözünen madde girişi" kütle aktarım hızını hızlandırdığı bulunmuştur [44]. Çözücülerin difüzyon katsayılarının ultrason ön işlemine bağlı olarak ayrı ayrı %117 ve %137 civarında arttığı saptanmıştır [45].

Yapılan araştırmalara göre ultrasonik işlemin daha fazla cam geçiş sıcaklığı sağladığını, su aktivitesinin, rehidrasyon oranının ve su içeriğinin azaldığını, yapının daha fazla parçalandığını ve ayrıca daha az çatlak oluşturduğunu ayrıntılı bir şekilde açıklamıştır [46]. Ayrıca ultrason uygulamasının tavşan gözü yaban mersininin ozmotik dehidrasyonu sırasında nemin difüzyon hızlarını iyileştirdiği gözlenmiştir. Ancak bu antosiyaninlerin ve fenoliklerin kaybıyla ilgilidir [47].

Laboratuvar deneyleri, ultrason tedavilerinin kurutulmuş meyve ve sebze ürünlerinin rengini, dokusunu, lezzetini, antioksidan kapasitesini ve rehidrasyonunu önemli ölçüde iyileştirebileceğini kanıtlamıştır [48]. Ayrıca ultrason gibi ön işlemler kullanılarak büzülme ve su aktivitesi en aza

indirilebilir [49]. Yapılan bir başka araştırmada ultrason destekli ozmotik dehidrasyonun nar tohumları üzerindeki etkisi incelenmiştir. Sonucunda ise ultrason ön işleminin ozmotik çözelti sıcaklığında bir azalmayı içerdiğini ve işlem maliyetinde bir azalmayı desteklediğini göstermiştir [50]. Ayrıca ultrason destekli ozmotik dehidrasyon numunesinin dokusu, taze ve ozmotik dehidre numuneye kıyasla daha fazla sert bir yapı göstermiştir [51].

Enzimatik Ekstraksiyon ile Birleştirilmiş Ultrason (Ultrasound Combined with Enzymatic Extraction)

Ultrason destekli enzimatik ekstraksiyon (UAEE) olarak adlandırılır. Biyoaktif bileşenlerde enzim destekli ayırma işlemiyle kombine ultrason, bazı araştırmalarda araştırılmaktadır [52,53]. UAEE'nin birkaç ekstra ilgi noktası sağlayan tamamlayıcı stratejileriyle birleştirildiği bilinmektedir. Enzimler, enzim destekli ekstraksiyon (EAE) kapsamında hücre duvarının ve filmlerin parçalanması ve yırtılması yoluyla iyileşmeyi teşvik eder. Her durumda, hücre duvarları gibi enzimler de matrisi tamamen hidrolize etmez [53,54] . UAE, enzim destekli reaksiyonlara ve bunun sonucunda hedeflenen bileşenlerin boşaltılmasına izin vermek için boşluk süreci, matrisleri kolayca parçalayan ultrasonik güç tarafından uyarıldığından enzimatik ekstraksiyon sürecini geliştirir. Bunun aksine, çözücülerin, hedef parçacıkların ve enzimlerin ortamın içinde veya dışında kitlesel migrasyonu, tek başına enzimler tarafından iyileştirilemez. Bu nedenle, EAE'de, kütle değişiminde ilerleme sağlamak için sallama gibi diğer fiziksel yinelemelerden faydalanılabilir; bunların arasında BAE, matrislerin dış kısmı için değil, üstelik iç kısmı için olduğu gibi, kütle transferinin arttırılması için de mükemmel bir seçimdir [10,55].

Ultrason destekli ekstraksiyon, esas olarak sıvı bir ortamda akustik kavitasyona dayanmaktadır [56]. Bu ekstraksiyon tekniği, geleneksel ekstraksiyon yöntemleriyle karşılaştırıldığında en önemlisi azaltılmış ekstraksiyon süresi, azaltılmış enerji tüketimi ve solvent kullanımı gibi avantajlarından dolayı büyük ilgi görmüştür [57,58]. Yapılan araştırmalarda kombine enzimatik/ultrasonik ekstraksiyon yönteminin kullanılması, daha yüksek verim elde etmek ve aynı zamanda daha iyi kalitede pektin elde etmek için hedef bileşiklerin bozulmasını en aza indirmek için etkili bir yaklaşım olabilir. Mikrodalga ekstraksiyon tekniğine (%27,81) kıyasla kombine ultrason-mikrodalga ekstraksiyon tekniğiyle greyfurttan çok daha yüksek pektin verimi (%31,88) elde edildiğini bulunmuştur [56]. Yapılan diğer araştırmalarda muz posasından meyve suyu ekstraksiyonu için enzimatik tedaviyi ultrason tedavisiyle birleştirmişler ve meyve suyu veriminin arttığını, meyve suyunun viskozitesinin ise azaldığını gözlemlemişlerdir. Kombine işlem ile elde edilen meyve suyunun toplam çözünebilir katı miktarı ve berraklığı da daha yüksek bulunmuştur [59].

Süperkritik Sıvı Ekstraksiyonuyla Birleştirilmiş Ultrason (Ultrasound Combined with Supercritical Fluid Extraction)

Süperkritik akışkan ekstraksiyonu (SFE), akışkanların çözme gücündeki (kritik noktalarının üzerindeki) artışa bağlı olarak ekstraksiyon için yeni bir teknolojidir. Bu, gaz benzeri özelliklerin (kütle aktarımı) ve sıvı benzeri özelliklerin (çözünme), sıvılardan daha fazla difüziviteye sahip birleşik etkisi nedeniyle ekstraksiyonla sonuçlanmaktadır [60,61]. Birçok araştırmacı, maliyetinin az olmasının yanı sıra kullanıcı dostu profili ve yüksek ekstraksiyon potansiyeli nedeniyle CO_2 bazlı ürünler kullanmaktadır. SFE'nin başlıca faydaları arasında ön konsantrasyon etkileri, daha yüksek verim garantisiyle temizlik ve basit çalıştırma prosedürü yer almaktadır [12].

Yapılan araştırmalar süperkritik CO_2 ekstraksiyonu uygulamasında ultrasonik ön işlemini kullanarak *Iberis amara* tohumu yağı elde etmek için umut verici sonuçlar göstermiştir. Sonucunda ise, kombine işlemin %25'ten fazla yağ ürettiğini ve ayrıca süperkritik CO_2 ekstrakte edilmiş yağla karşılaştırıldığında yağın fizyokimyasal özelliklerini ve antioksidan aktivitesini iyileştirdiğini

göstermektedir [62].

Tablo 1'de ultrason teknolojisinin gıda işlemede kullanımı ve elde edilen sonuçlar verilmiştir.

Tablo 1
Gıda işlemede ultrason teknolojisinin diğer tekniklerle kombine kullanımı

Kombine uygulanan proses	Hedef Ürün	Sonuç	Referanslar
Mikrodalga	Pektin	Verimin artmasına işlem süresinin kısalmasına ve yüksek esterleşme derecesine ulaşmasına yardımcı olmuştur.	[63]
Yüksek basınç ile işleme	Kızılcık suyu	Organik asitlerin tutulması yükselmiştir, antosiyanin içeriğinde %24'e varan artış olmuştur.	[64]
Soxhlet	Vanilin	Verimi ve kütle transfer hızını arttırmıştır.	[65]
Ozmotik dehidrasyon	Patates	Verimlilik ve hız artmıştır. Yağ ve nem içeriğini azaltarak kızarmış patateslerin kalitesini arttırmıştır.	[66]
Enzim ekstraksiyonu	Selülaz preparatları	Aktivite artmıştır.	[56]
Süperkritik ekstraksiyon	Adaçayı	Verim artmıştır. Gelişmiş hidrasyon işlemi sağlanmıştır.	[67]

TARTIŞMA VE SONUÇLAR (DISCUSSION AND CONCLUSIONS)

Ultrason uygulaması günümüzde ilgi çeken bir teknik olmakla birlikte, gelecek senelerde de olumlu sonuçlar vaat etmektedir. Gıdaları işlemede ultrason kullanmanın avantajları olarak; daha iyi bir karıştırma, daha hızlı enerji, daha uygun maliyet, minimal ekipman boyutu, süreden kazanç sağlanması sıralanabilmektedir. Tek başına kullanımının yanı sıra diğer uygulamalar ile birleştirildiğinde, yapılan uygulamaların etkinliğinin arttığı saptanmıştır. Tüm bu avantajlarına ek olarak uygulamanın zorlukları da yok değildir. Öncelikle sistemin endüstride uygulanmasından önce sıkı bir şekilde test edilmesi ve güvenli olduğunun kanıtlanması gerekmektedir. Ultrason işlemlerinde karşılaşılan birtakım olumsuzluklarda bulunmaktadır. Yüksek enerjili ultrason uygulamalarında büyük hacimlerde ultrason etkisinin homojen bir şekilde dağılımının güçlüğü, viskozitesi yüksek ve katı ürünlerde etkisinin ya hiç olmaması veya etki süresinin uzaması, enerji tüketimi ve maliyetinin bazı proseslerde yüksek olması, uygulama sırasında oluşan ısı ve basınç sebebiyle bazı gıdaların besinsel, kimyasal ve fiziksel özelliklerin etkilenebilmesi gibi olumsuzluklar sıralanabilir. Bir ürünün termofiziksel (yoğunluk, sıkıştırılabilirlik ısı kapasitesi gibi) özellikleri hakkında fazlasıyla bilgiye ihtiyaç vardır. Bu sebeple, bilinmeyen özelliklere sahip sistemlerden elde edilen verilerin teorik analizi yetersizdir. Bu gibi olumsuzlukların da önüne geçildiği sürece ultrason teknolojisinin gıda endüstrisi ve diğer bilim dallarında uygulanmasının artması kaçınılmazdır.

Etik Beyan (Ethical Declaration)

Bu çalışma, Yavuz YÜKSEL danışmanlığında Balıkesir Üniversitesi Mühendislik Fakültesi Gıda Mühendisliği Bölümü öğrencisi Berre ÇETİN'in lisans bitirme projesinden üretilmiştir. Çalışmamızın tüm süreçlerinin araştırma ve yayın etiğine uygun olduğunu, etik kurallara ve bilimsel atıf gösterme ilkelerine uyduğumuzu beyan ederiz.

Yazar Katkıları (Authors Credit)

Araştırma Tasarımı Y.Y. (%100)

Veri Toplama (CRediT 2) Y.Y. (%50) – B.Ç. (%50)

Makalenin Yazımı (CRediT 12-13) Y.Y. (%80) – B.Ç. (%20)

Metnin Tashihi ve Geliştirilmesi (CRediT 14) Y.Y. (%100)

Finansman (Funding)

Bu çalışma kapsamında herhangi bir kurum/kuruluştan finansal destek alınmamıştır.

Çıkar Çatışması (Conflict of Interest)

Yazarların bu çalışma için beyan ettiği herhangi bir çıkar çatışması yoktur.

Sürdürülebilir Kalkınma Amaçları (SDG)

Sürdürülebilir Kalkınma Amaçları: Desteklemiyor

KAYNAKÇA (REFERENCES)

[1] Ç. Türksönmez, A. Diler, Gıda endüstrisinde ultrason uygulamaları, *Aydın Gastronomy*. 5(2), (2021), 177-191.

[2] A. C. Soria, M. Villamiel, Effect of ultrasound on the technological properties and bioactivity of food: a review, *Trends in Food Science & Technology*. 21(7) (2010), 323-331. doi:10.1016/j.tifs.2010.04.003

[3] N. N. Misra, O. Schlüter, P. J. Cullen, Cold plasma in food and agriculture: *Fundamentals and Applications*, Academic Press, 2016.

[4] M. S. Aday, Ultrasesin gıda işleme ve muhafazasında kullanımı, *MAS Journal of Applied Sciences.* 6(3) (2021), 661-684. doi:10.52520/masjaps.116

[5] M. Gallo, L. Ferrara, D. Naviglio, Application of ultrasound in food science and technology: A perspective, *Foods.* 7(10) (2018), 164. doi:10.3390/foods7100164

[6] J. Krautkrämer, H. Krautkrämer, Ultrasonic testing of materials, *Springer Science & Business Media,* 2013.

[7] M., Şengül, E. F. Topdaş, Katı-sıvı ekstraksiyonunda kullanılan modern teknikler ve bu teknikler arasında ultrason yardımlı ekstraksiyonun yeri, *Atatürk Üniversitesi Ziraat Fakültesi Dergisi.* 50(2) (2019), 201-216. doi:10.17097/ataunizfd.466649

[8] Z. J. Dolatowski, J. Stadnik, D. Stasiak, Applications of ultrasound in food technology, *Acta Scientiarum Polonorum Technologia Alimentaria*. 6(3) (2007), 88-99.

[9] N. Bhargava, R. S. Mor, K. Kumar, V. S. Sharanagat, Advances in application of ultrasound in food processing: A review, *Ultrasonics Sonochemistry*. 70 (2021), 105293. doi:10.1016/j.ultsonch.2020.105293

[10] F. Chemat, N. Rombaut, A. G. Sicaire, A. Meullemiestre, A. S. Fabiano-Tixier, M. Abert-Vian, Ultrasound assisted extraction of food and natural products. Mechanisms, techniques, combinations, protocols and applications. A review, *Ultrasonics Sonochemistry*. 34 (2017), 540-560. doi:10.1016/j.ultsonch.2016.06.035

[11] L. Z. Deng, A. S. Mujumdar, Q. Zhang, X. H. Yang, J. Wang, Z. A. Zheng, Z.J. Gao, H. W. Xiao, Chemical and physical pretreatments of fruits and vegetables: Effects on drying characteristics and quality attributes–a comprehensive review, *Critical Reviews in Food Science and Nutrition.* 59(9) (2019), 1408-1432.

[12] Y. Liu, H. Pu, D. W. Sun, Hyperspectral imaging technique for evaluating food quality and safety during various processes: A review of recent applications, *Trends in Food Science & Technology*. 69 (2017), 25-35.

[13] E. A. A. Elhussein, S. Şahin, Drying behaviour, effective diffusivity and energy of activation of olive leaves dried by microwave, vacuum and oven drying methods, *Heat and Mass Transfer*. 54 (2018), 1901-1911.

[14] N. Milićević, P. Kojić, M. Sakač, A. Mišan, J. Kojić, C. Perussello, B. Vojislav, P. Milica**,** B. Tiwari, Kinetic modelling of ultrasound-assisted extraction of phenolics from cereal brans, *Ultrasonics Sonochemistry.* 79 (2021), 105761. doi:10.1016/j.ultsonch.2021.105761

[15] G. Milani, M. Vian, M. M. Cavalluzzi, C. Franchini, F. Corbo, G. Lentini, F. Chemat, Ultrasound and deep eutectic solvents: An efficient combination to tune the mechanism of steviol glycosides extraction, *Ultrasonics Sonochemistry*. 69 (2020), 105255. doi:10.1016/j.ultsonch.2020.105255

[16] G. Yildiz, T. M. Rababah, H. Feng, Ultrasound-assisted cutting of cheddar, mozzarella and Swiss cheeses–Effects on quality attributes during storage, *Innovative Food Science & Emerging Technologies.* 37 (2016),1-9. doi:10.1016/j.ifset.2016.07.013

[17] T. S. Leong, M. Zhou, N. Kukan, M. Ashokkumar, G. J. Martin, Preparation of water-in-oil-in-water emulsions by low frequency ultrasound using skim milk and sunflower oil, *Food*

Hydrocolloids. 63 (2017), 685-695. doi:10.1016/j.foodhyd.2016.10.017

[18] A. Taha, E. Ahmed, A. Ismaiel, M. Ashokkumar, X. Xu, S. Pan, H. Hu, Ultrasonic emulsification: An overview on the preparation of different emulsifiers-stabilized emulsions, *Trends in Food Science & Technology*. 105 (2020), 363-377. doi:10.1016/j.tifs.2020.09.024

[19] J. P. Canselier, H. Delmas, A. M. Wilhelm, B. Abismail, Ultrasound emulsification—an overview, *Journal of Dispersion Science and Technology*. 23(1-3) (2002), 333-349. doi:10.1080/01932690208984209

[20] S. Freitas, G. Hielscher, H. P. Merkle, B. Gander, Continuous contact-and contamination-free ultrasonic emulsification—a useful tool for pharmaceutical development and production, *Ultrasonics Sonochemistry*. 13(1) (2006), 76-85. doi:10.1016/j.ultsonch.2004.10.004

[21] M. J. Luján-Facundo, J. A. Mendoza-Roca, B. Cuartas-Uribe, S. Álvarez-Blanco, Cleaning efficiency enhancement by ultrasounds for membranes used in dairy industries, *Ultrasonics Sonochemistry.* 33 (2016), 18-25. doi:10.1016/j.ultsonch.2016.04.018

[22] S. Mettu, S., Yao, Q. Sun, S. R. Lawson, P. J. Scales, G. J. Martin, M. Ashokkumar, Effect of bulk viscosity and emulsion droplet size on the separation efficiency of model mineral oil-in-water (O/W) emulsions under ultrasonic standing wave fields: a theoretical and experimental investigation, *Industrial & Engineering Chemistry Research*. 59(16) (2020), 7901-7912. doi:10.1021/acs.iecr.0c00616

[23] A. Vega-Gálvez, K. Di Scala, K. Rodríguez, R. Lemus-Mondaca, M. Miranda, J. López, M. Perez-Won, Effect of air-drying temperature on physico-chemical properties, antioxidant capacity, colour and total phenolic content of red pepper (*Capsicum annuum, L. var. Hungarian*), *Food Chemistry.* 117(4) (2009), 647-653. doi:10.1016/j.foodchem.2009.04.066

[24] M. Markowski, M. Zielinska, Influence of drying temperature and rehydration on selected textural properties of carrots, *International Journal of Food Properties*, 16(3) (2013), 586-597. doi:10.1080/10942912.2011.558229

[25] Y. Tao, M. Han, X. Gao, Y. Han, P. L. Show, C. Liu, X. Ye, G. Xie, Applications of water blanching, surface contacting ultrasound-assisted air drying, and their combination for dehydration of white cabbage: Drying mechanism, bioactive profile, color and rehydration property, *Ultrasonics Sonochemistry*. 53 (2019), 192-201. doi:10.1016/j.ultsonch.2019.01.003

[26] M. Lan, D. Luo, C. Yue, Z. Bai, P. Li, L. Wang, Ultrasound-assisted separation of wheat flour: Enhancing the degree of separation and characterization analysis, *Innovative Food Science & Emerging Technologies*. 90 (2023), 103493.

[27] A. C. Miano, J. D. C. Pereira, N. Castanha, M. D. D. M. Júnior, P. E. D. Augusto, Enhancing mung bean hydration using the ultrasound technology: description of mechanisms and impact on its germination and main components, *Scientific Reports.* 6(1) (2016), 38996.

[28] G., Cravotto, A. Binello, L. Orio, Yeşil ekstraksiyon teknikleri, *Agro Food Industry Hi-Tech*. 22(6) (2011), 57-59.

[29] M. Virot, V. Tomao, G. Colnagui, F. Visinoni, F. Chemat, New microwave-integrated Soxhlet extraction: an advantageous tool for the extraction of lipids from food products, *Journal of Chromatography A.* 1174(1-2) (2007), 138-144. doi:10.1016/j.chroma.2007.09.067

[30] A. Yılmaz, N. Tugrul, Effect of ultrasound-microwave and microwave-ultrasound treatment on physicochemical properties of corn starch, *Ultrasonics Sonochemistry*. 98 (2023), 106516. doi:10.1016/j.ultsonch.2023.106516

[31] L. Sillero, R. Prado, J. Labidi, Simultaneous microwave-ultrasound assisted extraction of bioactive compounds from bark, *Chemical Engineering and Processing-Process Intensification.* 156 (2020), 108100. doi:10.1016/j.cep.2020.108100

[32] O. N. Kernou, A. Belbahi, A. Amir, K. Bedjaoui, K. Kerdouche, S. Dairi, O. Aoun, K. Madani,

Effect of sonication on microwave inactivation of Escherichia coli in an orange juice beverage, *Journal of Food Process Engineering*. 44(5) (2021), e13664. doi:10.1111/jfpe.13664

[33] V. L. Singleton, J. A. Rossi, Colorimetry of total phenolics with phosphomolybdic-phosphotungstic acid reagents, *American journal of Enology and Viticulture*. 16(3) (1965), 144-158.

[34] H. W. Huang, S. J. Wu, J. K. Lu, Y. T. Shyu, C. Y. Wang, Current status and future trends of high-pressure processing in food industry, *Food Control*. 72 (2017), 1-8.. doi:10.1016/j.foodcont.2016.07.019

[35] A. C., Stratakos, E. S., Inguglia, M., Linton, J., Tollerton, L., Murphy, N., Corcionivoschi, A. Koidis, B. K. Tiwari, Effect of high pressure processing on the safety, shelf life and quality of raw milk, *Innovative Food Science & Emerging Technologies*. 52 (2019), 325-333. doi:10.1016/j.ifset.2019.01.009

[36] M. Hendrickx, L. Ludikhuyze, I. Van den Broeck, C. Weemaes, Effects of high pressure on enzymes related to food quality, *Trends in Food Science & Technology*. 9(5) (1998), 197-203. doi:10.1016/S0924-2244(98)00039-9

[37] V. M. Balasubramaniam, E. Y. Ting, C. M. Stewart, J. A. Robbins, Recommended laboratory practices for conducting high-pressure microbial inactivation experiments, *Innovative Food Science & Emerging Technologies*. 5(3) (2004), 299-306. doi:10.1016/j.ifset.2004.04.001

[38] L. Zhang, L. Liao, Y. Qiao, C. Wang, D. Shi, K., An, J. Hu, Effects of ultrahigh pressure and ultrasound pretreatments on properties of strawberry chips prepared by vacuum-freeze drying, *Food Chemistry*. 303 (2020), 125386. doi:10.1016/j.foodchem.2019.125386

[39] O. R. Alara, N. H. Abdurahman, C. I. Ukaegbu, Soxhlet extraction of phenolic compounds from Vernonia cinerea leaves and its antioxidant activity, *Journal of Applied Research on Medicinal and Aromatic Plants*. 11 (2018), 12-17. doi:10.1016/j.jarmap.2018.07.003

[40] M. Singla, N. Sit, Application of ultrasound in combination with other technologies in food processing: A review, *Ultrasonics Sonochemistry*. 73 (2021), 105506. doi:10.1016/j.ultsonch.2021.105506

[41] F. Al Juhaimi, N. Uslu, M. M. Özcan, The effect of preultrasonic process on oil content and fatty acid composition of hazelnut, peanut and black cumin seeds, *Journal of Food Processing and Preservation.* 42(1) (2018), e13335. doi:10.1111/jfpp.13335

[42] R. Prithani, K. K. Dash, Mass transfer modelling in ultrasound assisted osmotic dehydration of kiwi fruit, *Innovative Food Science & Emerging Technologies*. 64 (2020), 102407. doi:10.1016/j.ifset.2020.102407

[43] A. Rahaman, X. A. Zeng, A. Kumari, M. Rafiq, A. Siddeeg, M. F. Manzoor, Z. Baloch, Z. Ahmed, Influence of ultrasound-assisted osmotic dehydration on texture, bioactive compounds and metabolites analysis of plum, *Ultrasonics Sonochemistry*. 58 (2019), 104643. doi:10.1016/j.ultsonch.2019.104643

[44] S. Simal, J. Benedito, E. S. Sánchez, C. Rosselló, Use of ultrasound to increase mass transport rates during osmotic dehydration, *Journal of Food Engineering*. 36(3) (1998), 323-336. doi:10.1016/S0260-8774(98)00053-3

[45] J. A. Cárcel, J. Benedito, J. Bon, A. Mulet, High intensity ultrasound effects on meat brining, *Meat Science.* 76(4) (2007), 611-619. doi:10.1016/j.meatsci.2007.01.022

[46] Y. Deng, Y. Zhao, Effects of pulsed-vacuum and ultrasound on the osmodehydration kinetics and microstructure of apples (Fuji), *Journal of Food Engineering*. 85(1) (2008), 84-93. doi:10.1016/j.jfoodeng.2007.07.016

[47] J. Stojanovic, J. L. Silva, Influence of osmotic concentration, continuous high frequency ultrasound and dehydration on antioxidants, colour and chemical properties of rabbiteye blueberries, *Food Chemistry*. 101(3) (2007), 898-906. doi:10.1016/j.foodchem.2006.02.044

[48] B. Xu, E. S. Tiliwa, W. Yan, S. R., Azam, B., Wei, C., Zhou, H. Ma, B. Bhandari, Recent development in high quality drying of fruits and vegetables assisted by ultrasound: A review, *Food Research International.* 152 (2022), 110744. doi:10.1016/j.foodres.2021.110744

[49] F. R. Reis, C. Marques, A. C. S. de Moraes, M. L. Masson, Trends in quality assessment and drying methods used for fruits and vegetables, *Food Control*. 142 (2022), 109254. doi:10.1016/j.foodcont.2022.109254

[50] B. Bchir, M. A. Bouaziz, R. Ettaib, H. Sebii, S. Danthine, C. Blecker, S. Besbes, H. Attia, Optimization of ultrasound-assisted osmotic dehydration of pomegranate seeds (*Punica granatum L.)* using response surface methodology, *Journal of Food Processing and Preservation.* 44 (2020), e14657. doi:10.1111/jfpp.14657

[51] H. Bozkir, A. R. Ergün, E. Serdar, G. Metin, T. Baysal, Influence of ultrasound and osmotic dehydration pretreatments on drying and quality properties of persimmon fruit, *Ultrasonics Sonochemistry.* 54 (2019), 135-141. doi:10.1016/j.ultsonch.2019.02.006

[52] S. Nag, N. Sit, Optimization of ultrasound assisted enzymatic extraction of polyphenols from pomegranate peels based on phytochemical content and antioxidant property, *Journal of Food Measurement and Characterization.* 12 (2018), 1734-1743.

[53] N. Sit, S. C. Deka, S. Misra, Combined effect of ultrasound and enzymatic pretreatment on yield and functional properties of taro (*Colocasia esculenta*) starch, *Starch-Stärke*. 66 (2014), 959-967. doi:10.1002/star.201400085

[54] J. L. Capelo, A. M. Mota, Ultrasonication for analytical chemistry, *Current Analytical Chemistry.* 1(2) (2005), 193-201. doi:10.2174/1573411054021619

[55] H. Wu, J. Zhu, W. Diao, C. Wang, Ultrasound-assisted enzymatic extraction and antioxidant activity of polysaccharides from pumpkin *(Cucurbita moschata*), *Carbohydrate Polymers.* 113 (2014), 314-324. doi:10.1016/j.carbpol.2014.07.025

[56] J. T. Mason, F. Chemat, M. Vinatoru, The extraction of natural products using ultrasound or microwaves, *Current Organic Chemistry*. 15(2) (2011), 237-247. doi:10.2174/138527211793979871

[57] J., Azmir, I. S. M., Zaidul, M. M., Rahman, K. M., Sharif, A., Mohamed, F., Sahena A. K. M. Omar, Techniques for extraction of bioactive compounds from plant materials: A review, *Journal of Food Engineering*. 117(4) (2013), 426-436. doi:10.1016/j.jfoodeng.2013.01.014

[58] H. S. Jeong, H. Y. Kim, S. H. Ahn, S. C. Oh, I. Yang, I. G. Choi, Optimization of enzymatic hydrolysis conditions for extraction of pectin from rapeseed cake (*Brassica napus L.*) using commercial enzymes, *Food Chemistry*. 157 (2014), 332-338. doi:10.1016/j.foodchem.2014.02.040

[59] S. J. Bora, J. Handique, N. Sit, Effect of ultrasound and enzymatic pre-treatment on yield and properties of banana juice, *Ultrasonics Sonochemistry*. 37 (2017), 445-451. doi:10.1016/j.ultsonch.2017.01.039

[60] F. W. F. Bezerra, M. S. De Oliveira, P. N. Bezerra, V. M. B. Cunha, M. P. Silva, W. A. Da Costa, R.H.H. Pinto, R.M. Cordeiro, J.N. da Cruz, A.M.J. Chaves Neto, R. C. Junior, Extraction of bioactive compounds, *In Green Sustainable Process for Chemical and Environmental Engineering and Science*. (2020), 149-167. doi:10.1016/B978-0-12-817388-6.00008-8

[61] A. Gomez-Gomez, E. Brito-de la Fuente, C. Gallegos, J. V. Garcia-Perez, J. Benedito, Non-thermal pasteurization of lipid emulsions by combined supercritical carbon dioxide and high-power ultrasound treatment, *Ultrasonics Sonochemistry*. 67 (2020), 105138. doi:10.1016/j.ultsonch.2020.105138

[62] X. Liu, H. Ou, Z. Xiang, H. Gregersen, Ultrasound pretreatment combined with supercritical CO_2 extraction of Iberis amara seed oil, *Journal of Applied Research on Medicinal and Aromatic Plants*. *18* (2020), 100265. doi:10.1016/j.jarmap.2020.100265

[63] A. S. Döner, Şeker pancarı posasından ultrason destekli pektin eldesinin Taguchi yöntemi ile optimizasyonu, Yüksek Lisans Tezi, *Fen Bilimleri Enstitüsü*, Gıda Mühendisliği Ana Bilim Dalı, Kayseri, 2019.

[64] W. F. Gomes, B. K. Tiwari, Ó.Rodriguez, E. S. de Brito, F. A. N. Fernandes, S. Rodrigues, Effect of ultrasound followed by high pressure processing on prebiotic cranberry juice, *Food Chemistry*. 218 (2017), 261-268. doi:10.1016/j.foodchem.2016.08.132

[65] D. Jadhav, B. N. Rekha, P. R. Gogate, V. K. Rathod, Extraction of vanillin from vanilla pods: A comparison study of conventional soxhlet and ultrasound assisted extraction, *Journal of Food Engineering*. 93(4) (2009), 421-426. doi:10.1016/j.jfoodeng.2009.02.007

[66] V. M. Karizaki, S. Sahin, G. Sumnu, M. T. H. Mosavian, A. Luca, (Effect of ultrasound-assisted osmotic dehydration as a pretreatment on deep fat frying of potatoes, *Food and Bioprocess Technology*. 6 (2013), 3554-3563.

[67] S. B. Glisic, M. Ristic, D. U. Skala, The combined extraction of sage (Salvia officinalis L.): Ultrasound followed by supercritical CO_2 extraction, *Ultrasonics Sonochemistry*. 18(1) (2011), 318-326,. doi:10.1016/j.ultsonch.2010.06.011